Airborne in situ measurements of short-lived chlorocarbons and investigation of their pathways from northern hemispheric source regions into the lowermost stratosphere

---

Dissertation
zur Erlangung des Doktorgrades
der Naturwissenschaften

vorgelegt der
Bergischen Universität Wuppertal
Fakultät 4: Mathematik und Naturwissenschaften

von
Valentin Michael Lauther

Wuppertal, 2020

The PhD thesis can be quoted as follows:

urn:nbn:de:hbz:468-20210824-093734-9
[http://nbn-resolving.de/urn/resolver.pl?urn=urn%3Anbn%3Ade%3Ahbz%3A468-20210824-093734-9]

DOI: 10.25926/kqvq-hb36
[https://doi.org/10.25926/kqvq-hb36]

Abstract

Chlorine containing very short-lived species (Cl-VSLS) are predicted to threaten the timely recovery of the stratospheric ozone layer to pre-1980 values (Hossaini et al. 2015b, 2017, 2019). In addition, the contribution of Cl-VSLS to the reduction of ozone in the upper troposphere and lower stratosphere (UTLS) has an impact on surface climate (Riese et al., 2012). To the present day, there is no direct observational evidence for a fast transport pathway of Cl-VSLS from the source regions into the UTLS because in situ measurements of Cl-VSLS in the UTLS are complex and thus extremely rare. The aim of the present work is to identify and describe such fast transport pathways on the basis of airborne in situ observations in the UTLS above western Europe and the Atlantic Ocean.

In order to investigate transport processes and the distribution of Cl-VSLS in the UTLS, the airborne five channel trace gas analyzer HAGAR-V (High Altitude Gas Analyzer - 5 channel version; vom Scheidt, 2013b) was modified. For the two channel GC/MS module (two gas chromatographs (GC) coupled to one quadrupole mass spectrometer (MS)) of HAGAR-V a new sample preconcentration unit as well as a novel type of fast ramping temperature controlled GC column oven was developed and characterized. On its first successful deployment on the research aircraft HALO (High Altitude and LOng range) during the WISE (Wave-driven ISentropic Exchange) campaign in autumn 2017, the GC/MS module measured the two major Cl-VSLS (CH_2Cl_2 and $CHCl_3$) and five long-lived species (CH_3Cl, CFC-11, CFC-113, HFC-125, and HFC-134a) at a time resolution of 3 minutes and average precisions of about 1–4 % of tropospheric background depending on species. This was achieved by using only one of the two GC/MS channels.

The novel data set is analyzed for optimal processing routines to optimize the accuracy and the precision. The use of two different in-flight calibration gases provides several options for the calculation of mixing ratios. In general, a quadratic relationship between mixing ratios and MS detector response yields the most accurate results. Several in-flight diagnostic modes are used to derive specific data corrections and processing methods depending on flight and species. A comparison between CFC measurements with HAGAR-V's GC/MS and ECD (Electron Capture Detector) modules shows a generally good agreement with only insignificant differences between the two modules.

WISE measurements with the MS module in the lowermost stratosphere (LMS) reveal distinct entries of CH_2Cl_2-rich and CH_2Cl_2-poor air when correlated with the long-lived tracer N_2O. The CH_2Cl_2-rich air exhibits mixing ratios up to 130 % higher than CH_2Cl_2-poor air. These measurements are analyzed with the help of artificial tracers of air mass origin and backward trajectories calculated with the Chemical Lagrangian Model of the Stratosphere (CLaMS). In addition, the measurements are qualitatively compared to ground-based observations of the Advanced Global Atmospheric Gases Experiment (AGAGE) network as well as to low-level aircraft measurements from East Asia.

It is concluded that the WISE measurements of CH_2Cl_2-poor air in the northern hemisphere (NH) UTLS reflect the tropical CH_2Cl_2 surface background seasonality from along the western part of the Inter-Tropical Convergence Zone (ITCZ). Fast convection above the region of Central America (maximum averaged diabatic ascent rate 24 K/18 h) uplifts CH_2Cl_2-poor air from the boundary layer (BL) to the tropical tropopause layer (TTL) from where it isentropically enters the extratropical UTLS on a relatively direct path. Transport times along this pathway range between two weeks and two months and are short enough for the Cl-VSLS to enter the UTLS with barely reduced mixing ratios compared to the BL. This transport pathway primarily contributes to CH_2Cl_2-poor air in the NH LMS (mainly between $\sim$ 345 K and $\sim$ 375 K of potential temperature). In addition, the major hurricane Maria could be identified to have significantly contributed to the transport of CH_2Cl_2-poor air into the UTLS along this pathway. This study presents for the first time an observation-based transport analysis for CH_2Cl_2, connecting the BL along the western ITCZ to the NH LMS via convection above Central America.

Measurements of CH_2Cl_2-rich air in the LMS are identified to almost exclusively originate in southern and eastern Asia. It is shown that these air masses were transported via convective updraft of the Asian summer monsoon (ASM). Key part of this transport pathway into the NH LMS is the additional slow upwelling within the ASM anticyclone (ASMA) to potential temperature levels of 380 K or more. The transport of CH_2Cl_2-rich air continues eastward along the subtropical jet stream and enters the extratropical LMS above the Pacific or the Atlantic Ocean. Compared to the transport of CH_2Cl_2-poor air from the western ITCZ into the NH LMS, transport via the ASMA is relatively slow (on average two months). However, it is fast enough to cause tropospheric intrusions of particularly high CH_2Cl_2 mixing ratios into the NH LMS. In general, out of young (< 6 months) air masses those originating from southern and eastern Asia dominate the larger part of the

NH LMS in summer with air parcel fractions ≥ 50 %, thereby strongly impacting the trace gas distribution in the LMS with CH_2Cl_2-rich air. The present work provides the first direct evidence for the strong impact of CH_2Cl_2-rich air from Asian sources on the NH LMS on the basis of airborne in situ observations.

$CHCl_3$ shows similar but less pronounced features as CH_2Cl_2 when correlated with N_2O. It is very likely that relatively $CHCl_3$-rich air in the LMS originated from similar (anthropogenic) sources in southern and eastern Asia as the CH_2Cl_2-rich air. In contrast to CH_2Cl_2, $CHCl_3$ mixing ratios in the UT and the tropopause region can be equally high as the relatively $CHCl_3$-rich air from southern and eastern Asia in the LMS. Other sources thus likely contribute with relatively $CHCl_3$-rich air to the $CHCl_3$ distribution in the LMS. However, at least in the LMS, samples of CH_2Cl_2-poor air from the western ITCZ also contain $CHCl_3$-poor air. It is concluded that the extraordinarily high Asian CH_2Cl_2 and $CHCl_3$ emissions (e.g. Leedham-Elvidge et al., 2015; Oram et al., 2017; Feng et al., 2018; Fang et al., 2018) strongly enhance CH_2Cl_2 mixing ratios in the NH LMS but enhance those of $CHCl_3$ to a lesser degree (enhancement > 100 % and > 50 %, respectively).

Contents

Chapter 1

Introduction

Since the time of the industrialization in the 19th century a slow but steady change in the Earth's climate is observed (e.g. Arneth et al., 2019). The understanding and prediction of this change is subject to atmospheric research. The results of such atmospheric research provide the basis for public and policy action because consequences of climate change can have a strong impact on public health, on ecological and economical conditions, and are thus of political interest. It is therefore crucial to precisely understand the processes that cause a changing climate to be able to accurately describe and predict the consequences of it.

The Earth's atmosphere is a very complex system providing for the existence of most life on the planet. The following general information are described in more detail for instance by Wallace and Hobbs (2006). The atmosphere is organized in different layers based on its vertical temperature profile. The present work focuses only on the two layers closest to the surface which consist of about 90 % of the total mass of the Earth's atmosphere. The troposphere is closest to the surface and separated from the stratosphere above by the tropopause. The troposphere reaches much higher in the tropics (~ 16 km) than at the poles (~ 8 km) and is the source region of most trace gases. The stratosphere consists of dry and ozone (O_3) rich (known as the ozone layer) air. This ozone layer absorbs more than 97 % of the Sun's medium-frequency ultraviolet (UV) light and thus protects most life forms on the planet from exposure to this hazardous radiation. As a consequence to the UV absorption the temperature in the stratosphere rises with altitude, thus providing an enhanced static stability compared to the troposphere where the opposite is the case.

The following information are described in more detail for instance by WMO (2018). With the begin of an excessive industrial production and release to the atmosphere of chlorine

(Cl) containing long-lived substances (e.g. chlorofluorocarbons (CFCs), hydrochloroflourocarbons (HCFCs), halogenated hydrocarbons) in the 1950s, rising numbers of chlorine reached the stratosphere threatening to deplete the ozone layer via a catalytic reaction[1]. Relatively fast global reactions to that threat, by successively banning these ozone depleting substances (ODS) from global production, yields a slow but steady recovery of the ozone layer to pre-1980 values probably in the next 30–40 years (Figure 1.1, left). The global restrictions for the production of ODSs were recorded in the Montreal Protocol (1987) and its Amendments and Adjustments[2]. CFCs like CFC-11, CFC-12, and CFC-113 are not only strong ODSs they are also strong greenhouse gases. After recognizing their (stratospheric) ozone depleting potential (ODP[3]) in the 1980s they were short after banned from production and replaced by the weaker ODSs, the HCFCs, which themselves were successively banned from production in the early 2000s to be replaced by HFCs. The HFCs do not impact the ozone layer but are greenhouse gases contributing to the global warming and the production of some HFCs have thus currently been regulated in the latest Amendment of the Montreal Protocol.

Figure 1.1 (right) shows the trends from 1950 to 2100 of atmospheric abundance of the most prominent ODSs. At some time in the 20th century most species show a fast increase of mixing ratios indicating strongly enhanced emissions. In particular the CFCs as well as anthropogenic halogenated hydrocarbons show slowly declining (depending on atmospheric lifetime) atmospheric mixing ratios at the beginning of the 21st century, indicating less anthropogenic emissions than atmospheric removal by natural sinks. For these species the global restrictions from the Montreal Protocol already show a positive effect. The emissions of HCFCs are still larger than the atmospheric sinks can compensate and thus the turning point of declining atmospheric HCFC abundance has yet to come but it is predicted to be in the near future.

The main transport of trace gases from the troposphere (source region) to the stratosphere occurs in the tropics and follows the global Brewer-Dobson circulation (Brewer, 1949; Dobson, 1956). The transport time of any trace gas from the troposphere to the extratropical stratosphere via the Brewer-Dobson circulation is on the order of years with few short-cut possibilities at the tropical lower stratosphere (e.g. Volk et al., 1996). Mainly due to the relatively slow transport from the troposphere to the stratosphere (and consequently to the ozone layer) only long-lived ODSs of anthropogenic origin were globally banned from

---

[1] The reaction is: $\mathrm{Cl} + \mathrm{O_3} \rightarrow \mathrm{ClO} + \mathrm{O_2}$; $\mathrm{ClO} + \mathrm{O} \rightarrow \mathrm{Cl} + \mathrm{O_2} \overset{\text{net.}}{\Rightarrow} \mathrm{O} + \mathrm{O_3} \rightarrow 2\mathrm{O_2}$

[2] Further just referred to as the Montreal Protocol

[3] The ODP describes the impact on stratospheric ozone relative to CFC-11

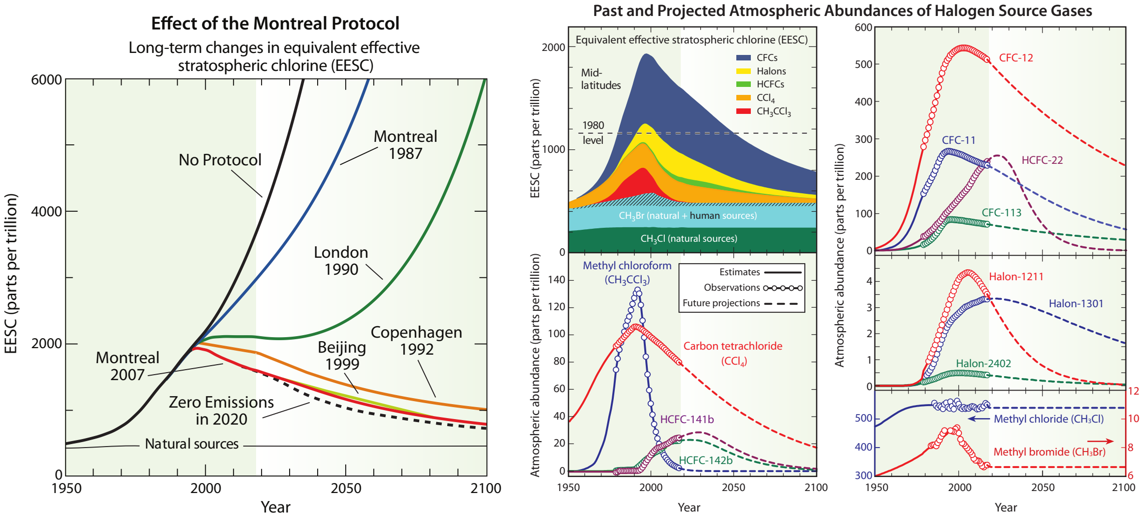

Figure 1.1: Observed and predicted trends of equivalent effective stratospheric chlorine for different scenarios depending on the regulations formulated in the Montreal Protocol and its Amendments and Adjustments (left). Observed and predicted mixing ratios of several ODSs (right). Figures taken from Salawitch et al. (2019).

production. Halogenated very short-lived species (VSLS) with an atmospheric lifetime < 6 months are excluded from this ban of production.

Dichloromethane (CH_2Cl_2) and chloroform (trichloromethane; $CHCl_3$) are referred to as chlorine containing very short-lived species (Cl-VSLS) due to their tropospheric lifetime of about 3–7 months (e.g. WMO, 2014, 2018). Due to this short lifetime and therefore believed low risk of entering the stratosphere in significant numbers the production of both species is not controlled by the Montreal Protocol. In the last decade a strongly increasing emission of chlorine containing short-lived species, in particular of dichloromethane (CH_2Cl_2), gives new reason to question the predicted recovery of the ozone layer (e.g. Hossaini et al., 2015a; Fang et al., 2018). Estimates about the impact on stratospheric ozone from Cl-VSLS exist on the basis of model calculations validated by whole air samples collected on scientific aircrafts (e.g. Hossaini et al. 2015b, 2017, 2019). More detailed information about Cl-VSLS is given in Section 1.3.

Even small changes in the distribution of greenhouse gases and ODSs in the lower stratosphere can have a strong impact on radiative forcing and surface temperatures (Riese et al., 2012; Hossaini et al., 2015a). Thus, the upper troposphere and lower stratosphere (UTLS) is a key region for the understanding and prediction of climate change (Hegglin and Shepherd, 2009; Solomon et al., 2010). Consequently it is of crucial importance to identify and quantify transport and mixing processes in the UTLS (Gettelman et al., 2011). Up to the present day, not all of the processes influencing the distribution of trace gases in the UTLS are fully understood. Hence, predictions of climate changing effects from model calculations, which are additionally limited in their accuracy due to computational constraints, still need improvement provided by the analysis of observations.

The important question addressing which transport pathway, from the source region into the stratosphere, is fast enough that a significant number of Cl-VSLS reaches the stratosphere, could not be clearly answered on the basis of obsrervations to this day. To determine such a transport pathway highly resolved measurements of Cl-VSLS in the UTLS are crucial. The present work is primarily addressing the question for an efficient transport pathway for Cl-VSLS into the stratosphere on the basis of experimental in situ observations of CH_2Cl_2 and $CHCl_3$ in the UTLS region. To achieve these measurements a novel airborne instrument was modified and optimized over the course of the present work. In the following sections more specific and profound scientific background is given to provide the necessary context for the following chapters.

1.1 Transport into the lowermost stratosphere

A very interesting (and for Cl-VSLS particularly important) part of the stratosphere is called the lowermost stratosphere (LMS[4]). The unequally distributed tropospheric height from the equator to the poles causes isentropic surfaces[5] from the tropical troposphere to enter the stratosphere in the extratropics (e.g. Figure 1.2). The part of the stratosphere that shares isentropes with the troposphere up to a potential temperature of about 380 K is called the LMS (Hoskins et al., 1985). The main transport pathways into the LMS are either on isentropes from the troposphere or by downwelling from the stratosphere (Holton et al., 1995).

To reach the LMS from the troposphere, the tropopause has to be crossed. In general, the (thermal) tropopause is defined to be the lowest surface of an atmospheric layer (of at least 2 km in height) for which the vertical temperature gradient (lapse rate) is ≥ -2 K/km. However, for practical use, the thermal tropopause is not always a good measure for the location of the tropopause. On the one hand, the value of -2 K/km is quite arbitrarily fixed and on the other hand the tropopause is thermally undifferentiated in the area of dynamical disturbances (e.g. Bethan et al., 1996). The tropopause height can also be defined by the distribution of chemical tracers, dependent on the gradient of the tracer's

---

[4] If not further specified in the course of the present work, LMS implicates the lowermost stratosphere of the northern hemisphere

[5] surfaces of constant entropy /constant potential temperature

mixing ratios between the troposphere and the stratosphere. For the definition of the chemical tropopause trace gases, aerosols and tracer-tracer correlations (e.g. Hoor et al., 2002; Section 1.2) can be used. The advantage of a chemical tropopause derived from in situ measurements of high temporal and spatial resolution is the identification of small scale structures in the tropopause. However, this method is most effective for the investigation of local events while the thermal definition of the tropopause is preferred to analyze mesoscale and global meteorological events. In the present work mostly the chemical tropopause derived from N_2O measurements is used.

The following example schematically describes the transport of differently composed air into the LMS on the basis of the general transport mechanisms described in Holton et al. (1995). Figure 1.2 shows a cross-section through the LMS from equator to pole on a schematic drawing. The solid black lines indicate surfaces of constant potential temperature and the bold black line shows the tropopause. The troposphere is below and the stratosphere above the tropopause. The gray shaded area shows the LMS while the two gray blocks indicate horizontal transport barriers. This schematic view shows reservoirs of differently composed air and their respective potential transport pathway into the LMS. The boundary layer is the source region of most trace gases in the atmosphere. Atmospheric dynamics cause air from the different reservoirs shown in Figure 1.2 to have spent different time away from their source region and to have experienced different atmospheric surroundings. This implies that each reservoir consists of air of different age therefore the chemical composition is different in each reservoir caused by the different atmospheric lifetimes of various chemical species. For example on one hand downwelling air from the polar vortex (only in winter) has gone through the whole Brewer-Dobson circulation. In this example it represents the oldest air that has experienced the highest altitudes (highest chances of photolysis) and thus consists only of species with large atmospheric lifetimes. On the other hand air from the free troposphere consists of much younger air and can potentially bring a detectable amount of short-lived species into the LMS via isentropic transport.

In summer isentropic transport from the troposphere into the LMS is dominant while in winter the largest entry into the LMS comes from the stratosphere above (Hoor et al., 2005; Bönisch et al., 2009). The time of enhanced isentropic transport into the LMS coincides with the season of the Asian summer monsoon (ASM). The ASM was found to be a major transport pathway for greenhouse gases like water vapor and methane (e.g. Ploeger et al., 2013; Vogel et al., 2014, 2016; Rolf et al., 2018; Nützel et al., 2019) as well as other pollutants (e.g. Lelieveld et al., 2002; Randel et al., 2010; Yu et al., 2017) from Asia into the northern hemispheric extratropical lower stratosphere.

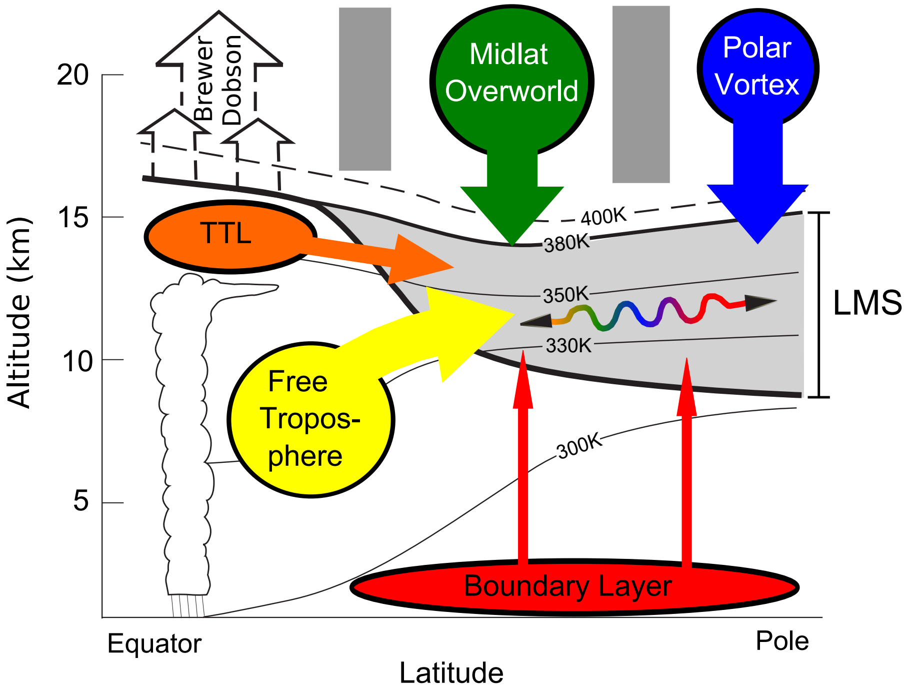

Figure 1.2: Schematic drawing of transport pathways from different reservoirs containing differently composed air into the lowermost stratosphere (LMS, gray shaded area). The gray blocks indicate horizontal transport barriers in the stratosphere. The solid black lines represent the surfaces of constant potential temperature. The bold black line indicates the tropopause with the troposphere being located below and the stratosphere being located above that line. From the troposphere fast convective updraft from the boundary layer (red) can (rarely) enter the LMS. More frequent is isentropic transport from the free troposphere (yellow) and the tropical tropopause layer (TTL; orange) into the LMS. Downwelling from the stratosphere to the LMS comes from the mid-latitude overworld (green) and the polar vortex (blue, only in winter). The multi colored arrow indicates the mixing of air from the different reservoirs in the LMS. Background of panel adapted from Holton et al., 1995.

Between June and September two large monsoon systems (low pressure systems) over India and over Southeast and East Asia are unifyingly referred to as the ASM (e.g. Yihui and Chan, 2005). The ASM is linked to fast vertical transport of surface air to the upper troposphere (~ 360 K of potential temperature). Above that, in the UTLS, is the large ASM anticyclone (ASMA), a high pressure system that spreads over almost whole Asia south of the subtropical jet stream (~ 40°N). The ASMA was observed to further transport the convected air upwards on spiraling trajectories to higher potential temperatures (e.g. Müller et al., 2016; Vogel et al., 2016). To some degree air inside the ASMA is somewhat horizontally confined due to a transport barrier at the ASMA's edge, characterized by a potential vorticity gradient (Ploeger et al., 2015). The ASMA is a dynamical structure and meridional displacements, splits, or eddy-shedding events allows air from within the

ASMA to escape. The air can thereby be horizontally transported westwards to enter the tropical tropopause layer (TTL; Popovic and Plumb, 2001; Randel and Park, 2006) or follow the subtropical jet stream eastwards to subsequently cross the tropopause entering the lower stratosphere via eddy-shedding events (e.g. Dethof et al., 1999; Hsu and Plumb, 2000; Vogel et al., 2014, 2016). These eddy-shedding events are frequently triggered by Rossby wave activity and transport significant parts of tropospheric air from Asia into the LMS (e.g. Vogel et al., 2014, 2016; Müller et al., 2016). The present work focuses on the latter transport pathway induced by the ASM because a significant rise in the Asian emissions of Cl-VSLS (e.g. Leedham-Elvidge et al., 2015; Hossaini et al., 2017; Oram et al., 2017; Feng et al., 2018; Fang et al., 2018; Chipperfield et al., 2020) gives reason to believe that a rising number of these ozone depleting substances are able to reach the stratosphere to consequently delay the recovery of the stratospheric ozone layer to pre-1980 values (e.g. Hossaini et al., 2019; Claxton et al., 2019). Cl-VSLS are discussed in detail in Section 1.3.

1.2 Tracer-tracer correlation

The interpretation of observed trace gas distributions in the UTLS is often very difficult due to the complexity of transport processes. The interpretation is particularly complex for one-dimensional measurements from a moving platform in a 3-dimensional dynamical space, e.g. in situ measurements from an instrument on an aircraft. An ideal reference frame for the interpretation of aircraft measurements is the tracer-tracer-space, a 2-dimensonal space where the measurements collected in 3-dimensional space can be separated into different regions indicating their origin (e.g. stratosphere or troposphere). Tracer-tracer correlations to determine atmospheric transport and mixing processes were first introduced by Plumb and Ko (1992). The concept was fast adapted and established to extract information from aircraft measurements primarily to quantify transport, stirring, and mixing of different air masses in the UTLS and to determine respective timescales for these processes (e.g. Boering et al., 1994; Volk et al., 1996, 1997; Waugh et al., 1997; Plumb et al., 2000; Plumb, 2002; Hoor et al., 2002; Ray, 2002; Jost, 2002; Müller et al., 2005; Werner et al., 2010).

In general, tracers are defined as quantities that are conserved for a longer time than the transport time scales in the regarded environment (here the UTLS). These tracers can be dynamical tracers as the potential temperature or the potential vorticity (conserved for days to weeks) as well as chemical tracers with chemical lifetimes larger than weeks. Another category are passive tracers in numerical simulations (e.g. conserving the geographical information of air parcel origin).

The static stability of the stratosphere inhibits vertical mixing and most efficient transport is quasi-horizontal (isentropic; Plumb, 2007). In the stratosphere transport time scales for large-scale quasi-horizontal flow are on the order of a few days and nearly adiabatic. The correlation of two tracers is linear only when the lifetime of both tracers is large compared to the vertical transport time. Then the tracer-tracer correlation slope is independent of the place of measurement and only defined by the local lifetime of the tracers.

Among the many advantages of the interpretation of tracer-tracer correlations is the elimination of temporal and spatial atmospheric variability affecting both tracers alike, i.e. tracer-tracer correlations are compact. The compactness is climatological and based on transport, such that long-lived tracers, even with different sources or sinks, express a (geometrically) similar distribution in the stratosphere (Plumb and Ko, 1992). Any disturbance of this compactness represents an anomaly that can be interpreted in the atmospherical context, e.g. could be the result of in-mixing of air from a different reservoir (cf. Section 1.1). The different reservoirs in the stratosphere (tropics, mid-latitues, and the winter polar region) are mostly confined by transport barriers and each reservoir expresses different correlation curves, providing the basis for the analysis of exchange between these reservoirs.

The stratospheric concept of tracer-tracer correlations can somewhat be extended to the upper troposphere with its less separated reservoirs by including the analysis of tracers with shorter lifetimes. However, this requires more profound understanding about the source regions and global emission distributions of the short-lived tracers to avoid misinterpreting the correlations. Using the short-lived tracer carbonmonoxide (CO; photochemical lifetime on the order of weeks to months), correlations with O_3 were used to determine transport processes around tropopause folds (e.g. Danielsen et al., 1987; Hipskind et al., 1987), convective updraft in the extratropics (e.g. Dickerson et al., 1987; Poulida et al., 1996), to define the extratropical tropopause (Pan et al., 2004; Konopka and Pan, 2012), and to determine transport and mixing processes in the UTLS region (Zahn et al., 2000; Hoor et al., 2002; Konopka and Pan, 2012; Müller et al., 2016), and have been described for the polar lower stratosphere (Fischer et al., 2000). CO correlations with the long-lived tracer N_2O (photochemical lifetime of 123 years; Ko et al., 2013) have also been used for the analysis of mixing processes in the polar lower stratosphere (Krause et al., 2018). The complexity of tracer-tracer correlations with CO is that CO has atmospheric sources.

The Cl-VSLS CH_2Cl_2 and $CHCl_3$ both have longer atmospheric lifetimes than CO (3–7 months in the troposphere, WMO, 2018; 1–2 years in the stratosphere, Hossaini et al., 2017) and no known atmospheric sources. This implies that transport of enhanced Cl-

VSLS mixing ratios from the troposphere into the LMS can be identified in tracer-tracer correlations of Cl-VSLS with long-lived tracers. Due to the relatively short lifetime and large global emission gradients, it is expected that the correlation of CH_2Cl_2 and $CHCl_3$ with a long-lived tracer is not linear but also different from the clear “L-shape” of the CO-N_2O correlation. To this day no tracer-tracer correlation transport analysis of the UTLS region based on real-time in situ measurements of CH_2Cl_2 or $CHCl_3$ has been conducted and is for the first time presented in this work (Chapter 4).

1.3 Overview on CH_2Cl_2 and $CHCl_3$

The main focus of the analysis presented in this work is on the two Cl-VSLS CH_2Cl_2 and $CHCl_3$. The following sections give an overview on these two species organized by different topics relevant for the context of the analysis presented in Chapter 4.

1.3.1 Sources of CH_2Cl_2 and $CHCl_3$

The sources of either CH_2Cl_2 or $CHCl_3$ are not accurately known. In the latest report on ozone depletion (WMO, 2018) the anthropogenic fraction of released CH_2Cl_2 has been approximated with 90 % and 50 % of released $CHCl_3$. The residual 10 % and 50 % of released CH_2Cl_2 and $CHCl_3$, respectively, are further of natural origin. While in other literature there is general agreement for CH_2Cl_2 being almost exclusively of anthropogenic origin, $CHCl_3$ seems much more difficult to estimate, partly due to a strong variability of its regional anthropogenic sources (Gentner et al., 2010). In the beginning of this century the anthropogenic fraction of $CHCl_3$ is estimated to have declined from about 50 % in 1990 to about 30 % (Worton et al., 2006) or even down to only 10 % (McCulloch, 2003) while studies from Antarctic firn air suggest an anthropogenic fraction of 60 % (Trudinger et al., 2004).

The most important natural source of $CHCl_3$ is the release from offshore seawater probably induced by algae and by bacterial activity followed by the emission from natural processes in soil like the chlorination of soil acids (McCulloch, 2003). Further can termite mounds, forests, volcanic activities and other geological processes be added to important natural $CHCl_3$ emission sources (Laturnus et al., 2002). CH_2Cl_2 has similar natural sources (Gribble, 2010) although not much research on that topic has been conducted. With a CH_2Cl_2 emission estimate mangroves in the tropics were assumed to contribute only with 0.3 % to the total global CH_2Cl_2 emissions (Kolusu et al., 2018).

The oceans themselves have long been considered to be both a source and a sink for chloromethanes. Moore (2004) found the ocean to be no permanent CH_2Cl_2 sink (besides the absorption of about 0.1 % of industrial emissions) with the ability to temporarily store CH_2Cl_2 and further release it back to the atmosphere. He did not find any evidence of an oceanic CH_2Cl_2 source. Nevertheless, for the CH_2Cl_2 present in ocean water Kolusu et al. (2017) showed that its release is not coupled to the sea surface temperature. In the same paper they find no correlation between CH_2Cl_2 and CH_3Cl (Chloromethane) — a species with predominantly natural sources (WMO, 2018) — in seawater implicating different oceanic sources for the two species. This could also be an indication that CH_2Cl_2 is only temporarily stored in the oceans from the atmosphere and has no natural sources in the ocean. In contrast, the oceans are considered to contribute about half of the total natural $CHCl_3$ emissions due to the production from micro- and macroalgae (Laturnus et al., 2002).

Anthropogenic sources of CH_2Cl_2 and $CHCl_3$ emissions are better understood and come partly from the non-chemical industry like pulp and paper manufacture, drinking, waste and cooling water treatment as well as from the chemical and pharmaceutical industry (Aucott et al., 1999; McCulloch, 2003). Both CH_2Cl_2 and $CHCl_3$ are the main co-products needed for any manufacturing process of chloromethanes. On average, the relative production ratio was 40:60 (CH_2Cl_2:$CHCl_3$) in the phase of large HCFC production but that changed to a fraction of 50:50 due to the reduced need in HCFC-22 ($CHClF_2$) for the production of which almost all of the produced $CHCl_3$ is needed (Oram et al., 2017). The production of HCFC-22 is controlled by the Montreal Protocol and about 55 % to 65 % of the total global emissions within the last decade are estimated to be of Chinese production (Simmonds et al., 2018). Once used to manufacture another chloromethane the feedstock cannot be further released into the atmosphere. From all the produced $CHCl_3$ the amount that is converted into other materials has been estimated to be over 95 % (McCulloch, 2003; Chipperfield et al., 2020). Only 15 % of the produced CH_2Cl_2 was estimated to be used for the production of HFC-32 in 2016 (Chipperfield et al., 2020). The remainding fraction not used as feedstock for the production of other chloromethanes (~ 5 % of $CHCl_3$; ~ 85 % of CH_2Cl_2) gets emitted into the atmosphere in form of chemical solvent, paint stripper, and degreasing agent (McCulloch and Midgley, 1996; Montzka et al., 2011) as well as through foam blowing and agricultural fumigation (Oram et al., 2017). This is consistent with the comparably high atmospheric abundance of CH_2Cl_2 with at the same time much lower relative release from natural sources than $CHCl_3$.

Biomass burning as a source for CH_2Cl_2 has declined over the last 3 decades. Air measurements in 1991 at the Ivory Coast suggested biomass burning to be a major source of global CH_2Cl_2 emissions contributing with ~ 15 % of the total emissions in the 1980s and being the most important source in the southern hemisphere (Rudolph et al., 1995). The same measurements showed $CHCl_3$ to be only slightly released from biomass burning and Rudolph et al. (1995) estimated biomass burning sources to be 1–2 % of the global $CHCl_3$ emissions. A few years later during the INDOEX[6] aircraft campaign in 1999 over India and Southeast Asia, Scheeren et al. (2002) found that biomass burning is a small but significant source of both CH_2Cl_2 emissions as well as $CHCl_3$ emissions. To the same suggestion for $CHCl_3$ come Bourtsoukidis et al. (2017) during the OMO[7] aircraft campaign in 2015 by correlating Benzene with $CHCl_3$. Latest publications regarding biomass burning emissions of CH_2Cl_2 state to have found no evidence of CH_2Cl_2 being emitted in biomass burning events all over the globe. Boreal forest fires in 2009 showed no evidence of CH_2Cl_2 emissions being correlated to that event (Simpson et al., 2011). Neither did fires from the Brazilian rainforest nor IAGOS-CARIBIC[8] measurements near the equator show any connection between biomass burning events and enhanced CH_2Cl_2 (Leedham-Elvidge et al., 2015) and during several forest burn measurements in Tasmania Simmonds et al. (2006) found rather good correlations of CH_2Cl_2 with the purely industrial tracer HFC-134a in contrast to correlations of CH_2Cl_2 with the biomass burning tracer CO. Hence most recent and long-term observations do not find CH_2Cl_2 being significantly released by the burning of biomass of different biological composition and/or regional origin. In contrast, research tends to find $CHCl_3$ being at least in small amounts emitted by biomass burning.

To summarize, the total emission sources of CH_2Cl_2 can be identified to be of about 90 % of industrial origin with few natural sources from which oceanic and biomass burning emissions could be excluded. $CHCl_3$ is believed to be of only 50 % of anthropogenic origin and about half of the natural emission sources are located in the oceans and the other half of natural emission sources are land based.

1.3.2 Global source regions of CH_2Cl_2 and $CHCl_3$

Based on NOAA[9] surface measurements, Hossaini et al. (2017) estimate the global emission sources of CH_2Cl_2 to be 1 Tg/year (~ 0.84 (Tg Cl)/year) which is more than any other major ODS at their peak emission time (e.g. CFC-11: ~ 0.3 (Tg Cl)/year in 1986; Daniel et al., 2007). On the basis of flask sample analysis from low level aircraft flights in 2016,

---

[6] Indian Ocean Experiment

[7] Oxidation Mechanism Observation

[8] In-Service Aircraft for a Global Observing System-Civil Aircraft for the Regular Investigation of the atmosphere Based on an Instrument Container

[9] National Oceanic and Atmospheric Administration

north and south India are contributing about 10 % to the global emissions of CH_2Cl_2 (Say et al., 2019). According to Feng et al. (2018) China contributes with 25–37 % to the global CH_2Cl_2 emissions, with an annual growth rate of about 11.6 % of their CH_2Cl_2 emissions. With a different approach Oram et al. (2017) estimated the contribution of Chinese CH_2Cl_2 emissions in 2015 to be about 45 % of the global emissions. Nevertheless, in both cases China plays a significant role in the global emissions of CH_2Cl_2. Stating a constant rise since 2005 Feng et al. (2018) further estimate the annual CH_2Cl_2 emissions from China to be about 700 Gg in 2030.

Data obtained in the tropopause region from IAGOS-CARIBIC show a two- to fourfold increase of CH_2Cl_2 emissions from India between 1998 and 2008 whereas Asia in general seems to have gained importance in the last years regarding the emissions of CH_2Cl_2 (Leedham-Elvidge et al., 2015; Oram et al., 2017). Clear enhancement of CH_2Cl_2 mixing ratios were found between ~ (25–50)°N during the Asian Summer Monsoon (ASM) season but almost no gradient of mixing ratios between ~ (10–50)°N during the non-ASM seasons has been observed where smaller elevations below ~ 20°N mostly originated from Southeast Asia (Leedham-Elvidge et al., 2015). They also observe a rise of about 60 % in the elevation of CH_2Cl_2 mixing ratios during the ASM season between 1998 and 2008 indicating an increase of industrial production in the core region of the ASM.

Regarding $CHCl_3$ Fang et al. (2018) found by combining the ground-based observations of the AGAGE[10] network with model results an average decrease in mixing ratios of -0.7 %/year during 1995–2010 and an increase of 3.5 %/year in the period of 2010–2015. Interestingly their non-Asian measurement stations did not show any significant increase in sources. Scheeren et al. (2003) measured clearly elevated $CHCl_3$ mixing ratios in Asian air plumes during the MINOS[11] campaign already in 2001 whereas CH_2Cl_2 has only been slightly elevated in these plumes. This could implicate that $CHCl_3$ played a more important role in Southeast Asian industrial emissions than CH_2Cl_2 at the beginning of this century. With an average increase of ~ 8 %/year of CH_2Cl_2 mixing ratios between 2000 and 2010 (Hossaini et al., 2015a) and a doubling of the growth rate from 2005–2015 (Hossaini et al., 2017) this drastically changed soon after.

During the INTEX-B[12] aircraft campaign (April–May, 2006) whole air samples have been collected from pollution plumes associated with China, other Asian countries, and the USA. Barletta et al. (2009) analyzed these samples for CH_2Cl_2 and $CHCl_3$ and found an average increase above background mixing ratios in Chinese plumes of 91 % and 86 %, in

---

[10] The Advanced Global Atmospheric Gases Experiment

[11] Mediterranean INtensive Oxidant Study

[12] The Intercontinental Chemical Transport Experiment - Phase B

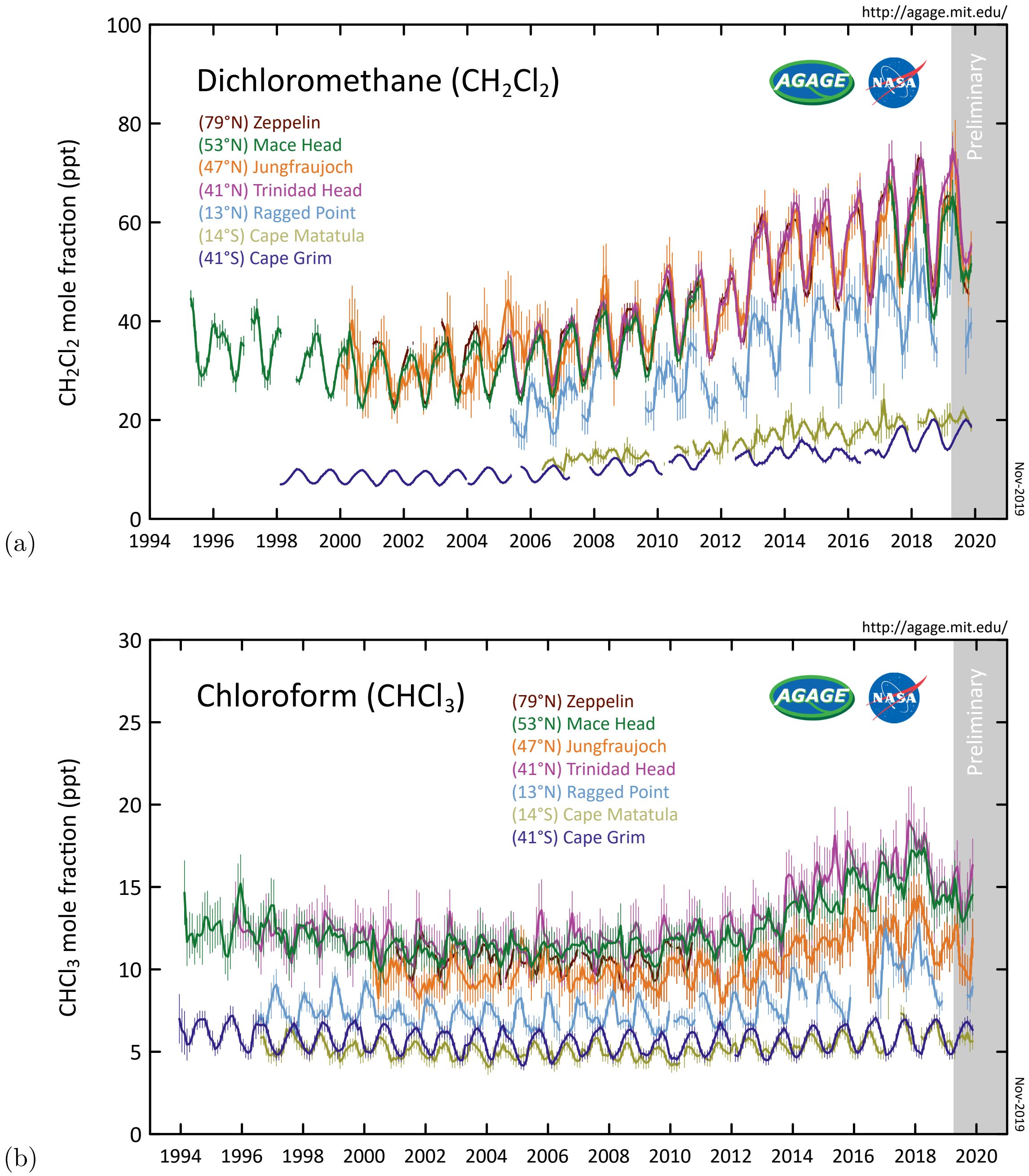

Figure 1.3: Ground-based long-term observations of (a) CH_2Cl_2 and (b) $CHCl_3$ from the AGAGE network (Prinn et al., 2000, 2018). Figures taken from http://agage.mit.edu/data/agage-data.

plumes from other Asian countries of 72 % and 55 %, and in USA plumes an increase of 55 % and 56 %, respectively. This suggests an enhanced emissive industrial use of CH_2Cl_2 and $CHCl_3$ in China and a relatively larger industrial emission of CH_2Cl_2 than $CHCl_3$ in other Asian countries. Based on model analysis Fang et al. (2018) show that ~ 87 % of all East Asian $CHCl_3$ emissions between 2007 and 2015 came from China, thereby covering almost all of the global emission increases in 2015 since 2010. They also state that it is very unlikely that these increases of $CHCl_3$ are of natural origin.

The northern hemispheric (NH) mixing ratios of CH_2Cl_2 in mid latitudes are by a factor of 3 larger than those of the southern hemisphere (SH) which is clearly a consequence of large industrial emissions in the NH (Hossaini et al., 2017). Measurements on a ship cruise showed no latitude dependent changes of CH_2Cl_2 mixing ratios in the SH but in the NH the mixing ratios linearly increased with latitude between the equator and ~ 10°N (Kolusu et al., 2017). Koppmann et al. (1993) also saw this linear increase starting at the ITCZ[13] (~ 10°N) up to 45°N and found constant CH_2Cl_2 mixing ratios over the southern Atlantic which indicate that the largest source region of CH_2Cl_2 is in the mid latitudes of the NH. A linear decrease towards southern latitudes was seen in CARIBIC data too and suggested that the main source of SH CH_2Cl_2 is the NH industry (Leedham-Elvidge et al., 2015). Although in the SH Cox et al. (2003) analyzed elevated mixing ratios in Tasmania from 1998–2000 and found that the source regions were large industrial, highly populated areas in Australia. The CARIBIC data showed also variations of CH_2Cl_2 mixing ratios in the NH depending on the distance to industrial activities, where the values are elevated. The data of long-term ground-based measurements from the NOAA[14] and the AGAGE[15] network confirm the asymmetric distribution of CH_2Cl_2 over the hemispheres and the data from the AGAGE network show a similar behavior for $CHCl_3$. Figure 1.3 shows the ground-based observations of CH_2Cl_2 and $CHCl_3$ from the AGAGE network (Prinn et al., 2000, 2018).

1.3.3 Sinks and lifetime

The major atmospheric sink of both CH_2Cl_2 and $CHCl_3$ is the reaction with hydroxyl radicals (OH) and to a very small extend also with atomic chlorine (Cl). In the SH where few industrial sources influence the distribution of the two species the background mixing ratios of both species are clearly anticorrelated to the seasonal cycle of OH having their maximum in late SH winter and early SH spring (Cox et al., 2003). In the NH seasonal anthropogenic use of products that release $CHCl_3$ to the atmosphere (e.g. landfill and chlorination of water) have been observed to have a small impact on the background seasonality of $CHCl_3$ which is induced by the seasonal cycle of atmospheric OH (Gentner et al., 2010).

---

[13] Inter-Tropical Convergence Zone, cf. Figure F.3

[14] https://www.esrl.noaa.gov/gmd/

[15] http://agage.mit.edu/, e.g. figures 4.5 and 4.14

However, the global distribution of OH also shows significant regional dependencies (e.g. Spivakovsky et al., 2000; Hanisco et al., 2001; Lelieveld et al., 2016).

As a consequence to the strong dependency on the distribution of OH it is very complex to determine a global lifetime for either of the two Cl-VSLS. Hossaini et al. (2019) estimate the annual mean lifetime of CH_2Cl_2 in the planetary boundary layer to be 102 days and in the upper troposphere (UT, at ~ 10 km) to be 245 days. As a general number they suggest to use a lifetime of 168 days for the Troposphere and Hossaini et al. (2017) estimate a partial lifetime of 1–2 years in the stratosphere outside the polar regions. With CH_2Cl_2 and $CHCl_3$ having comparable reaction rates with OH (Hsu and DeMore, 1994) their atmospheric lifetimes are comparable. A $CHCl_3$ lifetime of 149 days is suggested by WMO (2018).

1.3.4 Impact on ozone

Chlorine containing species with a very short lifetime are not controlled by the Montreal Protocol because it was assumed that these species only have a non-significant influence on the depletion of ozone by depositing chlorine in the stratosphere. In a study on transit times in the tropical tropopause layer (TTL) Park et al. (2010) show that VSLS like CH_2Cl_2 and $CHCl_3$ have longer local lifetimes in the TTL than the average transit time thus being able to reach the stratosphere once they have entered the TTL. Using model simulations Hossaini et al. (2015b) showed that at the LZRH (Level of Zero Radiative Heating) in the TTL there has been an increase of average CH_2Cl_2 mixing ratios of about 83 % (e.g. from 18 ppt to 33 ppt) from 2005 to 2013. However, measurements of Laube et al. (2008) showed lower CH_2Cl_2 mixing ratios in the TTL in summer 2005 (~ 11 ppt at 15 km near the equator in Teresina, Brazil at 5°S). The measured difference to the average mixing ratios from the model could be a result of the strong seasonal cycle and local differences in the distribution of CH_2Cl_2. Further model studies suggest that around 80 % of the global average mixing ratio of CH_2Cl_2 at the surface eventually enter the stratosphere (Hossaini et al., 2019).

Based on model simulations there has been a ~ 52 % increase of total chlorine entering the stratosphere coming from VSLS (CH_2Cl_2, $CHCl_3$, C_2Cl_4, and CH_2ClCH_2Cl) in the period of 2005 to 2013 (Hossaini et al., 2015b) and an increase of ~ 61 % from 2000 to 2017 (Hossaini et al., 2019). The resulting increase of CH_2Cl_2 intrusion into the stratosphere fits well with the increase of CH_2Cl_2 observed at the surface. However, a recent study based on observations in the Asian UTLS during the monsoon season in 2017 finds that the estimated chlorine from Cl-VSLS in the lower stratosphere in 2017 has been underestimated by 8–

Table 1.1: Ozone depleting potentials (ODP) of several long-lived species as well as of the Cl-VSLS CH_2Cl_2 and $CHCl_3$ which is depending on region and season.

Species	ODP	Source
CFC-11	1.0	WMO (2018)
CFC-113	0.81	
CCl_4	0.87	
HCFC-22	0.034	
CH_3Cl	0.015	
CH_2Cl_2	0.0097–0.0208	Claxton et al. (2019)
$CHCl_3$	0.0143–0.0264	

26 % (Adcock et al., in review). On the assumption that stratospheric chlorine coming from VSLS is composed of more than 80 % source gases and less than 20 % being product gases (e.g. $COCl_2$ (Harrison et al., 2019; Claxton et al., 2019), CHClO, HCl) Hossaini et al. (2019) estimate a mean growth rate of stratospheric chlorine from VSLS of 3.8 ppt/year between 2004 and 2017. They further state that this would change the relative contribution of VSLS to stratospheric chlorine from 2 % in 2000 to ~ 3.8 % in 2017 but the contribution of the most abundant Cl-VSLS (CH_2Cl_2) to total inorganic chlorine is still less than 10 %. Note that between 2000 and 2017 in general stratospheric chlorine declined (cf. Figure 1.1, left).

In a model study on the ODP of Cl-VSLS, Claxton et al. (2019) found a relatively efficient transport for VSLS from continental East Asia into the lower stratosphere. Consequently they find a factor of 3 higher impact on ozone from Cl-VSLS originating from Southeast Asia than from Europe. They calculate an ODP range for CH_2Cl_2 and for $CHCl_3$ depending on region and season. Table 1.1 lists the ODPs of several long-lived species as well as those of CH_2Cl_2 and $CHCl_3$.

The recovery of Antarctic ozone to pre-1980 values is estimated to occur at around 2070 but without the consideration of Cl-VSLS in particular CH_2Cl_2 (WMO, 2018). Hossaini et al. (2017) predict a delay of the return to pre-1980 Antarctic ozone values of ~ 5 years considering constant CH_2Cl_2 emission from 2016. They also use an annual mean CH_2Cl_2 emission growth rate of 6.1 ppt (observed between 2012 and 2014) and predict for this scenario that there will be no ozone recovery at all. In the same article it is shown that the impact on SH spring time ozone loss by CH_2Cl_2 has doubled from 2010 to 2016 (from ~ 1.5 % to ~ 3 %). However, today according to Chipperfield et al. (2018) VSLS still have only a small effect on lower stratospheric ozone trends. It is further believed that an impact of VSLS is only relevant on upper stratospheric ozone and lower stratospheric ozone at the poles where the ozone concentrations are not dominated by dynamical processes. This implies that the entry of Cl-VSLS in the Brewer–Dobson circulation and in particular the direct transport from the troposphere with higher mixing ratios into the LMS on isentropes or fast overshooting updraft can unfold their low but significant ODP.

There is no reason to assume that Cl-VSLS become major players in stratospheric ozone depletion in the near future although they have to be closely watched. The major anthropogenic injection of chlorine into the stratosphere is still originating from CFCs and HCFCs which are globally almost completely banned from production and slowly decline in the atmosphere because of their relatively long lifetimes (e.g. WMO, 2018). However, this implies that the relative impact on ozone from unregulated Cl-VSLS will rise even if their emission rates would not grow any further.

1.4 Aircraft measurements of CH_2Cl_2 and $CHCl_3$

To investigate changes in the distribution of CH_2Cl_2 and $CHCl_3$ in the UTLS region as well as to find evidence for an efficient transport pathway for these Cl-VSLS from the source region into the UTLS, observations of these species in the UTLS are mandatory. In general, trace gases in the UTLS can be observed remotely by satellites or from ground-based measurement stations. Both methods are generally efficient but often limited in spatial resolution, measurement precision, or in the choice of observed species. To the best of my knowledge there is no reported publication of CH_2Cl_2 or $CHCl_3$ measurements in the UTLS region from a remote sensing instrument, neither from a satellite nor ground-based. The most straight forward method is to measure in real-time from aboard an aircraft directly in the UTLS region to be able to investigate the Cl-VSLS in the regions of interest on site. However, the technical requirements for such an instrument are numerous and in most cases the instrument has to be customized for the specific requirements of the aircraft in addition to satisfying the scientific goals.

The most common technique to measure CH_2Cl_2 and $CHCl_3$ mixing ratios in air samples is the use of gas chromatography and mass spectrometry (GC/MS). Sometimes other detectors like an electron capture detector (ECD) or a flame ionization detector (FID) are used in combination with GC to determine the Cl-VSLS. Mainly depending on the number of measured species the GC measurement technique is rather slow. The measurement duration of one sample of most commercial instruments in laboratory conditions is on the order of 20 to 60 minutes to properly measure around 10 to 50 different species. For the investigation of transport processes in the UTLS based on real-time GC/MS measurements from a platform that moves with around 200 m/s in space, the optimization of the measurement frequency of such an instrument is an important requirement regarding the spatial resolution.

In particular due to the complexity of operating a GC/MS instrument aboard an aircraft, most existing airborne in situ measurements of CH_2Cl_2 and $CHCl_3$ are from post-flight laboratory analysis of air samples collected from aboard the aircraft. There are two main advantages of collecting air samples over real-time measurements from aboard an aircraft:

1. The in-flight operation is much less complex. Whole air samplers usually consist basically of an inlet pump system to compress outside air into sample canisters (e.g. Schuck et al., 2009, 2020). A GC/MS instrument additionally needs to preconcentrate the air sample, chromatographically separate the different species (both processes usually involve extreme temperature gradients with temperature differences of up to several hundred degree Kelvin), and detect the sample at vacuum ($\sim 10^{-4}$–10^{-5} mbar) condition (e.g. Apel, 2003; vom Scheidt, 2013b; Bourtsoukidis et al., 2017).

2. The freedom to analyze a large number of species in a controlled environment without being directly restricted by the measurement frequency.

The main disadvantages of whole air sample analysis over real-time measurements from aboard an aircraft are as follows:

1. The behavior of the collected air samples inside the sample containers is unknown and difficult to characterize (e.g. Schuck et al., 2020). The chemical composition and the residence time of the air sample as well as the surface material and the temperature of the environment of the sample container can all have a biasing influence on different species.

2. Due to the limited space inside an aircraft to store sample containers ($\sim$ 1–2 l each), the number of maximum air samples collected during a flight is usually much lower than the possible number of real-time measurements from most existing airborne in situ instruments.

Table 1.2 (upper table) lists whole air samplers and the laboratories performing the ground-based analysis used in most publications considering airborne Cl-VSLS measurements.

Airborne instruments for real-time measurements of Cl-VSLS from aboard an aircraft are extremely rare due to the above mentioned complexity and requirements for such an instrument. In addition, publications of real-time Cl-VSLS measurements from aboard an aircraft are even fewer even though more data might exist. This could be due to the fact that all existing airborne instruments able to measure Cl-VSLS also are able to measure several other species of great atmospheric interest. It has to be believed that also the time consuming on-ground maintenance of airborne GC/MS instruments plays a part in the low number of publicized Cl-VSLS data analysis from relatively small groups operating such an instrument, focusing only on the analysis of a small number of different measured species. Only in recent years species like CH_2Cl_2 and $CHCl_3$ became of significant interest for atmospheric studies above the troposphere. However, CH_2Cl_2 and $CHCl_3$ still only play a minor role in publications of airborne real-time in situ measurements where these two species are analyzed (e.g. Andrews et al., 2016; Bourtsoukidis et al., 2017). Table 1.2 (lower table) lists airborne instruments for real-time measurements of CH_2Cl_2 and $CHCl_3$ operated on aircafts and which are mentioned in publications. Other airborne GC/MS instruments able to measure Cl-VSLS might exist but no reviewed publications are available.

For the analysis of Cl-VSLS and their impact on the UTLS region much more measurements with a preferably high measurement frequency and precision have to be performed from aboard aircrafts. This would provide on the one hand the possibility for transport analysis, specifically for the analysis of the transport of CH_2Cl_2 and $CHCl_3$, which are predicted to further rise in concentration in the UTLS region (e.g. Hossaini et al., 2019). On the other hand this would provide more observational background to validate and optimize climate models and consequently would contribute to improve our understanding of future developments of the changing climate.

Table 1.2: Airborne instruments for the analysis of CH_2Cl_2 and $CHCl_3$ sorted by operating altitude. Upper table: whole air samplers; lower table: online measuring instruments.

Airborne whole air samplers with on-ground analysis of CH_2Cl_2 and $CHCl_3$

Technique	samples/flight	Max. alt. [km]	Aircraft	Institution	Source
GC/MS	∼ 16	∼ 22	Geophysica	University of Utrecht, University of East Anglia	Adcock et al. (in review)
GC/MS	max. 60	∼ 19	NCAR Gulfstream V, NASA Global Hawk, WB-57F, NOAA WP-3	University of Miami	Millet et al. (2009); Park et al. (2010) Atlas (2014); Andrews et al. (2016); Hossaini et al. (2015b, 2017, 2019)
GC/ECD	every ∼ 15 min	13	Cessna Citation-II, DLR Falcon	University of Utrecht	Scheeren et al. (2002, 2003)
GC/MS	max. 168	∼ 12	NASA DC-8, NSF/NCAR C-130	University of Irvine	Millet et al. (2009); Barletta et al. (2009); Simpson et al. (2011)
GC/MS	max. 12–28	∼ 10–12	Passenger aircrafts	MPI Mainz, UEA	Leedham-Elvidge et al. (2015)
GC/MS	-	< 8	FAAM BAe-146	University of York	Andrews et al. (2013, 2016)
GC/MS	∼ 44	< 8	FAAM BAe-146	University of Bristol	Say et al. (2019)

Airborne instruments of real-time measurement of CH_2Cl_2 and $CHCl_3$

Name	Technique	Time res. [min]	Max. alt. [km]	Aircraft	Institution	Source
PANTHER	GC/MS	∼ 3	∼ 15	NASA DC-8, NCAR Gulfstream V	NOAA	Moore et al., 2006; Wofsy, 2011
TOGA	GC/MS	∼ 2	∼ 15	NCAR Gulfstream V	NCAR	Apel (2003); Andrews et al. (2016)
SOFIA	GC/MS	3	∼ 15	DLR HALO	MPI Mainz	Bourtsoukidis et al. (2017)
GhOST-MS	GC/MS	∼ 6	∼ 15	DLR HALO	University of Frankfurt	Sala et al. (2014)
In situ GCMS	GC/MS	5	< 8	FAAM BAe-146	University of York	Andrews et al. (2016)

1.5 Outline of this thesis

For airborne real-time measurements of long-lived CFCs, halocarbons, and CO_2, as well as perfluorocarbons (PFC) the five channel instrument HAGAR-V (High Altitude Gas Analyzer-5; vom Scheidt, 2013b) was developed. The first aim of the present work is the modification and optimization of the two-channel GC/MS module of HAGAR-V in particular for the measurement of Cl-VSLS. In this process significant modifications of the preconcentration system and of the GC column ovens are presented and characterized in Chapter 2. Technical results from the first successful deployment on the High Altitude and LOng range research aircraft (HALO[16]) are as well presented in this chapter.

The second aim of this work is the characterization of an optimal data processing method for the novel GC/MS aircraft data of HAGAR-V. Several in-flight diagnostic modes and the use of two in-flight calibration gases are analyzed and result in specific ways to best calculate the mixing ratios of the different species measured by the GC/MS module of HAGAR-V. In addition, the comparison of measurements from the GC/MS module with HAGAR-V's ECD module is used to support the derived calibration methods. The analysis of the second aim of this work is presented in Chapter 3.

The third aim of this work is the analysis of HAGAR-V Cl-VSLS measurements in the UTLS. On the basis of tracer-tracer correlations of CH_2Cl_2 as well as $CHCl_3$ vs N_2O, tropospheric intrusions into the LMS of different CH_2Cl_2 sources and different $CHCl_3$ sources are identified. With the support of model simulations of artificial tracers of air mass origin and backward trajectory calculations[17] the source regions are located and efficient transport pathways into the UTLS for the Cl-VSLS are identified. Differences between the tropospheric intrusions of CH_2Cl_2 and $CHCl_3$ into the LMS are analyzed; possible reasons for the differences are discussed with the help of ground-based long-term observations and whole air samples from low-level aircraft flights within the source regions. In addition, the influence of the large scale hurricane Maria on the distribution of CH_2Cl_2 and $CHCl_3$ in the UTLS is analyzed. The whole transport analysis of the Cl-VSLS is presented in Chapter 4.

A synthesis of the main results of this thesis is given in Chapter 5 where also further aims and suggested improvements are given.

---

[16] https://www.halo.dlr.de/

[17] provided by Dr. Bärbel Vogel, Jülich Research Center, Institute for Energy and Climate Research - Stratosphere (IEK-7)

Chapter 2

HAGAR-V hardware development and characterization

In this chapter new modifications of the aircraft instrument HAGAR-V are presented and characterized. Changes to previous configurations of the instrument are discussed. The new modifications are characterized and their performance during the first successful deployment on the research aircraft HALO analyzed. The information provided in this chapter is rather technical and to keep the text short and readable several details are given in Appendix A–C.

2.1 The instrument and its measurement principle

Gas chromatography (GC) is the most versatile technique of sample preparation to spatially separate a large variety of molecules in complex matrices of gaseous samples to this date. Driven by a carrier gas (e.g. He or N_2) the molecules in a gaseous sample pass through a long tube or capillary packed or coated with adsorbing material (stationary phase). Each species of molecules interacts differently with the stationary phase and thus has a different migration velocity. In addition low temperatures can slow and high temperatures can fasten the migration velocity of any species. Having different migration velocities the different species get separated and leave the tube or column at a different time (retention time) in statistically distributed peaks[1].

The detector used together with GC influences the number of detectable species and their detection sensitivity. An electron capture detector (ECD) for example is extremely sensi-

---

[1] For more information about GC see e.g. Dettmer-Wilde and Engewald (2014)

tive to only a specific class of species while a quadrupole mass spectrometer (MS) is able to detect almost any species but with lower sensitivity than an ECD. To increase the sensitivity of a MS larger samples can be used and preconcentrated before the GC separation. Sample preconcentration uses the same principle as GC with the difference that none of the species of interest leave the adsorbing tube (or column) of the preconcentration unit. Thereby only the species of interest get trapped inside the preconcentration unit in a volume much smaller than the original air sample, and this preconcentrated sample ideally gets stripped of unwanted species (e.g. in air samples primarily N_2 and O_2). The preconcentrated sample further gets separated via GC and the individual species are detected separately by the MS[2].

The drawback of sensitively measuring many different species is the time needed for each individual measurement step (e.g. preconcentration, separation, detection, and preparation for the next measurement cycle). In addition, in order to achieve real-time atmospheric air sampling of the upper troposphere and the lower stratosphere the instrument has to be deployed on an airborne platform (like an aircraft or a baloon) which implicates many constraints. An instrument operated on an aircraft is limited in space, power, and weight in addition to many safety regulations regarding the use of electricity and chemical substances as well as mechanical properties of the instrument. The development of an instrument that fulfills all the limitations for the use on an aircraft in addition to the optimization of its operational speed and functionality is a difficult and iterative process. Almost no part of such an instrument can be used as bought off the shelf but has to be adapted or developed from scratch. Such an instrument — HAGAR-V — was previously developed (vom Scheidt, 2013b) and has been further certified, optimized and partly redeveloped in the frame of the present work.

HAGAR-V (High Altitude Gas AnalyzeR - 5 channel version) is a novel multi-tracer measurement system for the deployment on the High Altitude and LOng range research aircraft (HALO). It is a modernized and extended version of HAGAR (e.g. Riediger, 2000) which has been operated successfully on the M55 Geophysica aircraft on more than 130 flights since 1998. Similar to HAGAR, HAGAR-V comprises a non-dispersive infrared (NDIR) analyzer detecting CO_2 (precision 0.15 ppm, i.e. 0.04 %) with a time resolution of about 3 seconds and two GC channels with packed GC columns coupled to ECDs to measure the long-lived trace gases SF_6, CH_4, CFC-11, CFC-12, CFC-113, and CCl_4 every 90 seconds (in the 2017 configuration). To gain sensitivity for CH_4 one channel is “doped” with N_2O as reactant gas (Werner, 2007).

---

[2] For more information about MS see e.g. Gross (2011)

In addition to HAGAR, HAGAR-V comprises a novel two channel GC module coupled to one MS. Originally developed for the detection of several perfluorocarbons (PFC) (vom Scheidt, 2013b), the target species of this module changed at the beginning of the present work to a broader variety of tracers like volatile organic compounds (VOC), chlorinated hydrocarbons, chlorofluorocarbons (CFC), and hydrofluorocarbons (HFC). Thereby the focus was held on tracers with different lifetimes that range from days to hundreds of years.

In the configuration described in the present work the MS module measures 12 different species every 180 seconds with shown in-field precisions ranging from a few per mill to a few percent (relative to tropospheric background air) depending on species (see Table 2.3). However, the GC/MS module can measure much more than 12 species, and its time resolution can be halved by the use of its second channel. This has only recently been shown for the first time in the field and will not be described in the present work. In any case, the MS module of HAGAR-V has already proven its comparably fast and precise in situ measurements of a large suite of atmospheric tracers with low concentrations to this date.

Key factors for this success were the developments of a novel preconcentration unit and ultra fast GC capillary ovens. The MS module uses sample preconcentration to measure species with mixing ratios on the order of a few ppt (parts per trillion by mole fraction) down to several ppq (parts per quadrillion by mole fraction) (see Table 2.2). The above described processes to measure a large variety of species is relatively slow in particular due to the requirement of repetitive extreme temperature changes. Optimizations for fast temperature ramps have been shown by vom Scheidt (2013b). In the present work the units are further optimized and redeveloped for the benefit of a more efficient and reliable use on the aircraft.

In this chapter the development of a unique preconcentration unit and two different models of ultra light GC systems (Low Thermal Mass columns) for the MS module is presented. Advantages and disadvantages are determined and characterized. In the last part of this chapter an example of the first successful deployment on the HALO research aircraft is presented. Further system characterizations regarding the processing and quality of in-flight data obtained during the aircraft campaign WISE (see Section 3.1) are discussed in Chapter 3. Detailed information on the different modules of HAGAR-V is given in Appendix A.

2.2 Preconcentration unit

The general principle of HAGAR-V's preconcentration unit has been described by vom Scheidt (2013b), but major changes have been made since then leading to a revision of the development process to the current configuration.

2.2.1 Preconcentration unit design

To keep the choice of measured species as liberal as possible the sample preconcentration trap needs to get as cold as possible. The usage of liquid Nitrogen (LN_2) would require regular service, logistical effort and special safety regulations when operating the instrument on an aircraft (e.g. Bourtsoukidis et al., 2017). Under these restrictive conditions a cooling system run by electricity comes in more handy (e.g. Sala et al., 2014). There have been some reports on the usage of peltier elements where the traps reached temperatures of −40 °C or even −50 °C (e.g. Ou-Yang et al., 2016; Simmonds et al., 1995, respectively). However, in the case of HAGAR-V most efficient electrical cooling is accomplished with a Stirling cooler reaching reported temperatures as low as −165 °C depending on size and model (e.g. Song et al., 2012; Lerner et al., 2017; Obersteiner et al., 2016). Being restricted in space and electrical current a rather small Stirling cooler (Twinbird SC-UD08, 80 W FPSC module) was chosen for use in HAGAR-V with a nominal minimum temperature of −100 °C.

To accomplish optimal separation of the compounds a narrow peak of each target species inside the column has to be achieved. As a first step a very focussed injection from the preconcentration trap resulting in a very narrow injection peak in the separation column is mandatory. To achieve that, large heating rates for desorption are important so that ideally all adsorbed compounds are desorbed at the same time. For the heating either an external heating device can be applied on the trap (e.g. GERSTEL, 2008; vom Scheidt, 2013b) or the trap itself is used as the heating device (e.g. Lanning et al., 1988; Simmonds et al., 1995; Obersteiner et al., 2016; Bourtsoukidis et al., 2017). For the latter version high electrical currents are needed because of the low resistance of stainless steel (tubing material of the trap). Avoiding it by the use of a different metal with higher resistance for the trap tubing, decomposition of halogenated VOC might be a consequence (Klemp and Sacks, 1991). Therefore and for security reasons HAGAR-V preconcentration traps get heated by applying a voltage of 48 V on a wire (~ (7–8) Ω at ~ 20 °C) wrapped around the 1/16 " tube that is housing the adsorbent.

For HAGAR-V two different preconcentration trap designs have been developed. The first version is a dynamical setup and described by vom Scheidt (2013b). This first version has been modified for HAGAR-V's first deployment on the research aircraft HALO in 2015 and is reviewed in the following section. The second version was developed to overcome the disadvantages of the first version of HAGAR-V's preconcentration trap and will be discussed in more detail. In all the following sections the second version of preconcentration unit is implicated (if not specified otherwise).

2.2.1.1 First version preconcentration unit

The cold housing was an aluminum box mounted on the cold head of the Stirling cooler. The 1/16 " stainless steel trap passed through the housing via slits at both ends of the aluminum box. The trap was insulated with a layer of a two-component-ceramic-glue ($\sim 10^3$ Ω at 400 °C) against the Cu/Ni-44 heating wire. The heating wire was wrapped around the ceramic insulated trap and around a Pt100 temperature sensor which controlled the temperature at the center of the trap. The plugs of the wire were fittingly embedded in small blocks of DoTherm insulation material which themselves were glued to the tube with ceramic glue (comparable to the second version shown below in Figure 2.3).

Servo motors were employed to lift the whole trap tubing up or push it down to decouple or couple the preconcentration trap with the bottom of the cold aluminum housing, respectively. Differing from the preconcentration unit described by vom Scheidt (2013b) the trap tested in the present work was not pressed into a fitting slot inside the bottom of the aluminum housing for the cooling process. Instead, the trap had an aluminum plate glued to its downside for a larger contact area on a flat surface. This change was necessary because the slots in the bottom needed to have some tolerance in their dimensions so that the cooling was more efficient by contacting two flat surfaces. Nevertheless this first version of preconcentration unit tested in the present work still impled a number of complications which proved impractical for the use on an aircraft:

- ▷ The cooling efficiency was limited due to the slits in the cold housing needed to allow movement of the trap tubing. Only a minimum temperature of ~ -20 °C could be reached within the few minutes of measurement cycle time common in fast GC.
- ▷ Icing of the preconcentration unit could not be avoided. Moisture entered the aluminum box through the necessary slits and caused corrosion and short-circuits. In addition this contributed to the high minimum temperature limit mentioned above.

- ▷ The temperature distribution inside the trap was extremely inhomogeneous with differences of up to ± 200 °C and could be controlled only at one point of the preconcentration trap.
- ▷ The temperature sensor turned out to be very fragile and difficult to electrically insulate. Temperatures could exceed 400 °C which often damaged the insulation material. Due to the repetitive dynamical movement of the whole trap the wiring got worn down fast and broke, implicating the destruction of the whole preconcentration trap.
- ▷ The servo motors were extremely sensitive to overheating which caused internal parts of the motor to melt and made the electrical movement of the trap impossible. Attaching the servo motors close to the cold housing only caused a small delay for them to internally melt and get stuck, thereby changing the whole ad- and desorption characteristics of the preconcentration trap. The attempt to use springs for a natural mechanical pull towards the cooling position relieved the larger part of the mechanical pressure from the servo motors and proved to be the most promising improvements for their overheating issue.
- ▷ The whole electrical insulation of the preconcentration unit relied solely on ceramic glue. The glue did not stick well to the stainless steel tube and exhibited cracks after several days of repeated temperature cycles. Other glues that could withstand a temperature range from -100 °C to > 400 °C were rare to find and did not exhibit any advantages over the used ceramic glue. Thus it always remained a risk of short-circuiting the heating wire with the MS module structure which implies errors on many other units of the instrument. A PEEK (organic polymer) union at both ends of the trap to electrically insulate it from the connecting tubing turned out to be impractical because of space limitations and leaks when connected to the thin walled trap.

2.2.1.2 Second version preconcentration unit

To overcome the problems of the dynamical design of the first version preconcentration unit a new model has been developed and will be described in detail and referred to as the second version.

Like the first dynamical version the second version trap still contains a 1/16 ” stainless steel tube with a very thin wall (0.1 mm) to keep the thermal mass low and maximize the volume for the adsorbent. Silicon coatings ($\leq$ 1200 Å of SilcoNert 2000, SilcoTek GmbH,

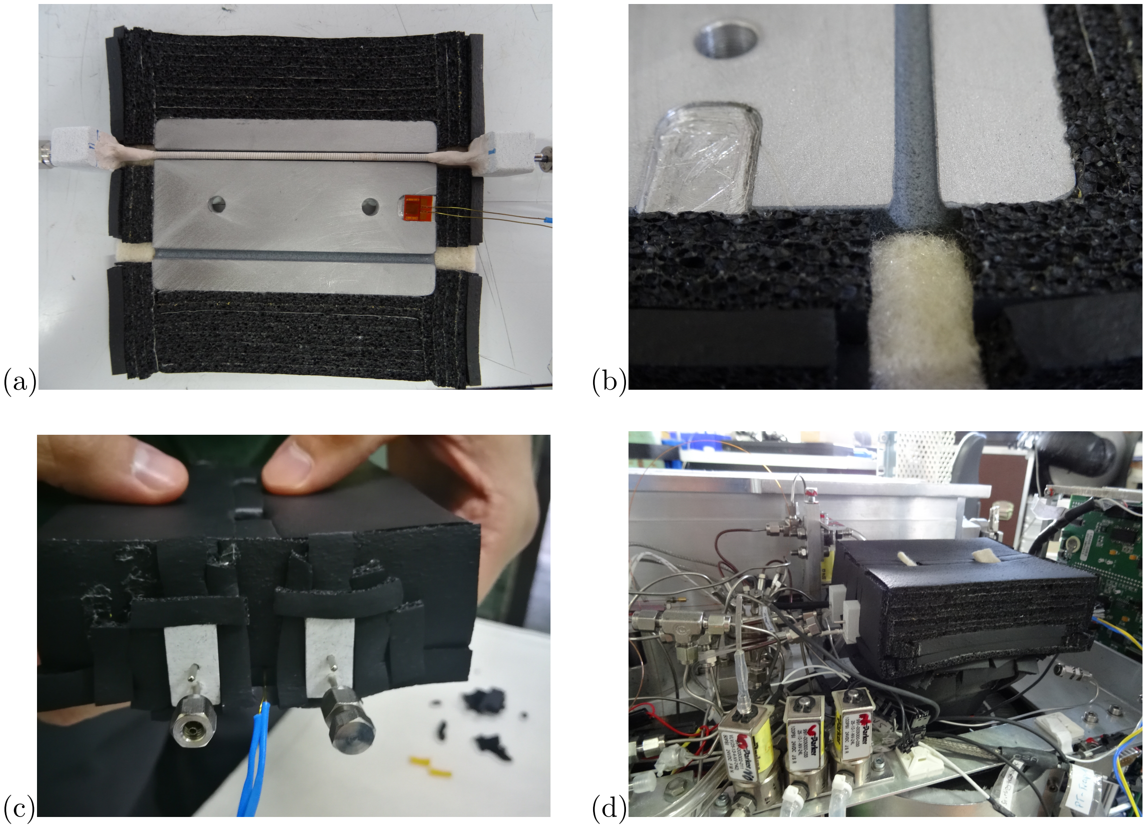

Figure 2.1: Pictures of the preconcentration unit developed for the HAGAR-V MS module. (a) Bottom aluminum plate with one preconcentration trap (note that the shown trap does not have electrical insulation; cf. Figure 2.3), temperature sensor and thermal insulation; (b) detail of ceramic coated slot in the aluminum plate; (c) outside view of the preconcentration unit when equipped with two preconcentration traps; (d) preconcentration unit mounted on the Stirling cooler.

Germany) for the tube were tested but so far no significant differences to untreated tubes have been found.

Instead of the voluminous aluminum box the new trap is embedded in a slot of an aluminum plate and covered with a similar aluminum lid so that the trap is fully fixed and enclosed in the construction (Figure 2.1). The slot surfaces are coated with a ~ 100 µm layer of Al_2O_3/TiO_2 ceramic (Rauschert GmbH, Germany) so that the trap has no direct contact with current leading aluminum. This ceramic layer is only an additional precaution to prevent a short-circuit if the trap were to strongly overheat (> 500 °C) or if mechanical rupture removed the electrical insulation of the current leading wire on the trap itself.

The two aluminum plates are connected to the cold head of the Stirling cooler and are well insulated with an insulation tape (HT/Armaflex, Armacell GmbH, Germany) against

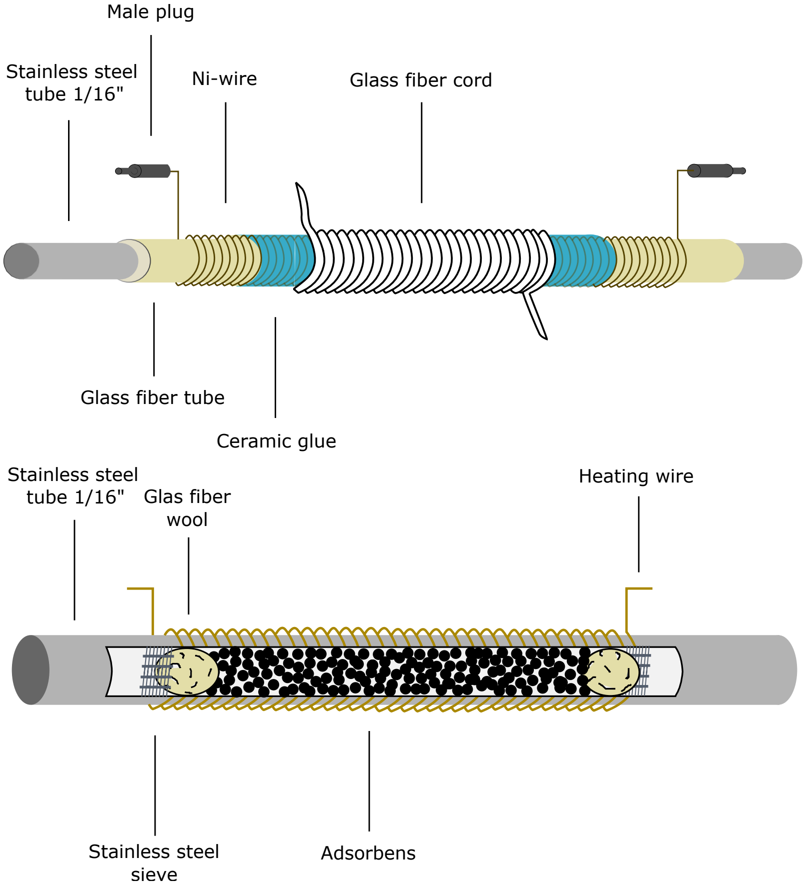

Figure 2.2: Schematic drawings of a second version of a self built preconcentration trap with a view on the different layers outside the tube (upper scheme) and a view on the structure inside the tube (bottom scheme).

outside temperatures. A Pt100 temperature sensor is also embedded between the two plates to monitor the cold head temperature of the Stirling cooler. With this housing a minimum temperature of ~ -120 °C can be reached[3]. However, in working mode when heat is indirectly applied to the cold head of the Stirling cooler, a realistic minimum of about -80 °C can be achieved within the typical measurement cycle time of a few minutes. This is a huge improvement compared to the previous version.

Instead of the fragile ceramic glue layer the electrical insulation of the heating wire against the tube is now realized by a tightly woven glass fiber tube (ocher color in Figure 2.2 and visible in Figure 2.3). This insulation layer has a thickness of about 0.1 mm and fits tightly

---

[3] This is even 20 °C lower than the nominal minimum temperature of the used Stirling cooler

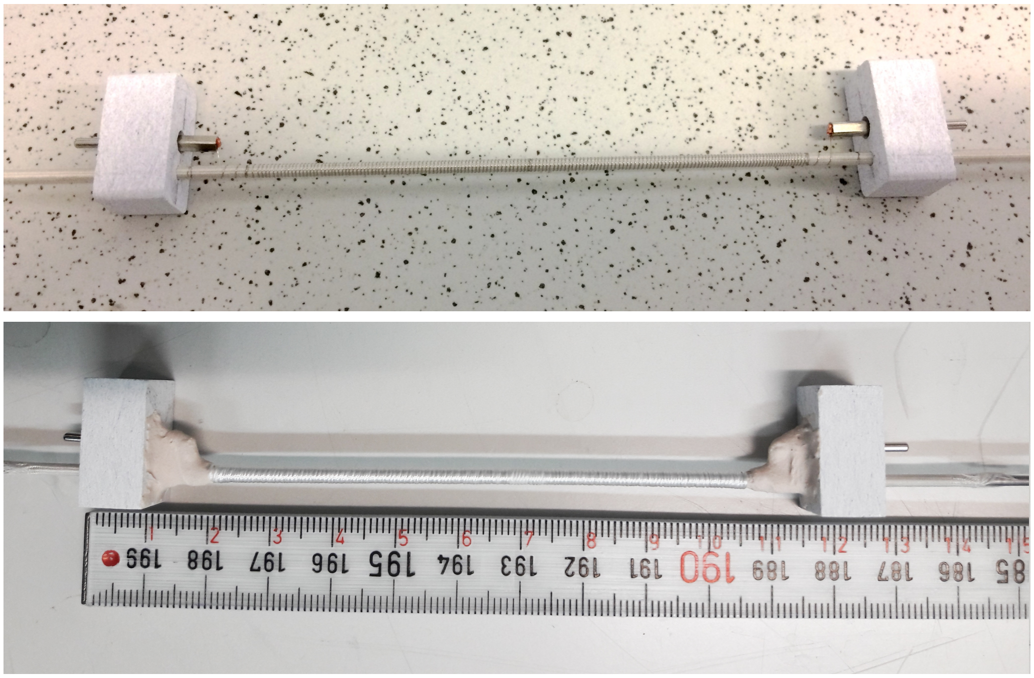

Figure 2.3: Pictures of a self built preconcentration trap in different phases of building. A view on the heating wire/temperature sensor (upper picture) and a view on the glass fiber cord insulated preconcentration trap and fixed plugs with ceramic glue on DoTherm blocks (lower picture).

around the stainless steel tube. With an electrical resistance of (20–80) kΩ the electrical insulation for an applied voltage of maximum 48 V is sufficiently achieved.

The heating wire is wrapped around the tube over a length of ~ 90 mm with winding density decreasing at the ends (upper picture in Figure 2.3). Sieves and glass wool plugs (to fixate the adsorbent) are positioned toward the tube ends, but still underneath heating wire to get warmed as well during the desorption process. The adsorbent is positioned in between over a length of ~ 80 mm to ensure most efficient heating. In the first version of the preconcentration trap the adsorbent could be positioned only over a length of ~ 65 mm. The new version thus allows to increase the amount of adsorbent by 20 %.

Similar to the previous version the gaps between the convolutions of the wire are filled with a two-component ceramic glue that has a thermal conductivity of 1.15 W/(m·K) (blue color in Figure 2.2). Compared to the previous version a higher yield of heat uptake and a more homogeneous heat distribution alongside the tube is achieved by a different technique of applying the glue assuring no encapsulated air.

The fragile temperature sensor of the first version was removed to further reduce weight and instead measure the temperature via the resistance of the heating wire itself. This makes the system much more robust than the previous version, with less fragile parts to malfunction or break. In addition, the mean temperature of the whole trap is determined rather than the temperature at a single position alongside the wire.

A Nickel (Ni) wire with a diameter of 0.125 mm, a resistance of 8 Ω/m at room temperature and change of resistance of about 0.05 Ω/K is suitable as a heating wire and a temperature sensor at the same time with the given instrumental power limits. In addition, the wire, with a total length of about 1 m to cover most of a trap's surface, does not consume more power than the instrument's converters can provide when operated with 48 V at temperatures far below freezing point (i.e. when the wire has a low resistance). However, there is a natural power reduction for increasing temperatures induced by an increasing resistance of the heating wire, thus reducing the heating rate for higher temperatures. The upside is that it also prevents the trap from overheating and makes regulating higher temperatures much easier. This implicates that temperature overshoots — due to the extreme heating rate — can easily be avoided (e.g. Figure 2.10).

The insulation of the wire towards the preconcentration unit is realized by a tightly wrapped glass fiber sewing string that is wound over the whole trap and forms a tight insulation layer of ~ 0.3 mm (see figures 2.2 and 2.3). Due to the wire's self regulation temperatures exceeding 500 °C, which would melt the glass fiber insulation, are not possible. Only mechanical rupture could damage the insulation. In such a case the above mentioned ceramic layer on the aluminum slots would still provide for the electrical insulation between heating wire and instrument. This makes the operation of the preconcentration trap much more secure and the probability of a short circuit has changed from a high risk to nearly impossible with this new version of the preconcentration trap.

2.2.2 Temperature measurement for the preconcentration trap

The temperature measurement is implemented by switching the applied voltage from 48 V (heating) to 5 V (temperature measurement) and measure the current at a shunt resistance to calculate the resistance of the temperature wire. This technique has been described by vom Scheidt (2013b) but in the previous version of the preconcentration trap this technique could not be applied because the used heating wire did not much change its resistance with temperature. The currently used Ni heating wire exhibits sufficient change and from the relationship between temperature and resistance (characterized beforehand) the actual temperature of the wire can be calculated.

Due to the coil of the wire around the tube, induction currents appear while heating with 48 V. To avoid signal corrupting disturbances the temperature measurement needs to be

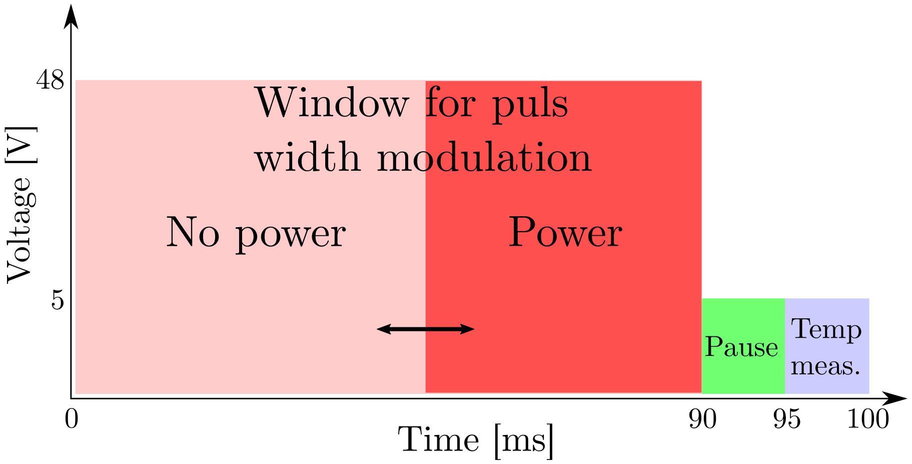

Figure 2.4: Schematic drawing of a heating and temperature measurement cycle of the preconcentration trap. The heating is accomplished by a 48 V pulse width modulation within a time window of 90 % of a 100 ms cycle length. Within the remaining 10 % of a cycle length 5 V are applied. For about 5 ms after a heating pulse inductive currents disturb the temperature measurement. Five temperature measurements at the end of a cycle get averaged and interpreted as the trap's current temperature.

delayed for about 5 ms after the switch to 5 V. With a heating cycle length of 100 ms, a 5 ms time window for temperature measurement, and a measurement frequency of 1000 Hz this leads to a loss of maximum heating power of about 10 % and a temperature value averaged over 5 measurements every 100 ms (Figure 2.4). The heating pulse is positioned in the given time window in such a way that the pause before temperature measurement always has the same duration. This avoids temperature biases that would occur when the length of this pause could differ and thus the temperature of the wire could cool down differently each cycle. The circuit is materialized on a small circuit board and implemented in the regulation software.

Even when no heating is needed the periodic 5 V for temperature measurement are regularly applied causing a current through the trap that ranges from (0.14–0.86) A for a temperature range from ~ 400 °C to ~ −80 °C, respectively. This leads to a slight passive warming of the wire and has a significant effect if low temperatures are desired. Figure 2.5 shows an example of the temperature differences between the cold head of the Stirling cooler and the central position inside of a preconcentration trap as a function of the Stirling cooler's cold head temperature. The temperature inside the preconcentration trap was measured with a thin thermocouple at the center inside the empty tube of a preconcentration trap. It is assumed that the measured temperature inside the trap is representative for a trap filled with adsorbent. The presence of an adsorbent probably only causes a slight temporal

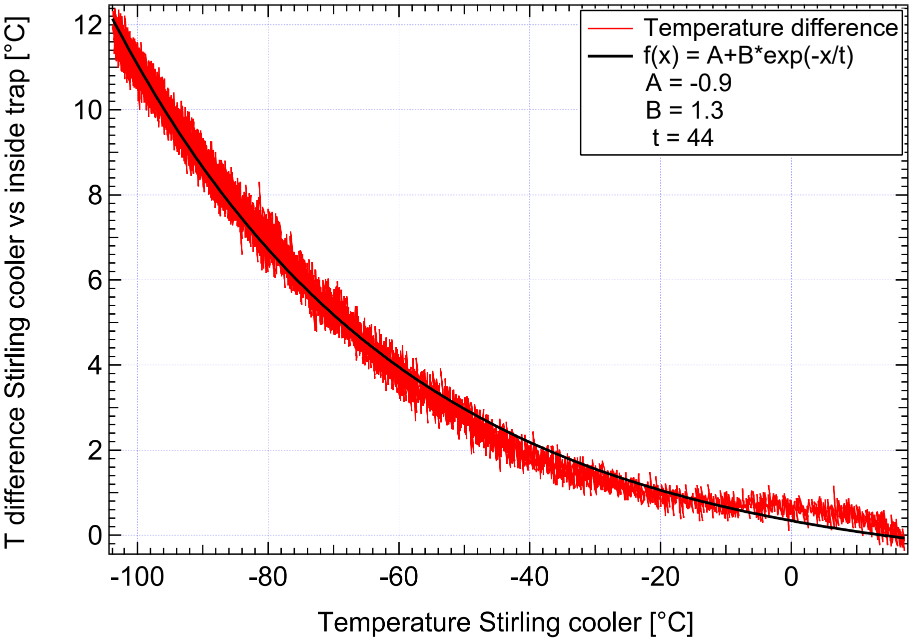

Figure 2.5: Example of temperature differences between the Stirling cooler and the center inside of a preconcentration trap as function of the Stirling cooler's temperature. The temperature inside the preconcentration trap was measured with a thermocouple inside the empty trap. The lower the Stirling cooler's temperature the lower is the resistance of the trap's temperature sensor and thus the stronger is the passive heating via the applied 5 V during temperature measurement. An exponential function roughly describes the dependency.

delay to equlibrate to the determined temperature difference due to a higher thermal mass inside the trap.

Figure 2.5 exhibits the result of an increasing current through the heating wire with lower cold head temperatures. It shows that at lower cold head temperatures the difference to the temperature inside the trap becomes larger. The following empirical function can be used to approximate the differences for a given cold head temperature:

$$f\left(T_{Stirling}\right) \backsimeq -0.9 + 1.3\exp\left(-\frac{T_{Stirling}}{44}\right) \tag{2.1}$$

This shows that for a cold head temperature of -80 °C a temperature inside the preconcentration trap of about -73 °C can be expected. This difference gets significantly smaller at higher cold head temperatures.

2.2.3 Temperature characterization for the preconcentration trap

Each preconcentration trap is handmade and therefore unique. Characterization has to be conducted before putting a new trap into use. The resistance of the heating wire at different temperatures has to be investigated as well as the temperature distribution inside the trap (see Figure 2.6).

The following example shows the characterization of trap GF-Ni-5 which has been used for all but the last flight during the WISE campaign (see Section 3.1). In Figure 2.6 the temperatures of the heating wire, of the cold head of the Stirling cooler, and of five specific positions inside this trap are plotted. The temperature at the different positions inside the trap has been measured with a thermocouple each at a separate cycle of heating and cooling. The five different measurements are comparable because the software-controlled temperatures are extremely well reproducible (on the order of mK). In the shown characterization of the inner trap temperature extreme temperatures were analyzed. Therefore the initial overshoot of the heating wire is programmed to achieve the maximum heating rate but still stay below the maximum temperature of 400 °C (max. temperature of adsorbent) at any time anywhere inside the trap.

In Figure 2.6 the heating wire shows a mean temperature ramp of ~ 270 K/s within the first second of heating and ~ 500 K/s within the first 0.2 s when the wire's resistance is lowest (~ 4 Ω). However, the heating rates inside the trap are clearly lower. There is a delay of about 0.8 s before the thermocouple inside the trap registers a change in temperature. This is partly due to the inertia of the sensor itself. For all tested positions the inside temperature ramp is rather constant at about 80 K/s for the first four seconds (since the first noted temperature change).

The preconcentration traps' cooling rates depend strongly on the cold head temperature of the Stirling cooler. With a cold head temperature of ~ -80 °C a cooling from ~ 350 °C down to ~ -50 °C inside the trap is possible within ~ 30 s. The cooling rate has thereby more than doubled compared to the first version of preconcentration traps (cf. vom Scheidt, 2013b). In addition temperatures far below -20 °C were not possible within the few minutes of a fast GC cycle with the first version of the preconcentration unit but can now easily be accomplished.

Even in this extreme test the increase in the cold head temperature of the Stirling cooler due to heating the trap is small (~ 7 °C in ~ 20 s) and could be recovered within ~ 100 s. In this test the cooler is working almost at its minimum temperature where its cooling power is weakest and external heating has the largest impact. Therefore, the impact of

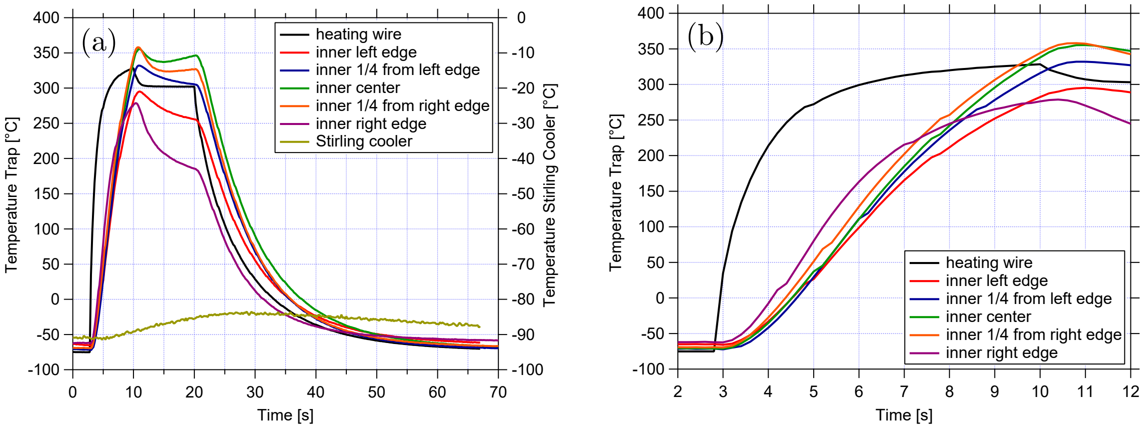

Figure 2.6: Example plots of the temperature characterization of the self built preconcentration trap used during the aircraft campaign WISE. Five separate tests with a thermocouple at five different positions inside the empty tube of the preconcentration trap are represented by the different colored lines. The temperature curve of the temperature/heating wire is shown in black and the temperature of the Stirling cooler with its own axis on the right hand side is shown in ocher. (a) depicts a total overview of the five test positions; (b) shows only the temperature ramp during flash heating.

trap heating on higher cold head temperatures is even smaller and the recovery time is faster.

Differences between the different positions inside the trap become visible at higher temperatures. Where the three central points (trap center and around 2.5 cm to each side of it) are agreeing well within about 30 °C, the two points at the trap's edges reach lower final temperatures and even exhibit slight cooling after they reach the temperature setpoint. This can be understood because for this test the trap is open to both sides and cool outside air from the unheated ends of the tube can easily influence the temperature sensor inside. An indication for this is the difference between the red and the purple line in Figure 2.6. For the red line the thermocouple was inserted from the trap's edge more or less covering the open end, while the purple line was measured with the tip of the thermocouple pointing towards this side's open end. A lower final temperature and a faster decline of the same can be observed in the latter case.

Hot and cold spots inside the trap are barely avoidable but the temperature distribution inside the trap should be as homogeneous as possible. In particular the outermost edges of the trap tend to show temperature extremes. Large temperature differences inside the trap can lead to incomplete desorption and/or decomposition of adsorbent material. Depending on the target species and the used adsorbent the tolerance for temperature differences inside the trap can vary. For the proper functionality of a preconcentration trap, regarding the target species and adsorbent used in the present work, tests suggested a maximum temperature difference inside the trap of about ± 50 °C of the mean inner trap temperature (Section 2.2.5).

The main cause of temperature differences inside the trap is most probably incomplete contact with the cold aluminum housing. The traps are handmade and might exhibit small differences in diameter along the tube. These differences can be due to a slightly uneven tube, a varying distribution of glue along the tube or some slightly overlapping glass fiber cords. In addition, the ceramic coating on the slots holding the traps is not perfectly even. To compensate a resulting uneven contact with the cold slots the insulating glass fiber cord functions as a mechanical buffer zone to allow the installation of slightly wider traps. However, it is still possible that some traps have less overall contact to the slot than others. Traps slightly narrower than the volume of the slot holding the trap result in higher heating rates and maximum temperatures as well as in a lower cooling rate than thicker traps. In addition, narrow or uneven traps exhibit a tendency to cold and hot spots inside the trap depending on how exactly they are positioned in the slots of the aluminum housing. Externally applied mechanical tensions (e.g. due to strong vibrations or forces from the connected tubing) might change the strength and location of contact within these slots leading to a change in temperature distribution inside the trap. Therefore, the results of an inner trap temperature characterization of such narrow traps may somewhat change after they are filled with adsorbent and reintegrated in the instrument. More reliable are traps slightly larger in diameter that tightly fit into the aluminum housing. The cooling of these traps is faster but of course, the drawbacks are smaller heating rates and maximum temperatures.

It has to be noted that temperature measurements inside a trap are performed on empty trap tubes. Filling the trap with adsorbent could have an influence on the temperature distribution inside the trap but once the trap is filled the inside temperature cannot be measured anymore. However, it is assumed that a trap filled with adsorbent could exhibit a more homogeneous temperature distribution than determined from the characterization on the empty trap due to a better heat transfer from the adsorbent tightly packed inside the trap. Nevertheless, traps expressing larger inside temperature differences than other traps tend to cause stronger memory effects when filled with the same adsorbent (Section 2.2.5). Such observations indicate the comparability and usefulness of the empty trap inner temperature characterization even without the presence of adsorbent.

A future improvement could be to enlarge the slots of the aluminum plates and use 1–2 more layers of insulating glass fiber cord around the traps. The extra layers of glass fiber would function as a mechanical buffer zone to allow tiny differences in the individual trap's dimensions and appearance and still fully fixate each individual built in the aluminum housing. On one hand this would reduce the risk of a change in temperature homogeneity due to some freedom of movement for slightly smaller or uneven traps. On the other hand the additional glass fiber insulation layer(s) could reduce the efficiency of cooling when the trap is tightly fixed in the aluminum housing.

2.2.4 Breakthrough volumes for different adsorbents

The idea of a preconcentration trap is to reduce the migration velocity of specific molecules within an air sample passing through the trap in such a way that only these species remain inside the trap while the rest of the air sample leaves the trap unhindered. This can be accomplished by low temperatures and neutral surfaces (e.g. glass beads) or actively adsorbing material (e.g. molecular sieves, activated materials). Each species of interest interacts differently with the adsorbing material, and the choice of adsorbent is a compromise toward a material that does not adsorb too strong but also not too weak. Thus it has to be investigated on one hand if all molecules completely desorb in one desorption process (Section 2.2.5) and on the other hand how large an air volume can be sampled at a given adsorption temperature without loosing molecules of interest during the preconcentration process.

The tests regarding the maximum sample volume performed in the present work followed a general procedure. For a fixed preconcentration time and temperature several measurements of a test gas at a fixed head pressure of ~ 3 bar(a) were conducted at a fixed sample volume to gain statistical information on that sample volume. This was repeated for several different sample volumes (set by regulating the sample flow rate). A linear increase of detector signal (peak area) with sample volume implies the regarded species does not break through the preconcentration trap under the given conditions. A breakthrough is visible when the detector signal does not increase linearly with sample volume anymore (indicating a less efficient adsorption than for smaller sample volumes) or does not increase at all with larger sample volumes (total breakthrough). The same procedure was repeated with a lower preconcentration temperature in case a target species breaks through. The reached maximum sample volume in this test is limited by the flow restriction of the trap due to the packing of the adsorbent, which limits the flow that can pass the trap at 3 bar(a) head pressure.

A species that breaks through the preconcentration trap with the parameters used in the test cannot be measured for scientific purpose under these conditions. In addition each preconcentration trap is self built and therefore unique (Section 2.2.1). Not only can the

Table 2.1: Results of tests for breakthrough volumes on self built preconcentration traps filled with different adsorbents. The numbers are given in ml and if assigned with ">" no breakthrough could be found in the respective test and the number represents the maximum sample volume possible.

~ 65 mg	Carboxen 572	Graphsphere 2017			Carb. 572/Graphsph. 2017*			
[ml]	20 °C	20 °C	0 °C	−40 °C	20 °C	0 °C	−20 °C	−40 °C
CH_2Cl_2	> 240	> 130	> 130	> 130	> 130	> 220	> 220	> 220
$CHCl_3$	> 240	> 130	> 130	> 130	> 130	> 220	> 220	> 220
CH_3Cl	> 240	0	0	> 130	> 130	> 220	> 220	> 220
CFC-11	> 240	> 130	> 130	> 130	> 130	> 220	> 220	> 220
CFC-113	> 240	> 130	> 130	> 130	> 130	> 220	> 220	> 220
HFC-125	> 240	0	0	> 130	> 130	> 220	> 220	> 220
HFC-134a	N/A	0	~ 40	> 130	> 130	> 220	> 220	> 220
CCl_4	N/A	> 130	> 130	> 130	> 130	> 220	> 220	> 220
C_2Cl_4	> 240	> 130	> 130	> 130	> 130	> 220	> 220	> 220
HFC-32	N/A	N/A			~ 40	~ 170	> 220	> 220
C_2H_2	N/A	N/A			0	0	< 50	~ 50
i-Pentane	> 240	> 130	> 130	> 130	> 130	> 220	> 220	> 220
n-Pentane	> 240	> 130	> 130	> 130	> 130	> 220	> 220	> 220

*1:2 (Carboxen 572:Graphsphere 2017)

temperature distribution within each different trap vary; also the density and amount of the used adsorbent might differ for each individual trap, which can have an impact on the preconcentration behavior of the trap. To ensure that the preconcentration process does not bias the results each preconcentration trap has to be tested first before put into use.

Tested were preconcentration traps filled with Carboxen 572, Graphsphere 2017, and a combination of both adsorbents with a ratio of 1:2 (Carboxen 572:Graphshere 2017) (all adsorbents from Supelco, Inc). The tests have been conducted during different phases of this PhD; thus the analyzed species and adsorption times (60 s or 40 s) vary. Detailed information on the tests are given in Appendix B.1 and the summarized results are shown in Table 2.1.

Both tested adsorbents are recommended by the manufacturer to be used primarily for the trapping of molecules with analyte size comparable to C2–C5[4] n-alkanes. The results of the breakthrough tests show that Carboxen 572 is the stronger adsorbent of the two. At room temperature the maximum sample volume within 60 s adsorption time causes no tested

---

[4] Number of containing Carbon atoms

species to break through. Graphsphere 2017 exhibits trapping difficulties in particular for HFCs and the low boiling CH_3Cl. A combination of both adsorbents makes it possible to efficiently trap all the tested species with temperatures easily accomplished by the novel HAGAR-V preconcentration unit. The combination of a strong and a weaker adsorbent is necessary to avoid difficulties in fully desorbing all target species when only the strong adsorbent is used (Section 2.2.5).

2.2.5 Memory effects

Retentive units like the preconcentration trap as well as unheated tubing are located within the HAGAR-V MS module's sample line. Thus there is a non-negligible risk that not all molecules of the previous measurement(s) have been totally purged out of the sample line, potentially leaving their traces in the upcoming measurement(s). This can lead to so called memory effects. Even with all possible precautions taken (e.g. pre-column back flush, purging the sample line before measurement, long heating and purging times of the preconcentration trap, etc.) memory effects can appear.

The preconcentration trap has the highest potential to cause memory effects. This mainly depends on the inhomogeneity of the trap's inner temperature distribution (Section 2.2.3) and the choice of adsorbent. Therefore each unique trap can exhibit different characteristics regarding memory effects.

In particular the strong adsorbent Carboxen 572 is very sensitive to cold spots inside the trap. The trap used during WISE exhibited a very homogeneous inside temperature distribution (cf. Section 2.2.3), and except for C_2Cl_4 memory effects were not noted within the order of measurement precision (cf. Appendix B.2.1). However, other traps filled with Carboxen 572 with inside temperature differences larger than 50 °C exhibited memory effects up to 20 % of the previous sample depending on trap and species.

To minimize the dependence on a perfectly built preconcentration trap and to increase tolerance for potential colder spots a weaker adsorbent can be positioned in front of the stronger one (see also Appendix C.2.4). Thus the more “sticky” molecules get trapped on a weaker adsorbent that promises a more complete desorption of these molecules. The low boiling molecules might break through the weaker adsorbent but then get adsorbed by the stronger one. As the flow direction is reversed between ad- and desorption the “sticky” molecules never come into contact with the strong adsorbent.

A direct comparison between differently packed traps is difficult due to the influence of the differences between individual traps themselves. However, tests have shown that memory effects for a multi adsorbent trap (2:1; Graphsphere 2017:Carboxen 572) can be minimized to insignificance. Even C_2Cl_4 only left a small trace in a single following measurement, which could also be due to unheated tubing. Details about such a test are given in Appendix B.2.2.

As a conclusion can be drawn that in particular for a single adsorbent trap with a strong adsorbent the homogeneous temperature distribution inside the trap is of crucial importance[5]. The most reliable packing of a preconcentration trap with the freedom to trap a large variety of species is the combination of a weak and a strong adsorbent[6].

2.3 Fast gas chromatography

Gas chromatography (GC) is a very popular and widely used technique for the separation of a large variety of gaseous molecules. It is a relatively slow technique and has therefore been optimized in its operation speed since the early 1950s (e.g. Luong et al., 2006). The application of heating devices to the columns has been an important experimental focus in accelerating the separation process. A huge step was accomplished when the first low thermal mass (LTM) column was built in 1995 and first patented in 1998 by Mustacich and co-workers[7]. The principal concept is to tightly pack a heating wire together with the column in a torus of low thermal mass. With this construction much faster temperature ramps can be achieved thereby shortening the duration of a chromatogram when analyzing large numbers of species. In addition the cooling to the initial temperature can be accomplished faster due to the low thermal mass. Thus the waiting time between two samples is shortened for the benefit of a higher measurement frequency.

Commercially built LTM columns are expensive, have considerably long delivery times and in our case have to be customized to fit into the design of HAGAR-V. To be faster and independent in the production process own LTM columns have been developed following the basic principles of the LTM columns mentioned in Luong et al. (2006), with modifications needed to fit into HAGAR-V and avoiding the usage of special construction machinery.

---

[5] This also applies to the adsorbent HayeSep D (Supelco, Inc) which has only recently been used in a HAGAR-V preconcentration trap

[6] A third adsorbent of intermediate strength could be thought of but is most likely of limited benefit given the loss in total adsorbent volume due to the extra use of glass wool separators

[7] R. Mustacich. U.S. Patent 5,782,964, July 21, 1998
R. Mustacich and J. Richards. U.S. Patent 6,209,386, April 3, 2001
R. Mustacich and J. Everson. U.S. Patent 6,217,829, April 17, 2001
R. Mustacich and J. Richards. U.S. Patent 6,490,852, December 10, 2002
R. Mustacich, J. Richards, and J. Everson. U.S. Patent 6,530,260, March 11, 2003
R. Mustacich and J. Everson. U.S. Patent 6,682,699, January 27, 2004

2.3.1 Self-built LTM columns

For HAGAR-V two different versions of LTM columns have been built. Both models comprised a torus of a coiled 0.4 mm fused silica column. The torus has a 7 cm inner diameter and the loose column ends are connected to ~ 50 cm of deactivated guard columns of the same dimensions. The torus of the coiled column as well as the column connectors are held together by a wire that is wrapped crosswise to the column. The two guard columns are unbound and not part of the tightly coiled torus.

In the first as well as in the second generation of self built LTM columns pre- and main-columns were constructed. They differ in length (the pre-column usually is shorter than its partner main-column) and in resistance of heating wire. The resistance of the heating wire is ~ 15 Ω and ~ 6.5 Ω for the pre- and the main-column respectively. The lesser total resistance of the main-columns' heating wire is chosen to compensate the relatively lesser power available in HAGAR-V by using only 28 V compared to the 48 V which is used for the pre-columns.

As separation column an Al_2O_3/Na_2SO_4 fused silica PLOT column was chosen with an inner diameter of 0.25 mm (Agilent J&W). Although alumina, in particular in contact with chlorine or water, behaves as an acidic catalyst decomposing partly halogenated VOC (Noij et al., 1988), good experience with this type of column has been made in former studies (Lauther, 2015). In addition due to the small diameter the column can be coiled into the torus size needed to fit into HAGAR-V. However, it has to be mentioned that the decomposition of species like CH_3Cl, CH_2Cl_2, and $CHCl_3$ can probably only be avoided when pre- and main-column together do not exceed a length of ~ 10 m and are operated at low temperatures and pressures as it was done during WISE (see Table C.2). What could not be avoided was the decomposition of CH_3CCl_3 (Methylchloroform) resulting in a clear peak of CH_2CCl_2 (Vinylidene chloride) as it has been observed in Noij et al. (1988) on an Al_2O_3/KCl column as well.

2.3.1.1 First version LTM column

In the first generation of self built LTM columns the binding wire was used for heating and two Pt100 temperature sensors were fixed underneath it. In addition the whole torus was covered in ceramic glue for electrical insulation and a more homogeneous temperature distribution. To connect the guard columns with the separation column the first generation of self built LTM columns used Press$_2$Fit Repair Unions (InnovaQuartz LLC, USA) made of glass. The advantage of this model was a comparably easy and inexpensive built.

Unfortunately, even with the usage of supporting polyimide resin the connectors leaked in nine out of ten cases and the ceramic glue made it impossible to change them or anything else of the LTM column once it was built. Also the Pt100 temperature sensors were not very reliable due to fragile wiring and complicated insulation from high temperatures. The temperature regulation was based on the measurement at only one point of the LTM column, which, however, did not have a negative effect on the reproducibility of temperature ramps and chromatography.

2.3.1.2 Second version LTM column

The second generation of self built LTM columns is closer to the commercially available LTM columns mentioned in Luong et al. (2006) and is used as default in HAGAR-V since WISE (Section 3.1). A 0.125 mm Ni wire with a length of about ¾ of the columns length is used as a temperature sensor and tightly pressed onto the column by a PTFE shrinking tube that engulfs both (see Figure 2.7). A PTFE insulated heating wire is wound in parallel to the column and the temperature sensor.

For the main-columns longer heating wires with lower resistance (larger diameter) are used to get a more homogeneous temperature distribution within the LTM column. This additional thermal mass does not have a significant effect on the heating/cooling rates of the main-column. The length of the used column is the dominant factor determining the rates of temperature change.

The guard columns are connected to the separation column by tiny and ultra light micro unions (µ-Union, SGE) which proved to be leak free with a comparably easy installation. To obtain an optimal temperature distribution aluminum foil is wrapped around the torus.

This self built type of LTM column provides the freedom to choose column type, length and diameter, and the heating wire. In particular shortening the column or readjusting the wires or unions is always possible with minimum effort. In addition this model can be operated with only one wire that is pressed tightly onto the separation column as temperature sensor and heating wire at the same time, similarly as done for the preconcentration trap (Section 2.2.2). However, there was not enough space in HAGAR-V to implement the circuit board necessary for the use of this technique within the instrument. Thus the LTM columns in the present work each have a heating wire and a temperature sensor in form of two separate wires. The characterization of the temperature sensor is done in a commercial GC oven where the temperature can be regulated to a precision of 0.1 °C.

Figure 2.8 shows how the columns are mounted via glass fiber insulated wires inside two aluminum boxes. The boxes are used as a wind tunnel for the cooling fans that are mounted

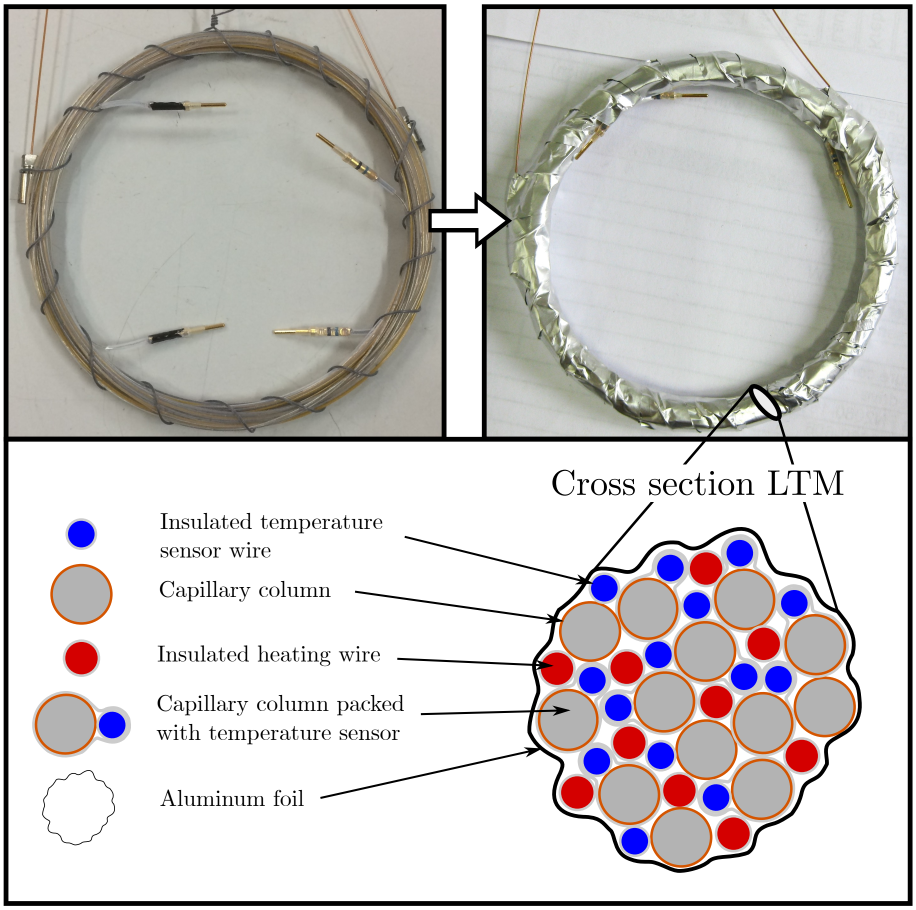

Figure 2.7: Pictures of a self built second version LTM column without and with aluminum foil. Plugs of temperature sensor and heating wire as well as μ-union column connectors underneath the binding wire are visible in the upper left picture. The μ-unions connect the separation column with a guard column. Electrical insulation is accomplished by PTFE shrinking tubes. A schematic cross section of the self built LTM column explains the inner part of the torus.

each on one of the two open ends of these boxes. Thereby the longer column (here main-column) is put closer to the fan and the shorter column (here pre-column) is positioned behind the larger one. This positioning favors the cooling of the larger column (which has a higher thermal mass) over the shorter column which is exposed to the waste heat of the larger column. Hence, this positioning balances differences in the cooling rate of pre- and main-column when one pair of columns get cooled by only one fan. The aluminum housing has the additional effect to minimize the influence of external air movement on the columns and thus increases their temperature stability.

Even the version of self built LTM columns that uses two separate wires for temperature measurement and heating exhibits very fast heating and cooling properties at the given

Figure 2.8: Mounting of a full set of four self built LTM columns inside a housing for controlled temperature regulation. Insulated wires hold each column almost contact free in the wind tunnel. One fan cools one pair of columns. The housing also protects the columns from temperature disturbing outside air movements.

instrumental conditions. The maximum heating rates range between ~ 20 °C/s (4 m pre-column) and ~ 12 °C/s (17 m main-column) and mainly depend on column length. These values exceed the needed temperature ramps in all the chromatographic applications that have been used with this system so far.

The cooling rates also depend on the columns length but additionally the ambient temperature plays a significant role for the convective cooling via fans. Within ~ 60 s (4 m pre-column) to ~ 75 s (17 m main-column) a cooling from 200 °C down to 35 °C can be accomplished at ambient temperatures of ~ 25 °C. The cooling rate drops significantly the closer the column temperature is to the ambient temperature (cf. Figure 2.10).

2.4 Linearity of signal response

In general a MS detector (MSD) signal response is proportional to the mixing ratio and size of the sample. However a perfect linear relationship is not always given. Parameters like the pressure inside the MS vacuum chamber, the water content of a sample, and also other parts of the instrument, in particular the preconcentration trap and the separation columns, can induce non-linearity in the resulting signal response. To determine the relationship between mixing ratio and signal response tests were performed where the test air was diluted with different fractions of synthetic air. The dilution of test air translates into a

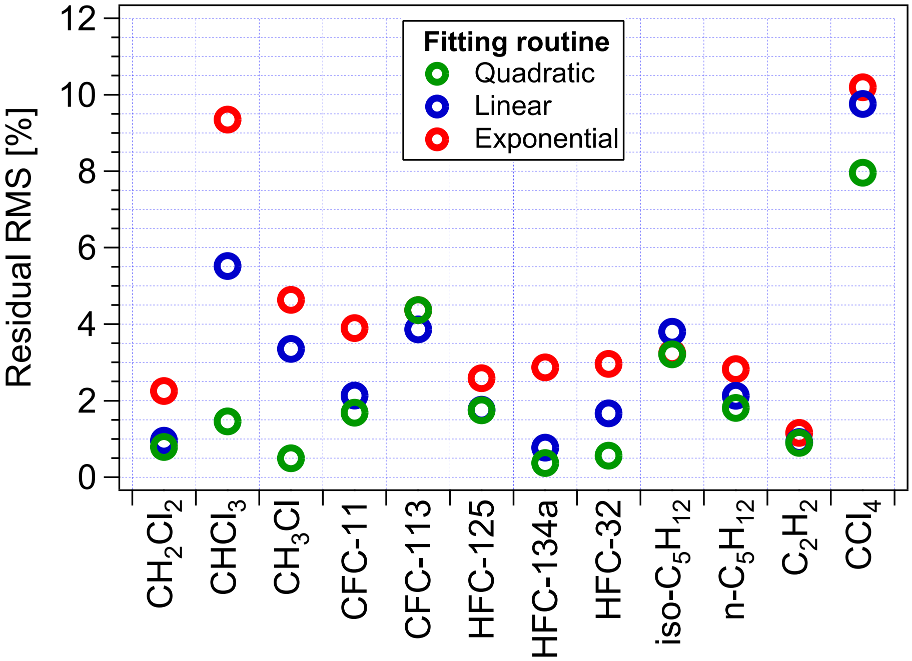

Figure 2.9: Residual RMS for different fitting routines applied on relative signal response vs relative mixing ratio.

respective change of mixing ratios. For more information about the measurement setup see Appendix B.3.

Twelve species have been analyzed. The signal was linearly detrended by the use of the calibration gas SPAN (see Table E.2; more about detrending in Section 3.3.1). The four (or less if some were left out) measurements per fraction of test air were averaged and normalized to the maximum signal to yield values relative to the signal from the undiluted test air sample.

To quantify the (non-)linearity of each species a line fit as well as a quadratic and an exponential fit were applied to the data. The resulting residual root mean square (RMS) — a measure for the scatter of data points around the fit — were compared as a measure of fit quality. The results are plotted in Figure 2.9.

Except for CFC-113 all analyzed species showed the lowest residual RMS for a quadratic fit. This implies a preferred quadratic non-linear relationship between signal response and mixing ratio for most of the target MS species. However, significant differences between linear and quadratic relationships could only be shown for $CHCl_3$, CH_3Cl, CCl_4, and HFC-32.

The non-linear detector response for these chlorine containing species could be a result of the use of an Al_2O_3 separation column that could potentially chemically alter halogenated VOC (as discussed in Section 2.3.1). It could also be that the strong adsorbent Carboxen 572 might desorb some species differently depending on mixing ratio. However neither of these hypotheses could be proven to this date.

Novel tests on the combination of another adsorbent (HayeSep D, Supelco) and a different column type (DB-624, Agilent J&W) promise a more linear signal response. This would suggest that the linearity of the signal response depends on the choice of the stationary phases (adsorbent and column type). Thus in particular for the affected species when measured with the use of Carboxen 572 and Al_2O_3 separation columns a non-linear calibration of in-flight data (Section 3.3.2) is advised to avoid measurement bias due to non-linear detector response.

2.5 First operation on the HALO research aircraft

The novel preconcentration traps and LTM columns as key parts of the MS module were both integrated in HAGAR-V and deployed on the HALO research aircraft during the WISE mission (Section 3.1). In this section an example is presented for a one channel MS measurement cycle where the preconcentration trap and the LTM columns work together in unison with the other parts of the MS module.

2.5.1 A MS measurement cycle

A MS module measurement cycle during WISE generally started with flash heating the preconcentration trap to desorb the sample that was enriched at the end of the previous cycle (Figure 2.10). Within a few seconds the sample is desorbed from the trap and gets refocused on the (relatively cold) pre-column due to their temperature and thereby mobility differences. By heating the pre-column the sample gets transported further onto the (relatively cold) main-column where the sample gets refocused a second time.

When the last species of interest have left the pre-column the carrier gas flow on the pre-column is reversed (“backflush”) to flush out molecules with lower migration speed. On the main-column the species get further separated. This separation process is sped up by an appropriate temperature ramp. The detection is timed in such a way that the MSD only measures in the time interval when the species of interest elute and is otherwise turned off. At the end of a MS cycle the preconcentration trap has reached its adsorption temperature

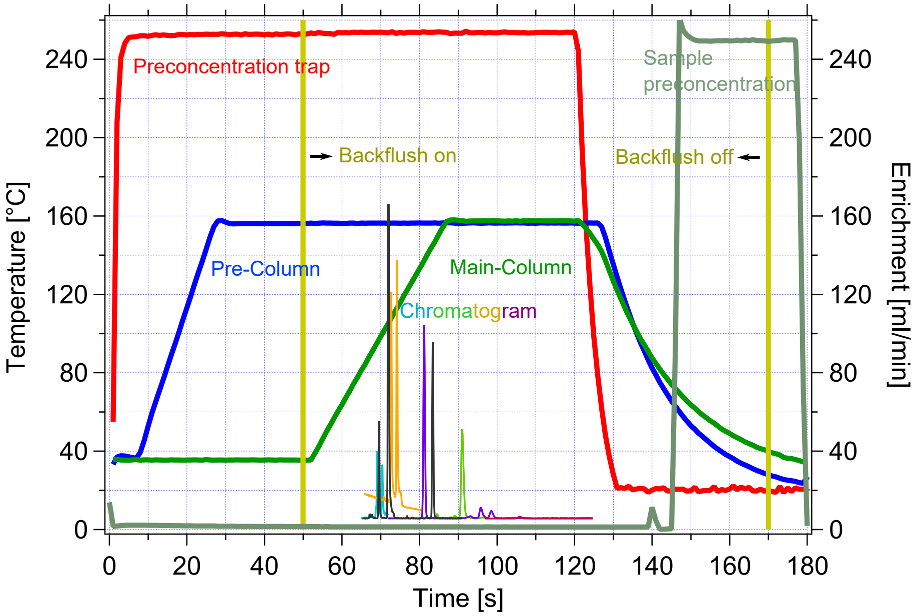

Figure 2.10: Example of a measurement cycle of the MS module during WISE flight #13. House keeping data of temperatures and preconcentration flow are depicted. Sample preconcentration on the 20 °C preconcentration trap occurs at the end of a cycle. At the beginning of a cycle the trap desorbs the sample by flash heating onto the cold pre-column to refocus it. The pre-column speeds the sample further onto the colder main-column by heating for a second refocus effect. Once the last species has left the pre-column the backflush reverses the carrier gas flow direction on that column. A chromatogram is recorded only when the species of interest elute from the main-column. The main-column is heated to accelerate the elution.

to further preconcentrate a new sample and the columns get cooled down by fans to their initial temperatures. Technical details of these processes are given Appendix A.5.2.

The second MS channel has not been used for the first deployment of the newly developed instrumental parts. Figure 2.10 shows house keeping data of WISE flight #13 to visualize a whole MS cycle of one channel. In particular the temperature stability of the preconcentration trap and the columns underline the successful design of the developed parts. It also becomes visible that due to the fast temperature ramps and the two sample refocusing steps the actual chromatogram takes only about 30 % of the time available in one MS cycle. As it has recently been shown (but will not be discussed in this work) the MS can be used for almost continous recording of chromatograms by using the second channel thus doubling the measurement frequency. For the presented one channel method Table C.2 gives an overview of the most important parameters of the MS module and how they changed over the flights during WISE.

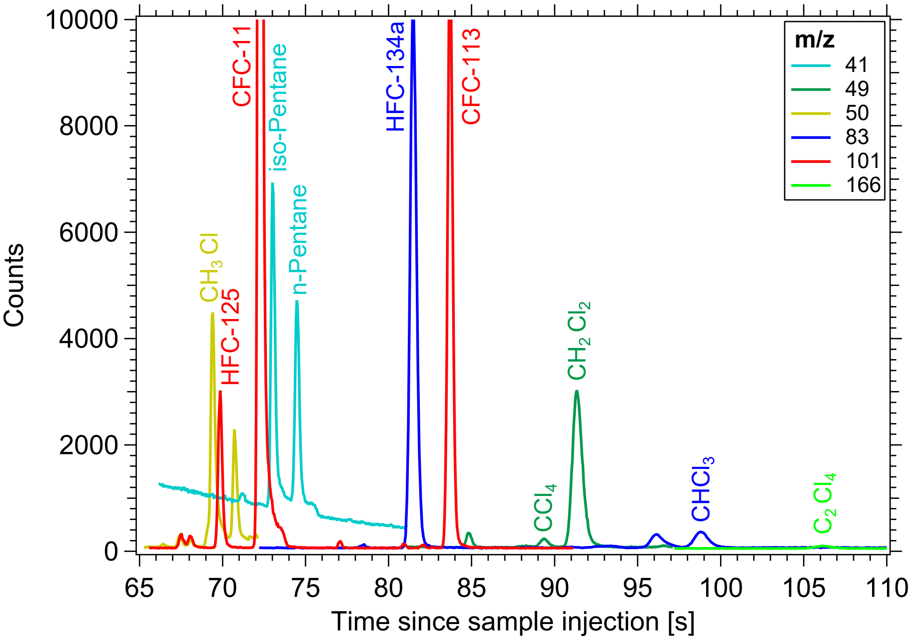

Figure 2.11: Example chromatogram of the MS module during WISE. Different species are measured on different mass fragments.

2.5.2 Adapting MS measurements to fast GC

Figure 2.11 shows the chromatogram of an in-flight measurement of the MS module during WISE. The total of 11 species measured on 6 mass channels elute within a time window of ~ 40 s which starts around one minute after the sample injection. Due to the possibility of a fast temperature control of the two self built LTM columns the sample gets refocused twice resulting in peak widths of the eluting species that are typically < 1 s. As a consequence the scan mode of the MS where all mass fragments (up to m/z = 700) get scanned for measurement in an iterative process is too slow for the detection of such narrow peaks. Instead time windows within the chromatogram have to be programmed beforehand where only a few selected mass fragments are measured[8]. Depending on the number of mass fragments scanned and the individual dwell times (the integration time for a resulting data point of a mass fragment) the number of data points per peak can be selected. It is advised to use dwell times as large as possible and the manufacturer of the MS (5975C, Agilent Technologies) sets the default dwell time for each mass fragment to 75 ms. In addition, it is more secure to measure at least two mass fragments per species in case of unexpected coelutions or other needs to verify a species. The drawback are less resolved peaks because

---

[8] The so called SIM (Selected Ion Monitoring) mode

Table 2.2: Limit of detection (LOD) determined from WISE flight #12.

	LOD [ppt]
CH_2Cl_2	0.20
$CHCl_3$	0.28
CH_3Cl	4.2
CFC-11	0.06
CFC-113	0.06
HFC-125	0.13
HFC-134a	0.12
iso-Pentane	1.9
n-Pentane	1

only one mass fragment can be measured at a time. Therefore, to receive at least 20 data points for a properly resolved peak only one mass fragment per species was selected with dwell times that were mainly kept below 10 ms depending on peak width and the number of coeluting species. Chosen as representative mass fragment of a target species was the most abundant mass fragment of the respective mass spectrum that did not show any other coeluting species.

With the minimum dwell time of 1 ms isotopic water (m/z = 19) has been measured as a proxy to monitor water inside the system. An overview of the used MS detection windows and selected mass fragments is given in Table C.3.

The exact arrangement of the SIM windows plays an important role for the peak resolution and signal-to-noise ratio. Only the drastic reduction of measured mass fragments and their respective dwell times can yield highly resolved peaks but longer dwell times can significantly smooth the background noise. This is particularly important for the measurement of short lived species in order to improve the limit of detection (LOD) and has been considered while programming the SIM windows. However, this choice of SIM parameters is strongly based on experience and has to be considered individually for the respective species[9].

With the SIM parameters chosen during WISE detection limits of a few ppt down to the order of parts per quadrillion (ppq; 10^{-15}) are reached (see Table 2.2 and Appendix

---

[9] The measurement frequency is equal for all contemporaneously measured mass fragments. The dwell time can be set for each individual mass fragment thereby affecting the measurement frequency. Considered were expected peak widths including retention time shifts as well as priority (regarding peak or background measurement) of mass fragment at each given retention time. In general: LOD $\propto$ 1/noise $\propto \sqrt{\text{dwell time}}$.

B.4). This is far below the expected atmospheric abundance in the upper troposphere and lower stratosphere (UTLS) for almost all of the regarded species. This indicates that the MS module is well suited for the deployment on the research aircraft HALO with this instrumental setup.

2.5.3 Measured species and instrumental precision

The different mass fragments and their corresponding peaks are shown in Figure 2.11 as measured in-flight during WISE. Seven of the eleven drawn species could be processed for scientific use. C_2Cl_4, CCl_4, iso-, and n-Pentane were rejected. Only C_2Cl_4 had to be rejected due to instrumental issues; the other three were below the detection limit or not measured on a proper mass channel (for more details see Appendix C.2.5). The remaining seven species of the chromatogram were analyzed and measured very precisely.

The precision of a measurement is very important if detailed information about atmospheric processes is sought from the data. For the air measurements the precision was estimated as the standard deviation of the detrended measurements of one of the two in-flight calibration gases called CAL (see Table E.2). Table 2.3 shows the precision for each species and flight with useful data. The precision is given as absolute value in units of mixing ratio and as a relative value in percent of the tropospheric background gas CAL.

The fact that measurement precisions on the order of 1 % of tropospheric background air were achieved with the instrument operating on an aircraft under extreme conditions proves the efficiency of the newly developed hardware. Many parameters can influence the measurement precision but the repeatability of the operation of the preconcentration trap and the separation columns play the key role in such successful measurements.

Table 2.3: Overview on the measured MS species during WISE flights and their respective data quality. The Precision is taken from the standard deviation of detrended CAL measurements in flight.

WISE	CH_2Cl_2		$CHCl_3$		CH_3Cl		CFC-11		CFC-113		HFC-125		HFC-134a	
Flight	ppt	%*	ppt	%*	ppt	%*	ppt	%*	ppt	%*	ppt	%*	ppt	%*
#7	1.8	3	0.62	5.5	x		x		x		x		x	
#8	1.1	1.9	0.16	1.4	x		x		0.81	1.1	x		x	
#9	0.87	1.5	0.48	4.3	15.5	2.6	2.3	1	0.83	1.1	0.27	1.2	x	
#10	0.97	1.6	0.77	6.9	26.2	4.4	2.5	1.1	0.77	1.1	0.33	1.4	1.2	1.3
#11	0.64	1.1	0.26	2.4	13.8	2.3	3.5	1.5	0.63	0.88	0.4	1.7	0.97	1
#12	1	1.7	0.25	2.2	15.2	2.5	2.4	1	0.99	1.4	0.31	1.3	0.89	0.92
#13	0.44	0.73	0.24	2.2	9.6	1.6	2	0.84	0.74	1	0.35	1.5	0.51	0.53
#14	0.93	1.6	0.2	1.8	18.9	3.1	2.7	1.2	1.1	1.5	0.31	1.3	0.6	0.62
#15	1.3	2.3	0.34	3.1	20.5	3.4	4	1.7	1.3	1.9	0.5	2.2	1.6	1.6
#16	2.5	4.2	0.74	6.7	x		x		x		0.28	1.2	1	1.1
Mean	1.2	2	0.4	3.7	17.1	2.8	2.8	1.2	0.9	1.2	0.34	1.5	1	1

* relative to tropospheric CAL gas (see Table E.2)

Chapter 3

Analysis and processing of WISE MS data

For the processing of HAGAR-V data the graphing and analysis software IGOR PRO (Version 4.0.1.0, WaveMetrics Inc.) has been used including the analysis package NOAHChrom originally developed by NOAA, USA. In the last 20 years NOAHChrom has been further adapted for the processing of HAGAR GC-ECD data operated on the M55 Geophysica (e.g. Riediger, 2000; Ivanova, 2007).

During its first successful deployment at the WISE campaign (Section 3.1) the MS module of HAGAR-V produced a novel set of data to be processed, for which more options had to be implemented in NOAHChrom. In addition HAGAR-V's various in-flight diagnostic modes were used to get a more profound understanding of HAGAR-V's GC-MS data quality. In this chapter a detailed analysis and eventual corrections for HAGAR-V MS aircraft data are discussed implicating important new implementations for NOAHChrom. These include in particular the EMG fitting routine (Section 3.2) and a larger choice of options for the calculation of mixing ratios (Section 3.3).

The last section of this chapter focuses on the comparison of HAGAR-V MS and ECD measurements. The results of different methods of data processing were thus tested and analyzed strengthening the confidence in optimal MS module in-flight data quality.

The analysis presented in Chapter 3 is based on detailed considerations. Supplemental information is given in appendices D and E.

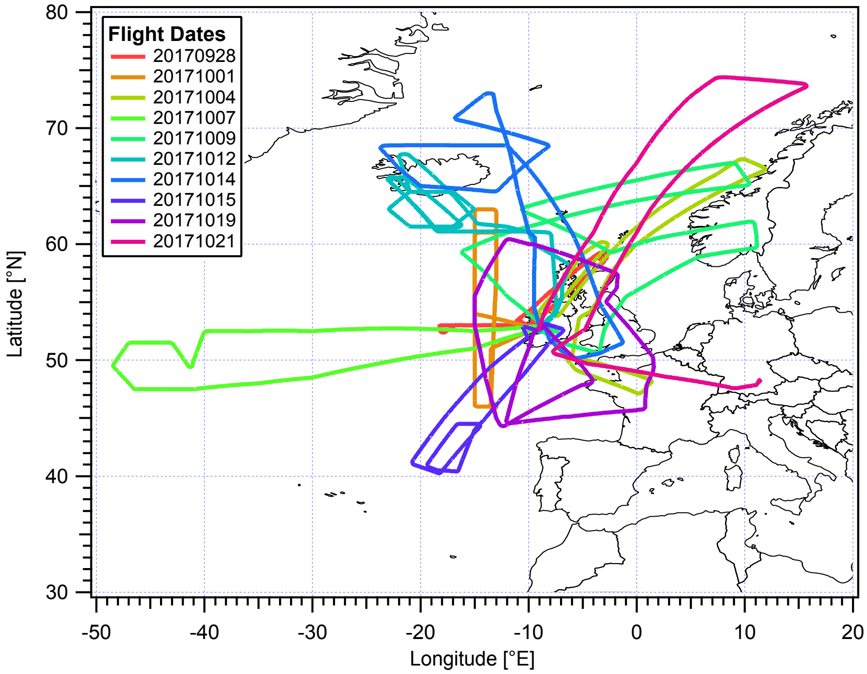

Figure 3.1: Flight paths of all successful measurement flights for the MS module during WISE.

3.1 WISE (Wave-driven ISentropic Exchange)

From August 7 until October 21 in 2017 the aircraft campaign WISE (Wave-driven ISentropic Exchange[1]) to investigate the mid latitudinal UTLS region over the Atlantic Ocean and western Europe was conducted. During WISE 16 flights with the German research aircraft HALO (High Altitude and LOng range[2]) were performed with a total of 134.5 flight hours. This includes two flights from and to Oberpfaffenhofen, 12 flights from and to Shannon, Ireland, and two transfer flights between the two locations with scientific goals. The payload comprised 12 different instruments including three remote sensing and nine in situ instruments.

WISE was coordinated by the research center Jülich (Prof. Dr. M. Riese & Dr. M. Kaufmann) and the University of Mainz (Prof. Dr. P. Hoor & Dr. D. Kunkel). Other partners of the joint project were Karlsruhe Institute of Technology (KIT), German Aerospace Center (DLR), PTB Braunschweig, and the Universities of Frankfurt, Heidelberg, and Wuppertal. The key scientific goals of WISE are listed as following:

---

[1] https://www.wise2017.de/

[2] https://www.halo.dlr.de/

Table 3.1: Overview of WISE flights, dates and objectives. The start and landing times are given in UTC.

#	Date	Start	Landing	Objectives
7	Sept, 28	13:16	21:05	Highly structures tropopause
8	Oct, 01	12:05	21:58	Outflow from hurricane MARIA and Asian Monsoon
9	Oct, 04	09:35	19:03	Filaments in decaying trough, SVC* in outflow of WCB**
10	Oct, 07	12:45	20:36	Rossby-wave breaking – early stage
11	Oct, 09	08:31	17:22	Rossby-wave breaking – later stage
12	Oct, 12	10:00	18:57	Strong TIL*** and air mass mixing
13	Oct, 14	08:27	17:22	Decay of filament in trough (follow on flight #9)
14	Oct, 15	12:54	19:08	WCB outflow and pot. impact of hurricane OPHELIA
15	Oct, 19	08:59	17:31	Air sampling around hyperbolic point and related mixing effects
16	Oct, 21	04:25	12:49	Rossby-wave breaking and transfer

*Streamwise vorticity current

**Warm conveyor belt

***Tropopause inversion layer

- ▷ Investigation of transport and mixing in the region of the Extratropical Tropopause Layer (ExTL[3]) and the influence of the Tropopause Inversion Layer (TIL[4])
- ▷ Understanding of horizontal transport into the extratropical lower stratosphere above the ExTL
- ▷ Determining the role of halogenated VSLS for ozone depletion and radiative forcing in the UTLS region
- ▷ Investigating the occurrence and effects of sub-visual cirrus clouds in the LMS

---

[3] The ExTL is defined by strong trace gas gradients between the troposphere and the stratosphere also known as mixing layer, e.g. Hoor et al. (2002, 2004); Pan et al. (2004); Hegglin et al. (2009).

[4] The TIL is commonly defined as a vertically confined layer of enhanced static stability in the equatorial, mid-latitude, and polar UTLS region, e.g. Birner et al. (2002); Gettelman and Wang (2015). In the extratropics, the TIL is co-located with the ExTL, e.g. Hegglin et al. (2009); Kunz et al. (2009); Schmidt et al. (2010).

The in situ tracer measurements of HAGAR-V (Appendix A) contribute to the first three of these four key scientific goals of WISE. During the first six flights excessive hydrating of the air samples by the dehydration unit made it impossible to use HAGAR-V MS data for scientific purposes for these flights. From flight #7 onward a solution was found (see Appendix C.2.2) and thus the HAGAR-V MS WISE data comprise only measurements from flight #7 to flight #16 (i.e. from September, 28 to October, 21). The solution implies that HAGAR-V MS measurements were only conducted at low ambient water vapor levels, i.e. at the tropopause region and the stratosphere. Figure 3.1 shows the flight paths of all successful measurement flights of the MS module covering a wide spread area above the Atlantic ocean and parts of western Europe. Table 3.1 shows the scheduling and scientific objectives for the WISE flights relevant to the data from the MS module. Daily working routines and noticeable issues during WISE, mainly concerning the MS module, are discussed in Appendix C.2.

3.2 Peak fitting

For the processing of HAGAR-V GC-MS chromatograms fitting functions are used. The (discrete) chromatographic peaks are approximated by a function to allow a precise calculation of the peak height or peak area. Either of the two parameters can be used for the calculation of mixing ratios. The choice of fit function and the treatment of background signal is discussed in the following sections.

3.2.1 The EMG fit

In chromatography the ideal case is to obtain Gaussian peak shapes from the detector. In reality deformations of this ideal peak shape have to be expected. For example variations of the carrier gas velocity (e.g. Götmar et al., 1999), dead volumes, active sites or other nonlinear retentive effects (e.g. Hinshaw, 2009) can lead to tailing peak shapes. A common way in chromatography to best include these effects in the peak quantification is to use the exponentially modified Gaussian (EMG) distribution as a fit function (e.g. Delley, 1985; Kalambet et al., 2011). For the fitting of HAGAR-V MS peaks the following EMG expression is used (Kalambet et al., 2011):

$$f(x) = \frac{h\sigma}{\tau}\sqrt{\frac{\pi}{2}}\exp\left(-\frac{1}{2}\left(\frac{x-\mu}{\sigma}\right)^2\right)\exp\left(\frac{1}{\sqrt{2}}\left(\frac{\sigma}{\tau}-\frac{x-\mu}{\sigma}\right)\right)^2\operatorname{erfc}\left(\frac{1}{\sqrt{2}}\left(\frac{\sigma}{\tau}-\frac{x-\mu}{\sigma}\right)\right) \tag{3.1}$$

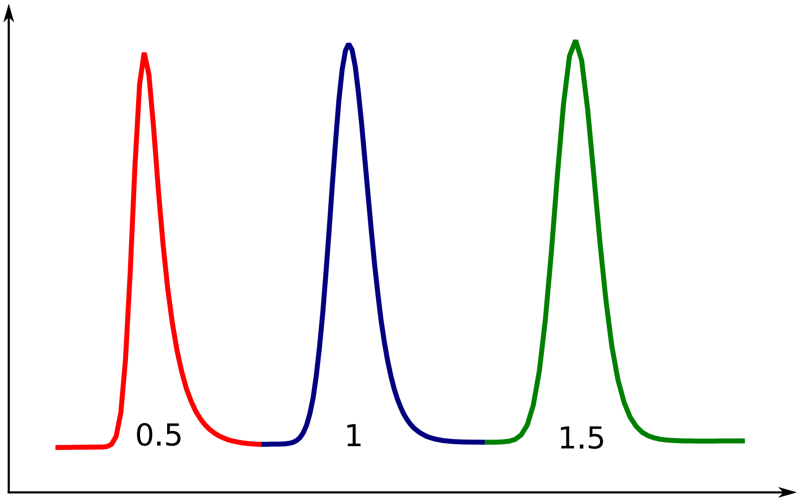

Figure 3.2: Examples of EMG peaks for different observed peak shapes (σ/τ values).

The complementary error function is $\mathrm{erfc}\,(x) = 1 - \mathrm{erf}\,(x) = \frac{2}{\sqrt{\pi}} \int_x^\infty e^{-t^2} dt$. As a Gaussian equivalent the letters used stand for h: peak height, σ: peak width, µ: peak center and the exponential equivalent τ: relaxation time.

The ratio σ/τ defines the peak shape, i.e. the strength of the peak tailing. In particular for narrow peaks of typical σ between ~ 0.07 s to ~ 0.3 s, as observed with the MS module during WISE, σ/τ can have a value < 1.5 to describe a clearly visible tail. Typical σ/τ values for peaks of the MS module during WISE ranged between 0.5 and 1.5[5]. Figure 3.2 shows example EMG peaks for different observed peak shapes (σ/τ values). Supplemental information about the used EMG function are given in Appendix D.1.

In general the peak areas were used for further data analysis. Only in the case of CH_3Cl where the peak had other unidentified species underneath its front and tail the height was used resulting in more reliable and stable results (see Appendix D.3).

3.2.2 Background fitting

In general, the background signal in chromatography is not zero and the peaks of interest emerge from the background consisting of a potentially variable baseline and potential signals of overlapping peaks. Therefore the background has to be quantified and included in the fits. For the MS data baselines were fitted as generally linear with variable slopes. Different modifications (quadratic and exponential baseline fits) have been implemented

---

[5] Typical σ/τ values during WISE: CH_2Cl_2: 1; $CHCl_3$: 1; CH_3Cl: 0.5; CFC-11: 0.85; CFC-113: 1.5; HFC-125: 1.1; HFC-134a: 1.4.

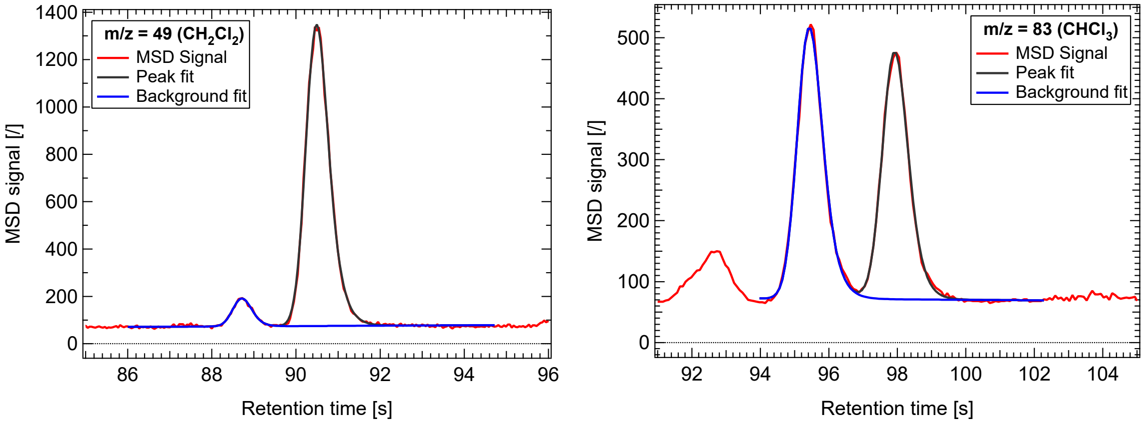

Figure 3.3: Examples of double peak EMG fit of WISE MS data from CH_2Cl_2 (left) and $CHCl_3$ (right). The neighboring peak (EMG) is included in the sloping linear background to improve the fit quality.

in the EMG fitting routine and tested but did not improve the fit quality and rather made it less robust due to overparametrization.

In order to accommodate the case of two neighboring peaks an additional EMG fit was added to the background to include the neighboring peak. With this routine not fully separated peaks can be properly fitted. In addition the background of baseline separated but closely neighboring peaks can be described more precisely due to a better approximation of the background. CH_2Cl_2 exhibited such a close neighbor peak (fragment of CCl_4) and by including it in the background the precision of CH_2Cl_2 improved in some flights by up to ~ 8 %.

The so called double peak EMG fit has been used for CH_2Cl_2 , CH_3Cl, and $CHCl_3$ of the WISE MS data set. Figure 3.3 shows as example a chromatogram of both CH_2Cl_2 and $CHCl_3$.

3.3 Calculation of HAGAR-V MS mixing ratios for WISE data

To correct for potential drifts in the measurement signal HAGAR-V GC data need to be detrended. This is done simultaneously with the calculation of mixing ratios (calibration). In addition several tests have been performed on in-flight HAGAR-V MS data that can demand further modification or special data treatment for the calculation of mixing ratios. The tests and their results are presented in this section and further consequences are discussed.

The combined results of all the tests presented in this chapter results in specific ways to calculate MS module mixing ratios depending on flight and species. The determined methods and corrections are listed in Table 3.2.

3.3.1 Detrending

In general, the detector response (R) to different mixing ratios (χ) can be described as a monotonic function, thus $\chi = f(R)$ where R is usually measured as peak area (alternatively height) normalized by sample size. For a linear detector like the MSD f is a linear function and $f(0) = 0$. However, processes like the sample preconcentration or the separation on retentive columns can produce a species dependent non-linear response. To investigate if this is the case, a test for linearity has been performed finding evidence for non-linear responses (Section 2.4).

HAGAR-V is equipped with two different calibration gases and during flight every five MS measurements a calibration is performed with one of them (in alternation; see Appendix C.3). The two calibration gases CAL and SPAN have different and known mixing ratios (see Table E.2). The combination of the detector response (R_i) from the calibrations with known mixing ratio (χ_i) of the respective calibration gas (i) provides the basis for determining for each air measurement during flight a local relationship (f) between the detector response and the mixing ratio of a target species.

The usage of two different calibration gases allows various options for the relationship $\chi = f(R)$ for each species. In either case, the calculated mixing ratio is a function dependent on the response of one or both of the calibration gases in addition to the response of the measurement itself. For example $\chi = f(\chi_{CAL}, \chi_{SPAN}, R)$ for the use of both working standards. The mixing ratios χ_{CAL} and χ_{SPAN} of CAL and SPAN are known and R_{CAL} (R_{SPAN}) is the respective response at the time of an air measurement estimated by interpolation in time between the two CAL (SPAN) measurements closest to the current measurement (with response R).

This process detrends the data iteratively applying a linear interpolation between two calibration gas measurements of the same gas. As a consequence non-linear signal drifts cannot properly be detrended even with every fifth measurement being a calibration gas. During WISE short non-linear drifts over the relevant interval of 10 measurements appeared only occasionally for a few species at the beginning of a flight. Such affected data has consequently been rejected or else its influence becomes visible in the measurement precision.

3.3.2 Calibration methods

To calculate the mixing ratios of MS measurements during WISE the following calibration methods could be used:

- ▷ Single-point calibration: Linear relationship determined by a single calibration gas CAL (or SPAN) and zero (i.e. $f(0) = 0$)
- ▷ Linear two-point calibration: Linear relationship determined by two calibration gases CAL and SPAN
- ▷ Non-linear two-point calibration: Quadratic, exponential or logarithmic relationship determined by two calibration gases CAL, SPAN, and zero (i.e. $f(0) = 0$)

The single-point calibration assumes a linear detector response and $f(0) = 0$. With the availability of two different calibration gases and the possibility of non-linear detector responses the single-point calibration is rarely considered in the present work (example below).

Without using the constraint $f(0) = 0$ the linear two-point calibration is robust against (constant) system contamination. In addition, this method considers non-linear detector responses just that the response curve $f(R)$ is linearly approximated between the two calibration gases. This requires relatively small variations of the air samples' mixing ratios and the mixing ratio of one of the two calibration gases to be close to the minimum and the mixing ratio of the other calibration gas to be close to the maximum mixing ratio of the air samples. The determined calibration curve of a linear two-point calibration should not be used outside the mixing ratio range of the two calibration gases in case of a non-linear detector response. Figure 3.4 (left) gives an example of different response curves calculated for CH_2Cl_2 during WISE flight #12. The non-linearity in the relevant mixing ratio range is barely visible but it has a significant impact on the mixing ratio depending on the calibration method. In this example, showing only a small non-linearity, the use of the linear two-point calibration can bias (here overestimate) the mixing ratios of air measurements that are not close to those of CAL or SPAN. The linear two-point calibration is efficiently used for the calculation of HAGAR ECD mixing ratios of long-lived trace gases and additional information is given by Riediger (2000), Werner (2007), Ivanova (2007), and Hösen (2013).

The most versatile method of calculating HAGAR-V MS mixing ratios is the non-linear two-point calibration. In general, a quadratic function best describes the non-linearity of most of the HAGAR-V MS response curves (Section 2.4). However, some cases of strong

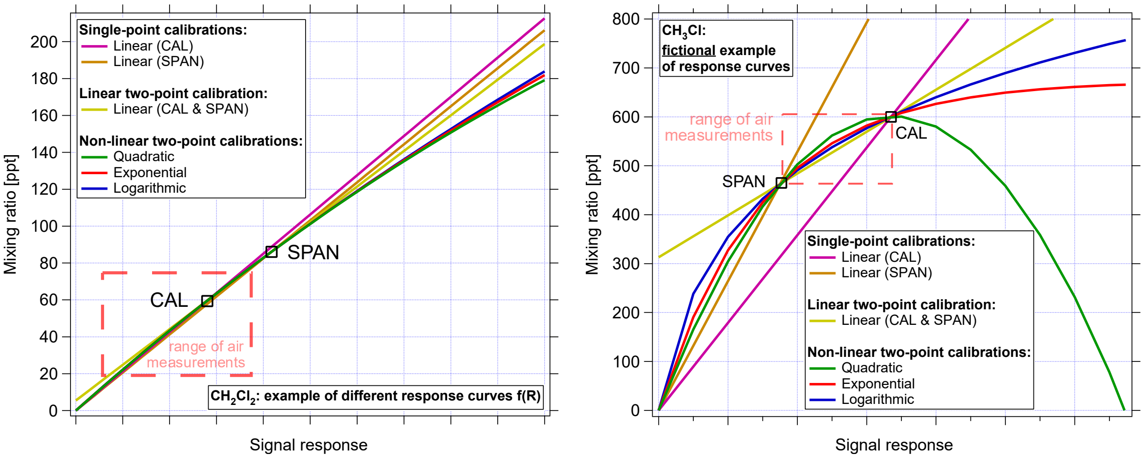

Figure 3.4: Examples of different response curves calculated with different calibration methods. The left graph shows a real example of different $f(R)$ calculated for CH_2Cl_2 measurements of WISE flight #12. The right graph shows a fictional example of response curves calculated for manipulated CH_3Cl data with a strongly amplified non-linearity to emphasize the possibility of a variety of different results depending on the choice of calibration method. The red boxes indicate the respective range of mixing ratios of air samples measured during WISE. CAL and SPAN indicate the respective χ_{CAL} and χ_{SPAN} value used for the calculation of the response curves.

non-linearity can be thought of where the use of a quadratic calibration curve can result in the calculation of an unrealistic, non-monotonic response curve (Figure 3.4, right). In such a case an exponential or logarithmic function can be used to more accurately describe the response curve. Nevertheless, it is of crucial importance to characterize a significant detector non-linearity to know which calibration method based on the given calibration gases provides valid results for the mixing ratio range of the analyzed air samples. Figure 3.4 (right) emphasizes this argument using the example of manipulated CH_3Cl data of strongly amplified non-linearity.

As illustrated in the example of CH_2Cl_2 (Figure 3.4, left) the air measurements of some target MS species (in particular of the short-lived species) are not well bracketed between the two calibration gases, indicating a linear two-point calibration unfit for the calculation of mixing ratios. Thus, in case of a possible non-linear signal response (cf. Section 2.4) a non-linear two-point calibration should be used to determine the most realistic mixing ratios of the air measurements. Ideally, the three points determining a non-linear curve (i.e. χ_{CAL}, χ_{SPAN}, and zero) should be spaced roughly evenly and encompass the mixing ratio range of all measurements. However, it is possible that for some species the mixing ratios of CAL and SPAN are very close together. The closer the mixing ratios of these two working standards are the more important their measurement precision and accuracy becomes. In particular when the mixing ratio of the air samples is significantly different from these two calibration gases, imprecise calibrations can result in large fluctuations of the derived calibration curves and thus can have a strong influence on the detrending of the data. Additionally, in the worst case (particularly with strong drifts) it can happen that for some air measurements the interpolated response of the calibration gas with lower mixing ratios becomes larger than for its complementary calibration gas such that no physically meaningful monotonic calibration curve can be established for these measurements.

As shown below in Section 3.3.4 the quality of the calibration gas measurements can differ between the two gases. In general it has been observed during WISE flights that for most of the target MS species the measurements of CAL gas tend to be more precise than those of SPAN. In addition large fluctuations of the calibration gases might not always be reflected in air measurements. Thus in case of a small mixing ratio difference between the two calibration gases and a large difference to the air samples it can be useful to minimize the strong influence of the measurement noise by detrending based on only one of the two gases.

This is achieved as follows: A mean CAL/SPAN response ratio (R_{CAL}/R_{SPAN}) is derived by averaging the respective responses of CAL and SPAN over the whole flight. This ratio contains the information of signal non-linearity which is assumed to not change during the flight. Thus virtual CAL (SPAN) responses are calculated from SPAN (CAL) responses using this mean CAL/SPAN ratio, and these virtual CAL (SPAN) responses are used instead of the measured ones to derive the local non-linear calibration curve for each air sample. The detrending is thus based on only one calibration gas, while the other one is only used as average over the flight to determine the average non-linearity. The noise of one calibration gas is thereby eliminated and the measurement uncertainties of the calibration gases do not amplify each other to cause false results. Thus a non-linear signal response as well as possible detrending errors due to a small mixing ratio difference between the calibration gases in combination with measurement imprecision can be best treated by using this averaging method.

One important requirement for this averaging method is a sufficient amount of calibrations to determine the proper CAL/SPAN ratio for each individual flight. In case of signal jumps (Section 3.3.3) and a systematic bias on half of the SPAN measurements (Section 3.3.4) the amount of useful calibrations for the calculation of the average CAL/SPAN ratio might be strongly reduced. This could lead to significantly differing CAL/SPAN ratios between the flights causing varying calibration curves. The calibration curves have a strong influence in particular on air samples with very different mixing ratios than those

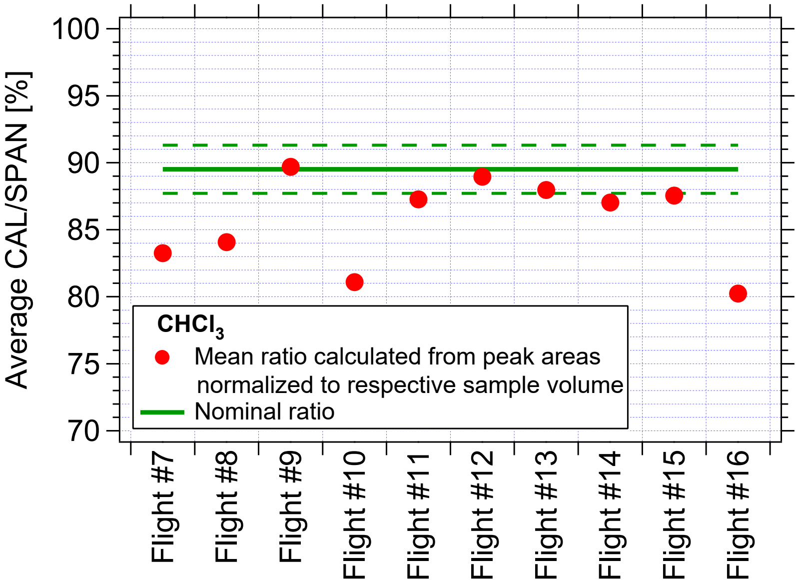

Figure 3.5: Calculated CAL/SPAN signal ratio of $CHCl_3$. The ratios are determined from flight-averages of the CAL and SPAN peak areas normalized to the respective sample volume. Due to signal drifts no error bars are included. The green line shows the nominal χ_{CAL}/χ_{SPAN} ratio according to the determined mixing ratios in the gas bottles (see Appendix E.1).

of the calibration gases (Figure 3.4). In case the resulting flight-to-flight difference of non-linear signal response is caused by such bad statistics and not by real instrumental variations the resulting calculated mixing ratios can be biased.

In case the CAL/SPAN ratios vary significantly for a few flights and the variation is caused by poor statistics one can consider to use an average ratio of all flights without the inclusion of the questionable ones. However, at this point in the above depicted chain of evaluation it should also be considered if a linear single-point calibration yields more realistic results than the non-linear two-point calibration under the given circumstances.

$CHCl_3$ is the only MS target species during WISE for which all the above mentioned scenarios apply. This species has a small CAL to SPAN mixing ratio difference (ratio ~ 89.5 %, see Table E.2) and air samples were observed down to ~ 20 % of the CAL value during WISE. As a consequence the regular quadratic two-point calibration with the use of the measured (local) CAL and SPAN values could not be applied to $CHCl_3$ without causing extreme mixing ratio irregularities. The use of the above mentioned averaging method made the calculation of mixing ratios possible by the use of CAL signals and the calculated (virtual) SPANs from average CAL/SPAN signal ratios. Figure 3.5 shows for $CHCl_3$ the different mean CAL/SPAN signal ratios for each flight.

The calculated $CHCl_3$ CAL/SPAN signal ratio is similar for most flights, around 88 %, but WISE flights #7, #8, #10, and #16 exhibit clearly smaller ratios. This would suggest higher mean CAL or lower mean SPAN signals implying a differing signal non-linearity or biased calibration gas measurements. However, these four flights also exhibit different flight conditions than the others[6] and less calibration gas measurements to calculate the mean values. The mixing ratios were first calculated with the use of the CAL/SPAN ratios from each individual flight and a quadratic two-point calibration. The resulting mixing ratios led to less compact correlations with other tracers (cf. Section 1.2) than the linear single-point calibration using only CAL. This strongly suggests that for $CHCl_3$ the uncertainty of the calculation of mixing ratios is larger overall when determining the non-linearity flight by flight than under the assumption of a linear signal response.

Further, the usage of a "WISE average CAL/SPAN signal ratio" calculated from the flights less compromised by statistical deficits (instead of using the ratios determined individually per flight) was analyzed for its advantage over a linear single-point calibration. Obviously, this "average quadratic" method is only beneficial if the WISE average CAL/SPAN signal ratio ((88.08 ± 0.43) %) is significantly different from the nominal χ_{CAL}/χ_{SPAN} ratio ((89.5 ± 1.8) %). The uncertainty of χ_{CAL}/χ_{SPAN} was calculated from the CAL and the SPAN measurement precision for the calibration of the mother bottles[7] ($\sigma_{A_{\boldsymbol{Bottle}}}$ in Appendix E.1).

On the basis of this comparison the two ratios do not significantly differ. This implies that the signal non-linearity as reflected in the averaged CAL/SPAN ratio determined for the WISE flights is smaller than the precision of the nominal values. Therefore a quadratic two-point calibration on the basis of the "WISE averaged CAL/SPAN signal ratio" with the use of the nominal CAL and SPAN mixing ratios projects the uncertainty of two calibration gases on the data without the benefit of a proper correction for signal non-linearity. Thus for $CHCl_3$ a linear single-point calibration with the usage of only one working standard overall generates the smallest uncertainties. CAL has been chosen as calibration gas to calculate the $CHCl_3$ mixing ratios. This calibration gas is — unlike SPAN — not affected by a systematic bias (Section 3.3.4) and closer to the air samples' typical mixing ratios.

This analysis has shown that even with the best intentions for an optimal calculation of mixing ratios certain requirements need to be fulfilled to make good use of two in-flight calibration gases:

---

[6] e.g. different instrumental settings (#7 & #8), extreme amounts of water vapor inside the sample line (#10), or different preconcentration trap (#16)

[7] mother bottle defines the primary working standard, the flight bottles, used for in-flight calibration, are filled with gas from the mother bottle

- ▷ The difference of the mixing ratios of the two in-flight calibration gases should be large compared to the individual variability of their responses during flight in order to be less affected by signal drifts and measurement precision.
- ▷ The mixing ratios of the air samples should be close to those of the calibration gases to be less affected by errors in the calibration curve. Ideally the air samples are between CAL and SPAN.

3.3.3 Correction of jumps in the detector response

During WISE it occurred that the detector response suddenly jumped to significantly higher but equally stable signals. The cause of this type of event could not be determined and most likely has to do with the mass spectrometer's intrinsic programming or wiring[8]. Such a jump happened usually once per flight. Exceptions are flights #7, #12, and #14 where it did not appear at all and flight #10 where two jumps were noted. In all cases these sensitivity jumps were visible equally in all selected mass fragments. In addition, the first measurement affected by such a jump exhibited an extraordinarily high signal (see outlier in Figure 3.6).

These sensitivity changes make the calculation of mixing ratios more complicated. Flights with the occurrence of such an event had to be split into different sections separated by the outlying measurement initiating the sensitivity jump. Thereby few air measurements at the edges of these sections close to the jump might not be well bracketed by two valid calibrations. Consequently they are detrended using only the one available neighboring calibration thereby ignoring potential drifts. The maximum number of air measurements that could be affected by this effect is four (when both standards are used for detrending). Fortunately these sensitivity jumps did not appear at the beginning of a flight where drifts were observed to be the strongest. Therefore the bias introduced by neglecting drift at a section's edge close to the jump was found to be insignificant compared to the respective measurement precision in all noted cases. As shown in Figure 3.6 (right) the presented section-wise treatment of signal jumps results in a gapless time series of mixing ratios without a disturbance at the location of the signal jumps.

---

[8] A similar phenomenon is known to be caused occasionally by the mass spectrometers' filaments used for the ionization shortly before the end of their lifetime. A change of filament did not end the appearance of the observed signal jumps and has therefore been ruled out as their potential cause.

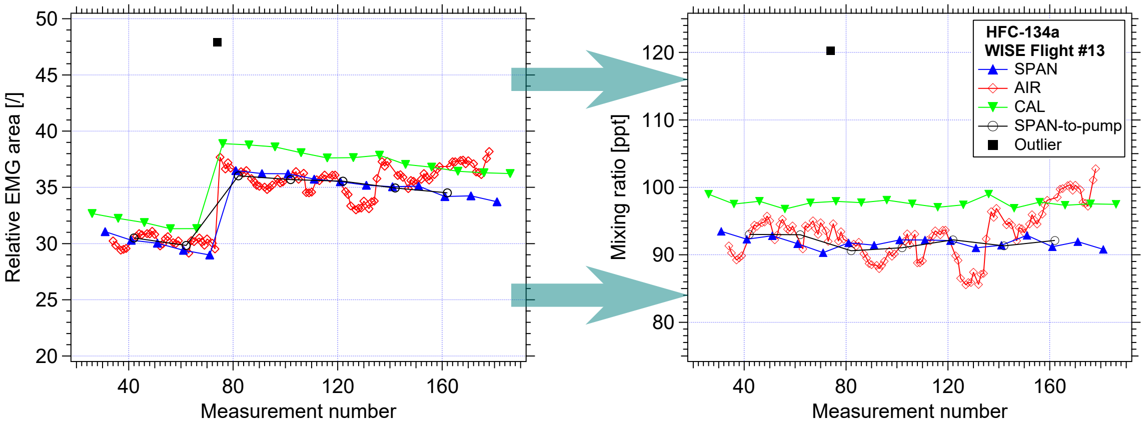

Figure 3.6: Example of a detector signal jump during WISE flight #13 for HFC-134a (left) and the result after the jump correction and detrending (right).

3.3.4 Systematic bias of in-flight SPAN measurements

The two in-flight calibration gases CAL and SPAN were measured alternately every five sample injections (Appendix C.3). In addition, every 20 injections a N_2 blank measurement was conducted in such a way that the SPAN measurements alternately followed an air sample or a blank measurement. For some species it is visible that measurements of the calibration gas SPAN following a blank measurement tend to have lower responses than the SPAN measurements following an air sample. Figure 3.7 shows an extreme example of this effect on the EMG heights of the CH_3Cl peak normalized by their respective sample volumes during WISE flight #12.

A comparison with the ECD module (Section 3.4) suggests that the SPANs that follow a blank measurement are biased. The exact reason for this phenomenon is unclear. It behaves like a memory effect that only applies to the measurement following a blank. Other measurements seem to be unaffected and general memory effects have been ruled out (Appendix B.2.1). It is assumed that a blank measurement — with a matrix much different from any kind of air sample — disturbs the equilibrium of the conditioned sample line, thus causing the following sample to pass through a different environment which might have a disturbing (adsorbing) effect on a few sensitive species. This effect could not be reproduced in the laboratory and its origin therefore not further be investigated.

However for the WISE measurements two things had to be analyzed. First for which flight and species a significant difference between an average of all SPAN responses and only the unbiased ones can be detected. Second in case of a significant difference it was tested if the gain of SPAN accuracy from the removal of the biased SPAN measurements (every

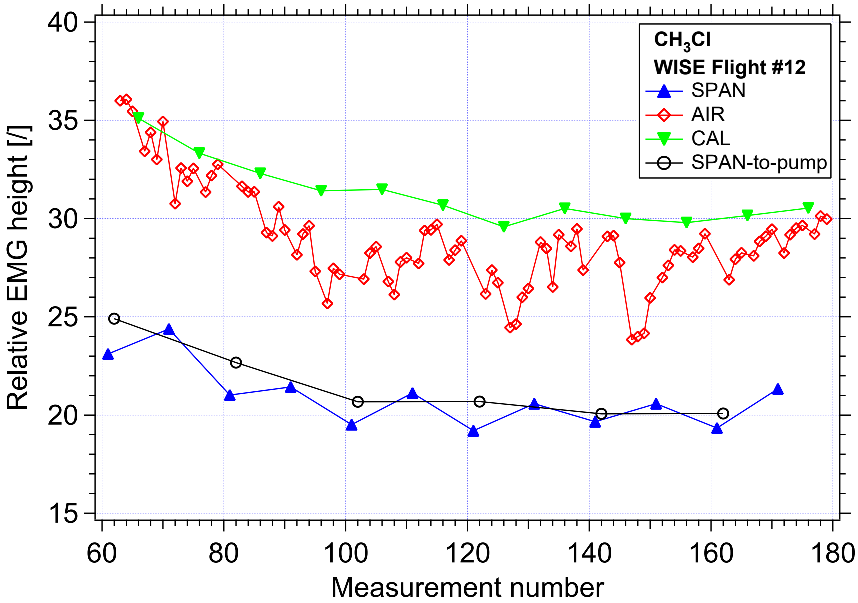

Figure 3.7: Example plot of relative CH_3Cl data from WISE flight #12. Systematic irregularities are visible in SPAN measurements that were alternating measured after an air and a blank sample. Blanks were measured every 20 measurements starting at number 60.

2nd SPAN) also outweighed the disadvantage of detrending of potentially non-linear signal drifts.

In general the average response difference over all flights between all SPANs and only the unbiased ones is $< 1\ \%$ for almost all target species. Biased SPAN measurements of individual flights were only discarded for a species if the difference to all SPANs was significant and if this would not make the SPAN precision worse. In almost all cases where the SPAN differences were significant also the SPAN precision improved by discarding the biased SPANs. HFC-125 and HFC-134a were the only target species that did not exhibit a significant SPAN bias in any of the WISE flights. More details about the analysis are given in Appendix D.2. The individual results are listed in Table 3.2.

3.3.5 System contamination during WISE

The qualitative analysis from Appendix B.2.1 shows no indication of memory effects for the seven MS target species during WISE. Thus the analysis of in-flight blank measurements is assumed to give an insight on internal system contamination. System contamination can bias the signal of a species if any source along the sample flow releases some traces of that species during the phase of desorption. The difference to a memory effect is that the

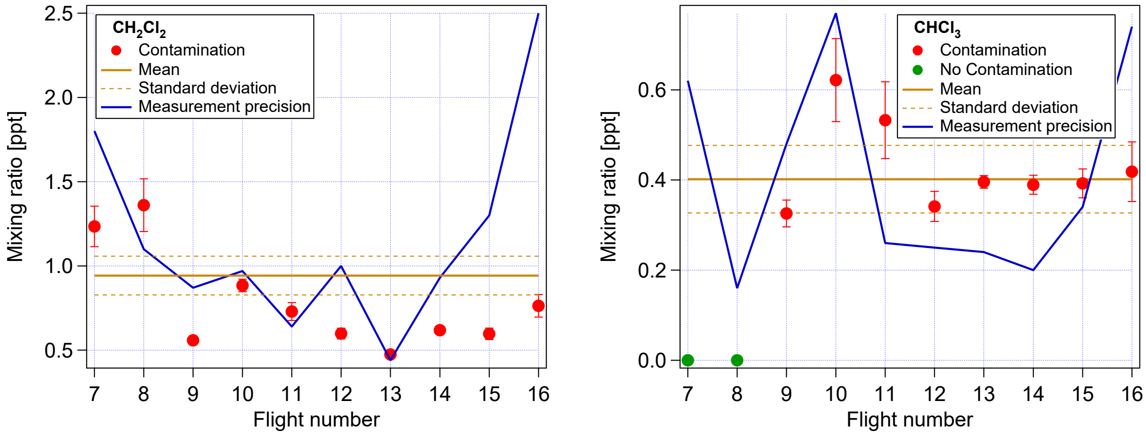

Figure 3.8: System contamination found during WISE flights for CH_2Cl_2 (left) and $CHCl_3$ (right). The blue line represents the measurement precision of each flight according to Section 2.5.3. The solid ocher line shows the average contamination found in all WISE flights. The contamination found for CH_2Cl_2 was considered not significant for correction.

contamination is independent of the sample and constantly present in every measurement while the memory effect is dependent on the measurement(s) directly preceding the current one.

To quantify system contamination every 20 MS cycles during flights a blank sample with the preconcentration of purified N_2 was conducted (cf. Appendix C.3). Any trace in form of a significant peak ($R_{blank} > 0$) that a target species left in these blank measurements was fitted and calibrated according to Section 3.3. The resulting mixing ratios were averaged over the whole flight ($\overline{\chi}_{blank}$) and compared to the measurement precision (Section 2.5.3) to determine their significance.

Without convincing evidence for significant system contamination no corrections of the measured data are applied. However, in cases where the majority of the flight-averaged blank mixing ratios of blank measurements is significantly larger than the respective measurement precision of the regarded species data correction is considered. In such a case the response of the affected species is considered to be contaminated and consequently all WISE flights were corrected for the respective contamination of this species. In case of obvious outliers only the outlying flights were corrected after a detailed consideration.

Figure 3.8 shows as examples the species CH_2Cl_2 and $CHCl_3$. For the majority of flights, contamination for CH_2Cl_2 is smaller than the measurement precision. Therefore no correction for contamination was applied. The opposite is the case for $CHCl_3$ such that for this species all flights were corrected. The full analysis and detailed considerations are given in Appendix D.4.

The correction for system contamination was included in the calculation of mixing ratios. The contamination observed in the blank measurements appeared mostly with small variations during a flight. Therefore, if correction for contamination was necessary by the chosen criteria the flight averages of the contaminated blank responses ($\overline{R}_{blank}$) were used for correction. The mixing ratio (χ) of a species corrected for system contamination was then calculated using $\hat{R}_i = R_i - \overline{R}_{blank}$, by subtracting $\overline{R}_{blank}$ from each individual response R_i, calibration gases and air samples alike, indicating $\chi = f\left(\hat{R}_{air}, \hat{R}_{CAL}, \hat{R}_{SPAN}\right)$. Note that this correction is not necessary for the linear two-point calibration method because this method does not need the assumption $f(0) = 0$ (Section 3.3.2).

Comparisons of measurements corrected for contamination with other tracers showed no unexpected influence on tracer-tracer-correlations if a change could be noticed at all. This gives confidence in this method of correction for system contamination. Among others Table 3.2 gives an overview of the flights and species that were corrected for system contamination.

3.3.6 Influence of inlet pumps

HAGAR-V's calibration gases do not pass the inlet suction pumps when selected as sample. This would bare the risk of wasting calibration gas over the pump's pressure relief valves (see Appendix A.2). However, the suction pumps can have mixing ratio affecting influences on the air sample that passes through. Depending on external conditions (e.g. temperature and pressure), the sample flow, and molecular properties a target species could be more or less adsorbed and/or even gassing out of the pump system's membranes. These potential effects were considered and their risk minimized during the process of HAGAR-V's Base module development, where the pumps were chosen accordingly. Nevertheless the possibility for biasing effects caused by the different pathways of calibration gas and air sample should not be ignored and will be analyzed in this section.

To provide an in-flight quality control during WISE every 20 measurements the SPAN calibration gas was sampled in such a way that it passed through the pumps similar to the sampled outside air (see Figure A.4). The dehydrating unit was bypassed since WISE flight #7 (Appendix C.2.2) implicating that only the influence of the suction pumps and the following tubing was monitored. A comparison of these so called SPAN-to-pump samples with the regularly taken SPAN measurements gives insight on a potential systematic bias caused by the different sample pathways.

The difference between the mean mixing ratio of the SPAN-to-pumps and the nominal SPAN gas value was calculated for each species and flight. Most of the target MS species

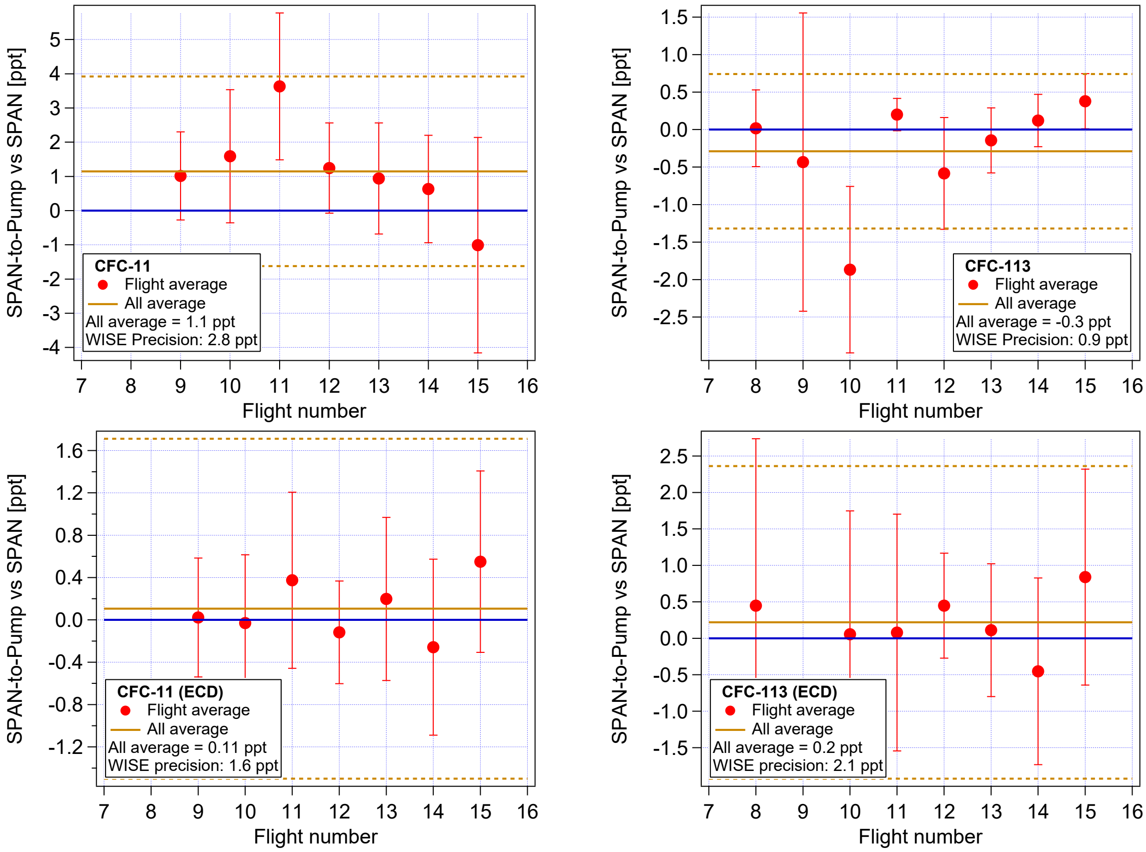

Figure 3.9: Differences between flight-average SPAN-to-pump measurements and the SPAN mixing ratio of CFC-11 and -113 of HAGAR-V's MS (upper plots) and ECD (bottom plots) module. The error bars represent two times the standard error of the SPAN-to-pump measurements. The solid ocher line shows the average difference over all flights and the dashed lines show the range of the average precision determined in Section 2.5.3.

showed tendencies towards SPAN-to-pump measurements above the nominal SPAN value. Individual flights could even show a significant difference. A comparison with CFC-11 and -113 measured by the ECD module suggests the biased SPAN-to-pump measurements to be a MS specific phenomenon. The ECD measurements showed no significant difference between the SPAN-to-pumps and the nominal SPAN value. Figure 3.9 shows exemplarily the differences for CFC-11 and -113 for the MS (upper plots) and the ECD module (bottom plots). Similar plots of all target MS species and a detailed analysis of the SPAN-to-pump measurements are given in Appendix D.5.

The analysis leads to the interpretation of the MS module's SPAN-to-pump measurements as a general indication for potentially biased air measurements. The source of such a potential bias has to be assumed to have complex origins perhaps not directly related to the inlet pumps and tubing. Attempts of zero order corrections (i.e. subtraction of the mixing ratio offset) proved to worsen the data in an atmospheric context. Only the offset correction of $CHCl_3$ on flight #16 showed a significant improvement on the basis of tracer-tracer correlation (see Figure D.6). This also strongly suggests that the source of the SPAN-to-pump offset may have complex origins or might not even be always directly transferable to air measurements.

Therefore the SPAN-to-pump analysis of the MS module could not provide a clear answer if the pumps did indeed have an influence on the air sample. The observed effects gave reason to correct $CHCl_3$ for one flight for a systematic bias but generally provided a measure for a systematc uncertainty that applies to all MS air measurements. The absolute uncertainty was formulated into a relative uncertainty in form of the all-flight-average of the absolute differences between SPAN-to-pump and SPAN relative to the SPAN mixing ratio for each species. The uncertainty estimates (σ_{S2P}) are listed in Table E.4.

3.4 Comparison with other instruments

In this section the measurements of two CFCs by the MS module are compared to those by the ECD module. Both modules separately measure CFC-11 and CFC-113. With 90 s the ECD module has a higher time resolution than the MS module, thus more data points are available for the comparison. In particular for CFC-11 the ECD measurements are more precise than the measurements of the MS module making a comparison more beneficial for MS data. In addition, ECD measurement techniques and the processing of ECD data has been optimized and quality checked in our group for more than 20 years (e.g. Volk, 1996; Riediger, 2000; Werner, 2007; Hösen, 2013), providing high confidence to trust the ECD data from HAGAR-V. With this in mind, it was assumed that the ECD module is an excellent reference instrument for comparison with the MS overlapping species.

The main focus of the comparison is laid on differences between the two instruments and in particular on investigating how these differences depend on the method of calculating MS mixing ratios. The air samples' mixing ratios of both species were well bracketed by CAL and SPAN mixing ratios providing the best options for a proper analysis of different methods to calculate their mixing ratios. However, the test for linearity showed for neither CFC-11 nor CFC-113 significant non-linearity between mixing ratio and detector response (Section 2.4). Therefore the following results might not directly be applicable to species with various conspicuities as described in Section 3.3. Nevertheless tendencies were found that support the interpretation for other species as well.

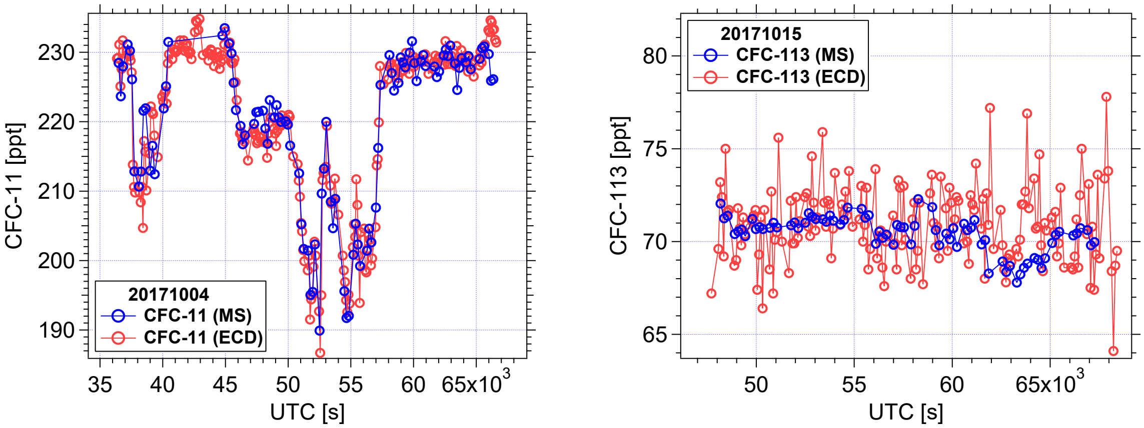

Figure 3.10: Exemplary flight data of both MS (blue) and ECD (red) module. Left: CFC-11 WISE flight #9. Right: CFC-113 WISE flight #14. The MS data are processed according to Table 3.2.

The CFC measurements were compared in two different ways. The direct differences of samples overlapping in time were analyzed as well as the (indirect) differences of the correlation with another long-lived tracer sampled at high time resolution. The indirect comparison does not exhibit the CFC variability due to the different sampling intervals but relies on the measurements of a third instrument. The most important findings of this comparison with the ECD module are summarized in this section. The detailed analysis and discussion is given in Appendix D.6. Figure 3.10 shows exemplary flight data of CFC-11 and CFC-113 from both the MS and the ECD module.

The direct comparison shows that there is a general agreement between the MS and the ECD CFC measurements. The CFC-11 (MS) data tend to yield higher mixing ratios than the ones from the ECD module (~ 0.5 ppt on average). The CFC-11 (MS) mixing ratios tend to overestimate more in the tropopause region than in the stratosphere. The reason for this tendency could not be identified. Nevertheless, on average this discrepancy between the two data sets is within the measurement precision of the MS module (Table 2.3).

The CFC-113 (MS) measurements tend to yield lower mixing ratios than the ones obtained from the ECD module. In particular WISE flight #8 exhibits ~ 2 ppt smaller mixing ratios for the CFC-113 (MS) measurements. The comparison alone with the ECD module and its much noisier CFC-113 measurements does not lead to a final conclusion about whether or not the CFC-113 (MS) mixing ratios of flight #8 are significantly biased. For the other flights CFC-113 (MS) differs on average less than 1 ppt from CFC-113 (ECD). For those flights barely significant differences for few different calibration methods are visible but all in the range of the CFC-113 (MS) measurement precision.

Thirteen different ways to calculate MS module mixing ratios have been tried out and compared to the respective measurements of the ECD module. From this comparison it is not possible to determine a single method for the calculation of mixing ratios that yields the optimal result for all species measured by the MS module. However, a few general assertions can be made.

The comparison of MS CFC-11 and -113 with the ECD module supports the (trivial) conclusion that in case of a non-linear detector response a non-linear two-point calibration (determined by two calibration gases and zero) tends to be the best choice for the calculation of MS mixing ratios. In the case of a linear detector response (CFC-113) the comparison shows that there is no significant difference between any linear or non-linear calibration method for the calculation of mixing ratios. Thus it is assumed that in any case the use of a non-linear two-point calibration is the best way to calculate MS mixing ratios if there are no specific reasons against this choice (e.g. see Section 3.3.2).

The calibration method that uses one calibration gas only as flight average to derive a mean CAL/SPAN signal ratio as described in Section 3.3.2 did not significantly worsen the results compared to the calibration method yielding the smallest differences to the results from the ECD module. However, the direct comparison suggests that this method should not be used if enough useful in-flight calibrations are available because real response variations get smoothed out by detrending with only one calibration gas instead of both. This supports the concept of this method and gives confidence that for a MS species for which such averaging is necessary a non-linear two-point calibration can still be applied and yields reasonable results.

Before the use of CAL and SPAN for detrending and calibrating it has to be determined for each species individually if there is a difference between the SPANs following an air sample and the SPANs that follow a blank measurement. This was discussed in Section 3.3.4. From the comparison of MS and ECD CFC-11 it becomes clear that in the case of systematically differing SPAN measurements the SPANs following a blank measurement are the ones that are biased. This is also the expected result. For the detrending and calibrating of other MS species this implies that in case of significantly differing SPAN measurements only the ones that follow an air sample should be used.

In addition it could be shown with CFC-11 that a visible difference between the different SPAN measurements does not necessarily imply that all SPANs following a blank measurement need to be discarded. In case of CFC-11 the difference between the SPAN measurements is small enough that the more accurate drift correction when using all SPANs

Table 3.2: Overview of corrections and calibration methods that have been applied to WISE MS data. It is shown which flight exhibited signal jumps (Section 3.3.3) and which species has been corrected for system contamination (Section 3.3.5) and biased calibration gas (SPAN) measurements (Section 3.3.4). The used methods to calculate mixing ratios are quadratic two-point or single-point calibrations with the use of CAL (C), SPAN (S), only SPANs that follow an air measurement (S/2), zero (0), or zero and correction for contamination (B).

	Jumps	Correction for...	**CH_2Cl_2**	**$CHCl_3$**	**CH_3Cl**	**CFC-11**	**CFC-113**	**HFC-125**	**HFC-134a**
Flight 7	0	Contamination	No	No	x	x	x	x	x
		SPANs	All	(All)					
		Calibration	C, S, 0	C, 0					
Flight 8	1	Contamination	No	No	x	x	No	x	x
		SPANs	All	(All)			All		
		Calibration	C, S, 0	C, 0			C, S, 0		
Flight 9	1	Contamination	No	Yes	Yes	No	Yes	No	x
		SPANs	All	(All)	After Air	All	After Air	All	
		Calibration	C, S, 0	C, B	C, S/2, B	C, S, 0	C, S/2, B	C, S, 0	
Flight 10	2	Contamination	No	Yes	Yes	No	Yes	No	No
		SPANs	After Air	(After air)	After Air	All	After Air	All	All
		Calibration	C, S, 0	C, B	C, S/2, B	C, S, 0	C, S/2, B	C, S, 0	C, S, 0
Flight 11	1	Contamination	No	Yes	Yes	No	No	No	No
		SPANs	All	(After air)	After Air	All	All	All	All
		Calibration	C, S, 0	C, B	C, S/2, B	C, S, 0	C, S, 0	C, S, 0	C, S, 0
Flight 12	0	Contamination	No	Yes	Yes	No	No	No	No
		SPANs	All	(All)	After Air	All	After Air	All	All
		Calibration	C, S, 0	C, B	C, S/2, B	C, S, 0	C, S/2, 0	C, S, 0	C, S, 0
Flight 13	1	Contamination	No	Yes	Yes	No	No	No	No
		SPANs	After Air	(After air)	After Air	All	After Air	All	All
		Calibration	C, S, 0	C, B	C, S/2, B	C, S, 0	C, S/2, 0	C, S, 0	C, S, 0
Flight 14	0	Contamination	No	Yes	Yes	No	No	No	No
		SPANs	All	(After air)	After Air	All	All	All	All
		Calibration	C, S, 0	C, B	C, S/2, B	C, S, 0	C, S, 0	C, S, 0	C, S, 0
Flight 15	1	Contamination	No	Yes	Yes	No	No	No	No
		SPANs	All	(All)	After Air	After Air	All	All	All
		Calibration	C, S, 0	C, B	C, S/2, B	C, S/2, 0	C, S, 0	C, S, 0	C, S, 0
Flight 16	1	Contamination	No	Yes	x	x	x	No	Yes
		SPANs	After Air	(After air)				All	All
		Calibration	C, S/2, 0	C, B				C, S, 0	C, S, 0

for detrending can compensate the small bias between the SPANs. This is also considered in Section 3.3.4 where discarding SPAN measurements is discussed.

The calibration methods individually chosen for each species and flight according to the criteria outlined in Section 3.3 are listed in Table 3.2. These methods were also evaluated by comparing the resulting data to the ECD data. It could be shown that in every comparison the chosen method matched best (or not significantly worse than from the method that matched best) to the ECD data. This provides high confidence that the applied methods and corrections based on the developed general criteria also yield the most reliable results for the other MS target species.

A lot has been learned about the performance of the MS module during its first successful deployment on HALO during WISE from the comparison with the ECD module. Many assumptions that were made during data processing could be supported and even complemented with new insights. Thus with the help of this detailed analysis the processing of MS module measurements yielded the most realistic data set including solid estimations of its uncertainties (Appendix E.3).

Chapter 4

Investigation of transport of CH_2Cl_2 and $CHCl_3$ into the UTLS

In this chapter HAGAR-V's WISE measurements of CH_2Cl_2 and $CHCl_3$ are analyzed. These measurements are used for tracer-tracer correlations (section 1.2) to identify tropospheric intrusions into the LMS of different CH_2Cl_2 and $CHCl_3$ source strengths. With the help of model simulations and backward trajectory calculations efficient transport pathways into the UTLS for these Cl-VSLS are derived and different source regions are identified (background information on transport are given in Section 1.1). In a case study the impact on the distribution of CH_2Cl_2 and $CHCl_3$ in the UTLS region by the large scale hurricane Maria is analyzed. This chapter provides the first transport study on CH_2Cl_2 and $CHCl_3$ in the UTLS region based on real-time measurements from aboard an aircraft. In Section 4.5 the most important results from this chapter are summarized. The necessary background information about the two Cl-VSLS are given in Section 1.3. The CLaMS tracer and backward trajectory calculations were provided by Dr. Bärbel Vogel, Jülich Research Center, Institute for Energy and Climate Research - Stratosphere (IEK-7).

4.1 Chemical Lagrangian Model of the Stratosphere

4.1.1 General model description

To investigate the origin of air parcels measured during the WISE campaign the Chemical Lagrangian Model of the Stratosphere (CLaMS) is used. Originally CLaMS calculated stratospheric transport only on isentropic levels (McKenna, 2002a,b) and was further extended to simulate three-dimensional transport in the stratosphere (Konopka et al., 2007,

2010) before it also included the troposphere (e.g. Konopka and Pan, 2012). Transport in CLaMS is realized on a Lagrangian basis by (reversible) advection and (irreversible) mixing. The advection of air parcels is driven by horizontal wind fields while the vertical velocities are defined by diabatic heating rates which also include latent heat release (Ploeger et al., 2010). CLaMS employs a hybrid vertical coordinate (ζ) which, in this study, transforms from a strictly isentropic coordinate (potential temperature, Θ) to a pressure-based coordinate system (σ coordinates) below a threshold of 300 hPa (more details are given by Konopka and Pan, 2012; Pommrich et al., 2014).

Mixing of air parcels is realized when a threshold of a defined minimum or maximum distance between two air parcels is crossed. In case the minimum distance is undercut the two original air parcels are replaced by a new air parcel and in case the maximum distance is exceeded a new air parcel is introduced. In both cases, the chemical composition of the new air parcel is calculated as the average of the two original parcels or of the two parcels drifting apart. The mixing parameters are deduced from observations for an accurate simulation of the controlling factors (i.e. the horizontal strain and vertical shear rates; Konopka et al., 2010, and references therein). This transport algorithm allows tracer gradients in the atmosphere to be preserved in the vicinity of transport barriers.

The model simulation for WISE was spatially constrained from the surface to 900 K potential temperature (~ 37 km altitude), a horizontal resolution of 100 km and a maximum vertical resolution of about 400 m (at the tropopause). For the advective transport ERA-Interim reanalysis data (Dee et al., 2011) were taken as provided by the European Centre for Medium-Range Weather Forecasts (ECMWF). A few changes to the ERA-Interim reanalysis data were implemented to optimize deep and mid-level convection. The irreversible part of transport was set to discrete mixing steps every 24 h.

4.1.2 Tracers of air mass origin

To gain information about the origin of air parcels so called tracers of air mass origin (also called emission tracers) can be simulated with CLaMS (Vogel et al., 2015). These artificial (passive) tracers of air mass origin mark defined regions in the Earth's boundary layer (BL, (2–3) km above the surface including orography) and are transported further with the simulation once the BL is left. At every mixing step (24 h) air parcels in the BL are marked with such an emission tracer depending on their geographical position. The sum of all different emission tracers in the BL is equal to 1 for a complete coverage of the Earth's surface. At the beginning of the model simulation, the emission tracers are set to zero for air parcels above the BL.

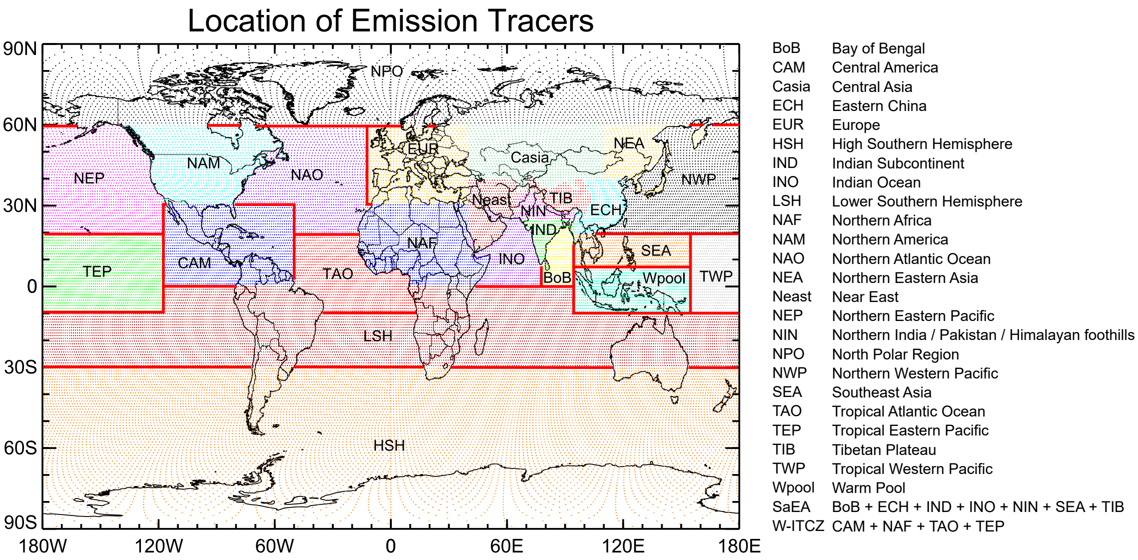

Figure 4.1: Global map of source regions for artificial tracers of air mass origin (emission tracers) simulated with CLaMS. Figure courtesy of Dr. Bärbel Vogel (with few adaptations made).

At every mixing step air parcels are released from the BL to the atmosphere with the respective regional information according to the emission tracers. The model simulation used in the present work was initialized with the meteorological data from May 1, 2017, and simulated for a period of six months (until the end of October). This implies that only emission tracers that left the BL within that six months period can be considered for analysis (this is further discussed below in Section 4.2.4). In the present work short-lived tracers are examined with the focus placed on relatively fast transport, thus this six months period should fully suffice for the analysis presented here.

In the CLaMS model simulation, the advective transport does not change the information of the emission tracers but the mixing does. For example if a simulated air parcel from the Tibetan Plateau BL (TIB = 1, ECH = 0) and one of the Eastern China BL (TIB = 0, ECH = 1) are released to the free troposphere and fulfill CLaMS's requirements of mixing, the model produces a new air parcel with the shared information of TIB = 0.5 and ECH = 0.5. Thereby the initial distribution of tracers is changed and after enough mixing steps the information of the fractions with different air mass origin can be extracted from the simulated air parcels.

Figure 4.1 shows the geographic information of the 24 individual emission tracers. The different source regions are separated by color. Over sea red lines mark the borders of constant latitude or longitude for the tracers. Otherwise the oceanic tracers are separated by the geographical coast lines. The continental separation of emission tracers is only marked by different colors. The full names of the respective tracers are listed next to the map. In addition the combination of several emission tracers summed up in the SaEA (Southern and Eastern Asia) and the W-ITCZ (Western ITCZ) tracers are listed.

4.1.3 Backward trajectories

Another approach to investigate the origin of measured air samples is the use of backward trajectories. Unlike the forward calculation for CLaMS's tracers of air mass origin, the backward trajectories of air parcels only include the advective part of transport without mixing (cf. Section 4.2.3). The advantage is that a single pathway for each air parcel can be calculated and analyzed.

The trajectory module of CLaMS (CLaMS-TRAJ) uses only advective transport to calculate backwards the trajectory of an air parcel starting at the time and position of the air parcels' in situ observation. For the trajectories of WISE measurements the ERA-Interim reanalysis data (Dee et al., 2011) with a resolution of 1° and 60 vertical levels from the surface up to 0.1 hPa were interpolated in time (1 h grid) and space onto the point of in situ observation. The resulting trajectories were calculated from the date of observation 120 days back in time and ended once they reached the model BL (i.e. the source region to the free troposphere).

4.2 The CH_2Cl_2-N_2O correlation

The correlation of chemical tracers with different lifetimes usually promises the highest potential to provide information about dynamical processes in the atmosphere. During the WISE mission the HAGAR-V MS module did measure CH_2Cl_2 — a chemical tracer with a considerably short lifetime of a few months and no atmospheric sources (cf. Section 1.3.3). A very good long-lived correlation partner for CH_2Cl_2 is N_2O with a lifetime of 123 years (Ko et al., 2013). N_2O was measured during WISE by the University of Mainz with the instrument UMAQS (University of Mainz Airborne QCL Spectrometer; Müller et al., 2015) at high measurement frequency of 1 Hz. To match the data of these two instruments the N_2O values have been averaged over the respective preconcentration time of the MS module (40–60 s; cf. Table C.2). In addition this further improves the precision of the N_2O data by smoothing out instrumental noise (regular precision ~ 0.05 % of tropospheric background; Kunkel et al., 2019).

Figure 4.2 shows the CH_2Cl_2-N_2O correlation for the last ten WISE flights (September 28 to October 21 in 2017). The chemical tropopause has been determined to correspond

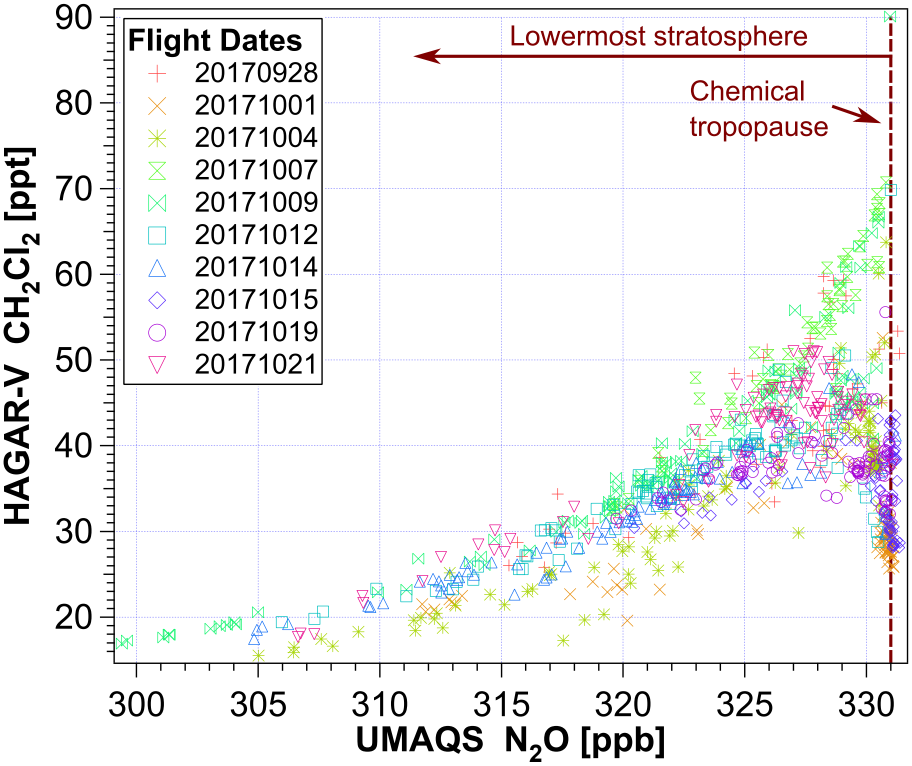

Figure 4.2: CH_2Cl_2-N_2O correlation for WISE flights #7–#16 (September 28 to October 21 in 2017). The coloration and the different symbols represent the individual flights.

to N_2O ~ 331 ppb (Kunkel et al., 2019) at the right edge of Figure 4.2. As described in Appendix C.2.2 the MS module measured mainly at water vapor values below 10 ppm (as usually found in the stratosphere), thus the majority of data points shown in the correlation was obtained in the lowermost stratosphere (LMS).

For lower N_2O mixing ratios (more older, chemically processed air samples) the correlation exhibits its expected compactness (with few exceptions[1]). Towards higher N_2O mixing ratios the correlation splits into two distinct branches. One — further referred to as the upper branch — exhibits measurements of particularly CH_2Cl_2-rich air and the other — further referred to as the lower branch — exhibits measurements of particularly CH_2Cl_2-poor air. These two branches each contain measurements from different flights with different flight routes (cf. figures 3.1, 4.4, and F.2). In the following sections this interesting correlation will be analyzed in detail.

---

[1] The outlying data points from flight #8 (20171001) and #9 (20171004) between 317–323 ppb N_2O could not be identified as biased measurements but could not be properly explained either. More clarification could be provided by a comparison to the correlation in a different season which is not available to this date.

4.2.1 Correlation branch filter

In order to differentiate between the upper and the lower branch of the CH_2Cl_2-N_2O correlation from WISE a filter was developed. Only using the observed correlation there is no a priori information about where either of the correlation branches begins or ends. Therefore the following approach to develop a filter was made considering the compactness of the lower part of the correlation to separate the branches by their visual distinctiveness. Although the separation of the data set with such a filter might not represent a complete physical picture, it plausibly singles out the obvious deviations from a smooth mean correlation curve.

A quadratic fit to describe the observed stratospheric background correlation was applied to the correlation data with $N_2O < 325$ ppb. This value was chosen as an upper limit because no visible breakup of the correlation's relative compactness appears for N_2O values below 325 ppb. The resulting quadratic function is assumed to be the "mean correlation" for the whole data set.

To be able to filter only the data in the distinctive branches mixing ratios below or above the "mean correlation" can be considered. In addition the filter reduces the data set of the correlation to values corresponding to $N_2O > 325$ ppb only. As shown in Figure 4.3 this choice of filter makes it possible to differentiate the correlation's distinctive branches.

In the present work, the upper branch (red) is defined for data points with at least 5 ppt higher CH_2Cl_2 mixing ratios as the "mean correlation" and the lower branch (blue) is defined for data points with at least 10 ppt lower CH_2Cl_2 mixing ratios as the "mean correlation". If not mentioned otherwise this filter definition range was used to separate the two branches in the present work. For the given branch filter range the upper branch contains on average 68 % higher CH_2Cl_2 mixing ratios than the lower branch ((57 ± 8) ppt vs (34 ± 4) ppt[2], respectively) at an average of 2.3 ppb lower N_2O mixing ratios than the lower branch ((328.3 ± 1.7) ppb vs (330.6 ± 0.6) ppb[3], respectively).

The two filtered data branches also differ in their potential temperature distribution. Figure 4.4 shows a scatter plot of potential temperature and CH_2Cl_2 with different colors to mark the correlation branches. The median potential temperature of air samples of the upper branch is 15.9 K higher than that of the lower branch (377.5 K vs 361.6 K[4], respectively). Combined with the result of different average N_2O values for the two branches this implies that the air samples of the upper branch were measured mainly in the LMS while

---

[2] Median CH_2Cl_2: Upper branch: 56.5 ppt; lower branch: 34.1 ppt

[3] Median N_2O: Upper branch: 328.4 ppb; lower branch: 330.8 ppb

[4] Average potential temperature: Upper branch: (374 ± 13) K; lower branch: (361 ± 10) K

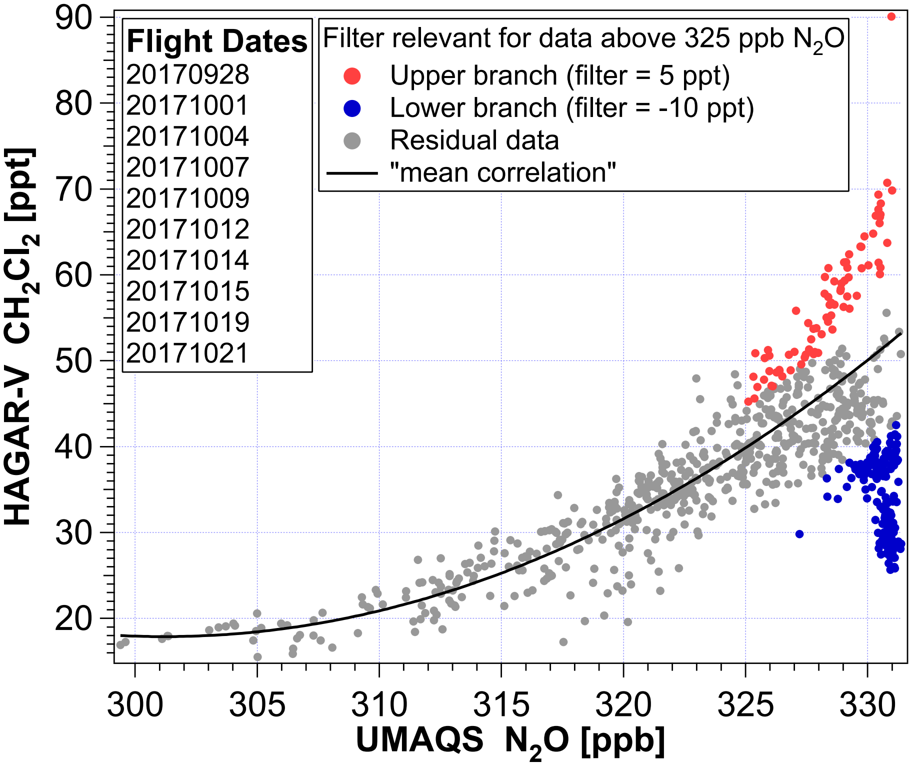

Figure 4.3: CH_2Cl_2-N_2O correlation with a quadratic fit up to 325 ppb N_2O that is extrapolated for higher N_2O mixing ratios as an approximated "mean correlation". The color indicates the separation of the distinctive branches selecting only the data with a relative offset from that "mean correlation" of ≥ 5 ppt for the upper branch (red) and ≤ -10 ppt for the lower branch (blue). In addition the thereby filtered data is limited to $N_2O \geq 325$ ppb. The defined filter parameters extract visibly extraordinary correlation data.

the air samples of the lower branch were obtained mainly around the chemical tropopause region. Further information on the separated branches with this filter definition is given in Table F.1.

This correlation branch filter is one possible approach to differentiate data and meant to support the analysis of extraordinary values. It has to be kept in mind that only the more compact part of the stratospheric "mean correlation" is represented in the filter. Thereby the "mean correlation" closer to the chemical tropopause is estimated based on the more stratospheric part of the correlation only. The focus of the present work is put on younger air masses closer to the tropopause region and with the given method the two branches can be sufficiently separated and filtered as intended. Below in Section 4.2.4, it will be shown that this filter definition yields a good agreement to the impact of different regional source regions on the CH_2Cl_2-N_2O correlation for air masses younger than six months.

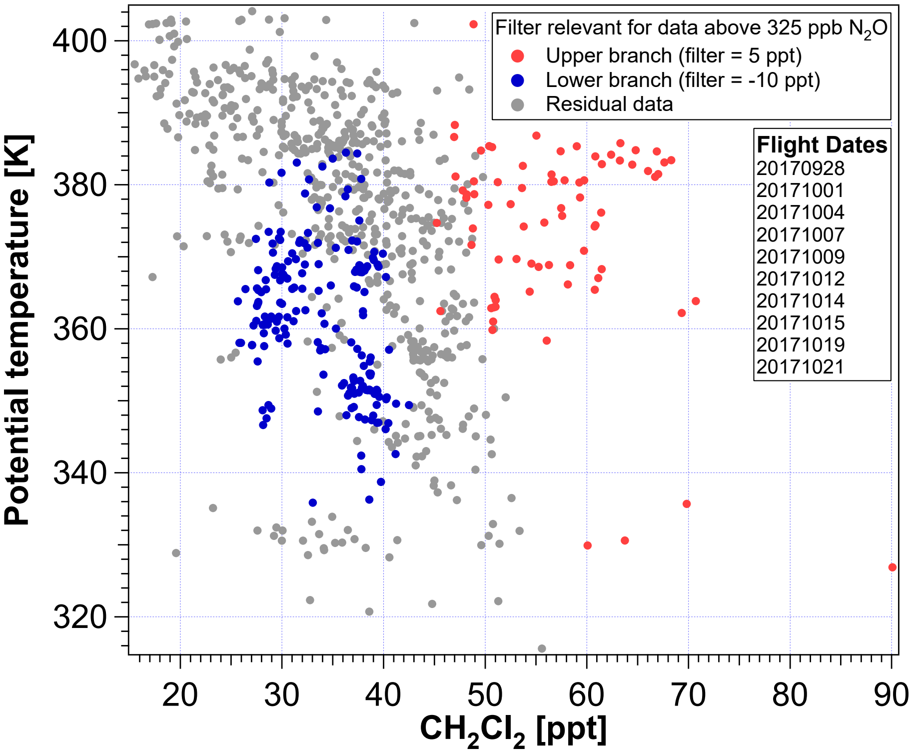

Figure 4.4: Scatter plot of potential temperature vs CH_2Cl_2. The colors mark the different correlation branches: upper branch (red) and lower branch (blue). The CH_2Cl_2-N_2O correlation color coded with potential temperature is shown in Figure F.1.

4.2.2 Background mixing ratios of CH_2Cl_2

The largest entry of tropospheric air to the LMS in late summer is expected to come from the tropics (e.g. Hoor et al., 2005; Bönisch et al., 2009). The major (and nearly exclusive) sink of CH_2Cl_2 in the troposphere is the hydroxyl (OH) radical (cf. Section 1.3.3) which is rather homogeneously distributed in the tropical troposphere (e.g. Lelieveld et al., 2016). Thus without any particularly strong or weak local sink in the tropical troposphere it is assumed that the observed low CH_2Cl_2 mixing ratios at the chemical tropopause region (N_2O ~ 331 ppb) can be considered to be CH_2Cl_2-poor background air while elevated CH_2Cl_2 mixing ratios exhibit the influence of stronger sources (CH_2Cl_2-rich air). However, the strength of the tropospheric sink varies in time due to the seasonality of OH and makes the interpretation of the CH_2Cl_2-N_2O correlation more sophisticated.

To further analyze the CH_2Cl_2-N_2O correlation, publicly available long-term surface measurements of CH_2Cl_2 from the AGAGE network[5] were consulted. Figure 4.5 shows both

---

[5] http://agage.mit.edu/

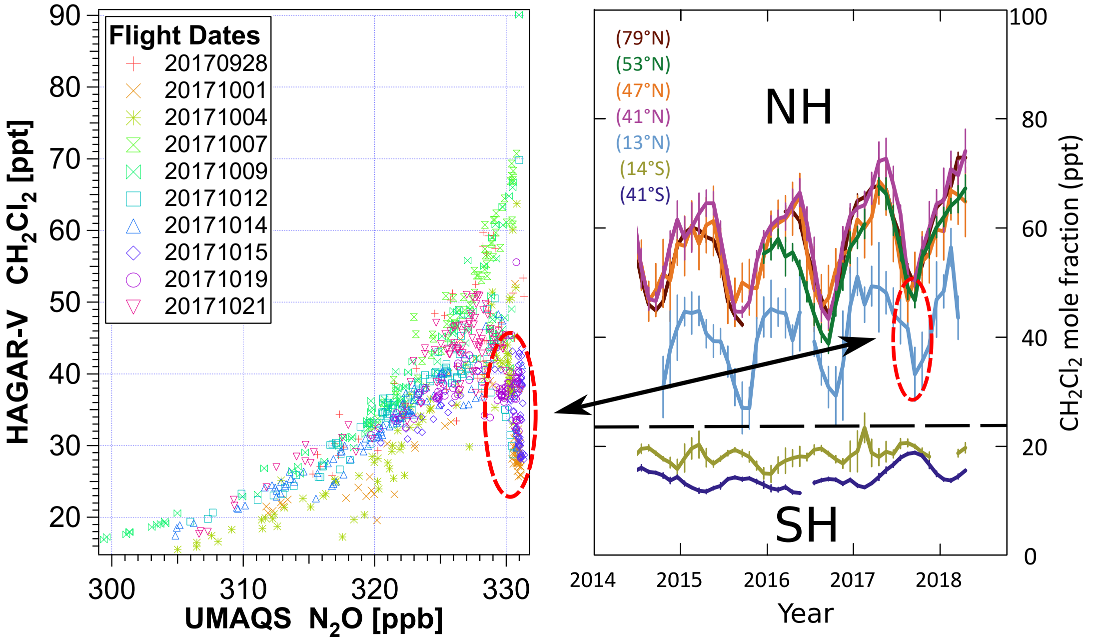

Figure 4.5: CH_2Cl_2-N_2O correlation for WISE flights #7–#16 (Sept, 28 to Oct, 21 in 2017) (left) and long-term CH_2Cl_2 surface measurements of the AGAGE network (right). The right panel shows monthly averaged measurements at different remote locations at different latitudes (41°S–79°N) with vertical lines representing the standard deviation. Tropical northern hemispheric minimum in 2017 is September. Minimum CH_2Cl_2 mixing ratios measured by HAGAR-V between ~ 328 ppb and ~ 331 ppb N_2O (red dashed ellipse, left panel) appear comparable to the tropical AGAGE measurements at 13°N (red dashed ellipse, right panel, light blue curve). The September minimum is visible at N_2O ~ 331 ppb. This memory effect preserves the source region's seasonal behavior of CH_2Cl_2 for a few months back in the UTLS. Right panel adapted from http://agage.mit.edu/ (Prinn et al., 2000, 2018).

the CH_2Cl_2-N_2O correlation from WISE as well as the monthly averaged long-term observations of the AGAGE network at different latitudes (Prinn et al., 2000, 2018). The AGAGE observations of CH_2Cl_2 show a strong seasonality in the northern hemisphere (NH). This seasonality is anticyclic to the seasonal cycle of OH, and the AGAGE measurements show the 2017 NH minimum at their station in the tropical Atlantic (light blue curve; 13°N, 59°W at Ragged Point, Barbados) in September. This tropical measurement station is a remote site far away from major chemical industry (i.e. CH_2Cl_2 sources) and the monthly averaged mixing ratios can be assumed to be a good representation of CH_2Cl_2-poor background air of the tropical marine boundary layer (MBL) in the NH.

A comparison of the CH_2Cl_2-N_2O correlation's lower branch with the AGAGE measurements in the NH tropics reveals their comparability. The annual tropical minimum of September from the surface measurements is mirrored in the minimum of the correlation at the chemical tropopause region measured in October — delayed by the time the respective air parcel needed to reach the tropopause after its release to the atmosphere from the surface.

A look deeper into the LMS ($N_2O < 331$ ppb) reveals minimum CH_2Cl_2 mixing ratios to rise with decreasing N_2O mixing ratios until the turning point at $N_2O \sim 328$ ppb. In other words there is an anticorrelation between the minimum CH_2Cl_2 mixing ratios and N_2O in the range ~ 328–331 ppb. This anticorrelation is also qualitatively consistent with the NH surface measurements of AGAGE. Average CH_2Cl_2 mixing ratios decrease in the NH background between June and September according to the measurements of AGAGE reflecting the observed decrease in the LMS from the youngest air ($N_2O \sim 331$ ppb) toward somewhat older air ($N_2O \sim 328$ ppb). The absolute values of the minimum CH_2Cl_2 mixing ratios in the observed LMS anticorrelation fall below the AGAGE NH surface measurements between June and September. This is expected due to chemical decomposition and mixing with older air during the transport time from the surface to the LMS. In addition the southern hemispheric (SH) AGAGE measurements in the tropics reveal much lower CH_2Cl_2 mixing ratios and it is possible that also low level CH_2Cl_2 mixing ratios from the SH tropics get transported into the NH LMS. However, the dominance of tropical NH surface background mixing ratios in the UTLS at the flight routes during WISE are evident in the correlation's lower branch based on comparisons with AGAGE measurements.

It is therefore assumed that negligable in-mixing of air of different origin or age makes it possible to see the footprint of the surface CH_2Cl_2 seasonality up to a few months into the past in the LMS. Unlike for long-lived tracers with a distinct seasonality (e.g. CO_2) CH_2Cl_2 in the LMS cannot easily be used as a time axis due to its short (and variable, cf. Section 1.3.3) lifetime and large gradients in global source distribution. Eventually this footprint gets mixed with enough air of different transport and chemical history that its distinctiveness is lost to the compact stratospheric correlation.

Based on the analysis of this section it was shown that the WISE measurements revealing the distinctive lower branch of the CH_2Cl_2-N_2O correlation can be considered to be consisting of mostly CH_2Cl_2-poor air from the NH tropical MBL. Further, this means that CH_2Cl_2 mixing ratios higher than those of this CH_2Cl_2-poor background air correlation are influenced by regional sources larger than the average sources that define these background mixing ratios. Therefore, the CH_2Cl_2-rich air of the distinctive upper branch most likely originated from one or more highly polluted regions.[6]

---

[6] It has to be mentioned that the relatively higher (compared to the NH tropics) AGAGE CH_2Cl_2 background measurements from the NH midlatitudes are barely reflected in the HAGAR-V measurements at the tropopause region. This might be due to the above and in Appendix C.2.2 mentioned requirement

4.2.3 Impact of different source regions

The measured data from the CH_2Cl_2-N_2O correlation were color coded with the different emission tracers from CLaMS. The seven Asian tracers BoB, ECH, IND, INO, NIN, SEA, and TIB are all showing comparable features at the measured data points (cf. Figure F.4). Therefore, in this study the sum of these emission tracers is summarized in one emission tracer referred to as Southern and Eastern Asia tracer (SaEA). The SaEA tracer is comparable (mainly missing only the area of the Wpool tracer) to the combined India/China and Southeast Asia tracers used in two other CLaMS simulations for the years 2008 (Vogel et al., 2019) and 2012 (Vogel et al., 2016). Both studies used comparable simulation constraints as in the present work and find that the combined India/China and Southeast Asia tracers on average show the largest fraction in the NH LMS between September and October (around 15–30 % at 360 K and around 15–25 % at 380 K potential temperature, rising with time). This gives reason to assume a comparable average impact on the NH LMS in 2017 from the SaEA tracer used in the present study.

Figure 4.6 shows the CH_2Cl_2-N_2O correlation measured during WISE and color coded by the SaEA tracer (top left), the CAM tracer for Central America (top right), and the W-ITCZ tracer for the western part of the ITCZ (bottom left). The maximum range of the respective color axis was defined by the range of most data points, outliers excluded (compare for example Figure F.5). Interestingly, these tracers (SaEA and CAM or W-ITCZ) of different air mass origin each highlight large parts of one of the two distinctive correlation branches.

Figure 4.6 (top left) shows almost all measurements in the stratosphere are remarkably influenced by the SaEA tracer and only at low N_2O mixing ratios (old air) the SaEA fraction is < 10 %. The upper branch exhibits enhanced fractions of the SaEA tracer and the lower branch exhibits extraordinarily enhanced fractions of the CAM tracer. By separating the data set with the correlation branch filter (Section 4.2.1) the average SaEA fraction for the upper branch is 46 % larger than for the lower branch ((35 ± 7) % vs (24 ± 6) %[7], respectively). The average SaEA fraction associated with the correlation's lower branch is comparable to what was found on average for this season in the NH LMS in the years 2008 (Vogel et al., 2019) and 2012 (Vogel et al., 2016). The average SaEA fraction associated with the upper branch is clearly higher than the expected mean fraction according to the simulations for 2008 and 2012.

---

for the MS module to measure only at low water vapor values. Thereby measurements in the tropopause region of air influenced by NH midlatitude background mixing ratios potentially were rejected.

[7] Median SaEA fraction: upper branch: 34 % , n = 77; lower branch: 23.7 %, n = 186; cf. Table F.2

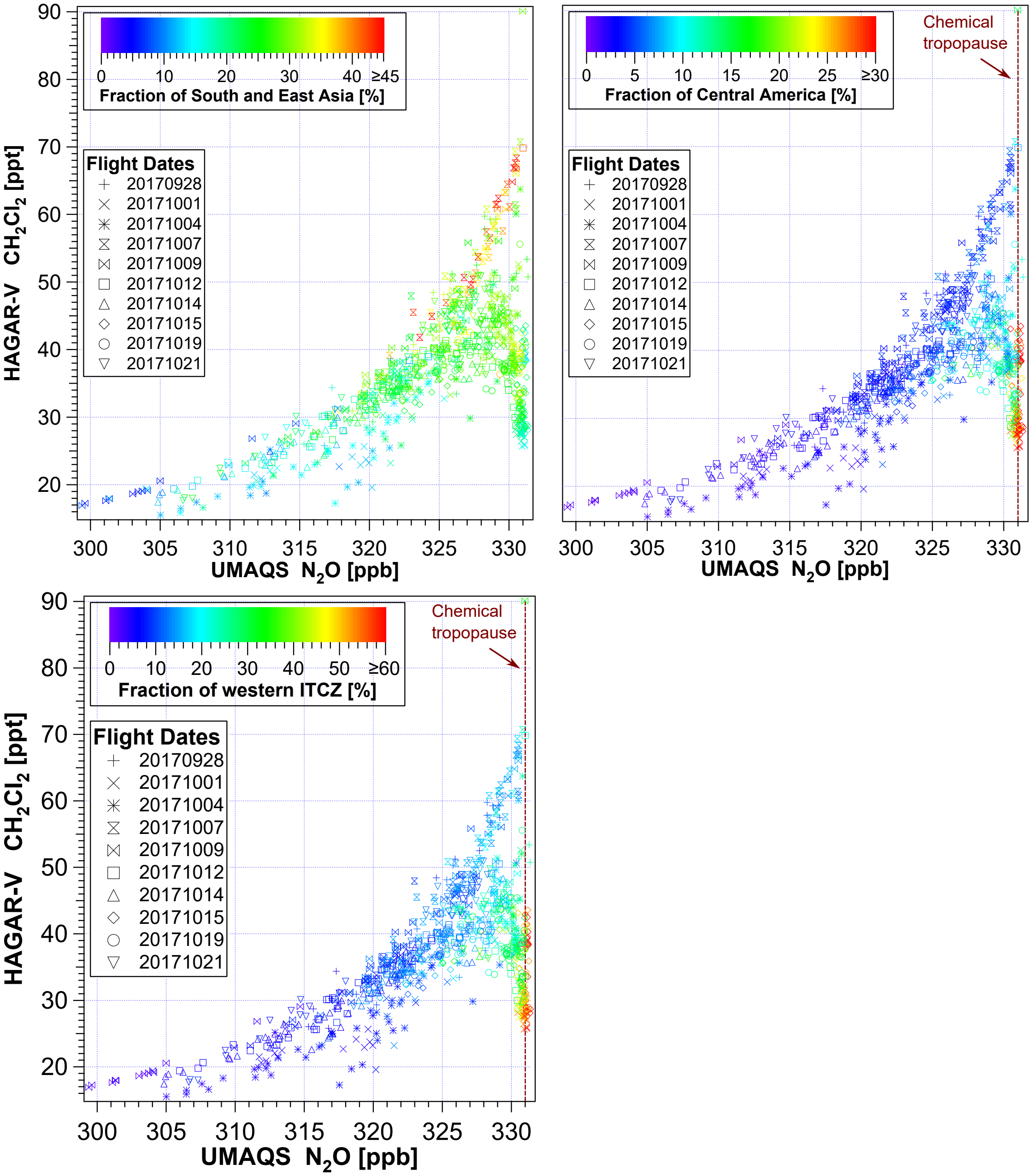

Figure 4.6: CH_2Cl_2-N_2O correlation color coded by the Southern and Eastern Asian (SaEA, top left), the Central American (CAM, top right), and the Western ITCZ (W-ITCZ, bottom left) emission tracers simulated by CLaMS. The color coding is limited to a maximum of 45 % (SaEA tracer), 30 % (CAM tracer), and 60 % (W-ITCZ tracer) to realize a better color visualization (otherwise spoiled by few outlying data points). The SaEA fraction is elevated in the upper branch. The CAM fraction as well as the W-ITCZ fraction are elevated in the lower branch.

With the major source regions of CH_2Cl_2 being located within the boundaries of the SaEA tracer (cf. Section 1.3.2) it is indeed very likely that the measured CH_2Cl_2-rich air of the upper branch is composed of a large fraction that originated in this major source region. This would also indicate that the transport of CH_2Cl_2-rich air from the main source regions in Asia into the NH LMS is highly significant and leaves there a distinct footprint with measured mixing ratios up to 130 % larger than what is assumed to be unpolluted tropical background (CH_2Cl_2-poor air) measured in the NH LMS in the same season (cf. Section 4.2.2).

The CH_2Cl_2-N_2O correlation color coded with the CAM tracer in Figure 4.6 (top right) provides a totally different picture. By separating the data set with the correlation branch filter the average CAM fraction for the lower branch is about 320 % larger than for the upper branch ((21 ± 11) % vs (5 ± 2) %[8], respectively). This large difference is partly due to the high CAM fraction in the UT and the chemical tropopause (average of (32 ± 10) %[9] at $N_2O \geq 331$ ppb) which is almost exclusively part of the lower branch. The large CAM fraction that marks most likely very young air at the chemical tropopause (cf. sections 4.2.4 and 4.2.5) could be the result of fast transport driven by large tropical cyclones from the region of Central America. Tropical cyclones have been shown to efficiently lift air from the MBL to the tropopause layer (e.g. Zhan and Wang, 2012; Vogel et al., 2014; Ratnam et al., 2016; Pan et al., 2016; Li et al., 2017). In particular in September 2017 the region of Central America was hit by tropical cyclones (here also called hurricanes) up to category 5[10] (i.e. hurricane Maria, September 16 – 30, Pasch et al., 2019) which could have provided the necessary updraft for an efficient transport into the UTLS. More details about that transport pathway will be examined in Section 4.2.6.

The source region of CAM contains the tropical NH measurement station of the AGAGE network at Barbados whose data have been compared to the lower correlation branch in Section 4.2.2. The result of the CLaMS simulation that a major fraction of the lower branch's air parcels originated from the region around this AGAGE measurement station clearly supports the interpretation suggested in Section 4.2.2. These findings also strengthen the statement that the lower branch mainly consists of CH_2Cl_2-poor background air from the MBL.

Not only the CAM tracer exhibits its largest fractions for data in the lower branch; this also holds for the tracers TEP, TAO, and NAF. These four tracers (combined as W-ITCZ

---

[8] Median CAM fraction: lower branch: 20.8 %, n = 186; upper branch: 4.4 %, n = 77; cf. Table F.2

[9] The median CAM fraction for $N_2O \geq 331$ ppb is 31.4 %; n = 48, i.e. 25 % of the data of the lower branch

[10] on the Saffir-Simpson Hurricane Wind Scale (for more information e.g. https://www.nhc.noaa.gov/aboutsshws.php)

tracer, cf. Figure 4.1), mainly mark the western region of the inter-tropical convergence zone (ITCZ) in NH summer, leaving out most of the eastern part of the ITCZ including the Asian monsoon region (plots expressing the ITCZ are shown in Figure F.3). The ITCZ is a convective belt around the world driving fast transport from the BL to the TTL where the air further is transported to the stratosphere (e.g. Levine et al., 2007). The W-ITCZ tracer exhibits an average fraction of (42 ± 14) %[11] for data in the lower branch (Figure 4.6, bottom left). Thereby fractions of 60 % and higher are noted only for data in the UT up to the chemical tropopause; above the chemical tropopause the W-ITCZ tracer marks mostly measurements of low CH_2Cl_2mixing ratios with fractions around 35 %. The source region of the W-ITCZ tracer covering the western ITCZ is mainly over sea and not known for major CH_2Cl_2 sources (cf. Section 1.3.2). This also gives confidence that the lower branch can be considered the footprint of mostly CH_2Cl_2-poor background air from the marine BL in the NH UTLS.

4.2.4 Seasonal dominance of regional sources

CH_2Cl_2 has a tropospheric lifetime of 168 days (Hossaini et al., 2017, cf. Section 1.3.3), thus only comparably fast transport from the source region (from the BL) into the UTLS can be significant for this Cl-VSLS. As described in Section 4.1.2 the tracers of air mass origin are defined for the analysis of air masses younger than six months. The first initialization of the emission tracers is on May 1, 2017, and the measurements of CH_2Cl_2 range from September 28 to October 21, 2017. Therefore, transport from the source region into the UTLS on timescales investigated in the present work can be sufficiently analyzed with this model definition. However, also air masses older than six months (i.e. released from the model BL before May 1, 2017) contribute to the composition of an air parcel. These air masses are from the free troposphere and the stratosphere. To remove the fractions from the free troposphere and stratosphere only the fractions from the emission tracers (listed in Figure 4.1) are considered in an air parcel. Therefore, the fractions from the individual emission tracers are normalized by the sum of all emission tracers.

The sum of all emission tracers marking each individual measurement are visualized in Figure 4.7 (top left). These fractions can be considered to be remotely comparable to an artificial age tracer. A fraction of 100 % of the sum of all emission tracers implies the regarded air parcel only consists of air masses that have left the BL after April 2017 (i.e. that are younger than six months). The smaller the fraction of all emission tracers are the larger is the fraction of air that was released to the atmosphere before Mai 2017 (i.e.

---

[11] Median W-ITCZ fraction of the lower branch: 43 %

the air parcel is composed of a mix of air that is partly older and partly younger than six months). As expected, the measurements at the UT and the chemical tropopause (highest N_2O mixing ratios) are associated with the largest fractions of the sum of all emission tracers (consist in the largest parts of young air masses). In contrast, the smaller the N_2O mixing ratios are the smaller is the fraction of air masses younger than six months (i.e. the larger is the fraction of older air).

Figure 4.7 (bottom) shows the CH_2Cl_2-N_2O correlation color coded by the normalized fraction of the SaEA tracer (left) and the normalized fraction of the western ITCZ tracer (right). The residual normalized emission tracers are shown in Figure 4.7 (top right).

The majority of the whole correlation exhibits a normalized SaEA fraction of minimum 50 % except for the data between the two branches (~ 40 %) and the lower branch (~ 30 %). This indicates that out of young air masses (time above BL $<$ 6 months) that mix into the LMS in most cases more than 50 % originated in the source region of the SaEA tracer in Asia. In particular air parcels of CH_2Cl_2-rich air are associated with a high fraction of the normalized SaEA tracer while air parcels of CH_2Cl_2-poor air are marked only with relatively small fractions from Asia. More generally, in NH summer air in the LMS is dominated by import of young air masses from southern and eastern Asia that steepens the CH_2Cl_2-N_2O correlation slope due to particularly CH_2Cl_2-rich air masses from that source region.

In contrast to the normalized SaEA tracer, the normalized tracer of the western ITCZ almost fully complements the emission tracer distribution (see also Appendix F.2.3). Data between the upper and the lower branch in the LMS show almost an equally high fraction of around 40 % from both normalized tracers (indicated as mixed air in Figure 4.7, bottom right). Like a gradient the normalized SaEA fraction rises while the normalized western ITCZ fraction falls with rising CH_2Cl_2 mixing ratios in the LMS close to the chemical tropopause. This suggests that in NH summer CH_2Cl_2-poor air from the western ITCZ enters the LMS and mixes with CH_2Cl_2-rich air from southern and eastern Asia to form the middle part of the correlation between the upper and the lower branch.

The fractions from the residual normalized emission tracers are generally small compared to the normalized SaEA and W-ITCZ tracers and show an almost constant fraction of ~ 20 % over the whole correlation (Figure 4.7, top right). Only at the lowest N_2O mixing ratios (oldest air) the normalized residual emission tracers are larger and for the highest N_2O values (youngest air) they are smaller than the overall average of (21 ± 3) %. This implies that in general the two emission tracers SaEA and W-ITCZ dominate the air masses younger than six months in the NH LMS with a fraction of about 80 % that is

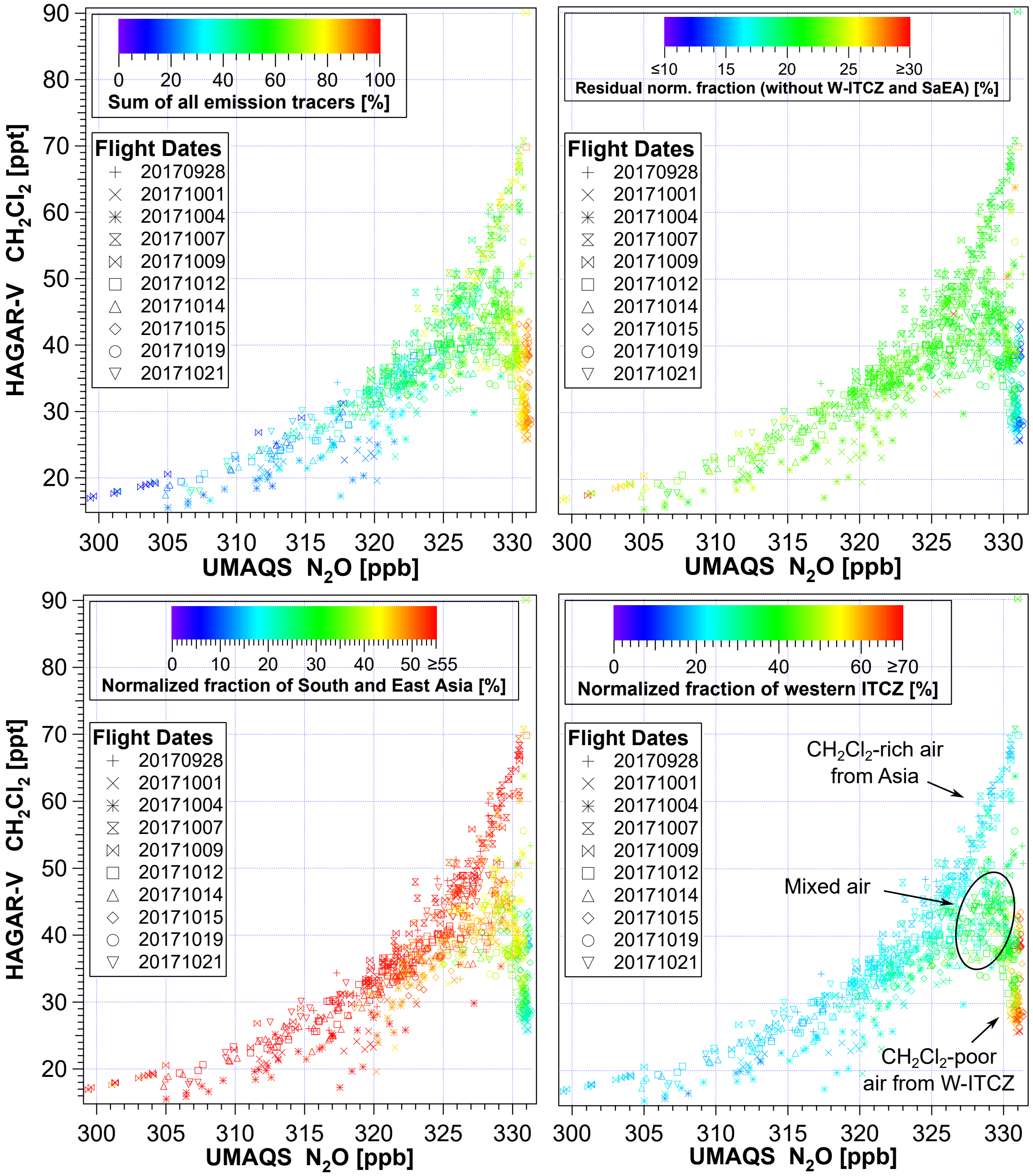

Figure 4.7: CH_2Cl_2-N_2O correlation color coded by: the sum of all emission tracers (top left); the normalized (to the sum of all emission tracers) fraction of the SaEA tracer (bottom left); the normalized fraction of the W-ITCZ tracer (bottom right); the normalized fraction of all emission tracers but SaEA and W-ITCZ (top right). The normalized fractions refer only to those elements of an air parcel that are younger than six months. The color coding is limited to a maximum of 55 % (normalized SaEA tracer) and of 70 % (normalized W-ITCZ tracer), and limited between 10 % and 20 % (normalized residual tracers).

up to 90 % in the UT region. This implies that generally the main impact of young air on the observed composition of the NH LMS comes from source regions in southern and eastern Asia and the western ITCZ region rather than from any other source region. Thus, southern and eastern Asia and the western ITCZ are the two source regions from where the most significant tropospheric intrusions of the short-lived CH_2Cl_2 into the LMS are expected.

On the one hand at the chemical tropopause and in the UT young air masses are dominated (fractions of 60 % and more) by air parcels that originated in the western ITCZ region. On the other hand the larger part of young air masses in the NH LMS is dominated by air parcels that originated in the region of southern and eastern Asia. This indicates two distinct transport pathways from boundary source regions into the LMS: one from the western ITCZ (CH_2Cl_2-poor air) and the other from southern and eastern Asia (CH_2Cl_2-rich air). As indicated by the different average potential temperatures of measurements of the upper and the lower branch (Table F.1) air from southern and eastern Asia might thus predominantly enter the LMS on higher potential temperatures than air from the western ITCZ. This would imply that in NH summer, where transport from the troposphere to the NH LMS is most significant (e.g. Hoor et al., 2005; Bönisch et al., 2009), CH_2Cl_2-rich air is mixed into the LMS at higher levels of potential temperature than CH_2Cl_2-poor air, indicating tropospheric intrusions (e.g. Pan et al., 2009; Vogel et al., 2011).

4.2.5 Trajectory transport times and source regions

Figure 4.8 shows the end points at the model BL of the backward trajectories that reached the BL within the 120 days of backward calculation. Figure 4.8a shows the trajectory end points of the observed measurements in the upper branch (CH_2Cl_2-rich air)[12] and Figure 4.8b shows the trajectory end points of the lower branch (CH_2Cl_2-poor air)[13]. The color code is the time in days the respective air parcel needed on its trajectory from the BL to the point of measurement.

The average transport time of air parcels from the BL to the point of measurement is (66 ± 24) days[14] for the upper branch and (47 ± 28) days[15] for the lower branch (cf. Table F.3). Data points with transport times smaller than 30 days are all at N_2O mixing

---

[12] 19 out of 77 data points in the upper branch did not reach the BL within 120 days, i.e. 25 % have longer transport times than 120 days and will be ignored in further trajectory analysis

[13] 18 out of 186 data points in the lower branch did not reach the BL within 120 days, i.e. 10 % have longer transport times than 120 days and will be ignored in further trajectory analysis

[14] n = 58; median: 65 days

[15] n = 168; median: 42 days

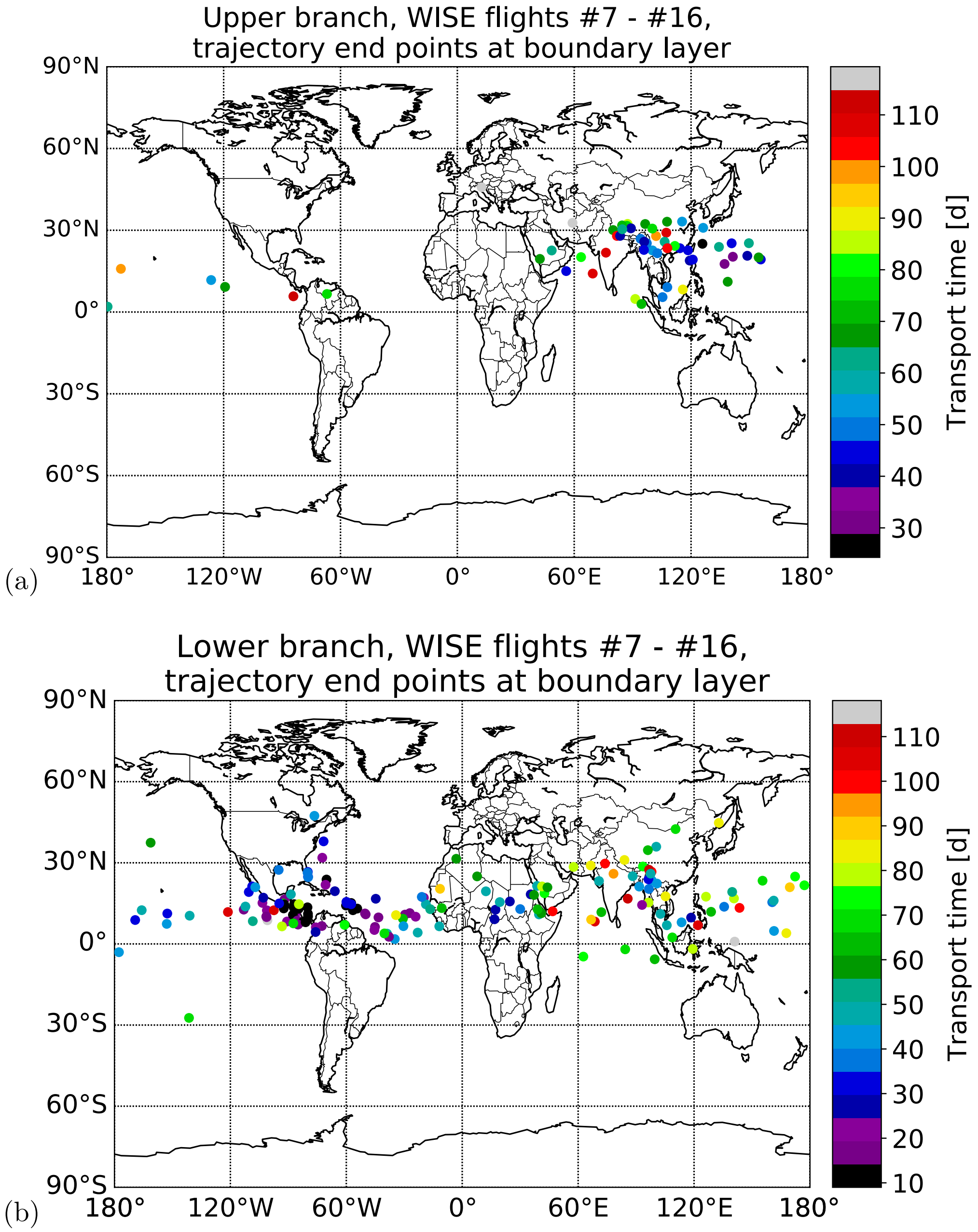
Upper branch, WISE flights #7 - #16, trajectory end points at boundary layer

Lower branch, WISE flights #7 - #16, trajectory end points at boundary layer

Figure 4.8: End points at the boundary layer (BL) of 120 day backward trajectories calculated with CLaMS for air parcels sampled during WISE. (a) shows the end points of the trajectories for data points of the upper branch, (b) shows the end points of the trajectories for the data points of the lower branch. The filtering was done according to Section 4.2.1. The color coding is the transport time from the point of measurement backwards to the BL.

ratios larger 330.5 ppb, i.e. at the chemical tropopause region and in the UT. This implies that the transport time from the BL to the LMS is at least one month for the air parcels sampled during WISE. In addition this supports the suggestion that the minimum CH_2Cl_2 mixing ratios of the lower branch measured in October at the chemical tropopause correspond to the seasonal CH_2Cl_2 minimum in September observed at the surface by the AGAGE network (Section 4.2.2). More generally, this supports the hypothesis that from LMS mixing ratios belonging to the lower branch preserve a footprint of CH_2Cl_2 surface seasonality up to a few months into the past.

The longer the backward trajectory calculation is the larger is the uncertainty of a single trajectory because mixing is not considered. However, using a bundle of backward trajectories of longer transport times can still be helpful for analyses. In particular the clearly different clustering of the trajectory's end points of measurements with high and low CH_2Cl_2 mixing ratios (upper and lower branch) shown in Figure 4.8 provide a good basis for interpretation.

The endpoints at the BL of the trajectories from the upper branch clearly cluster from India to the West Pacific and down to Southeast Asia (Figure 4.8a). This result is consistent with the findings using the tracers of air mass origin in a 3-dimensional CLaMS forward simulation including the mixing of air parcels (Section 4.2.3). This result shows that the strongly enhanced CH_2Cl_2 mixing ratios measured during WISE have been transported from the southern and eastern parts of Asia to the LMS above the Atlantic and Europe. With an average transport time of 66 days the release to the free troposphere of the air parcels measured in the upper branch (CH_2Cl_2-rich air) was therefore around July and August. This is the peak phase of the ASM season (June to September) and this is a strong indicator that the ASM is the main driver in transporting the CH_2Cl_2-rich air into the NH LMS. This claim will be corroborated in Section 4.2.7 by analyzing whole trajectories.

While the trajectories of upper branch air parcels almost exclusively reach the BL in southern and eastern Asia, the trajectories of lower branch air parcels (CH_2Cl_2-poor air) are widely spread around the globe mainly following the ITCZ[16] (Figure 4.8b). However, the highest density of backward trajectory end points of lower branch air parcels is in the region of Central America. This is in full agreement with the large fraction of the artificial emission tracer for the region of Central America (CAM) associated with the lower branch (Section 4.2.3).

The transport times of the trajectories associated with the lower branch exhibit a clear difference between the western and the eastern trajectory end points at the BL. For air parcels

---

[16] The ITCZ in July, August, September, and October 2017 is visualized in Figure F.3

of the lower branch originating from longitudes (0–180)°W the median trajectory transport time[17] is 26 days[18] and for those originating from (0–180)°E the median transport time is 64 days[19]. This suggests a fast and efficient transport pathway from the western ITCZ to the UTLS above the Atlantic Ocean and western Europe in September. In particular the transport from the BL of the region of Central America to the measurement region in the UTLS appears to have happened very fast with trajectory transport times down to one week. This implies that most of the air that originated in the region of Central America was measured in the tropopause region during WISE. The same result could be shown with the CAM tracer in Section 4.2.3.

The relatively slow transport from the eastern part of the ITCZ mainly includes trajectory end points in southern and eastern Asia which is dominated by the ASM at the time of air parcel release to the free troposphere. This suggests that the transport mechanisms that bring air into the UTLS from the western ITCZ and the ASM region are both efficient but the latter takes almost twice as long.

The 20 trajectories with transport times $\leq$ 14 days pertain almost all[20] to air sampled during WISE flights #8 (10 trajectories) and #15 (9 trajectories). Those two flights were aimed (among other goals) at probing the outflow of large hurricanes from the Atlantic and the Caribbean (cf. Table 3.1). Large low pressure systems like hurricanes could be an explanation for the observed fast transport into the tropopause region due to the extreme convection they can cause (e.g. Zhan and Wang, 2012; Vogel et al., 2014; Ratnam et al., 2016; Pan et al., 2016; Li et al., 2017). To directly connect the convection caused by a tropical cyclone to the WISE measurements the position of the largest updraft along the trajectories has to be evaluated and compared to the position of active hurricanes in the time period of the respective trajectories (Section 4.2.6).

4.2.6 Major updraft events

To investigate major events causing exceptionally fast transport into the UT, the maximum diabatic ascent rate over a time interval of 18 hours (max. $\dot{\Theta}$) along each backward trajectory was analyzed. Max. $\dot{\Theta}$ is derived as the maximum change in potential temperature over 18 hours along the backward trajectory. Figure 4.9 shows the locations of max. $\dot{\Theta}$ along each trajectory associated with (a) the data of the upper branch and (b) the data of the lower branch. The color code shows the respective max. $\dot{\Theta}$ in K/18 h. A large $\dot{\Theta}$

---

[17] Only for the backward trajectories that reached the BL within the 120 days of calculation

[18] n = 98; average: (35 ± 24) days

[19] n = 70; average: (65 ± 24) days

[20] Except for one trajectory during flight #14

implies a fast updraft of the respective air parcel at the shown position. Details about the calculation of $\dot{\Theta}$ are given by Hanumanthu et al. (2020).

Figure 4.9a shows that the majority of the sampled air parcels of the upper branch experienced the largest updraft over 18 hours in southern and eastern Asia, in particular in the region of the Tibetan Plateau, northern India, China, Southeast Asia and the western Pacific. Given the findings from sections 4.2.3 and 4.2.5 this major updraft is very close to the main source region of most of the air parcels of the upper branch. Thus it is very likely that CH_2Cl_2-rich air released to the free troposphere in the region of southern and eastern Asia was convectively transported to higher altitudes by the ASM's low pressure systems. To identify how this transport took place the full trajectories are analyzed in Section 4.2.7.

Figure 4.9b shows that there are two main regions which provided fast updraft for the air parcels of the lower branch. While the source regions have been identified along the ITCZ the fastest updraft seems to favor either the region of Central America or the region of southern and eastern Asia. This suggests that similar to the CH_2Cl_2-rich air of the upper branch also CH_2Cl_2-poor air of the lower branch was transported into the LMS due to the updraft of the ASM's low pressure systems.

The median maximum ascent rate over 18 hours ($\widetilde{\text{max. }\dot{\Theta}}$) in the range of (0–30)°N and (60–120)°W (Central America) for the trajectories of the lower branch is 20.7 K/18 h[21] while in the area of (0–40)°N and (60–160)°E (southern and eastern Asia) $\widetilde{\text{max. }\dot{\Theta}}$ is only 15.1 K/18 h[22]. $\widetilde{\text{Max. }\dot{\Theta}}$ in southern and eastern Asia for trajectories of the upper branch is comparably only 16.4 K/18 h[23]. Therefore, on median the fastest updraft for trajectories of both branches is found in the region of Central America which is about 30 % higher than the median of the fastest updrafts found in the region of southern and eastern Asia. However, this does not imply that air parcels from the region of Central America are lifted up to higher potential temperature levels than air parcels of the lower branch that experience convection above southern and eastern Asia. The average potential temperature at the point of measurement of air parcels with relatively faster updraft above the region of Central America is (361 ± 10) K while for the measurements of air parcels that experienced the fastest updraft over southern and eastern Asia it is similarly (362 ± 11) K[24].

The efficient updraft above the region of Central America is also associated with short transport times (Section 4.2.5). Thus it is very likely that the process causing the fastest

---

[21] n = 76; average: (24 ± 12) K/18 h

[22] n = 49; average: (18 ± 8) K/18 h

[23] n = 50; average: (18 ± 8) K/18 h

[24] Considering only data of the lower branch; both average potential temperatures are equal to their median

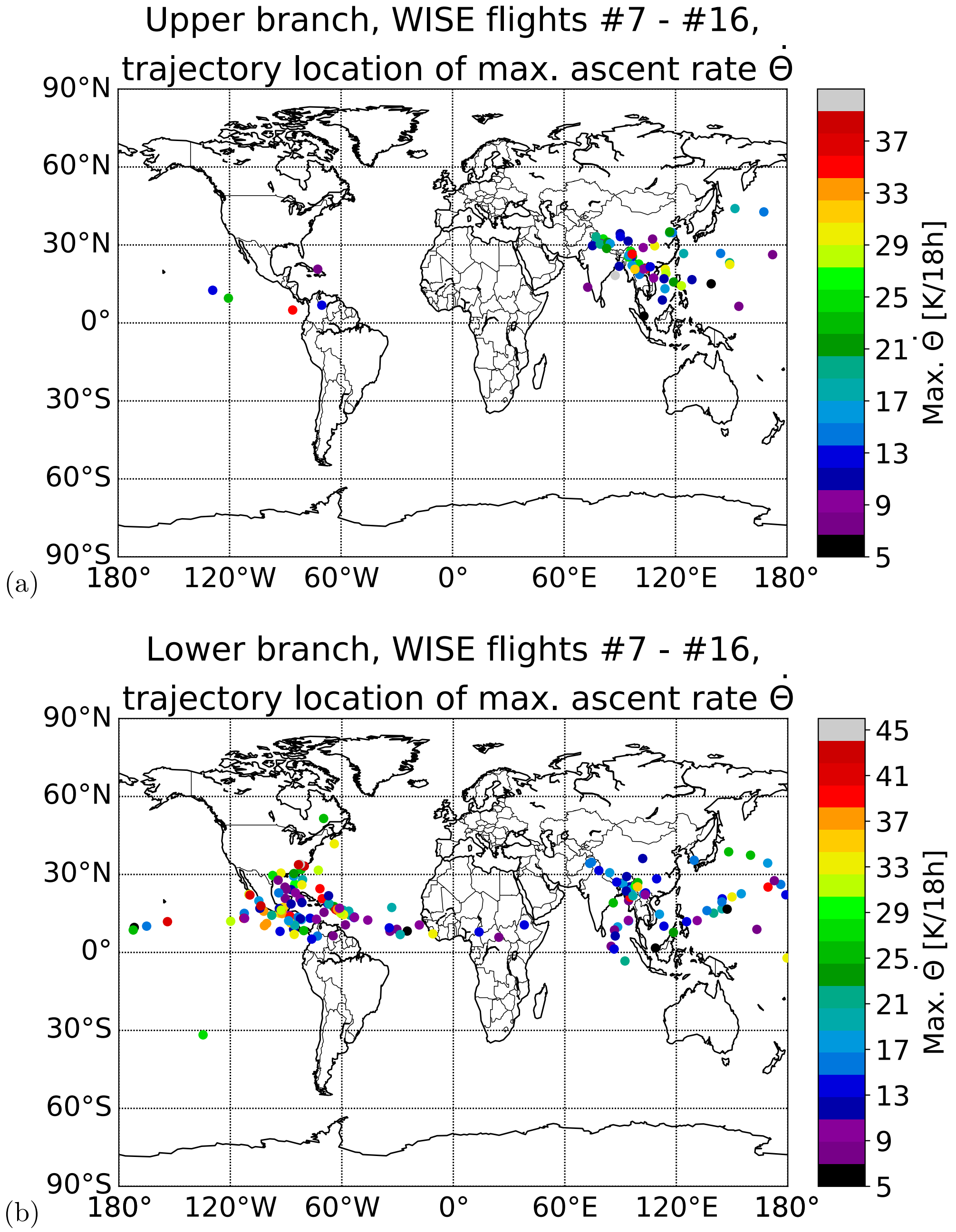

Figure 4.9: Geographic positions of largest diabatic ascent rates (max. $\dot{\Theta}$) evaluated over intervals of 18 hours along 120 day backward trajectories calculated with CLaMS for air parcels sampled during WISE. The shown points of maximum max. $\dot{\Theta}$ indicate the fastest updraft along a trajectory. (a) shows the trajectory positions of fastest updraft for data of the upper branch, (b) shows the trajectory positions of fastest updraft for data of the lower branch. The filtering for the different branches was done according to Section 4.2.1. The color coding represents max. $\dot{\Theta}$ in K/18 h at the shown position.

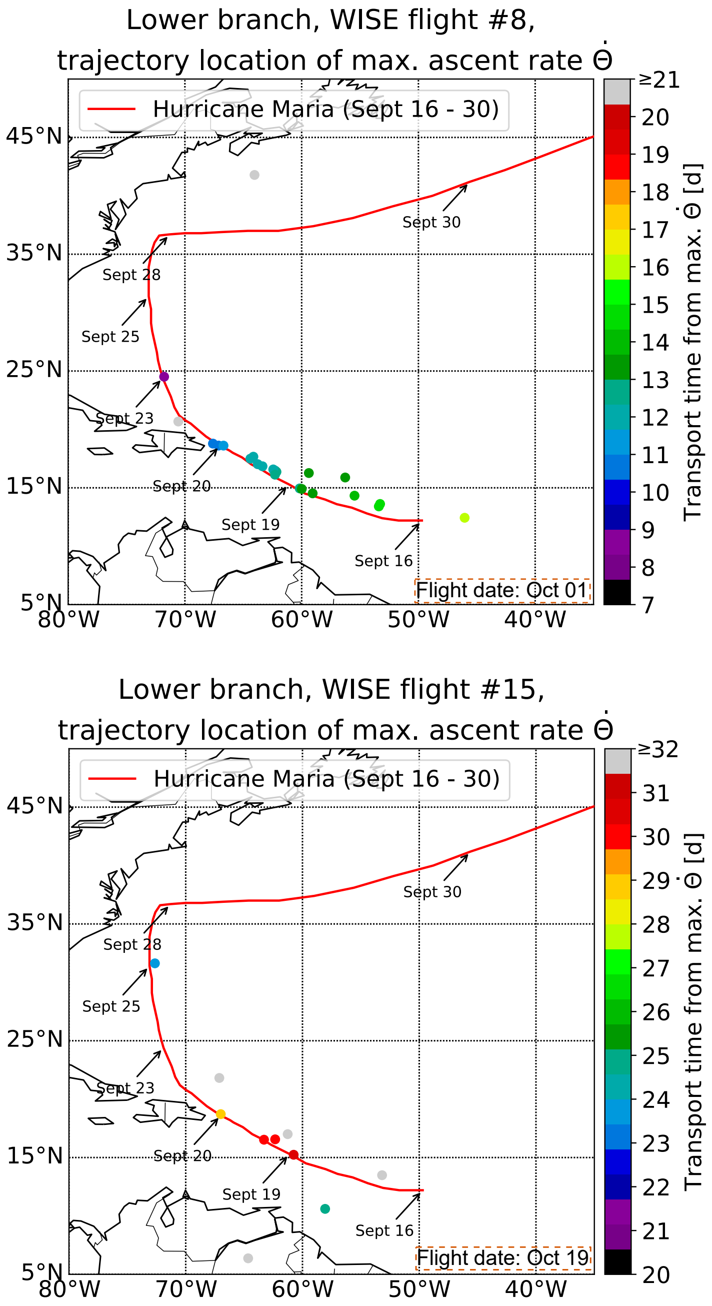

(a)

(b)

Figure 4.10: Storm track of the center of hurricane Maria (red line) and positions of maximum ascent rate over 18 h (max. $\dot{\Theta}$) along the backward trajectories of data points measured during (a) WISE flight #8 (on October, 1) and (b) WISE flight #15 (on October, 19). The color code indicates the transport time along the trajectory from the position of max. $\dot{\Theta}$ to the position of measurement. The dates on the arrows indicate the date and position of the center of hurricane Maria.

updraft along trajectories from this region is also the most important agent of regional transport into the UTLS. Figure 4.10 shows the track of the center of hurricane Maria (red line; Pasch et al., 2019) and the position of max. $\dot{\Theta}$ along each trajectory of air parcels of the lower branch. Figure 4.10a shows data of WISE flight #8 (on October 1) and Figure 4.10b shows data of WISE flight #15 (on October 19). The coloration exhibits the transport time along the respective trajectories from the position of max. $\dot{\Theta}$ to the position of measurement. The dates and arrows indicate the respective day and position of hurricane Maria along its track.

Figure 4.10 shows that several air parcels of measurements from WISE flights #8 and #15 experienced their largest change in potential temperature along their respective trajectory at a location close to the trace of the center of hurricane Maria. An analysis of the transport times from the positions of max. $\dot{\Theta}$ to the respective time and position of measurement shows that 18 trajectories from flight #8, 1 trajectory each from flights #13 and #14, as well as 6 trajectories from flight #15 can be directly associated to uplift by hurricane Maria. For these trajectories the positions of max. $\dot{\Theta}$ match the storm track of hurricane Maria to within a 1° radius. In addition, for these trajectories the calculated dates at the respective trajectory's locations of max. $\dot{\Theta}$ match the dates at which hurricane Maria was located at these positions to within a time window of 0.2 days. The 1° radius of tolerance has been chosen because it corresponds roughly to the hurricane's radius from its core and the ERA-Interim reanalysis data for the calculation of the backward trajectories also have a spatial resolution of 1°.

Figure 4.11 shows the CH_2Cl_2-N_2O correlation with different coloration. Figure 4.11a is colored according to the branch filter introduced in Section 4.2.1. Data of the upper branch is marked in light red, data of the lower branch is marked in light blue, data in between is marked gray. Measurements that were associated with transport by hurricane Maria are marked in blue. Figure 4.11b shows the correlation in gray and marks only the measurements associated with hurricane Maria with different symbols according to their flight dates. The color coding indicates the transport time from the position of max. $\dot{\Theta}$ to the point of measurement along the respective trajectory.

In Figure 4.11a it is clearly visible that the majority of measurements transported by hurricane Maria shows relatively low CH_2Cl_2 mixing ratios pertaining to the lower branch. This is consistent with their origin in the tropical marine BL (sections 4.2.2, 4.2.4, and 4.2.5).

Figure 4.11b shows a tendency for data uplifted by hurricane Maria to exhibit relatively higher CH_2Cl_2 mixing ratios when measured a longer time past the major updraft event.

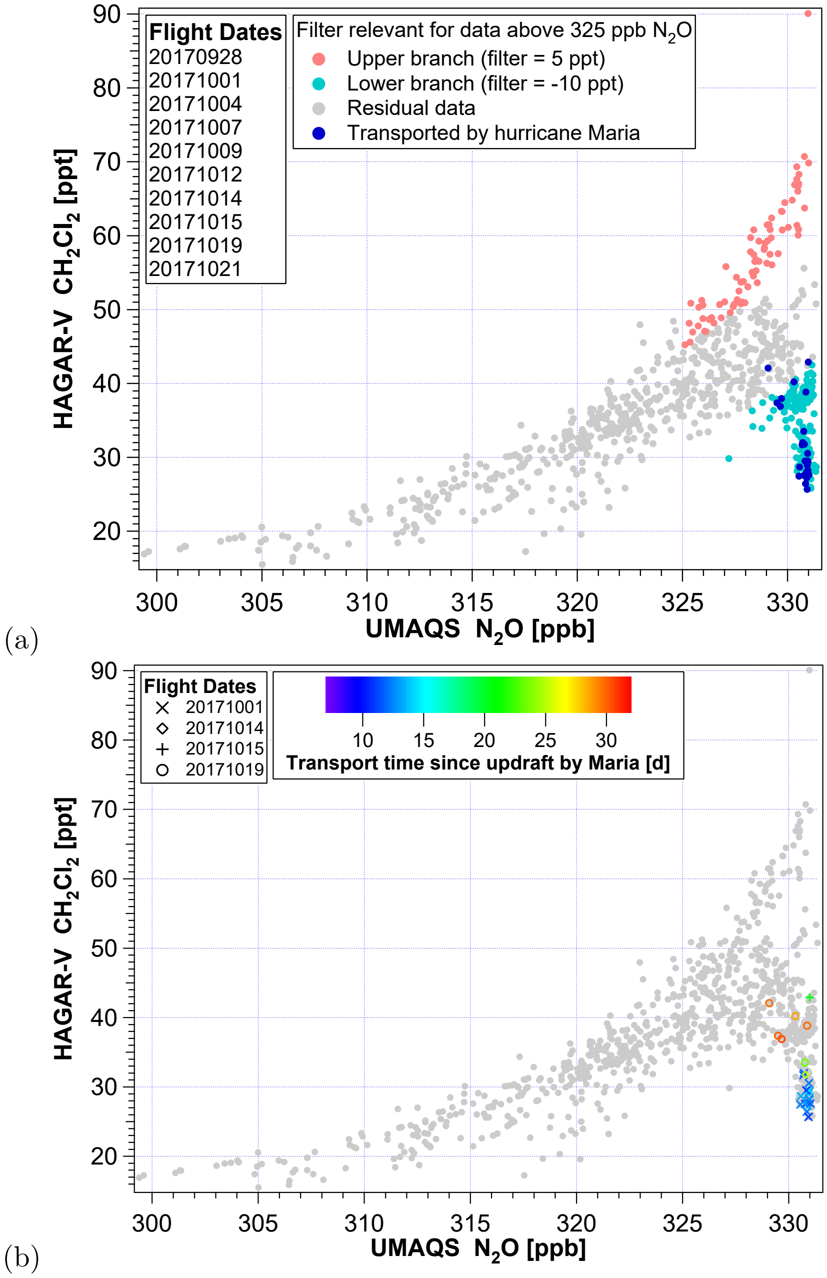

Figure 4.11: CH_2Cl_2-N_2O correlation with marked air parcels transported by hurricane Maria. The colors of (a) mark data transported by hurricane Maria in blue and mark the rest of the correlation according to the branch filter (upper branch: light red, lower branch: light blue, data between the branches: gray). (b) shows different symbols according to the flight date for the data transported by hurricane Maria. The colors of (b) indicate the respective transport time from the largest updraft by hurricane Maria to the position of measurement.

The longer an air parcel resides in the atmosphere the higher are its chances to mix with differently composed air parcels. It can also be assumed that CH_2Cl_2-poor air with the minimum NH background CH_2Cl_2 mixing ratios of September can only mix with air of equal or higher mixing ratios. Thus it appears very plausible that mixing ratios of air parcels lifted up by hurricane Maria increase with their residence time in the UTLS due to the mixing with differently composed air.

The max. $\dot{\Theta}$ from the 26 trajectories that were uplifted by hurricane Maria is 31.5 K/18 h[25]. This implies that the median updraft caused by hurricane Maria is faster than the median updraft found in the region of Central America (i.e. 31.5 K/18 h vs 20.7 K/18 h, respectively). The measurements of air uplifted by hurricane Maria were obtained at an average potential temperature of (364 ± 8) K[26]. This is not significantly higher than the average potential temperature of measurements with the max. $\dot{\Theta}$ located above the region of Central America (i.e. 364 K vs 361 K, respectively). Despite the relatively fast updraft hurricane Maria thus apparently does not cause a significantly higher uplift than other convective sources in that region. In particular, the significantly faster updraft caused by hurricane Maria transports air to lower potential temperatures than the median air parcel found to be lifted up above southern and eastern Asia during WISE (i.e. 364 K vs 375 K[27], respectively). The trajectory end points and the full trajectories of air parcels transported by hurricane Maria are shown in figures H.3 and H.10, respectively.

4.2.7 Transport pathways

In this section whole backward trajectories for air parcels of the upper and the lower branch are analyzed to investigate the whole transport pathway from the source in the model BL to the location of the measurement. Figure 4.12 shows as an example backward trajectories of data of the lower branch of WISE flight #8 (left) and of data of the upper branch of WISE flight #10 (right) from the position of measurement down to the model BL.

Figure 4.12 shows several characteristics of the trajectories of air parcels measured during WISE that were also observed in other flights (Appendix H). In general the backward trajectories show that air parcels originating in the region of southern and eastern Asia are lifted up by relatively fast convection to a potential temperature of around 360 K. The majority of air parcels then further spiral upwards most likely within the ASM anticyclone (ASMA; e.g. Hoskins and Rodwell, 1995). Following this upward spiraling process the

---

[25] Median: (29 ± 9) K/18 h

[26] Median: 364.4 K

[27] Max. $\dot{\Theta}$ within (0–40)°N and (60–160)°E: n = 310; average potential temperature at position of measurement: (372 ± 17) K; median: 374.9 K

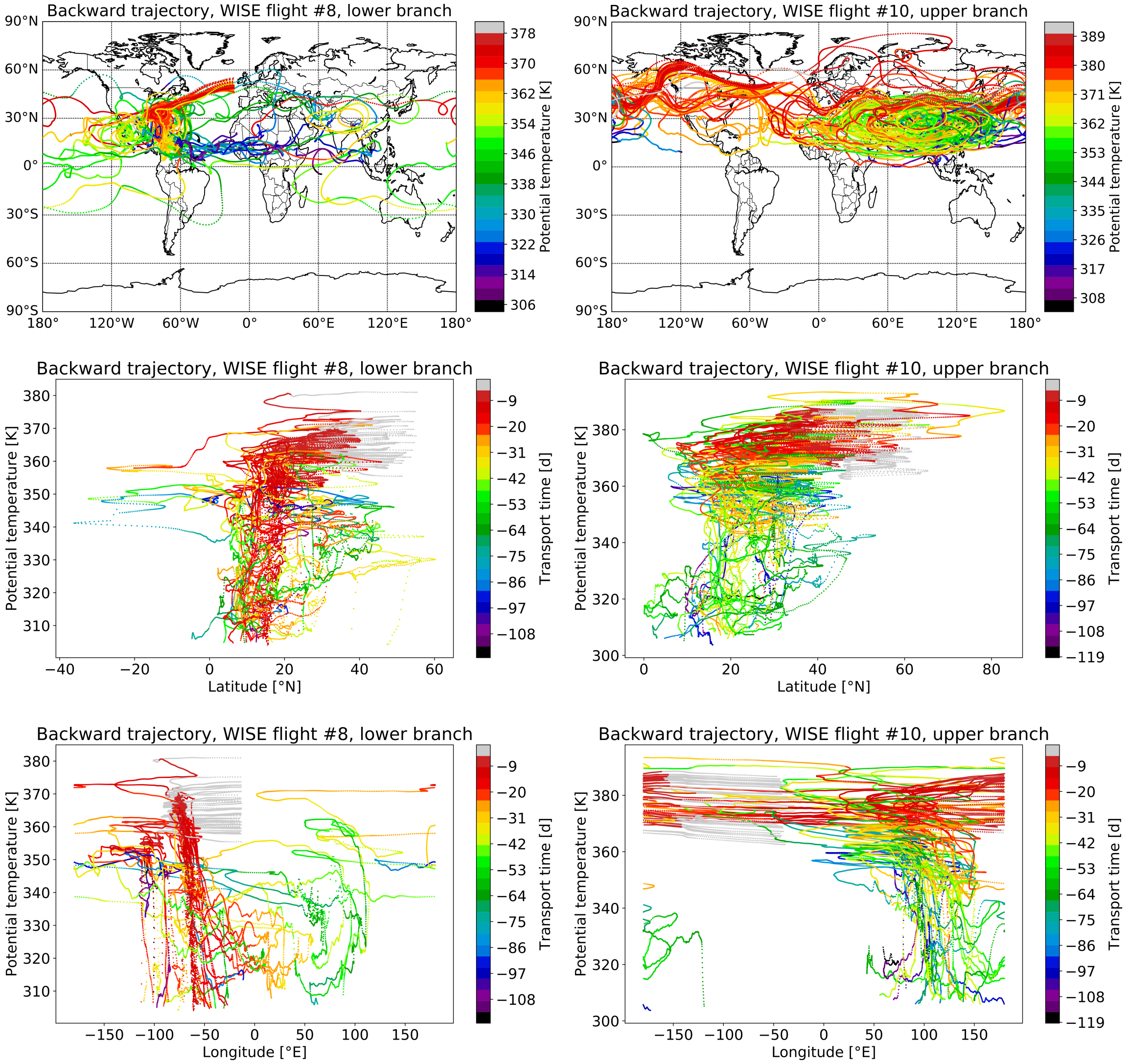

Figure 4.12: Backward trajectories for data of the lower branch of WISE flight #8 (left) and for data of the upper branch of WISE flight #10 (right) down to the BL. The upper row shows latitude vs longitude color coded with the potential temperature. The middle row shows the potential temperature vs latitude color coded with the transport time from the position of measurement to the respective position of the trajectory. The bottom row shows the same content as the middle row only plotted against the longitude instead of the latitude.

air parcels break out of the ASMA eastwards between potential temperatures of around 370 K to 400 K. Further on the trajectories mostly follow the subtropical jet at around 40°N until they move northwards above the Pacific or the Atlantic Ocean to the position of measurement. All trajectories suggest that the air parcels arrived from the west to the position of measurement and most trajectories suggest sinking potential temperatures a few days before measurement. This transport pathway via the ASMA was also observed for measurements taken during the HALO TACTS[28] campaign in August and September 2012 (Müller et al., 2016; Vogel et al., 2016; Rolf et al., 2018).

The fewer air parcels of the lower branch that were uplifted above southern and eastern Asia generally follow the same path as those of the upper branch. However, not all of them experience the upwards spiraling characteristics of the ASMA (cf. figures H.6, H.8, and H.9). This corresponds to the expectation that Asian source regions of lower branch (CH_2Cl_2-poor) air are located outside the main convective region of the ASM. These cleaner lower branch air parcels would thus be uplifted at the edge of the ASMA and follow its movement, but would soon break out eastward instead of entering the upward spiraling of the anticyclone. However, this hypothesis does not fit for all trajectories of the lower branch not entering the spiraling upward movement of the ASMA.

The result that air parcels of the lower branch uplifted above southern and eastern Asia are less likely to enter the ASMA than air parcels from the upper branch could contribute to the different potential temperatures between the measurements of the two branches. The median potential temperature ($\widetilde{\Theta}$) of air parcels of the lower branch lifted up above southern and eastern Asia[29] is 17.7 K lower than for the upper branch (i.e. 361.2 K[30] vs 378.9 K[31], respectively). Thus the upward spiraling by the ASMA most likely is the key part of transport from southern and eastern Asia to higher potential temperatures in the NH LMS compared to other convective systems. In addition, the backward trajectories suggest that the ASMA was almost the exclusive transport pathway of CH_2Cl_2-rich air into the NH LMS measured during WISE.

The second main transport pathway into the UTLS identified in the analysis of backward trajectories is above the region of Central America. The convective systems in this region are usually referred to as the North American monsoon (e.g. Adams and Comrie, 1997; Robertson et al., 2005) which is rarely subject of investigations on transport of trace gases into the UTLS (e.g. Ploeger et al., 2013). The relatively fast updraft identified in Section 4.2.6 mainly elevates air above the region of Central America to potential temperatures between around 360 K and 370 K. However, without a large high pressure system like the ASMA the air above the region of Central America is mostly not uplifted above 370 K before entering the extratropics. In addition, these air parcels mostly enter the extratropics above the North American east coast region and are thus transported on a more direct path into

---

[28] Transport and Composition in the Upper Troposphere and Lower Stratosphere

[29] Position of max. $\dot{\Theta}$ in the region of (0–40)°N and (60–160)°E, cf. Section 4.2.6

[30] $n = 49$; average: (362 ± 11) K

[31] $n = 50$; average: (375 ± 12) K

the NH UTLS above the Atlantic Ocean than air parcels transported by the ASMA. This results in comparably shorter transport times into the NH UTLS of air parcels originating in the region of Central America than of those from southern and eastern Asia.

4.3 The $CHCl_3$-N_2O correlation

In addition to the Cl-VSLS CH_2Cl_2 also $CHCl_3$ was measured by the HAGAR-V MS module during the WISE mission (cf. Section 2.5.3). Both species share similar chemical reactions and thus atmospheric sinks (Section 1.3.3), thus generally a similar correlation with N_2O would be expected (cf. Section 1.2). If the CH_2Cl_2-N_2O correlation and the $CHCl_3$-N_2O correlation for the same air samples were found to differ, it would show that CH_2Cl_2 and $CHCl_3$ have different regional sources and/or different source intensities.

Figure 4.13 shows the $CHCl_3$-N_2O correlation observed during WISE flights #7–#16 (cf. Table 3.1). Compared to the CH_2Cl_2-N_2O correlation (Figure 4.2) the $CHCl_3$-N_2O correlation shows a somewhat less pronounced split into two distinct branches towards higher N_2O mixing ratios. However, compared to the relatively compact part of the correlation for lower N_2O mixing ratios, a broader scattering of $CHCl_3$ values is visible towards higher N_2O mixing ratios (i.e. closer to the chemical tropopause). This could suggest similar conclusions as drawn for CH_2Cl_2 in Section 4.2. The analysis described in the following sections focuses on the interpretation of the $CHCl_3$-N_2O correlation and discusses how it differs from the CH_2Cl_2-N_2O correlation.

4.3.1 Background mixing ratios of $CHCl_3$

As discussed in Section 1.3 the seasonal cycle of $CHCl_3$ is not as clearly pronounced in NH background air as that of CH_2Cl_2. Figure 4.14 shows both the $CHCl_3$-N_2O correlation (left) and the monthly averaged ground-based $CHCl_3$ measurements of the AGAGE network (right; Prinn et al., 2000, 2018). Vertical lines express the standard deviation of the respective monthly averaged $CHCl_3$ mixing ratios. It has to be mentioned that a comparison of absolute values might not be very accurate due to the currently relatively large uncertainty of absolute $CHCl_3$ mixing ratios of the HAGAR-V MS module (Table E.4).

The AGAGE measurements show a much less pronounced NH seasonality for $CHCl_3$ than for CH_2Cl_2 (Figure 1.3). Nevertheless, a local minimum of monthly averaged mixing ratios in the NH tropics (light blue curve, at Barbados) in September, 2017, is similarly identified for both species. However, the standard deviations of the monthly averaged

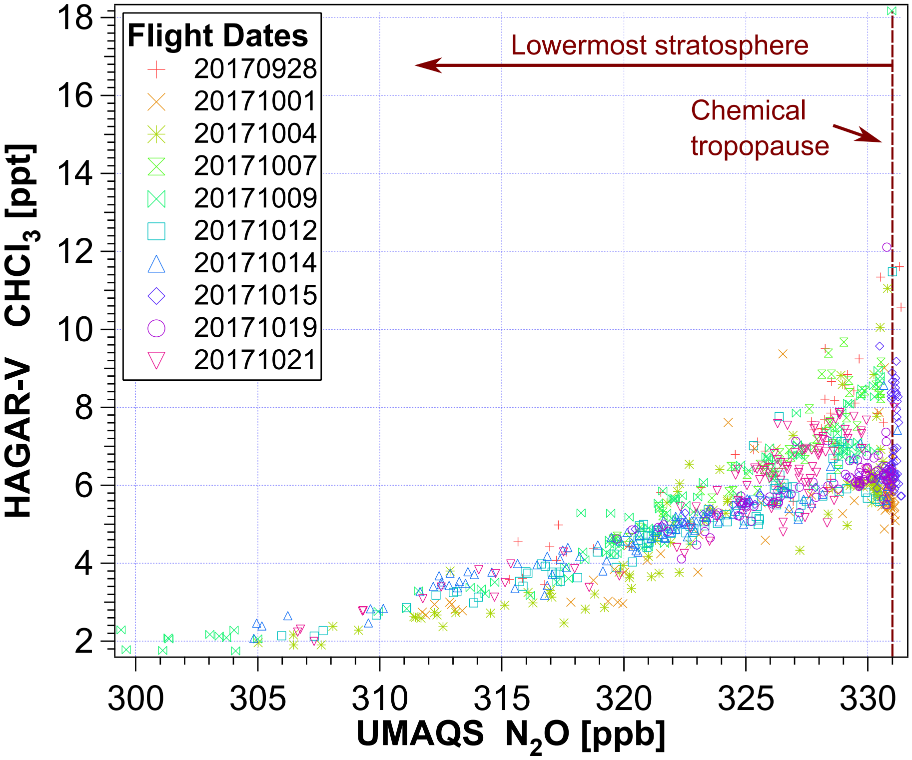

Figure 4.13: $CHCl_3$-N_2O correlation for WISE flights #7–#16 (September, 28 to October, 21 in 2017). The coloration and different symbols represent the individual flights.

$CHCl_3$ mixing ratios are larger than those of CH_2Cl_2 indicating larger variations of $CHCl_3$ background mixing ratios. The AGAGE observatory at Barbados is positioned remote from major anthropogenic Cl-VSLS sources. It can thus be assumed that the relatively large background mixing ratio variations are influenced by natural $CHCl_3$ sources. Natural sources contribute with a much higher fraction to the total $CHCl_3$ emissions (~ 50 %) compared to those of CH_2Cl_2 (~ 10 %; Section 1.3.1).

The analysis of CH_2Cl_2 in the previous sections has shown that WISE measurements at the chemical tropopause contain a large fraction of air parcels released to the free troposphere in September. The correlation displayed in Figure 4.14 shows minimum mixing ratios of $CHCl_3$ above N_2O ~ 329 ppb measured during WISE to decrease for increasing N_2O mixing ratios up to the chemical tropopause at N_2O = 331 ppb. This suggests that the surface seasonality of $CHCl_3$ observed in the tropics is reflected in the LMS, similarly as observed for CH_2Cl_2 (Section 4.2.2). However, the imprint of $CHCl_3$'s seasonality in the LMS is much less pronounced than that of CH_2Cl_2. The seasonal signal of CH_2Cl_2 can be discerned in the correlation down to N_2O ~ 328.5 ppb; the seasonal signal of $CHCl_3$ cannot

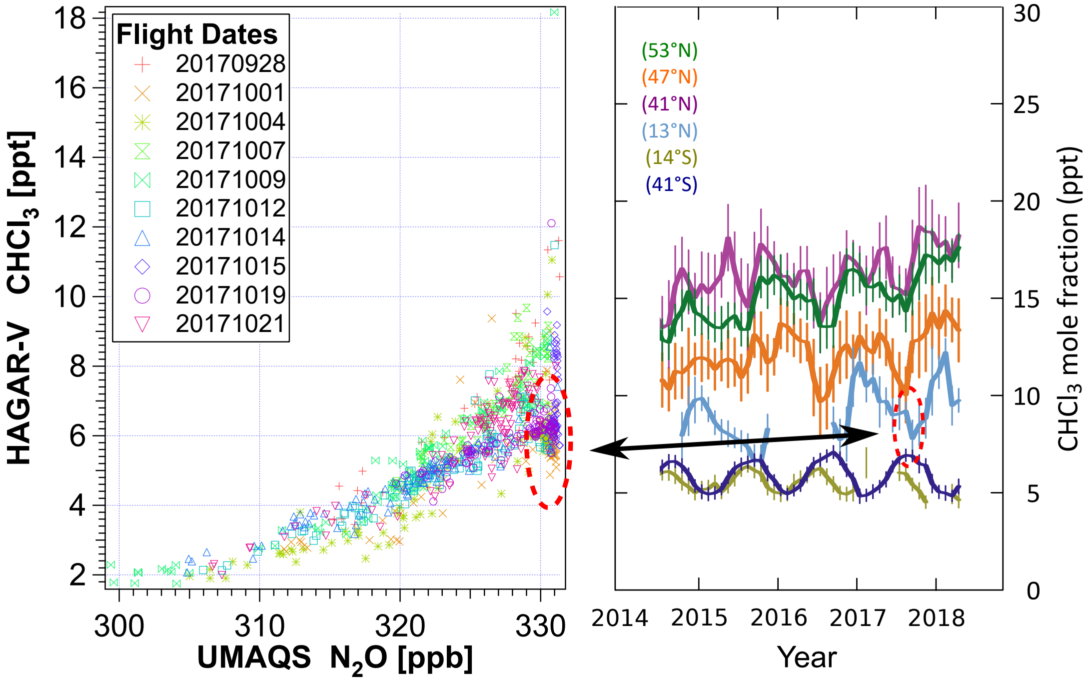

Figure 4.14: $CHCl_3$-N_2O correlation of WISE flights #7–#16 (September, 28 to October, 21 in 2017) (left) and monthly averaged ground-based $CHCl_3$ measurements at different remote locations at different latitudes (41°S to 53°N) of the AGAGE network (right). The vertical lines indicate the respective standard deviation. Tropical NH minimum of $CHCl_3$ mixing ratios is in September 2017. A clear $CHCl_3$ seasonal cycle is only visible in the SH. Minimum $CHCl_3$ mixing ratios measured by HAGAR-V between ~ 329 ppb and ~ 331 ppb N_2O (red dashed ellipse, left panel) reflect the tropical AGAGE measurements at 13°N (red dashed ellipse, right panel, light blue curve). Right panel adapted from http://agage.mit.edu/ (Prinn et al., 2000, 2018).

be discerned below $N_2O \sim$ 329.5 ppb, i.e.it cannot be traced in the LMS as long into the past as the seasonality of CH_2Cl_2. The relatively weaker imprint of the tropical $CHCl_3$ surface seasonality in the LMS and at the chemical tropopause could have two causes: (1) $CHCl_3$ at the tropical surface exhibits a smaller relative decline over the 3 months preceding the September minimum (cf. Figure 1.3 or figures 4.5 and 4.14), which translates into a less pronounced drop of the lower branch of the $CHCl_3$-N_2O correlation in the LMS for N_2O approaching 331 ppb. (2) Given natural sources, $CHCl_3$ likely has larger regional variations between tropical source regions feeding the TTL, which would translate into a less distinctive seasonal signal in the LMS compared to that of CH_2Cl_2. Nevertheless, based on the results of Section 4.2 it is very likely that the WISE measurements of $CHCl_3$ in the UTLS, similarly to CH_2Cl_2, reflect its seasonality in the tropical marine BL.

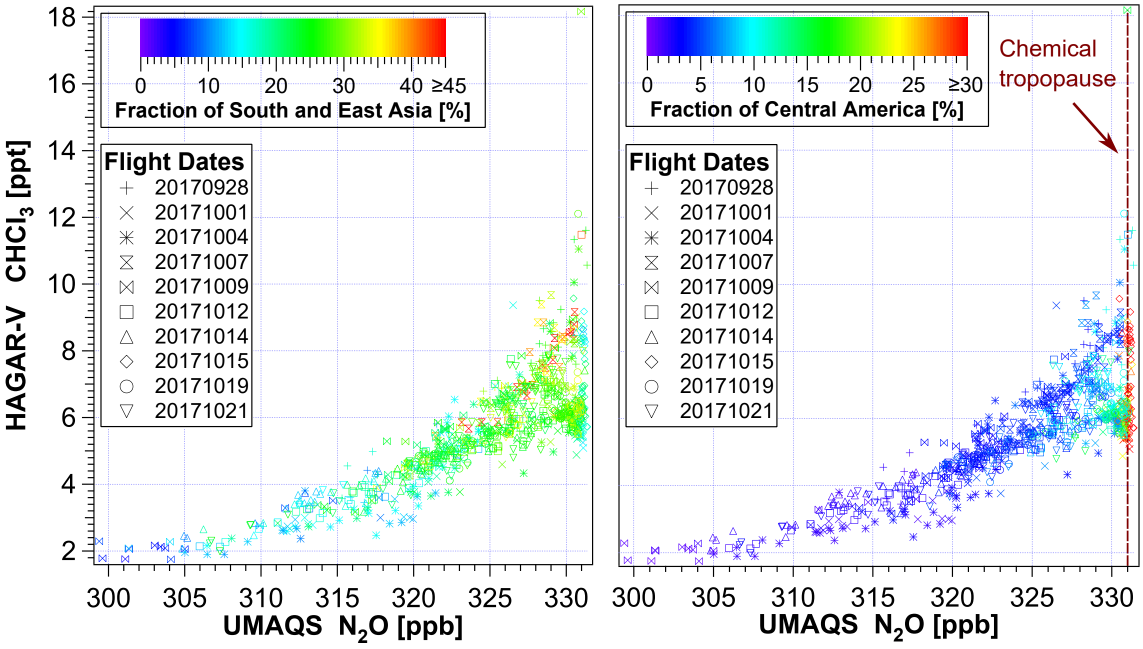

Figure 4.15: $CHCl_3$-N_2O correlation color coded with the Southern and Eastern Asia (SaEA, left) and Central America (CAM, right) emission tracer simulated by CLaMS. The color coding of the SaEA tracer is limited to a maximum of 45 % and that of the CAM tracer to a maximum of 30 %, representing the range of most fractions. The SaEA fraction tends to be elevated for higher $CHCl_3$ mixing ratios at $N_2O > 323$ ppb. The CAM fraction is strongly elevated in the UT and at the chemical tropopause and elevated in the LMS close to the chemical tropopause for lower $CHCl_3$ mixing ratios.

4.3.2 Impact of different source regions

In Section 4.1.2 artificial tracers of air mass origin calculated by CLaMS were introduced. To investigate the origin of air parcels in the less compact part of the $CHCl_3$-N_2O correlation in the UTLS region the different emission tracers were consulted. Figure 4.15 shows the $CHCl_3$-N_2O correlation color coded with the SaEA tracer (left) and the CAM tracer (right). The color scale of the SaEA tracer was limited to 45 % and that of the CAM tracer to 30 % similarly to Section 4.2.3.

According to CLaMS the fraction of air that originated in the source region of the SaEA tracer tends to be larger for air parcels with higher $CHCl_3$ mixing ratios in the less compact part of the $CHCl_3$-N_2O correlation at around $N_2O > 323$ ppb. Air parcels with relatively high $CHCl_3$ mixing ratios can contain fractions of the SaEA tracer of 40 % and higher. The air samples measured in the UT ($N_2O > 331$ ppb) are on average associated with a significantly lower SaEA fraction of (20 ± 6) %[32] for a range of $CHCl_3$ mixing ratios of

---

[32] $n = 47$; median: 19.2 %

about 5–9 ppt. This indicates on the one hand that $CHCl_3$-rich air in the LMS preferably originated in southern and eastern Asia but on the other hand that $CHCl_3$ mixing ratios in the UT in October can be equally high despite a relatively small fraction of air originating in southern and eastern Asia.

The largest fractions of the CAM tracer are associated with the air samples measured at the UT ($N_2O > 331$ ppb, average CAM fraction (32 ± 10) %[33]) for a range of $CHCl_3$ mixing ratios of about 5–9 ppt. The highest stratospheric CAM fractions are preferably associated with the lower $CHCl_3$ mixing ratios close to the chemical tropopause. In particular the $CHCl_3$-poor air reflecting the tropical surface seasonality (Section 4.3.1) contains the largest CAM fractions in the LMS of around 15 %.

In general the emission tracers exhibit similar patterns in the $CHCl_3$-N_2O correlation as those very clearly apparent for the two branches of the CH_2Cl_2-N_2O correlation. The SaEA fraction tends to be higher for $CHCl_3$-rich air while the CAM fraction is clearly higher for $CHCl_3$-poor air in the LMS close to the chemical tropopause. A clear difference to CH_2Cl_2 (where almost all samples in the UT are associated with the lower branch) is that $CHCl_3$ in the UT ranges from the lowest to the highest mixing ratios found in the LMS at $N_2O > 325$ ppb. This indicates that WISE measurements of $CHCl_3$ in the UT cannot be associated with either a particularly weak or a particularly strong $CHCl_3$ emission source region. Hence the data show only that southern and eastern Asia — the major source region of CH_2Cl_2-rich air in the LMS — is an important source region for $CHCl_3$-rich air in the UTLS but not the only one. This result is supported by an analysis of the normalized emission tracers investigating only the fraction of air parcels released to the atmosphere after April 2017 (Appendix G.3). That analysis as well as supplemental plots of the $CHCl_3$-N_2O correlation during WISE are given in Appendix G.

4.3.3 Comparison of $CHCl_3$ and CH_2Cl_2

Figure 4.16a shows the $CHCl_3$-N_2O correlation color coded with the measurements of the upper branch (red) and of the lower branch (blue) with branches defined by CH_2Cl_2 and N_2O in Section 4.2.1. Similar to the CH_2Cl_2-N_2O correlation a clear difference of $CHCl_3$ mixing ratios is visible between the measurements of the different branches. Measurements of CH_2Cl_2-rich air (upper branch) also contain $CHCl_3$-rich air. Unlike for CH_2Cl_2, most of these measurements of $CHCl_3$-rich air are not significantly higher than elevated $CHCl_3$ mixing ratios in measurements between the two correlation branches (gray data points in Figure 4.16). This indicates that the dominant source regions of CH_2Cl_2-rich air in the LMS

---

[33] n = 47; median: 31.8

are not the only source regions of $CHCl_3$-rich air in the LMS. Similarly to the CH_2Cl_2-N_2O correlation, the lower branch marks only measurements of $CHCl_3$-poor air, except for the measurements in the UT and at the chemical tropopause, which (unlike for CH_2Cl_2) also include samples of relatively $CHCl_3$-rich air. This suggests different CH_2Cl_2 and $CHCl_3$ sources effecting these air parcels. Without any large anthropogenic emission source known to be located in the main source regions of air of the lower branch (western part of the ITCZ; sections 1.3.2, 4.2.3, and 4.2.5) it is plausible that this relative difference between source strengths CH_2Cl_2 and $CHCl_3$ visible in the UT and at the chemical tropopause is due to the impact of natural sources. However, based on the given data this is only speculative.

Figure 4.16b shows a potential temperature-$CHCl_3$ scatter plot color coded with the two correlation branches. In this plot measurements of the lower branch (blue) are barely distinguishable from the data between the two branches (gray). The measurements of the lower branch are distributed between 345 K and 380 K with relatively constant $CHCl_3$ mixing ratios of $\sim$ 6 ppt. In contrast, most of the measurements of the upper branch (red) clearly stand out with elevated $CHCl_3$ mixing ratios at a potential temperature range between 370 K and 385 K. Figure 4.16b emphasizes the impact of $CHCl_3$-rich air from southern and eastern Asia on the LMS at around 380 K (although, this impact is somewhat weaker than in the case of CH_2Cl_2, cf. Figure 4.4).

Figure 4.17 (left) shows the $CHCl_3$-CH_2Cl_2 correlation of WISE measurements for data of the upper branch only. The two species correlate well in the upper branch with a Pearson's correlation coefficient $R = 0.84$. This suggests that upper branch measurements of CH_2Cl_2 and $CHCl_3$ were mostly effected by sources with relatively similar emission release ratios of the two species. Thus, for measurements of the upper branch a significant number of $CHCl_3$ and CH_2Cl_2 sources can be expected to emit both $CHCl_3$ and CH_2Cl_2. CH_2Cl_2 is almost exclusively emitted by anthropogenic sources (Section 1.3.1). Hence upper branch measurements of CH_2Cl_2-rich air are most likely of industrial anthropogenic origin and the significant correlation with $CHCl_3$ suggests that at least in parts this holds also for $CHCl_3$. Further, if measurements of the upper branch are dominated by anthropogenic emission sources, these sources do not exclusively dominate the distribution of $CHCl_3$-rich air in the LMS. This is particularly of interest because the upper branch's main source region (southern and eastern Asia) is also known for the worlds largest anthropogenic $CHCl_3$ emissions (Section 1.3.2). This implies that natural $CHCl_3$ sources could also have a significant impact on the distribution of $CHCl_3$-rich air in the LMS. This would support the current state of knowledge that a large fraction of global $CHCl_3$ emissions has natural

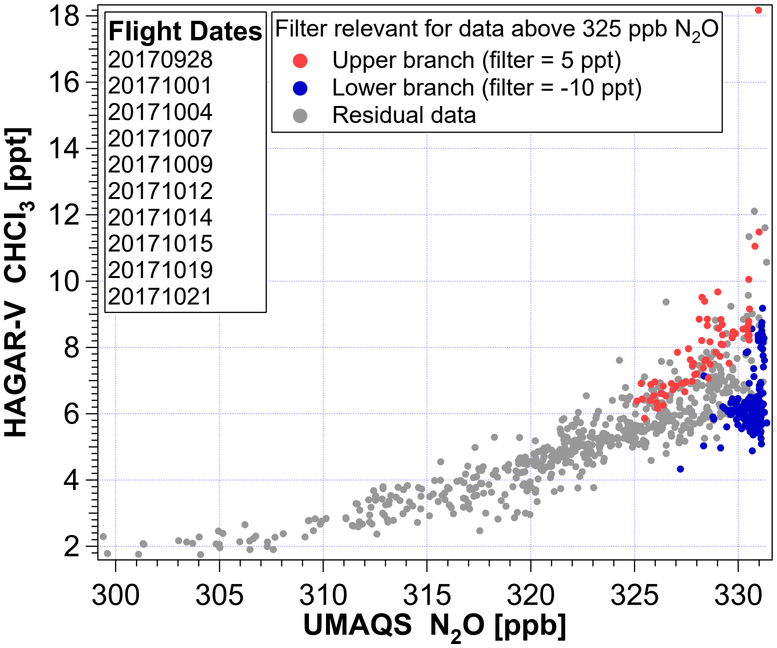

(a)

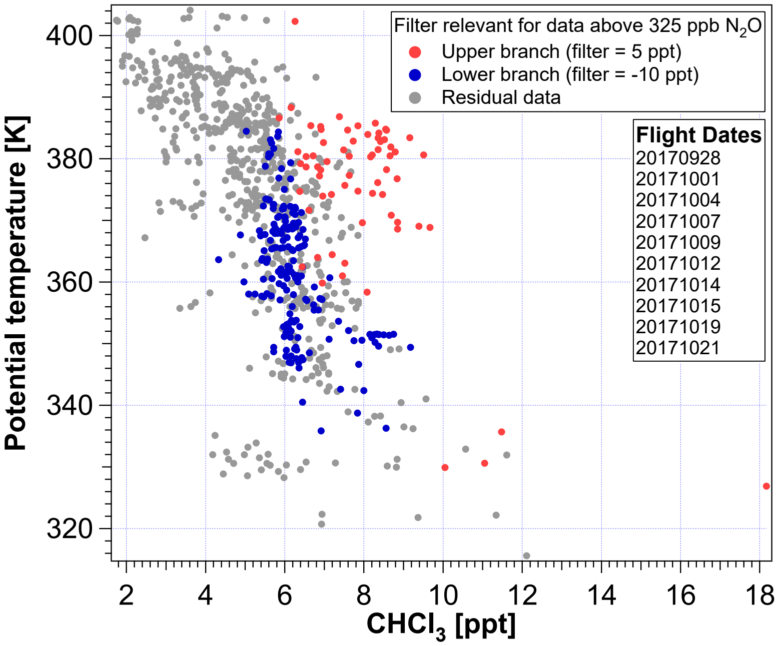

(b)

Figure 4.16: (a) CHCl$_3$-N$_2$O correlation during WISE marked with the branch filter introduced in Section 4.2.1. (b) Potential temperature-CHCl$_3$scatter plot color coded with the branch filter. Measurements of the upper branch are marked in red and those of the lower branch in blue. Measurements not associated with either of the branches are marked in gray.

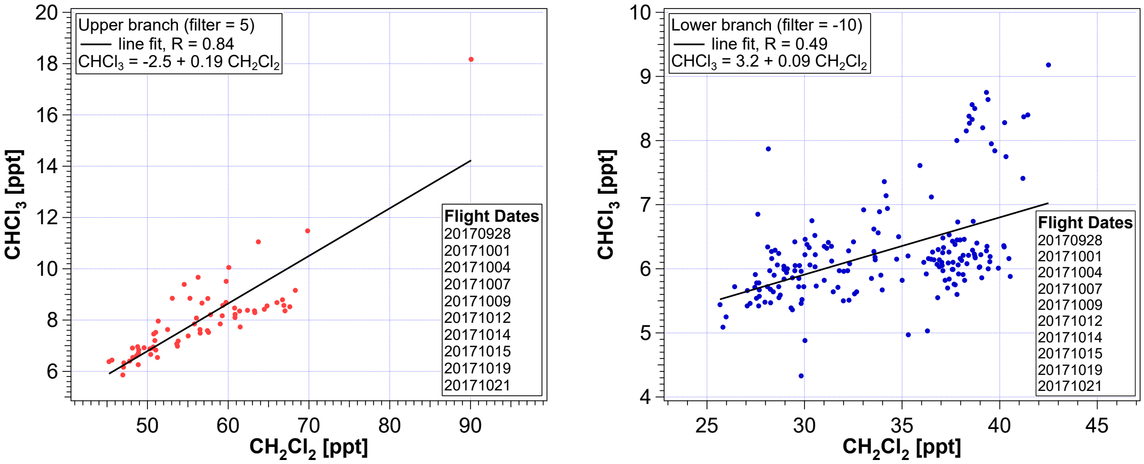

Figure 4.17: $CHCl_3$-CH_2Cl_2 correlation of measurements of the upper branch (left) and of the lower branch (right). A line fit is applied to each data set resulting in different Pearson's correlation coefficients. R = 0.84 (upper branch) and R = 0.49 (lower branch).

sources (~ 50 %; Section 1.3.1). The $CHCl_3$-CH_2Cl_2 correlation of emission plumes of major population centers in East Asia is further discussed in Section 4.4.

Figure 4.17 (right) shows the $CHCl_3$-CH_2Cl_2 correlation of WISE measurements using only data of the lower branch. The correlation is relatively weak with a Pearson's correlation coefficient R = 0.49. This suggests that the air of the lower branch is influenced by different emission sources with different emission ratios of $CHCl_3$ and CH_2Cl_2. The source regions of air parcels of the lower branch are distributed along the western part of the ITCZ (Section 4.2.5), thus a large variety of different emission sources is likely. This also implies that a large fraction of the lower branch originated above sea water where it was likely impacted by natural sources[34]. The oceans contribute about half of the natural $CHCl_3$ emissions (~ 25 % of total emissions; e.g. McCulloch, 2003) and provide only insignificant CH_2Cl_2 releases (Section 1.3.1). The impact of natural sources might thus be part of the explanation for the relatively weak correlation between the two species for air of the lower branch.

4.3.4 Impact of hurricane Maria

Several of the air parcels measured during WISE (mainly associated with the lower branch) were transported to the UTLS by the updraft of hurricane Maria (Section 4.2.6). Figure 4.18 shows the $CHCl_3$-N_2O correlation with different symbols marking the different flights

---

[34] Natural $CHCl_3$ emission sources above land contribute equally to the total $CHCl_3$ emissions as sources from above the sea (e.g. McCulloch, 2003) but are not as easy to distinguish from anthropogenic sources

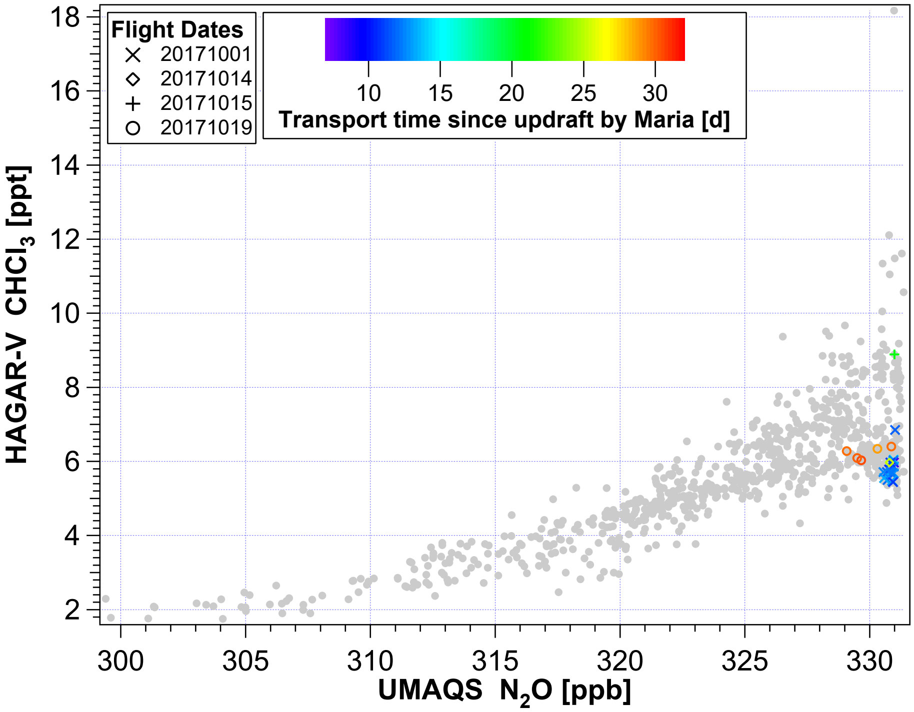

Figure 4.18: CHCl$_3$-N$_2$O correlation with different symbols marking the different WISE flights and measurements that have been transported by hurricane Maria. The color indicates the respective transport times from the location of max. $\dot{\Theta}$ (Section 4.2.6) to the position of measurement.

and color coded with the transport time from the location of max. $\dot{\Theta}$ along the trajectory to the position of measurement; marked in gray are the air parcels which were not uplifted by hurricane Maria (cf. Section 4.2.6). Similar to the observations of CH$_2$Cl$_2$, the majority of air parcels transported by hurricane Maria were CHCl$_3$-poor air. Hence, hurricane Maria could be identified to have acted as a convective source of transport into the UTLS of both CH$_2$Cl$_2$-poor and CHCl$_3$-poor air probed during WISE.

Similar to the results of Section 4.2.6 air parcels associated with uplift by hurricane Maria tend to contain higher CHCl$_3$ mixing ratios with increasing residence time in the atmosphere. However, for CHCl$_3$ this is not as clear as for CH$_2$Cl$_2$. This could be due to the larger variations of CHCl$_3$ background mixing ratios and the comparably more compact CHCl$_3$-N$_2$O correlation at high N$_2$O mixing ratios (cf. Section 4.3.1). Supporting information for this analysis is given in Appendix G.4

4.4 CH_2Cl_2 and $CHCl_3$ measurements around major population centers in East Asia

Another instrument of the atmospheric physics group of the University of Wuppertal that has flown on HALO is the whole air sampler MIRAH (Measurements of Stable Carbon Isotope Ratios aboard HALO). A detailed description of MIRAH and the processing of the whole air samples used in this section is given in Appendix I.1. Among others, MIRAH was deployed on HALO for the EMeRGE–Asia[35] mission. This mission was aimed at the experimental investigation of plumes from major population centers to understand transport and transformation patterns of pollution from Asian conurbations[36]. During March and April 2018 MIRAH collected a total of 133 air samples during 12 scientific flights in Asia, starting from Tainan, Taiwan. In addition, on seven days at the end of March 2018 a total of 18 canisters were filled with air on the ground in Manila, Philippines, and Taipeh, Taiwan. Figure 4.19 shows the averaged sampling locations of each canister color coded with the averaged flight altitude during the sampling process (circles) as well as the ground-based sampling positions (crosses). In-flight samples were mostly obtained in the BL and lower troposphere. Note that several samples were obtained at the same location but at different altitudes, therefore they overlap and cannot be separated in Figure 4.19.

The whole air samples of MIRAH were analyzed for CH_2Cl_2 and $CHCl_3$ by the use of a rather irregular processing method (for details see Appendix I) resulting in measurement precisions of 12.8 ppt and 2.4 ppt, respectively (~ 22 % of tropospheric background air CAL, Table E.2). Despite the relatively imprecise measurements the data extracted from the EMeRGE–Asia canisters still provide a very useful impression of emission sources from East Asia as part of the main source region of particularly CH_2Cl_2-rich air observed in the LMS during WISE.

Figure 4.20 shows the $CHCl_3$-CH_2Cl_2 correlation from all whole air samples (ground-based and in-flight) collected during EMeRGE–Asia. The coloration indicates the averaged altitude of the respective sampling position and is limited to a maximum of 5000 m. A Pearson's correlation coefficient R = 0.82 shows a clear $CHCl_3$-CH_2Cl_2 correlation for the EMeRGE–Asia whole air samples. This suggests these samples share some similar CH_2Cl_2 and $CHCl_3$ sources or source locations. In addition, the air of the collected samples very likely is dominated by anthropogenic sources due to the specific sampling of emission

---

[35] Effect of Megacities on the transport and transformation of pollutants on the Regional and Global scales – in Asia

[36] http://www.iup.uni-bremen.de/emerge/home/home.html

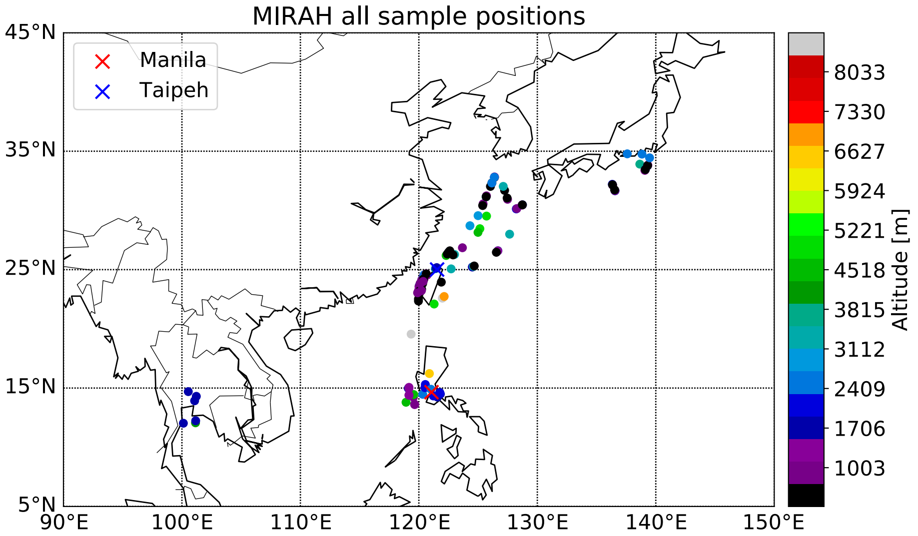

Figure 4.19: Averaged locations of flask sampling from MIRAH during EMeRGE–Asia color coded by the average altitude of the aircraft during each sample procedure. The crosses mark the locations of air sampling on ground in Manila (red) and Taipeh (blue). Note that several samples were obtained at the same location but at different altitudes.

plumes from major population centers during EMeRGE–Asia. This is also suggested by the clear correlation of the mainly anthropogenic tracer CH_2Cl_2 with the only partly anthropogenic tracer $CHCl_3$ (Section 1.3.1) in combination with significantly higher mixing ratios than observed on average in the NH BL by the AGAGE network (cf. Figure 1.3).

$CHCl_3$ and CH_2Cl_2 mixing ratios for the EMeRGE–Asia whole air samples are equally well correlated as WISE measurements associated to the upper branch in the LMS (Section 4.16). Fittingly, WISE measurements of the upper branch mainly originated in southern and eastern Asia while other WISE measurements show stronger influences of different source regions (Section 4.2.3 and 4.2.5). Hence, the air samples from EMeRGE–Asia and the WISE measurements of the upper branch are very likely compatible, making it plausible to assume they share similar source origins.

The average CH_2Cl_2 and $CHCl_3$ mixing ratios sampled below 2000 m (~ BL) during EMeRGE–Asia are 148.6 ppt and 21.9 ppt, respectively. These mixing ratios are clearly higher than the average NH measurements of the AGAGE network in spring (conservatively approximated: CH_2Cl_2 ~ 70 ppt and $CHCl_3$ ~ 15 ppt). Hence, the CH_2Cl_2 mixing ratios of EMeRGE–Asia are much more enhanced relative to NH AGAGE measurements than those of $CHCl_3$ (approximately elevated by ~ 115 % and ~ 50 %, respectively). This indicates relatively larger CH_2Cl_2 sources than $CHCl_3$ sources in the sampling region of EMeRGE–Asia compared to the vicinity of the NH AGAGE measurement stations. Com-

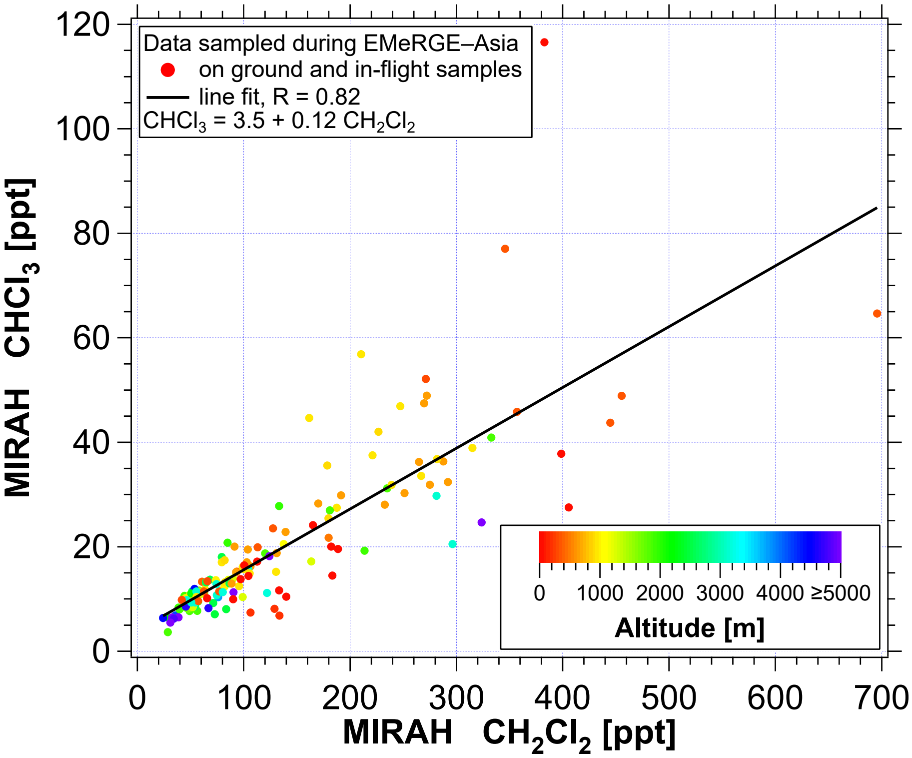

Figure 4.20: $CHCl_3$-CH_2Cl_2 correlation from whole air samples collected by MIRAH on the EMeRGE–Asia mission in April and March 2018 in East Asia. The colors indicate the averaged altitude of the aircraft during the sampling procedure. The color scale is limited to 5000 m. A linear fit (black line) shows a significant correlation between the two species.

parably high CH_2Cl_2 and $CHCl_3$ mixing ratios slightly less well correlated (R = 0.71) as observed during EMeRGE–Asia were measured by Say et al. (2019) in the Indian BL in June and July 2016. Thus, combining the two results from South Asia (Say et al., 2019) and East Asia (this study) it can be assumed that the relatively weaker enhancement over the NH background of $CHCl_3$ compared to that of CH_2Cl_2 holds for most anthropogenic emission sources in southern and eastern Asia. This could provide an explanation for the less pronounced enhancement of $CHCl_3$ compared to CH_2Cl_2 for WISE measurements originating in southern and eastern Asia (upper branch, Section 4.16).

The average CH_2Cl_2 and $CHCl_3$ mixing ratios sampled in the BL during EMeRGE–Asia are most likely not representative as average BL mixing ratios in southern and eastern Asia. However, to derive a plausibility assessment from EMeRGE–Asia air samples to link air masses from southern and eastern Asia to the measurements of the upper branch, the $CHCl_3$-CH_2Cl_2 correlation slopes are analyzed. The relative source strength of $CHCl_3$ and CH_2Cl_2 in EMeRGE–Asia air samples is expressed by their correlation slope (cf. Figure

4.20). The comparable results from India (Say et al., 2019) and East Asia (this study) lead to the assumption of a similar ratio of source strengths of $CHCl_3$ and CH_2Cl_2 throughout the region of southern and eastern Asia. This implies mixing of air within the southern and eastern Asia BL results in $CHCl_3$ and CH_2Cl_2 mixing ratios along the correlation slope derived from EMeRGE–Asia air samples, including the average mixing ratios in the BL. Within the ASMA air from the southern and eastern Asian BL is further diluted by mixing[37]. It can thus be assumed that on average mixing in the ASMA yields average Asian BL mixing ratios somewhere along the correlation slope derived from EMeRGE–Asia. Within the LMS air parcels from the ASMA primarily mix with air from the overworld (cf. Section 1.1). Thus, primarily air from the overworld could potentially change the $CHCl_3$-CH_2Cl_2 correlation slope of air parcels from southern and eastern Asia. The $CHCl_3$-CH_2Cl_2 correlation slopes from the upper branch (CH_2Cl_2-rich air) and from EMeRGE–Asia are comparable (1.9 vs 1.2, respectively, cf. figures 4.17 (left) and 4.20). This implies two things: (1) the $CHCl_3$-CH_2Cl_2 ratio of air of the overworld is similar to Asian sources or both species are zero in overworld air; (2) the $CHCl_3$-CH_2Cl_2 correlation from southern and eastern Asia is conserved during the transport from the source region into the LMS.

In addition to the assumptions derived from the EMeRGE–Asia whole air samples more profound understanding can be gained by further investigations. Processing the IRMS data instead of the MS data (cf. Appendix I) could provide more precise results and eventually change the correlation coefficient to provide a stronger link between the two Cl-VSLS's sources. This could be further supported with an analysis of backward trajectories of the EMeRGE–Asia samples. In addition, a comparison between the samples collected during EMeRGE–Asia and EMeRGE–Europe could help to assess on source differences between East Asian and European major population centers. These further investigations could also support the interpretation of the less enhanced southern and eastern Asian influence on stratospheric $CHCl_3$ compared to that on CH_2Cl_2 observed during WISE. Supplemental figures with data from EMeRGE–Asia are given in Appendix I.

4.5 Summary

HAGAR-V measurements of CH_2Cl_2 in the UTLS above Europe and the Atlantic Ocean during the WISE mission in autumn 2017 reveal two distinct entries of either CH_2Cl_2-poor or CH_2Cl_2-rich air when correlated with the long-lived tracer N_2O. Air samples with the

---

[37] Chemical reduction of the short-lived $CHCl_3$ and CH_2Cl_2 (lifetime of 168 days, Hossaini et al., 2019) most likely is insignificant due to the comparably fast transport from the Asian BL into the NH LMS (~ 66 days, cf. 4.2.5)

same N_2O mixing ratios can differ by up to 130 % in CH_2Cl_2 mixing ratios. A detailed analysis, using CLaMS tracer simulations and 120 day backward trajectory calculations, and observations within the BL, showed that these two different air masses entered the LMS on two different transport pathways.

The CH_2Cl_2-poor air reflects the tropical CH_2Cl_2 surface seasonality, including the September minimum, indicating little influence of anthropogenic emission sources. Artificial tracers of air mass origin showed that the largest fraction of this CH_2Cl_2-poor air (on average ~ 45 %) originated mainly at the BL above Central America and along the western part of the ITCZ (180°W to ~ 45°E) — a primarily maritime region without significant CH_2Cl_2 sources. In NH summer, CH_2Cl_2-poor air masses from that region enter the LMS up to potential temperature levels of about 380 K. However, the majority of CH_2Cl_2-poor air was observed between ~ 345 K and ~ 375 K. The analysis of 120 day backward trajectories showed that the CH_2Cl_2-poor air was convectively uplifted above the region of Central America into the TTL approximately to the same potential temperature level at which it was observed later in the UTLS during WISE. The convection above Central America is relatively fast with average ascent rates $\dot{\Theta} = 24$ K/18 h according to the trajectories. In addition to the general convection above the region of Central America caused by low pressure systems of the American monsoon, the large-scale hurricane Maria could be directly identified as a significant driver of transport of CH_2Cl_2-poor air into the NH LMS. The CH_2Cl_2-poor air crosses the subtropical jet stream north of the convection zone above Central America to enter the UTLS in the extratropics on a relatively direct path. Thus, the transport time from the BL source region along the western ITCZ into the NH UTLS of CH_2Cl_2-poor air is relatively short (on average ~ 30 days, primarily ranging from one week to two months).

The CH_2Cl_2-rich air observed in the NH LMS is mainly impacted by large anthropogenic emission sources. The largest fraction of CH_2Cl_2-rich air (on average 35 %) originated in the region of southern and eastern Asia, including the regions of India, China, and Southeast Asia which are known for extraordinarily high CH_2Cl_2 emissions (e.g. Leedham-Elvidge et al., 2015; Oram et al., 2017; Feng et al., 2018; Say et al., 2019). The 120 day backward trajectories showed that all sampled CH_2Cl_2-rich air is uplifted above southern and eastern Asia by low pressure systems of the ASM to potential temperature levels of about 360 K. The average ascent rate over southern and eastern Asia ($\dot{\Theta} = 18$ K/18 h) is smaller than that above Central America. However, the CH_2Cl_2-rich air is caught by the ASMA to slowly spiral upwards to higher potential temperature levels of ~ 380 K from where it escapes the ASMA eastwards following the subtropical jet stream. CH_2Cl_2-rich air can circle around the globe for a few times along the jet stream before crossing it northwards above the eastern Pacific or western Atlantic Ocean entering the extratropics. On average this transport into the NH LMS takes about two months. This is still fast enough for the short-lived CH_2Cl_2 (lifetime of ~ 168 days, Hossaini et al., 2019) to enter the NH LMS with up to 130 % higher mixing ratios than CH_2Cl_2-poor background air from the western ITCZ. In NH summer the larger part of the upper NH LMS is dominated by tropospheric intrusions and in-mixing of young (< 6 months) CH_2Cl_2-rich air from southern and eastern Asia (fraction ≥ 50 %), thereby significantly enhancing CH_2Cl_2 mixing ratios in the LMS. The key factor for this strong impact of CH_2Cl_2-rich air on the NH LMS is the uplift by the ASMA. No other convective system uplifts air masses to potential temperatures as high as the ASMA which provides the perfect basis for tropospheric intrusions of CH_2Cl_2-rich air into the stratosphere.

The analysis of another Cl-VSLS, $CHCl_3$, revealed similarities to the findings of the CH_2Cl_2 analysis. The much less pronounced (compared to CH_2Cl_2) seasonality of $CHCl_3$ is reflected in measurements of $CHCl_3$-poor air in the LMS close to the tropopause. It is concluded that in the LMS the CH_2Cl_2-poor air from the western ITCZ also contains $CHCl_3$-poor air, indicating small impacts of anthropogenic and natural sources. However, measurements of CH_2Cl_2-poor air in the UT partly contain $CHCl_3$-rich air. Thus, the correlation of CH_2Cl_2-poor air with $CHCl_3$ is relatively weak ($R = 0.49$), suggesting different sources. Here, the impact of natural oceanic $CHCl_3$ sources is suspected (oceanic sources contribute ~ 25 % to the total $CHCl_3$ emissions, CH_2Cl_2 has no significant oceanic sources).

The samples of CH_2Cl_2-rich air also contain $CHCl_3$-rich air with mixing ratios elevated abve those of the majority of measurements at the same potential temperature and/or the same N_2O mixing ratios. However, in contrast to CH_2Cl_2 theses are not the only samples of $CHCl_3$-rich air in the LMS. This implies two things: on the one hand, sources of $CHCl_3$ located in southern and eastern Asia have a significant but relatively less prominent impact on the NH LMS than those of CH_2Cl_2-rich air; on the other hand other sources of $CHCl_3$ have a relatively stronger impact on the composition of the NH LMS than those of CH_2Cl_2 for the same measurements. Thus, the WISE measurements suggest that sources of $CHCl_3$ are wider spread around the globe but weaker than the Asian sources of CH_2Cl_2. However, WISE measurements of CH_2Cl_2-rich air originating in southern and eastern Asia correlate well with $CHCl_3$ ($R = 0.84$), suggesting similar and industrial sources. A plausibility assessment comparing relative $CHCl_3$ and CH_2Cl_2 source strengths from East Asia with measurements from WISE showed good agreement, emphasizing the influence of anthropogenic Asian sources on the CH_2Cl_2-rich air observed in the LMS during WISE.

Chapter 5

Synopsis and outlook

5.1 Synopsis

In the order to investigate the two major Cl-VSLS the MS module of the airborne instrument HAGAR-V was successfully modified. Thereby the focus was laid on achieving high measurement frequency to benefit the analysis of transport and mixing processes using HAGAR-V MS measurements. Airborne real-time measurements of Cl-VSLS in the UTLS are very complex to achieve and thus extremely rare. To this day HAGAR-V has produced a unique data set of Cl-VSLS measurements in the UTLS during two successful aircraft missions (WISE in 2017 and SouthTRAC[1] in 2019). Key element for this success was the development of a novel sample preconcentration system and of fast-ramping temperature controlled GC column ovens presented in this work.

After the WISE mission the MS module has been further adapted to increase the number of measured species. The use of a single strong adsorbent was changed to a dual-adsorbent trap which strongly reduced the risk of memory effects. In addition, the focus of the MS channel presented in this work is currently shifting more towards the measurement of VOC to avoid chemical reduction of some chlorine containing species within the Al_2O_3 column. The second channel currently uses the adsorbent HayeSep D (Supelco) combined with two DB-624 columns (Agilent J&W) to measure several halogenated species. During the SouthTRAC campaign the MS module for the first time successfully measured 25 different species (CFCs, HCFCs, HFCs, halocarbons, and VOCs) with a time resolution of 2–4 minutes by running both MS channels anticyclically. Thereby HAGAR-V is contributing

---

[1] Transport and Composition of the Southern Hemisphere UTLS

to fill large gaps of airborne trace gas observations in the UTLS thus providing a unique basis for atmospheric investigations.

The processing of the first airborne HAGAR-V MS measurements and the various in-flight diagnostic modes provided very good control of data quality. It could be shown that in general instrumental characteristics are best determined at in-flight conditions but the use of regular in-flight blank gas measurements can have a disturbing influence on some measurements. Therefore, and to maximize the number of measured air samples, during the SouthTRAC campaign the in-flight diagnostic modes were reduced to the most necessary ones as determined in the present work, e.g. blank gas was only measured by the MS module before takeoff and after landing. In addition, the peak EMG fitting function introduced in this work was established to also be used for tailing peaks of the ECD module, thereby increasing the respective species' measurement precision. Together with the new in-flight calibration methods specifically developed for the processing of HAGAR-V MS data, the NOAHChrom processing package now can be used universally for the processing of measurements of all HAGAR-V GC modules.

Airborne in situ measurements of CH_2Cl_2 in the LMS are extremely rare and mainly model based studies have predicted a threat to stratospheric ozone by increasing CH_2Cl_2 mixing ratios in the stratosphere (e.g. Hossaini et al., 2015a). Based on observations of greenhouse gases and pollutants transported from the Asian BL into the LMS via the ASM (e.g. Vogel et al., 2016; Müller et al., 2016; Rolf et al., 2018; Lelieveld et al., 2018), it was assumed that this pathway similarly transports CH_2Cl_2 from Asia into the LMS. The analysis of HAGAR-V in situ CH_2Cl_2 measurements have provided the first observational evidence of two distinct transport pathways of CH_2Cl_2 into the NH UTLS in summer. In the present work it could be confirmed that the ASM is the main driver for the transport of CH_2Cl_2-rich air from southern and eastern Asia into the LMS. It could also be shown that this transport pathway has indeed a significant influence on the distribution of stratospheric CH_2Cl_2 up to at least 385 K potential temperature. It can thus be concluded that despite its short lifetime, due to the fast transport during the annual ASM season anthropogenic emissions of CH_2Cl_2 in southern and eastern Asia contribute to the destruction of stratospheric ozone (Claxton et al., 2019) and thus impact the greenhouse gas distribution in the LMS. Therefore, rising CH_2Cl_2 emissions in southern and eastern Asia indirectly also impact surface climate (Riese et al., 2012).

The second transport pathway determined in the present work involves the uplift by hurricanes in the larger region of Central America, which adds to uplift by regular regional convection in summer usually referred to as the North American monsoon. This trans-

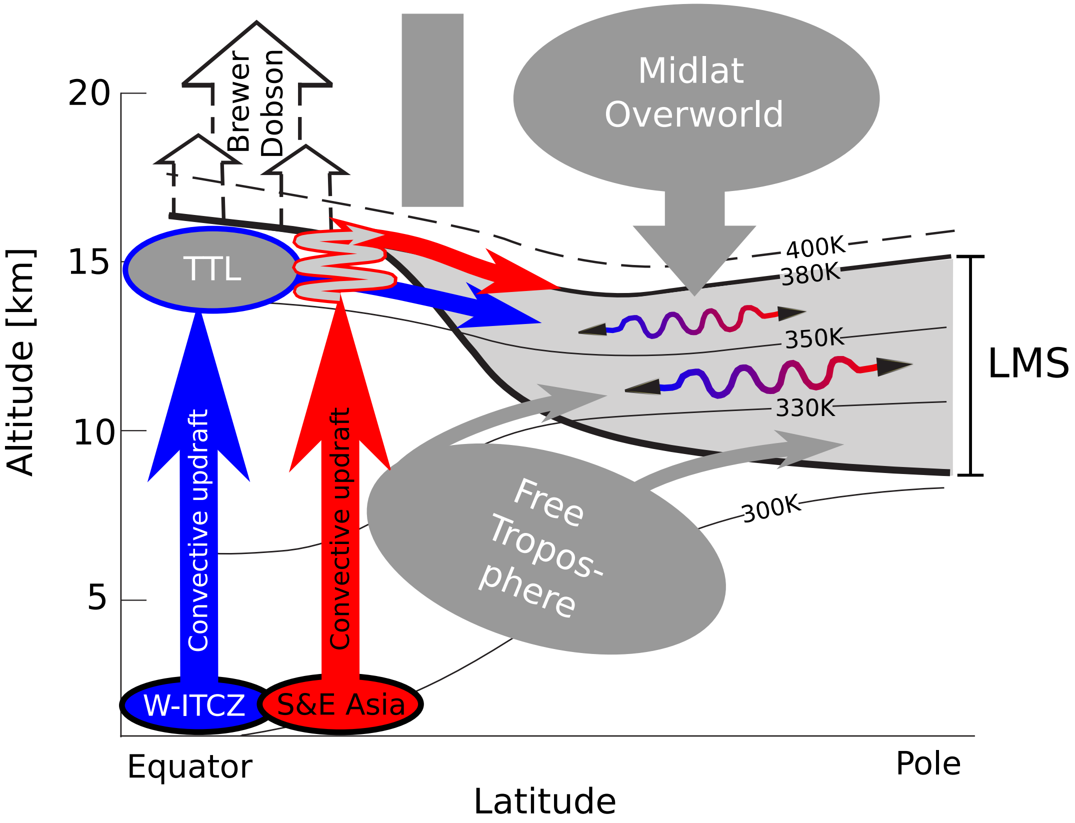

Figure 5.1: Schematic drawing of the two distinct transport pathways into the NH LMS in summer derived from HAGAR-V CH_2Cl_2 measurements during WISE. Convective updraft in the western part of the ITCZ includes a significant contribution by hurricanes above the region of Central America and the North American monsoon. This transport pathway primarily contributes with background air from the MBL to the composition of the UTLS in NH summer. Convective updraft above southern and eastern Asia is mainly driven by the ASM low pressure systems and is followed by slow upwelling within the ASMA above 360 K potential temperature. Air masses from this particular transport pathway were observed to contribute significantly to the composition of the upper NH LMS. In addition, the ASM is the main transport agent for CH_2Cl_2-rich air (up to 130 % larger mixing ratios than measured in CH_2Cl_2-poor air) into the NH LMS. Background of panel adapted from Holton et al. (1995).

port pathway into the LMS has not been fully analyzed and described before. Previous studies have concerned the North American monsoon and have usually investigated the uplift from a region north of 15°N and above potential temperature levels of 360 K (e.g. Nützel et al., 2019; Yan et al., 2019). The present study describes for the first time an efficient transport pathway of CH_2Cl_2-poor air into the LMS via convection in the region of Central America based on in situ observations and backward trajectory calculations down to the BL. CH_2Cl_2-poor air from this region mainly affects a somewhat lower layer of the LMS, centered at potential temperature of ~ 360 K and thus below the main entry level of

CH_2Cl_2-rich air from southern and eastern Asia. Hence, the impact of young CH_2Cl_2-poor air is weak in the highest layer of the LMS, which remains dominated by CH_2Cl_2-rich air from Asia, emphasizing the significance of the ASMA as an agent for efficient transport of polluted air from Asian source regions into the upper LMS.

Measurements of $CHCl_3$ are consistent with the above conclusions, although the enhancements in mixing ratios of air transported from southern and eastern Asia via the ASMA into the NH LMS were less drastic than for CH_2Cl_2. However, the impact of $CHCl_3$-rich air in the NH LMS originating in southern and eastern Asia could become more substantial if Asian $CHCl_3$ emissions continue to rise (e.g. Fang et al., 2018).

To summarize the main results of the present work Figure 5.1 shows a schematic drawing of the two identified transport pathways into the NH LMS during summer.The preferred transport pathway of CH_2Cl_2-poor air from the ITCZ into the NH LMS during WISE is shown in blue. Indicated in red is the transport pathway via the ASMA of CH_2Cl_2-rich air sampled in the LMS during WISE. Due to the additional slow ascent within the ASMA in the UT the CH_2Cl_2-rich air from southern and eastern Asia (red) preferably enters the LMS at higher potential temperature levels than the mainly CH_2Cl_2-poor air (blue) uplifted above the region of Central America.

5.2 Outlook

To this day, the HAGAR-V MS module has already shown its efficiently fast and precise measurements from aboard HALO during more than 280 flight hours. However, further modifications are recommended to further improve the performance of the HAGAR-V MS module. The most important improvement concerns the lifetime of the preconcentration traps. Due to the thin (0.125 mm in diameter) and fragile heating wire the continuous use with extreme temperature changes quickly wears the trap construct. On average a preconcentration trap in the current built lasts for about 10 flights before destruction. Changing a preconcentration trap during a campaign is paired with technical effort and a potential impact on the measurement procedure in addition to loss of data when the trap dies during flight. Thus, changing the trap design to achieve a longer lifetime without loosing any benefit of the current model is one important project for the near future.

MS module measurements during WISE were performed only at low ambient water vapor concentrations due to inefficient sample dehydration. Thus, most measurements in the free troposphere (~ 10 % of a flight) could not be used for scientific analysis. During SouthTRAC regular magnesium perchlorate was used instead of its prehydrated form to efficiently dehydrate the air samples. Performing MS measurements from takeoff to landing is now possible without varying water vapor content affecting the air samples. However, with a rising number of measured species, ad- and desorbing effects of the water trap have to be carefully characterized. In particular the measurements of VOC could be affected by magnesium perchlorate. Laboratory tests investigating the influence of the water trap on the target species have to be performed in addition to the regular in-flight diagnostics already included in HAGAR-V by using the "to-pump" mode.

Regarding data analysis, backward trajectories could directly link HAGAR-V measurements of CH_2Cl_2-poor and $CHCl_3$-poor air to the convective updraft of a major hurricane. The backward trajectories of HAGAR-V WISE measurements were investigated for coincidences in time and space with other hurricanes or typhoons but none could be verified with confidence. However, it would benefit the understanding of the derived transport pathways into the LMS, if further major convective events associated with these pathways, e.g. tropical cyclones, could be identified. The backward trajectories presented in this work were calculated on the basis of ECMWF ERA-Interim reanalysis data. It was shown that the use of the next generation of ECMWF reanalysis data, ERA5, can yield different and much more precise results able to better resolve convection by tropical cyclones (e.g. Li et al., 2020). Reviewing the backward trajectories connected to the HAGAR-V CH_2Cl_2 measurements on the basis of ERA5 reanalysis data could give additional insight on the impact of hurricanes and typhoons on the distribution of CH_2Cl_2 in the LMS.

The results of the present work have emphasized the importance of monitoring CH_2Cl_2 not only via ground-based observations, but also with frequent airborne measurements in order to derive present and future trends of stratospheric CH_2Cl_2. An upcoming HALO campaign (PHILEAS[2], scheduled for summer 2023) is aimed at investigating transport processes, pathways, and time scales for transport of air masses from Asia into the extratropical UTLS via the ASM. Measurements of HAGAR-V during this campaign will further provide detailed insight on the transport processes affecting CH_2Cl_2 and $CHCl_3$ complementing and extending the results of the present study.

---

[2] Probing High Latitude Export of air from the Asian Summer Monsoon

Appendix A

Detailed description of HAGAR-V

HAGAR-V is an aircraft instrument to investigate a large suite of trace gases with a wide range of different lifetimes designed by Prof. C. M. Volk and his group at the University of Wuppertal, built and certified in cooperation with enviscope GmbH, Frankfurt. The instrument is mounted in a HALO standard rack (R-G550SM; 65 x 55 x 163 cm, e.g. Figure A.11). For the certification to fly aboard HALO HAGAR-V was split into different modules. Each module is named "HAG_" followed by an individual number. Figure A.1 visualizes HAGAR-V and highlights the most important modules (HAG_01 to HAG_07). Each of these seven modules represents an independent unit (from a mechanical point of view) only connected by tubing, electrical wires, and the rack. Figure A.10 shows an overview of the plumbing of all modules connected by tubing.

Additional modules worth mentioning are HAG_08, HAG_97 and HAG_99-1. HAG_08 implies the external heaters of the inlet tubing, HAG_97 implies the several EMC (Electro-Magnetic Compatibility) grids in which HAGAR-V is cloaked in to prevent the propagation of electromagnetic radiation, and HAG_99-1 implies the inlet tubing through which air from outside the aircraft reaches the instrument (Figure A.11c).

The two modules that perform the measurements are HAG_04 and HAG_05. HAG_05 consists of two very different instruments — a two channel GC/MS and a NDIR (non-dispersive infrared absorption) instrument (LI-COR 7000). In the present work HAG_05 is further specified and referred to as either MS module or Licor depending on which instrument is addressed.

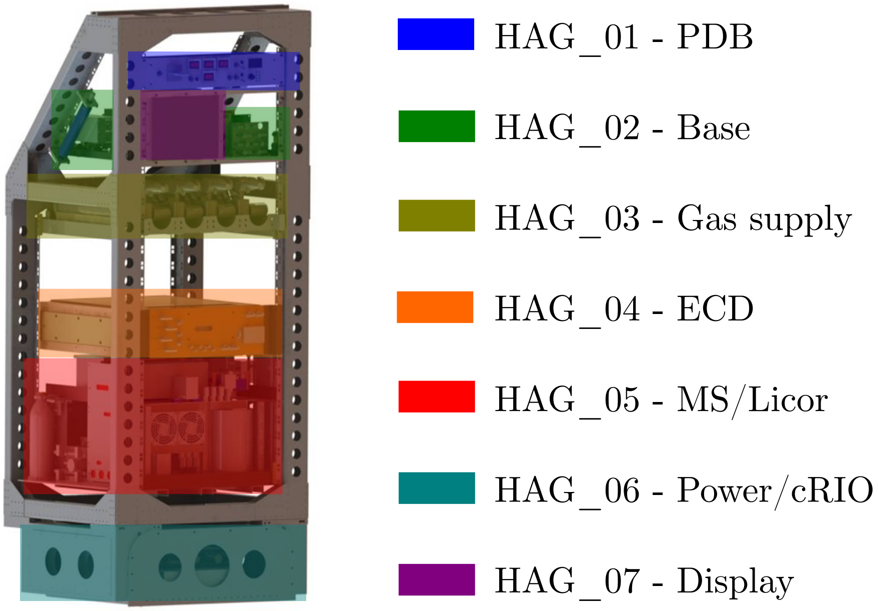

Figure A.1: Schematic drawing of HAGAR-V mounted in the rack. The different colors indicate the position of the respective module. Graphic adapted from enviscope GmbH.

A.1 HAG_01 - Power Distribution Box

The slide-in unit HAG_01 - PDB redistributes the external voltage for the usage in other modules of HAGAR-V. Via a two position switch (SW01) the three incoming 115 V (AC) phases can be connected and separated, thereby turning HAGAR-V on and off. In addition a three phased 10 A circuit breaker (CB01) can be used to separate the instrument from these phases as well. The incoming 230 V (AC) phase can be separated via a 5 A circuit breaker (CB02) and a green status LED next to CB02 glows when this phase is connected to the instrument. The 230 V are further distributed to HAG_05 because it is used only by the mass spectrometer.

The front panel of the PDB during operation on HALO is shown in Figure A.2. Four displays monitor the usage of electrical current from each of the four phases (upper row 115 V (AC) A, B, and C; second row 230 V (AC)). A fifth display monitors the current consumption of one of the internally converted eight DC voltages (HAG_06, see Appendix A.6). The displayed current consumption of one of the eight DC voltages is selected via a rotary switch. In addition, eight LEDs show the status of the individual DC voltages. If a light is off, the respective voltage is not available.

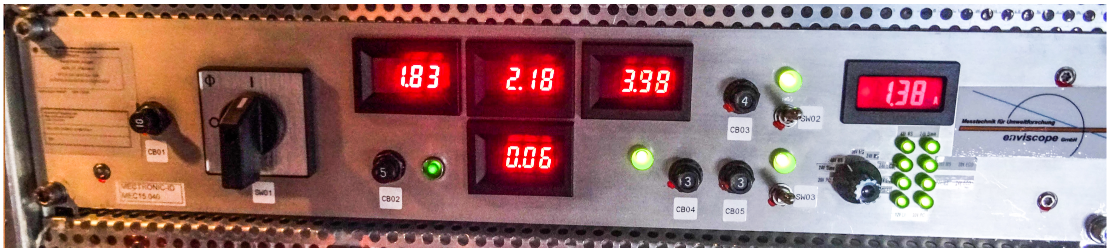

Figure A.2: Picture of the Power Distribution Box front panel when operated aboard HALO.

Inside the PDB are four temperature controllers (MINCO CT325) regulating the two heaters of the external TGI (Trace Gas Inlet, Enviscope GmbH) and the two heating wires that heat different segments of the inlet tubing (Figure A.11c) with 28 V (DC) provided by the power module (HAG_06, see Appendix A.6). Two switches can separately turn the TGI (SW02) or the inlet heaters (SW03) on and off; status LEDs glow to signal when a heater is switched on. Both TGI heaters combined can be separated by the circuit breaker CB03 and the inlet heaters separately by CB04 (half of the inlet tubing close to the TGI) and CB05 (half of the inlet tubing close to the instrument). The heaters are internally set to different temperatures via their respective controllers. To change the set point the PDB has to be removed from the rack and opened up to adapt the controllers mechanically.

A.2 HAG_02 - Base module and HAG_07 - Display

The base module (HAG_02) is positioned below the PDB in the rack (Figure A.1) and serves four main purposes:

1. To suck in and compress outside air via two suction pumps.
2. To select the air sample — choosing between outside air, one of the two calibration gases, or Nitrogen (N_2).
3. To treat (dehydrate and/or clean) and distribute the chosen air sample to the measuring modules (HAG_04 and HAG_05) at controlled pressure and flows which are also set in the base module.
4. It is the platform for an ITX (Information Technology eXtended) computer that is used as the user interface to control HAGAR-V, to save and export data as well as to directly control the mass spectrometer (MS) and acquire MS data via the software ChemStation (Version E.02.02.1431; Agilent Technologies).

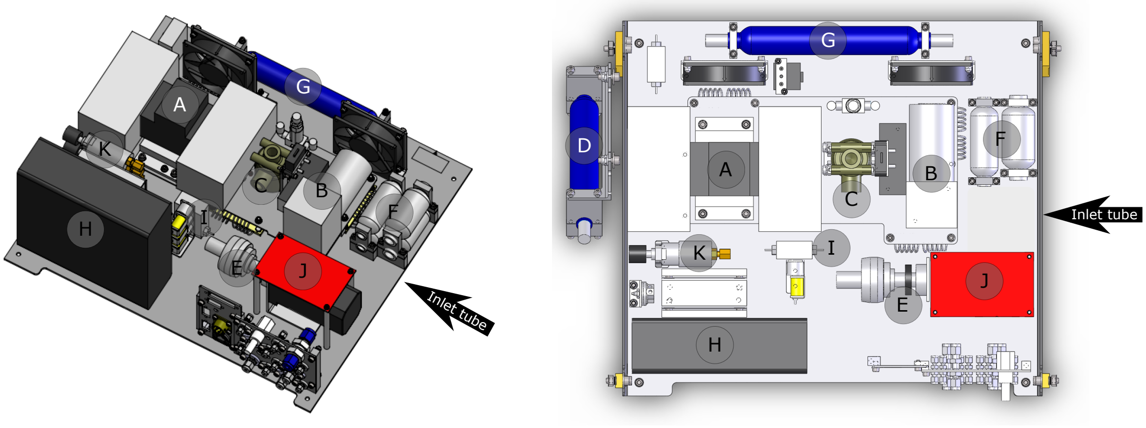

Figure A.3: Drawing of the Base module (HAG_02) in an angled (left) and top view (right). (A) KNF 813.5 suction pump; (B) KNF 814 suction pump; (C) TAVCO pressure relief valve; (D) temperature controlled dehydration unit filled with magnesium perchlorate; (E) Valco stream selection valve; (F) four cleaning units filled with charcoal Moleculite and Mole sieve 13X; (G) buffer volume for Licor (HAG_05) exhaustion line; (H) ITX computer; (I) BRONKHORST pressure controller to regulate the selected sample pressure; (J) circuit board of Base module; (K) three mechanical pressure regulators (for N_2 at the bottom, CAL in the middle, SPAN at the top). The black arrow indicates from where the inlet tube enters the Base module. Graphs adapted from enviscope GmbH.

The Base module is equipped with two in series connected suction pumps mounted on a separate board. This board is mechanically decoupled from the rest of the Base module to avoid transporting the pumps' vibrations onto other components. The air inlet is connected via a corrugated tube and a three-way valve (S01, Figure A.4) to the stronger of the two pumps (KNF 813.5; Figure A.3, A). This pump compresses the air from outside pressure (being as low as ~ 0.2 bar(a)) to ~ 1.3 bar(a) with a flow of around 1.5 standard liters per minute at 0.2 bar(a) front pressure. The second suction pump (KNF 814, Figure A.3, B) further compresses the air and pushes it through the dehydration unit (Figure A.3, D). To achieve constant front pressure for the second pump a pressure relief valve (Figure A.3, C) regulates the pressure between the two pumps to slightly above 1 bar(a), thereby changes of mass flow due to changes of outside pressure are avoided.

The pressure of the sample air chosen by the stream selection valve (SSV; Figure A.3, E) is regulated by an electrical front pressure regulator (Figure A.3, I; Figure A.4, p-contr.0). p-contr.0 is set to 3 bar(a) and excess sample pressure is exhausted. To avoid discarding calibration gas or zero gas (N_2) by p-contr.0, the sample pressure of each of these three gases can individually be adjusted to the set point of the pressure controller via sensitive mechanical pressure regulators (Figure A.3, K). These three gases are provided by the Gas supply module (HAG_03, see Appendix A.3). The zero gas is additionally purified by

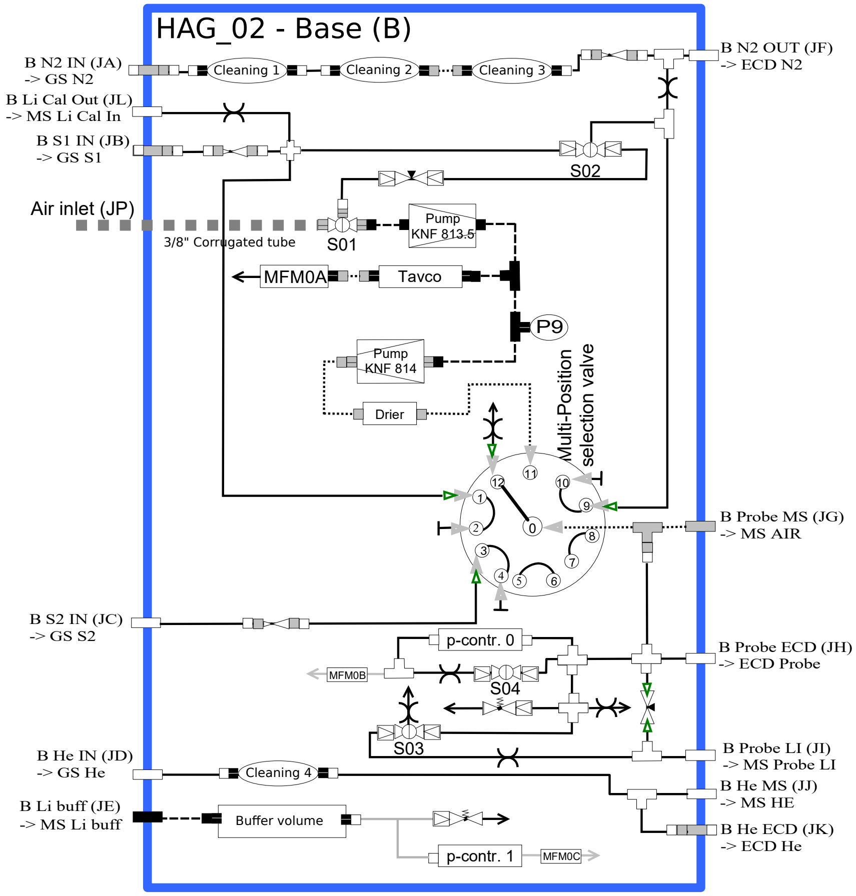

Figure A.4: Plumbing diagram of the Base module. An overview of all HAGAR-V modules connected by tubing is given in Figure A.10.

three filters (Figure A.3, F) of Moleculite (40 ml), Charcoal (50 ml), and Molsieve 13X (50 ml). The fourth cleaning unit contains Molsieve 13X (40 ml) and purifies N_2 or helium used as carrier gas for the ECD or the ECD and the MS module[1]. This fourth gas is also provided by the Gas Supply module.

The three-way valve (S01, see Figure A.4) connecting the air inlet with the first suction pump can be switched to cut off the inlet line; instead connecting either a calibration gas or the purified zero gas with the pumps. This mode can be used to analyze effects of the pumps and/or the dehydration unit on the air samples. Usually the the calibration gas and the zero gas bypass the pumps and the dehydration unit to save gas (see Figure A.4).

---

[1] Helium is only used here when the MS module operates in CI mode, see Appendix A.5.2. Currently N_2 is the preferred gas.

Several crimped lines, valves (S03 and S04, see Figure A.4) and open tubing ensure the permanent flushing of the sample line with fresh sample air and prevent high pressures that could damage p-contr.0. In addition, at high sample pressures additional mass flow can be distributed to the NDIR CO_2 analyzer which is the only instrument of HAGAR-V constantly probing sample air (HAG_05; Licor, see Appendix A.5.1). To minimize disturbances from changing pressure at the CO_2 analyzer a buffer volume (100 ml; Figure A.3, G) is placed in its exhaustion line in front of the pressure regulator controlling the exhaustion.

HAG_07 - Display is listed as a separate module because it is not mounted on the plate of the Base module and rather directly connected to the rack. However, in its function it is part of the base module. HAG_07 is a touch screen monitor (BCMT 10X02-R) and connected to the ITX computer. No key board is needed to operate HAGAR-V but can be attached at one of the two USB connections provided at the base modules front panel.

A.3 HAG_03 - Gas Supply

The gas supply module is positioned below the base module in HAGAR-V's rack and provides the calibration gases as well as the carrier gases for the ECD module. It consists of four slots fitting each to a 2 l composite gas bottle (Luxfer, L19C) that can be mounted horizontally into the module. By removing two screws, each bottle can be removed from the module individually. The tubing can be easily separated via quick connects (Swagelok) and the pressure regulator as well as high and low pressure sensors stay fixed on the removed bottle. It is of great advantage that the removal process can be done quickly, because refilling the bottles is a regular service to be done between flights (see Appendix C.1).

A.4 HAG_04 - ECD

The ECD module is a modernized version of the gas chromatograph of HAGAR (Riediger, 2000) and mounted in a drawer (19 " 3,1HE, series 75050, Enviscope GmbH) positioned below the Gas supply module HAG_03 in HAGAR-V's rack. HAG_04 is a two channel instrument comprising two electron capture detectors (ECD). The measurement technique is based on gas chromatography (GC) with packed columns. In the configuration flown during WISE (Section 3.1) channel 1 measures SF_6, CFC-12, and CH_4 and channel 2 measures CFC-11, -113, and CCl_4. The 1/8 " stainless steel columns are filled with different adsorbing material (channel 1: Molsieve, channel 2: Porasil n-octane). In this configuration

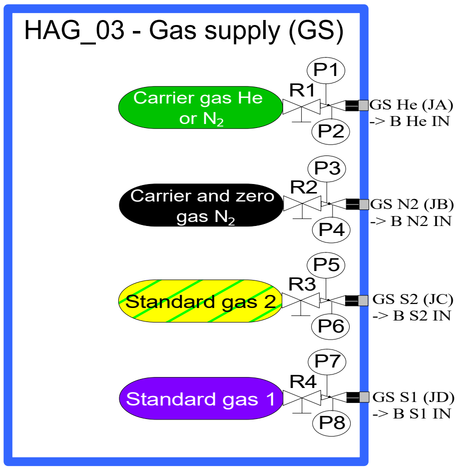

Figure A.5: Plumbing diagram of the Gas supply module. An overview of all HAGAR-V modules connected by tubing is given in Figure A.10.

both channels each comprise a 80 cm pre-column leading to the main-column of different length (channel 1: 180 cm, channel 2: 220 cm). In addition, to improve the sensitivity for CH_4 highly diluted N_2O (~ 0.125 % of the N_2 matrix) is added to the detector as a so called "doping gas" (Werner, 2007; Beckert, 2019). Another option is the usage of CO_2 as a "doping gas" for a higher sensitivity gain of H_2 similar to HAGAR.

The air sample (distributed by the Base module, Appendix A.2) is lead into the sample loop at a fixed pressure (regulated by PrC 2A, see Figure A.6) ensuring that each sample contains the same volume of air regardless of pressure variations in the sample line. By switching the two position valve (valve 2B or 2A, see Figure A.6) the sample gets injected onto the pre-column with the flow of a carrier gas (N_2 or He). Once the last species of interest has left the pre-column to get further separated on the main-column, the two position valve can be used to induce a backflush on the pre-column. The carrier gas flow reverses its direction only for the pre-column, purging out retentive species while the air sample of interest further gets carried through the main-column towards the detector. The resulting signal of the chromatogram is recorded with 10 Hz and can be viewed directly with the controlling program of HAGAR-V on the ITX computer (see HAG_02, Appendix A.2). The main advantage over HAGAR is the parallel mounted sample loops for a fully independent operation of each channel.

Electrically the module is supplied from HAG_06 with 28 V (DC) to operate the four column oven heaters as well as to heat the ECDs. In addition, the ECD module uses 24 V (DC) for the rest of the electrical consumers within the module. A programmable relay

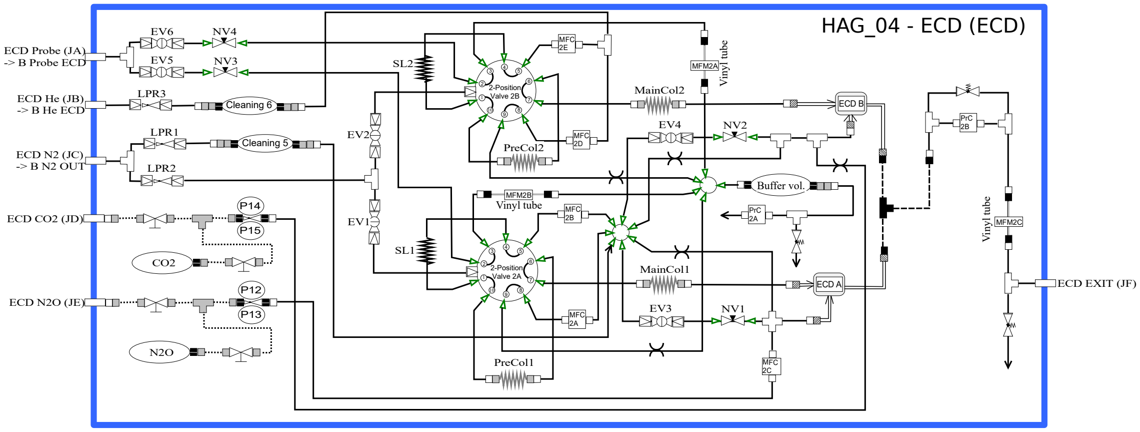

Figure A.6: Plumbing diagram of the ECD module. An overview of all HAGAR-V modules connected by tubing is given in Figure A.10.

(Ziehl, TR210) is used as a reversible fuse to end the heating of each ECD oven separately when a temperature higher than (350 ± 2.4) °C is detected.

A.5 HAG_05 - MS/Licor

The design of the HAG_05 module comprises two levels which are referred to as: the ground level, including everything that is mounted on the base plate of the module and the upper level including everything that is mounted on two horizontal supporting aluminum beams forming a non-continuous platform 25 cm above the base plate. HAG_05 comprises two different instruments that are referred to as Licor and MS module. In this section a separate description of the CO_2 analyzer (Licor) and the mass spectrometer (MS) module is given.

A.5.1 Licor

Licor, the sub-module of HAG_05, comprises a LI-7000 (LI-COR, Germany) for the measurement of CO_2 and water vapor. The water vapor measurement is mainly used for the correction of the CO_2 signal rather than for scientific analysis. The instrument has been stripped of almost every part of the original housing to make it fit into HAG_05. The core part — a temperature regulated and insulated box containing the calibration and the measurement chamber — is mounted on the ground level of HAG_05. The calibration chamber is continuously flushed with ~ 20 ml/min of a calibration gas supplied by HAG_03

(Appendix A.3) via HAG_02 (Appendix A.2). The measurement chamber is continuously supplied with the sample chosen in HAG_02.

The circuit boards needed to operate the instrument are mounted vertically on a supporting structure at the side of HAG_05. Electrically this sub-module is supplied by HAG_06 (Appendix A.6) with 12 V (DC) and immediately starts operating when the power of HAGAR-V is switched on at HAG_01.

A.5.2 MS

The MS module is designed to use two channels with only one detector by operating the channels anticyclical. Thereby the instruments' time resolution can be bisected and/or the number of target species can be enlarged compared to the use of only one channel. The MS module is separated from the sample line by a three-way valve (Figure A.7, S1G) controlling the time of sampling. By default the sample air selected in HAG_02 (Appendix A.2) gets flushed out of the valves' chimney with ~ 120 ml/min to keep the sample line purged and free from previously sampled gas. S1G is switched when preconcentration of the sample air is desired. A 10-port two-position valve (V 1A) selects which of the two preconcentration traps is in adsorption mode (Figure A.7, trap A). The other trap then is automatically in desorption mode. A mass flow controller (Figure A.7, MFC1A) behind the trap in adsorption mode regulates and measures the sample volume (10 Hz). To accomplish a higher sample rate a small pump (Pump4, GAST, 5D6070-101-1076) is positioned behind MFC1A. In adsorption mode the trap is usually set to low temperatures.

Once the preconcentration phase is over, S1G can be set to default again leaving the residual sample at the head pressure of currently 3 bar(a) inside the trap. There are two options to lower the residual sample pressure inside the trap before desorption, thereby minimizing the risk of an overload of the GC columns. One option is to leave MFC1A open after setting S1G to default and let Pump4 evacuate the sample air in the mobile phase out of the trap in direction of preconcentration. The other option is to open valve S1C to evacuate the sample air in the mobile phase out of the trap in direction of desorption. Of course both options can also be applied at the same time. The evacuation of the residual sample in the mobile phase has to be characterized well due to the risk of a breakthrough of target species in particular when evacuating in direction of desorption. In the present work only the evacuation in the direction of adsorption has been used for a time of 2 s after setting S1G to default.

To change from adsorption to desorption mode the two-position valve V 1A connects the trap of one channel to its pre-column and sets the other channel to the adsorption mode.

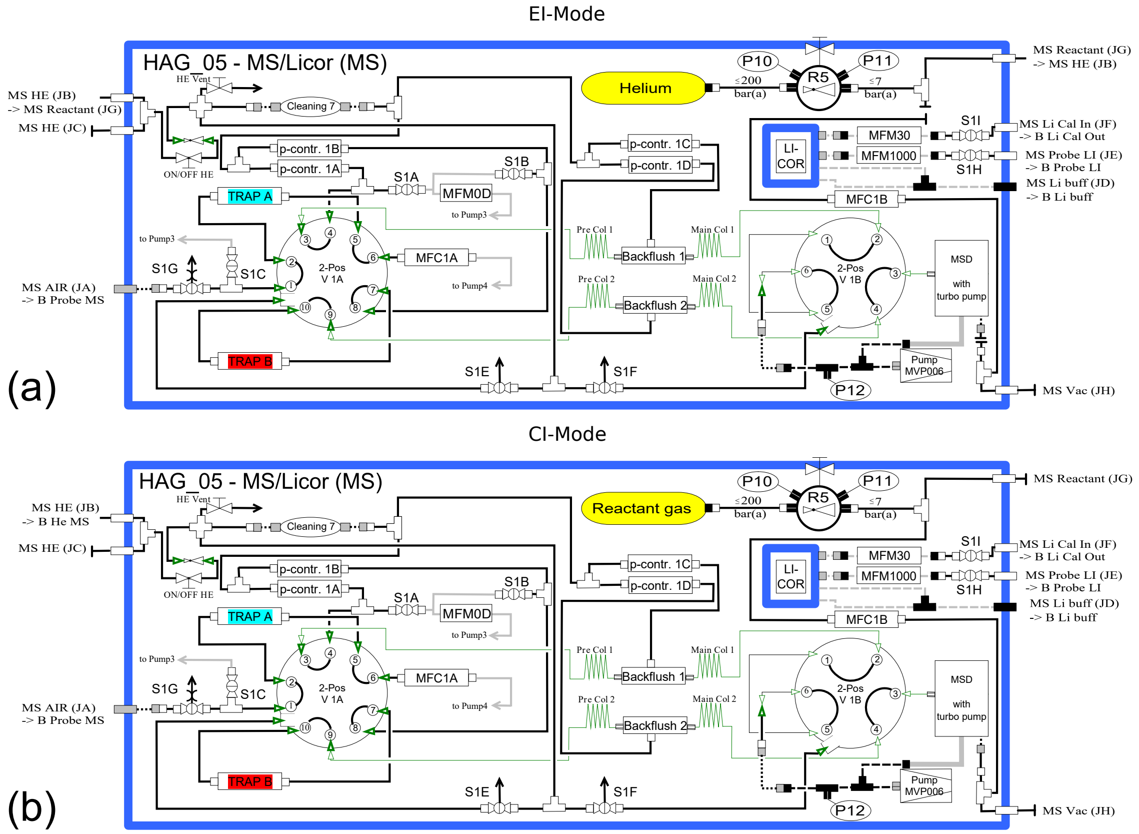

Figure A.7: Plumbing diagram of the MS/Licor module in EI mode (a) and in CI mode (b). An overview of all HAGAR-V modules connected by tubing is given in Figure A.10.

The carrier gas (regulated by p-contr. 1A/1B, Figure A.7) constantly purges pre- and main-column in the adsorption mode. In the desorption mode the carrier gas flushes the preconcentration trap in opposite direction of adsorption to enter the pre-column. Thereby the preconcentrated sample gets injected from the trap onto the pre-column. Usually the trap is set to high temperatures in desorption mode.

Both, pre- and main-column, are temperature controlled and connected via a T-connector (Backflush 1/2) to a pressure controller (p-contr. 1C/1D). The pressure controller regulates a carrier gas flow usually slightly diluting the sample in the columns by ~ 0.02 % to avoid a dead volume in the connector. Once the species of interest have left the pre-column, p-contr. 1A/1B is shut and p-contr. 1C/1D provides the necessary carrier gas flow to transport the sample within the main-column further towards the MS. The more retentive species still inside the pre-column get flushed backwards out of the pre-column by opening valve S1A/S1B. To aid the backflush, pump3 produces a vacuum and the resulting pressure gradient in this path enhances the purging of the pre-column. This procedure is possible in adsorption and desorption mode. Nevertheless, the respective trap should not be at low temperatures when backflushing in desorption mode.

Finally, the 6 port two-position valve (V 1B) selects the main-column leading to the MS. The respective other channel is then connected to the MS pre-pump keeping a pressure gradient upright to avoid disturbances in the chromatographic process. Valve V 1B can also be used to cut off unwanted parts of a chromatogram, e.g. when water or oxygen elutes.

The MS instrument can be operated in two different detection modes: The EI (Electron Ionization) mode where highly accelerated electrons cause the sample molecules to dissociate into characteristic distributions of detectable ions; the CI (Chemical Ionization) mode where a very soft ionization in combination with a reactant gas causes high detector sensitivity for certain species but without the characteristic mass spectrum of the EI mode. The EI mode allows more freedom in the choice of measured species with a lower risk of overlapping peaks, the CI mode yields a higher sensitivity for specific molecules. For example only by using the CI mode it could be accomplished to measure PFCs with a detection limit in the lower ppq (parts per quadrillion) range, as it was shown by vom Scheidt (2013b). The current working mode discussed in the present work is EI.

To switch between EI and CI mode a few changes have to be made (cf. Figure A.7). When operating the MS module in EI mode a 0.5 l gas bottle supplies the instrument with its carrier gas. In the CI mode this bottle is filled with reactant gas and connected via a mass flow controller (MFC1B) directly to the MSD. The carrier gas in the CI mode is supplied by HAG_03 (Appendix A.3), implying that channel 2 of the ECD module (Appendix A.4) also has to use helium as carrier gas. In addition, for the usage of the CI mode the ion source in the MS vacuum chamber has to be switched to an appropriate one. The carrier gas in both modes is used to switch the pneumatic two-position valves and gets purified (O_2, moisture and hydrocarbon removal, Super Clean Click-On Trap, Restek GmbH) within HAG_05.

Photographs of the MS module as operated during WISE are shown in Figure A.8.

A.6 HAG_06 - Power / cRIO

The HAG_06 - Power / cRIO module is positioned in the drawer below the rack (see Figure A.1) and comprises two key parts of the instrument (see Figure A.9). Built in a separate box inside the drawer are several AC/DC and DC/DC converters to convert the incoming aircraft power for the supply of all other modules with 12, 20, 24, 28, and 48 V (DC).

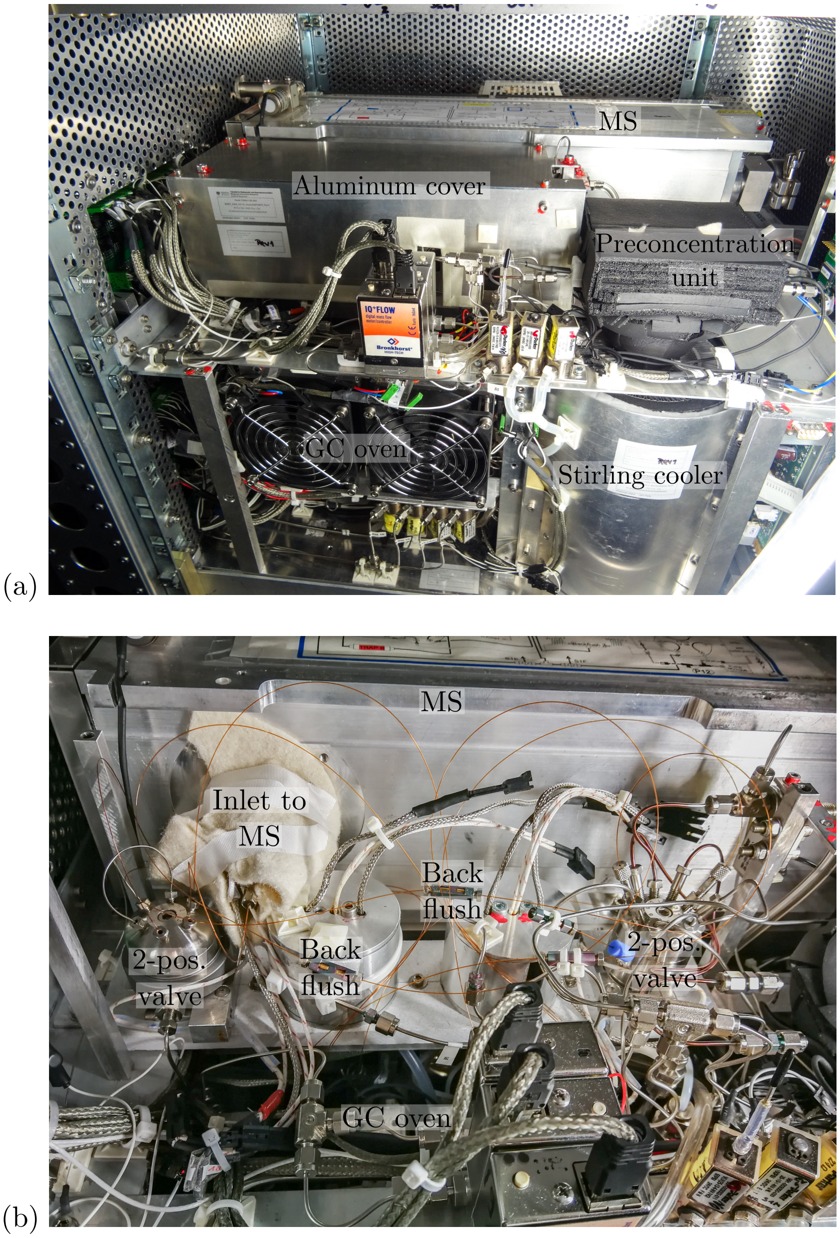

Figure A.8: Photographs of the HAGAR-V MS module as operated during WISE. (a) is a full view on the MS module and (b) shows details from underneath the aluminum cover. In the middle right of (a) the insulated preconcentration trap housing is visible (black cube). Underneath the preconcentration unit the Stirling cooler is visible (aluminum cylinder). In the front of (a) the EMC-grid covered fans of the GC oven are visible. The LTM columns are positioned behind the fans (not visible) and transfer lines go from the columns upwards to the two-position valves and back flush connectors (hidden under the aluminum cover in (a), visible in (b)). The inlet to the MS (wide stainless steel box in the back of (a)) is underneath the aluminum cover in (a) and covered in white insulation fleece in (b).

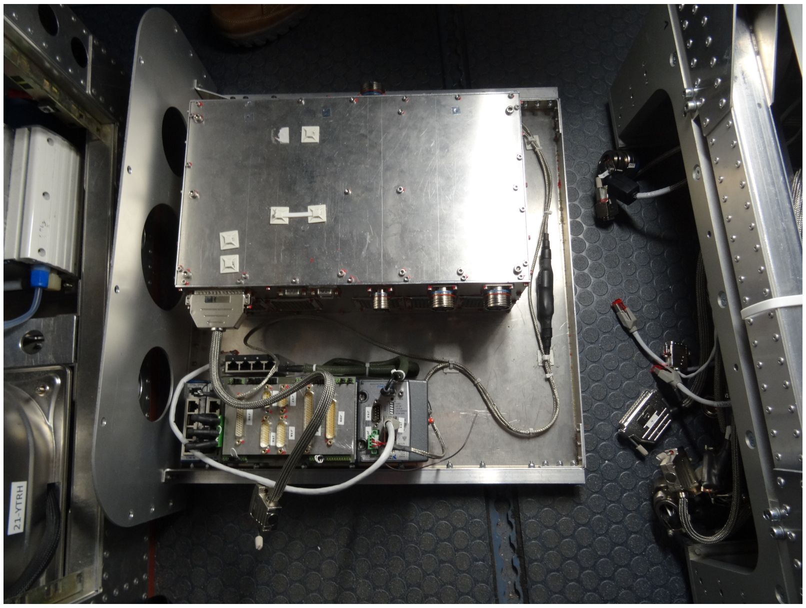

Figure A.9: Picture of HAG_06 - Power / cRIO module. The module supplies the other HAGAR-V modules with the appropriate power and comprises the control and data acquisition unit. Here only internal wires are depicted.

For the acquisition of data and to control HAGAR-V a cRIO system (compact RIO-9022, National Instruments) is positioned next to the power box in HAG_06. A self built circuit board realizes the connection between the cRIO and the modules HAG_02, _03, _04, and _05. All HAGAR-V modules have electrical wires connected to HAG_06.

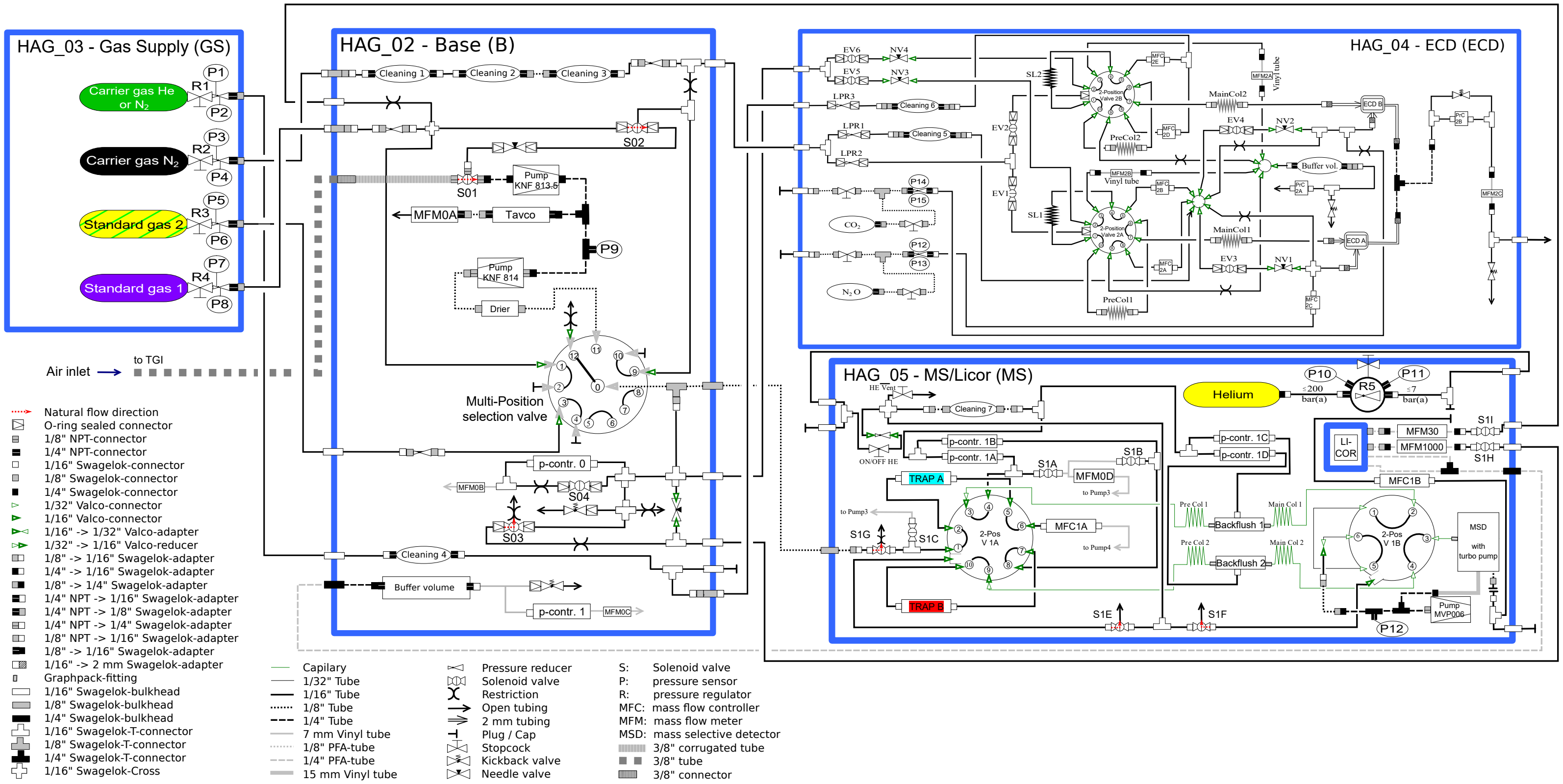

Abbildung A.10: Detailed plumbing diagram of HAGAR-V modules and their tubing connection. The MS module is in EI-mode.

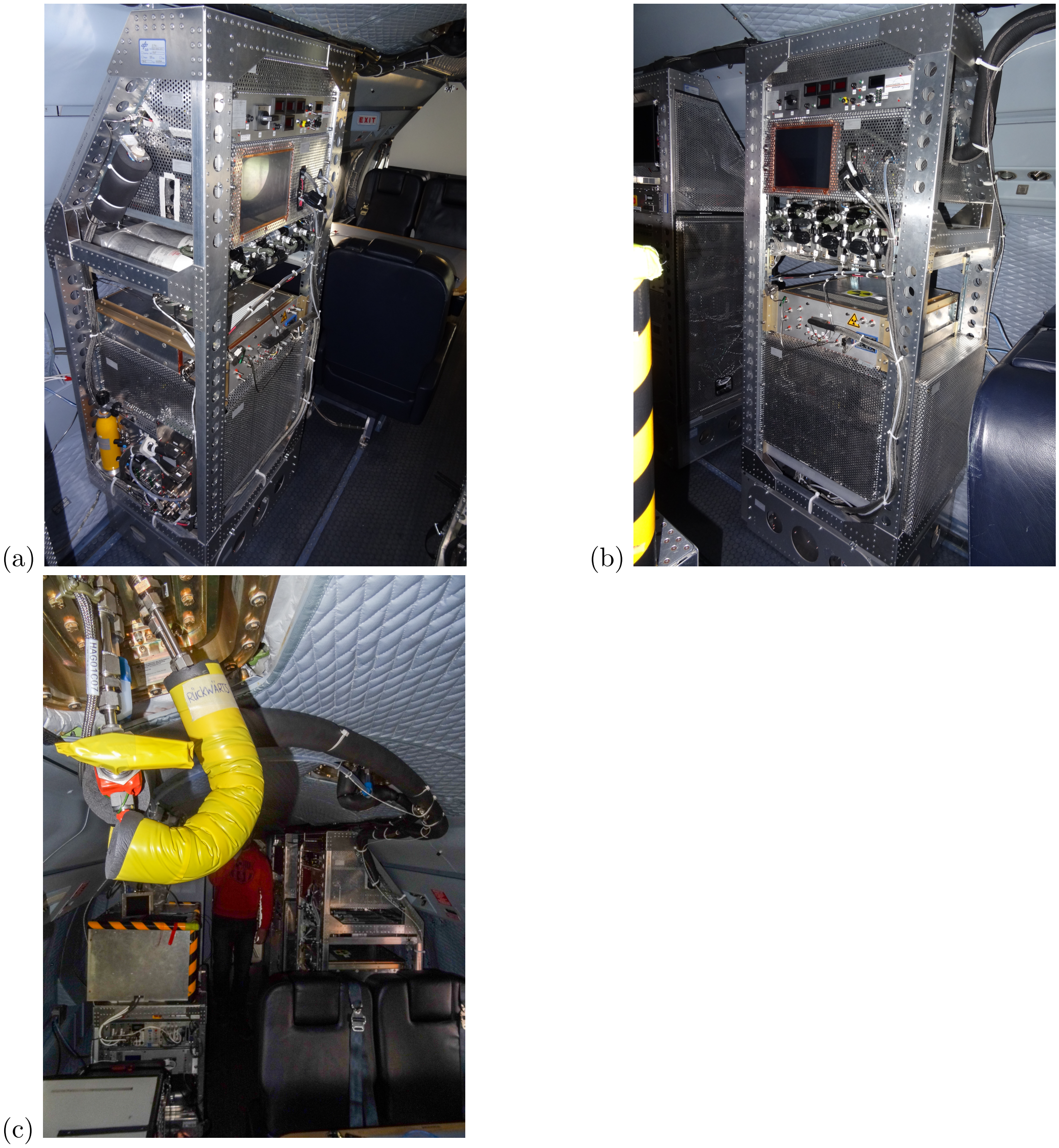

Figure A.11: Photographs of HAGAR-V aboard HALO. Usually HAGAR-V is positioned in the rear of the cabin just behind two of the four operator seats ((a), (b)). The inlet tube is connected to the TGI with the options of forward- (in flight direction) or backward-sampling (opposite flight direction) by the use of an mechanical 3-way ball valve (c). The inlet tube is temperature controlled and fixed to the airplane's cabin roof. Further in the back of HALO are only another instrument, the mission power and the baggage compartment (which also contains an instrument, not visible in the pictures). Opposite of HAGAR-V is another instrument and the board kitchen (not visible in the pictures).

Appendix B

MS module characterizations

In this part of the appendix supplemental information about the characterization of HAGAR-V's MS module is given.

B.1 Breakthrough volumes

B.1.1 BTV of the preconcentration trap used during WISE

This test was performed with the preconcentration trap used during all but the last WISE flights. Due to a shortage of time the test was performed on ground inside the aircraft between flights as a quick test and meant to be repeated properly in the laboratory once the campaign was over. Unfortunately, before the last flight this preconcentration trap was destroyed and only this quick test for break through volumes is available to analyze this trap and will be discussed here.

A preconcentration time of 60 s was decided to be the longest acceptable sample integration time during flight and used for this test. The preconcentration trap[1] was filled with ~ 0.07 g of the adsorbent Carboxen 572, two glass fiber plugs with a total volume of ~ 68 mm^3, and two custom made stainless steel sieves (~ 203 mesh; GERSTEL GmbH & Co. KG). Six different sample volumes were analyzed with the adsorption temperature set to 20 °C. The maximum sample volume tested implies the largest possible sample flow through the tested trap at 3 bar(a) head pressure.

At the time this test was conducted HFC-134a — as one of the target species during WISE — has not yet been measured. Nevertheless, HFC-134a does not have the lowest boiling

---

[1] internal serial number: GF-Ni-5

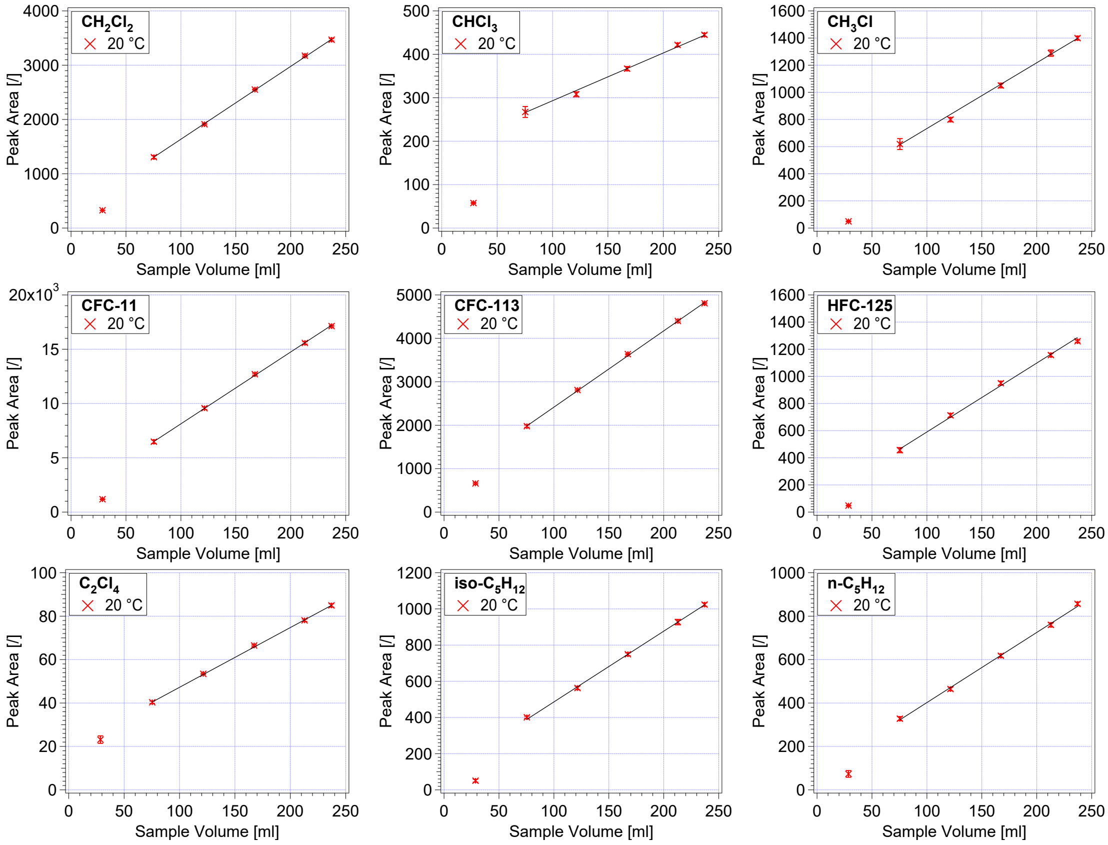

Figure B.1: Test for a breakthrough of different components. The preconcentration trap was filled with ~ 0.07 g of Carboxen 572 and has been used in all but the last WISE flights. The preconcentration time was 60 s at 20 °C. For all species there is a clear linear increase of detector signal (peak area) with sample volume visible. This implicates that for the given conditions all species of interest are properly preconcentrated. The lowest sample volume is an outlier and the MS was not properly conditioned explaining the offset in peak area.

point of the MS target species and appears in the mid section of the chromatogram. A breakthrough would be expected to appear first for molecules with the lowest boiling points or retention times (here HFC-125 and CH_3Cl, respectively[2]). Such a breakthrough could not be detected for the nine species analyzed.

In Figure B.1 the results of all measured species are presented. The lowest sample preconcentration is an outlier and shown only for transparency reasons. It was argued that during the time of measurement all species showed signs of a slight drift towards lower detector signals which could not be corrected afterwards for this quick test. The measurements were performed successively with increasing sample volumes but the lowest sample volume

---

[2] Boiling points according to GESTRIS Database (http://gestis.itrust.de; 16.01.2020): HFC-134a: −26.1 °C; HFC-125: −48.1 °C; CH_3Cl: −23.8 °C.

was measured at the end of this test. Therefore the slight drift might not significantly appear between 70 ml and 240 ml (although it is visible) but can have a larger effect for the lowest preconcentration that was measured at the latest. In addition, the instrument was properly conditioned for this test, visible in the offsets shown in most of the plots. However, no signs of a breakthrough in either of the tested species were apparent at sample volumes above 50 ml. This implies, with this trap and adsorbent at 20 °C, for the time of 60 s every possible sample volume can be chosen without the risk of losing target species.

B.1.2 BTV preconcentration trap with Graphsphere 2017

A preconcentration trap[3] filled with ~ 0.06 g of Graphsphere 2017 was tested for the breakthrough of several species. Graphsphere 2017 is a much weaker adsorbent than Carboxen 572 and adsorption temperatures as low as ~ −40 °C had to be applied. Maximum sample volumes of around 130 ml were possible within 40 s preconcentration time and 3 bar(a) head pressure. Three different adsorption temperatures were tested: 20 °C, 0 °C, and −40 °C.

The results of all tested temperatures and species are shown in Figure B.2. At positive temperatures clear breakthrough is visible only for CH_3Cl and the HFCs — the three compounds with the lowest boiling points in this analysis[4]. At −40 °C all of the tested species are properly adsorbed. Graphsphere 2017 could therefore be a possible alternative for the strong adsorbent Carboxen 572.

B.1.3 BTV of a multi adsorbent preconcentration trap

A multi adsorbent trap[5] was built filled with ~ 0.02 g of Carboxen 572 and ~ 0.04 g of Graphsphere 2017. The trap was tested for the breakthrough of components at three different adsorption temperatures (−40 °C, −20 °C, and 0 °C) for six different sample volumes ranging from ~ 10 ml to ~ 220 ml at 60 s adsorption time. The results are shown in Figure B.3.

Acetylene (C_2H_2), the species with the lowest boiling point (−84 °C[6]), could be trapped with no apparent loss at ~ −40 °C up to a sample volume of ~ 50 ml. HFC-32 might show signs of a breakthrough at an adsorption temperature of 0 °C and a sample volume

---

[3] internal serial number: GF-Ni-8

[4] Boiling points according to GESTRIS Database (http://gestis.itrust.de; 16.01.2020): HFC-134a: −26.1 °C; HFC-125: −48.1 °C; CH_3Cl: −23.8 °C.

[5] internal serial number: GF-Ni-6

[6] GESTRIS Database: http://gestis.itrust.de (16.01.2020)

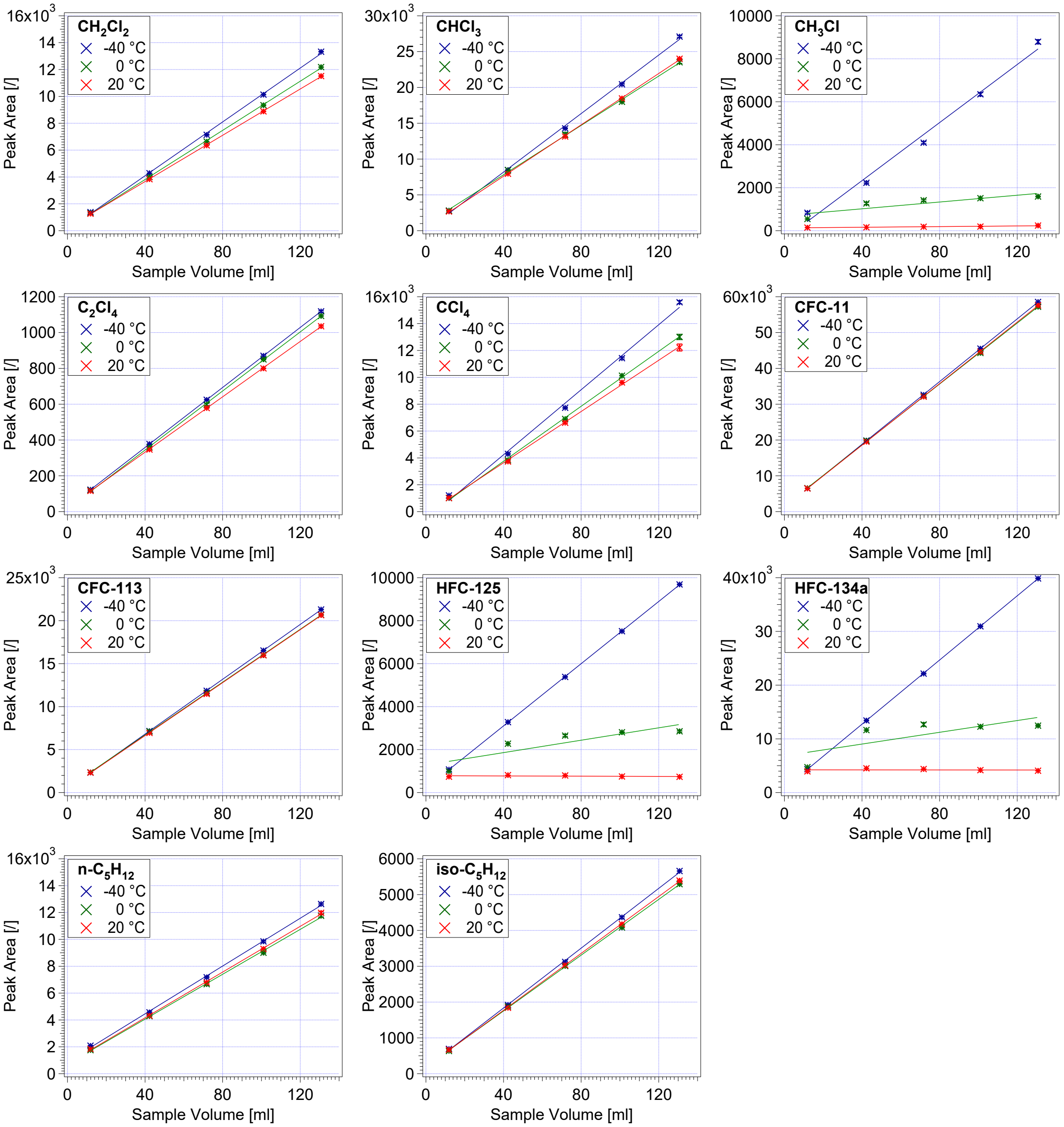

Figure B.2: Test for the breakthrough of components on a preconcentration trap filled with ~ 0.06 g of Graphsphere 2017. Three different temperatures were tested during 40 s of preconcentration time. With this adsorbent preconcentration temperatures of ~ -40 °C have to be chosen to efficiently trap all of the tested components in an air sample of ~ 130 ml at ~ 275 ml/min sample flow.

of ~ 170 ml. Several species — in particular CCl_4 — show slightly weaker detector signals with higher adsorption temperatures. This could indicate that at higher adsorption temperatures a small and linear loss of some species can appear.

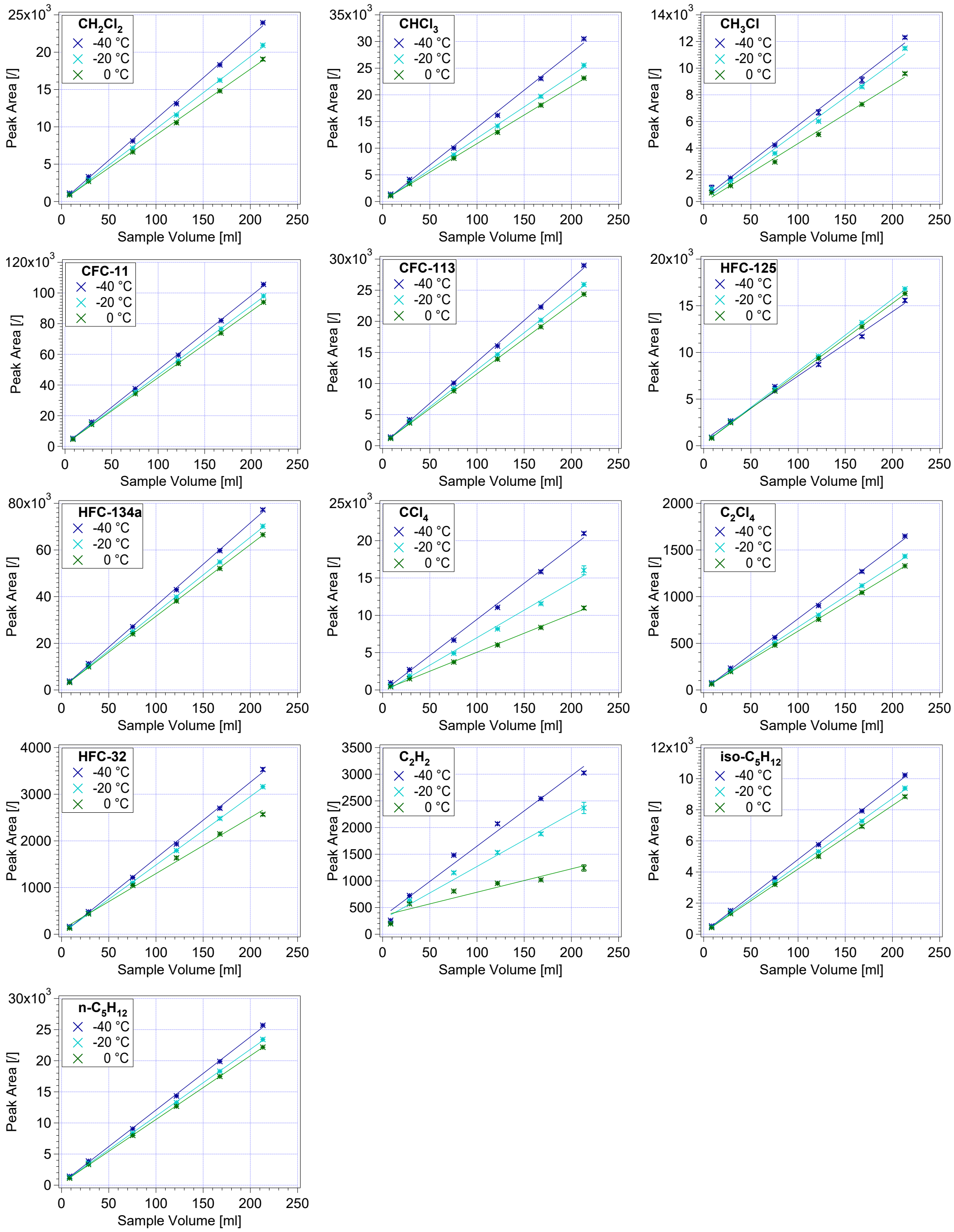

Figure B.3: Test for the breakthrough of components on a multi adsorbent preconcentration trap filled with ∼ 0.02 g of Carboxen 572 and ∼ 0.04 g of Graphsphere 2017. Three different adsorption temperatures were tested during 60 s of preconcentration time.

Another test with this preconcentration trap was performed with the additional adsorption temperature of 20 °C and only 40 s of preconcentration as it has been used in most of the WISE flights (cf. Table C.2). The results are shown in Figure B.4. The test shows that sample preconcentration at room temperature (similar to the settings during WISE) is also possible for most of the target species with this multi adsorbent trap. The promising adsorption results of this trap can further enlarge the list of species measured by the MS module during WISE and has recently been successfully put into use at the SouthTRAC[7] campaign.

B.2 Memory effects

B.2.1 Memory effects during WISE

Memory effects of a multi adsorbent trap are analyzed in Appendix B.2.2. Such a laboratory test could not be performed on the trap used during most of the WISE flights[8]. Nevertheless, memory effects, with the instrumental setup from WISE, can be (qualitatively) investigated by analyzing the on-ground calibrations of the flight-bottles (Appendix E.2). These calibrations sequence several measurements of the same gas (CAL or SPAN) before switching to the measurement of another gas with different mixing ratios. The memory effect of a target species would be expressed by a gradually decreasing mixing ratio when the measurements of the calibration gas with the lower mixing ratios succeed the ones with the higher mixing ratios and vice versa.

Figure B.5 shows representative examples from the most trustworthy on-ground calibrations of each analyzed species and in-flight data of C_2Cl_4. Due to a high level of water vapor inside the instrument the first part of the calibration was corrupted for some species and is therefore not shown in the plots. The error bars represent the standard deviation of the CAL (mother bottle[9]) measurements that were used for calibration. The error bars are drawn as a help to not misinterpret measurement variability, although they could also be biased if the regarded species would suffer from memory effects.

On the basis of this qualitative test, the measurements exhibit no significant indication for memory effects with the instrumental setup flown during WISE. Single exception is C_2Cl_4. The memory effects of C_2Cl_4 were also strongly visible in the measurements during flights,

---

[7] Southern Hemisphere - Transport Composition Dynamics

[8] Trap GF-Ni-5 was filled with ~ 0.07 g of the adsorbent Carboxen 572. Its inner temperature distribution is discussed in Section 2.2.3

[9] mother bottle defines the primary working standard, the flight bottles, used for in-flight calibration, are filled with gas from the mother bottle

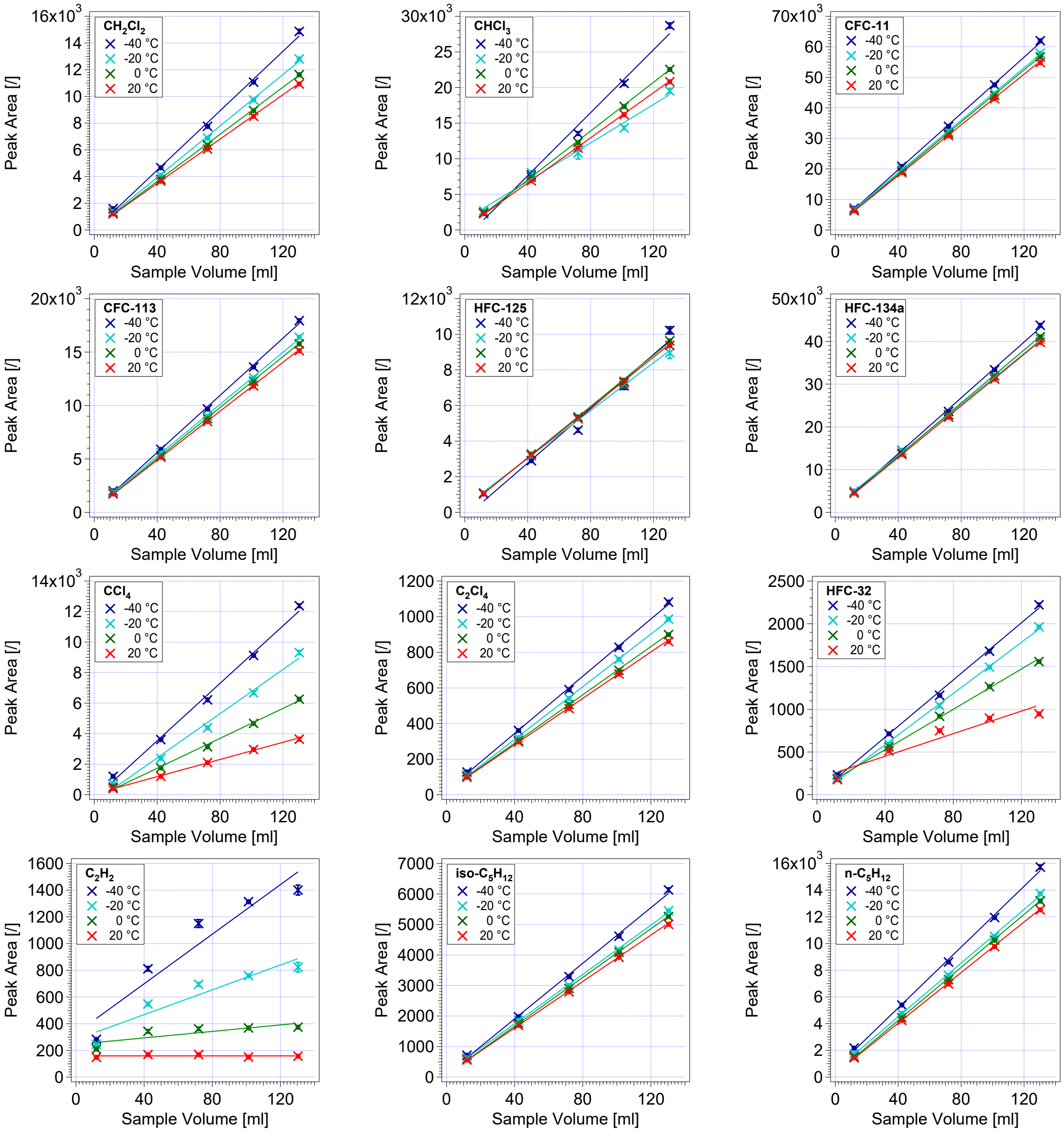

Figure B.4: Test for the breakthrough of components on a multi adsorbent preconcentration trap filled with ~ 0.02 g of Carboxen 572 and ~ 0.04 g of Graphsphere 2017. Four different adsorption temperatures were tested during 40 s of preconcentration time.

in particular due to the large difference between the mixing ratios of the used calibration gases and of the air measured in the UTLS region (Figure B.5, middle plot of bottom row). The obtained measurements of C_2Cl_4 could not be corrected for these memory effects and were thus not further analyzed.

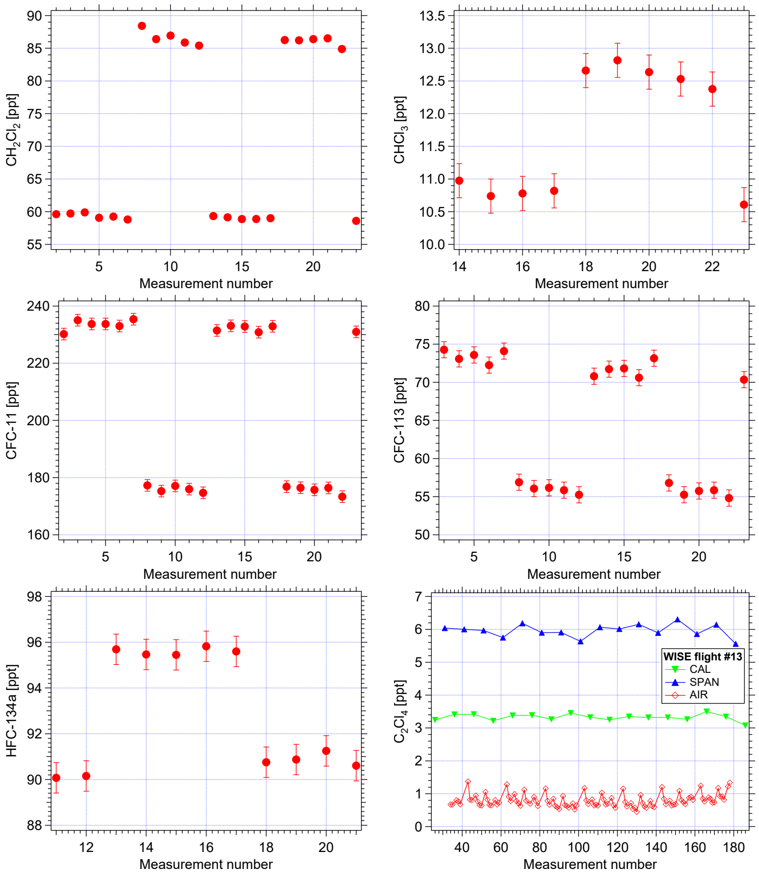

Figure B.5: Qualitative analysis of memory effects with the instrumental setup used during WISE. Two gases with different mixing ratios were used. The error bars represent the standard deviation of one of the two calibration gases used for calibrating the measurements. The plot for C_2Cl_4 (middle of bottom row) shows the two in-flight calibration gases and the air measurements of WISE flight #13. Only in this plot clear memory effects are visible.

B.2.2 Memory effects of a multi adsorbent preconcentration trap

A laboratory test for the investigation of memory effects was conducted on a multi adsorbent trap (see Appendix B.1.3). The temperature difference inside the used trap did not exceed ~ 40 °C (cf. Section 2.2.3). For this test the reference blank gas (helium 5.0[10]) was sampled until the few compounds visible in these blanks (n-Pentane, HFC-125, and CFC-11) showed stable peak areas, indicating the used helium's impurity for these species. The last of these samples was used as a reference for the contamination of the blank measurements.

---

[10] 5.0 implies a gas purity of 99.999 %, i.e. a maximum total impurity of 10 ppm of other gases

To investigate the strength of a memory effect and its influence on following samples, measurements of five subsequent samples of test air[11] were conducted followed by the measurement of five subsequent samples of helium. These measurements were repeated for three different adsorption temperatures (0 °C, -20 °C, and -40 °C). The results were detrended (see Section 3.3.1) and the three contaminated components in the blank gas were corrected by subtracting the determined contamination. The signals found in the blank measurements were normalized to the average signal of the test air to obtain fractions relative to the test air. The relative signals found in the blank measurements during this test are shown in Figure B.6.

A total of five species (C_2H_2, iso-Pentane, HFC-32, CFC-113, and CCl_4) did not exhibit any memory effect during the test. For the other compounds the memory effects were relatively small (< 1 % of test air for all but C_2Cl_4) which in all cases (except C_2Cl_4) was below the determined measurement precision[12] during the test (see legends in Figure B.6).

The results of this test were not verified for air samples with different mixing ratios by analyzing differently composed air samples. However, this result is very promising for future operations compared to traps containing only the strong adsorbent Carboxen 572.

B.3 Measurement setup of test for signal linearity

The preconcentration trap used for this test was filled with the adsorbent Carboxen 572[13]. It has to be noted that this preconcentration trap was different than the one used during WISE. The trap used for the following test showed larger temperature differences inside the trap and thus a few species[14] exhibited memory effects which have not been observed on the trap used during WISE (cf. Appendix B.2.1). It can therefore not be excluded that additional effects influence the relationship between signal response and mixing ratio. A transfer of the test's conclusions to data obtained during WISE has therefore to be treated with great care. During WISE in-flight calibrations were performed which can be analyzed for signal linearity regarding the data obtained during WISE (cf. Appendix E.2).

During the test for signal linearity four different gases were used: test air (see Table E.2), synthetic air — as a blank gas and to dilute the test air —, a calibration gas (SPAN), and N_2 — as a blank gas for the calibration channel.

---

[11] dehydrated air sampled and compressed in the city of Wuppertal with mostly elevated mixing ratios of anthropogenic tracers. See Table E.2

[12] Standard deviation of test air samples relative to test air mixing ratio

[13] internal serial number: GF-Ni-SN-5

[14] CH_2Cl_2, $CHCl_3$, CFC-11, Iso-, and n-Pentane

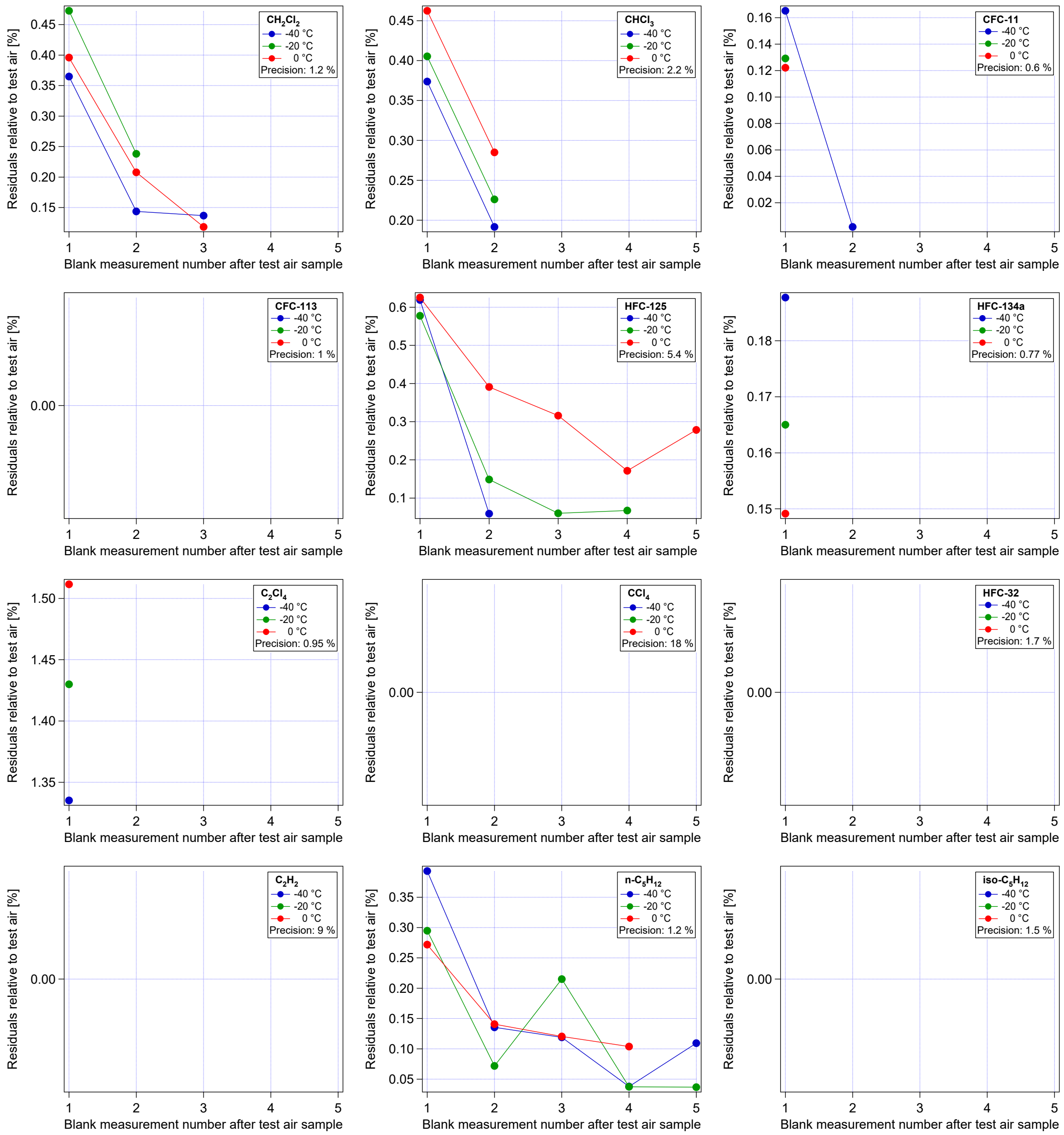

Figure B.6: Investigation of memory effects from components preconcentrated on a multi adsorbent trap filled with ∼ 0.02 g of Carboxen 572 and ∼ 0.04 g of Graphsphere 2017. Shown are five He blank measurements succeeding five measurements of test air. The blank gas measurements are given in relative values to the previous test air. Three different adsorption temperatures were tested for five measurements of test gas and five of He blank gas. Compared to the measurement precision no significant memory effects could be detected other than for C$_2$Cl$_4$.

The synthetic air and the test air were both regulated by flow regulators separately. They were mixed together in a volume (“gas mouse”) of about 150 ml. The “gas mouse” is made of glass and most likely exhibits tiny leaks at the connectors. To minimize the influence of air leaking into the diluting system it was always kept above ambient pressure. To realize stable pressure inside the diluting system a (front-) pressure regulator was positioned behind (in flow direction) it. With a total gas flow of around 2 l/min the diluting system could be flushed within seconds and stable mixing was realized in the short time between one to two measurement cycles (3–6 min). The pressure regulator was set to 3 bar(a) simulating the operational head pressure of HAGAR-V.

To detect drifts during the measurements the system regularly gets calibrated. Every four samples two measurements of calibration gas were made. This gives on the one hand the opportunity to have a backup calibration if one should be corrupted and on the other hand it gives the diluting system enough time to properly dilute the sample gas to a stable new gas mixture. The calibration gas could be chosen for sampling via the SSV (position known as the "CAL-port").

Eight different sample dilutions were measured with four subsequent measurements for each dilution. The dilutions were 0 %, 5 %, 10 %, 30 %, 50 %, 70 %, 90 %, and 100 % of sample air relative to synthetic air. The determined peak areas were averaged over all four measurements of the respective sample dilution. These averages were normalized to the average peak area of the undiluted test air. Figure 2.4 shows the results with error bars indicating the respective standard deviation of the averaged samples. A quadratic function is fitted to the measurements of each compound. The synthetic air was contaminated with C_2H_2, CFC-113, and with the two Pentanes causing a constant signal offset. CCl_4 exhibited strong signal drifts which explain the offset for this species as well as the tendency to a logarithmic relationship between relative signal and fraction of test air. The results are summarized in Section 2.4.

B.4 Limit of detection (LOD)

A chromatographic peak is considered to be too small for the application of a fitting function (Section 3.2) when its signal to noise ratio (S[15]/N) is smaller than 3 (e.g. Skoog and Leary, 1996). Thus, the mixing ratio corresponding to a peak with S/N = 3 determines the limit of detection (LOD) of the analyzed species. Performing a measurement that produces peaks with S/N = 3 is not possible. Nevertheless, the LOD can be determined from the relationship between the MS detector response and different corresponding mixing ratios

---

[15] In Section 3.3 the signal is abbreviated with R, indicating either peak height or peak area, here S is used specifically for the peak height

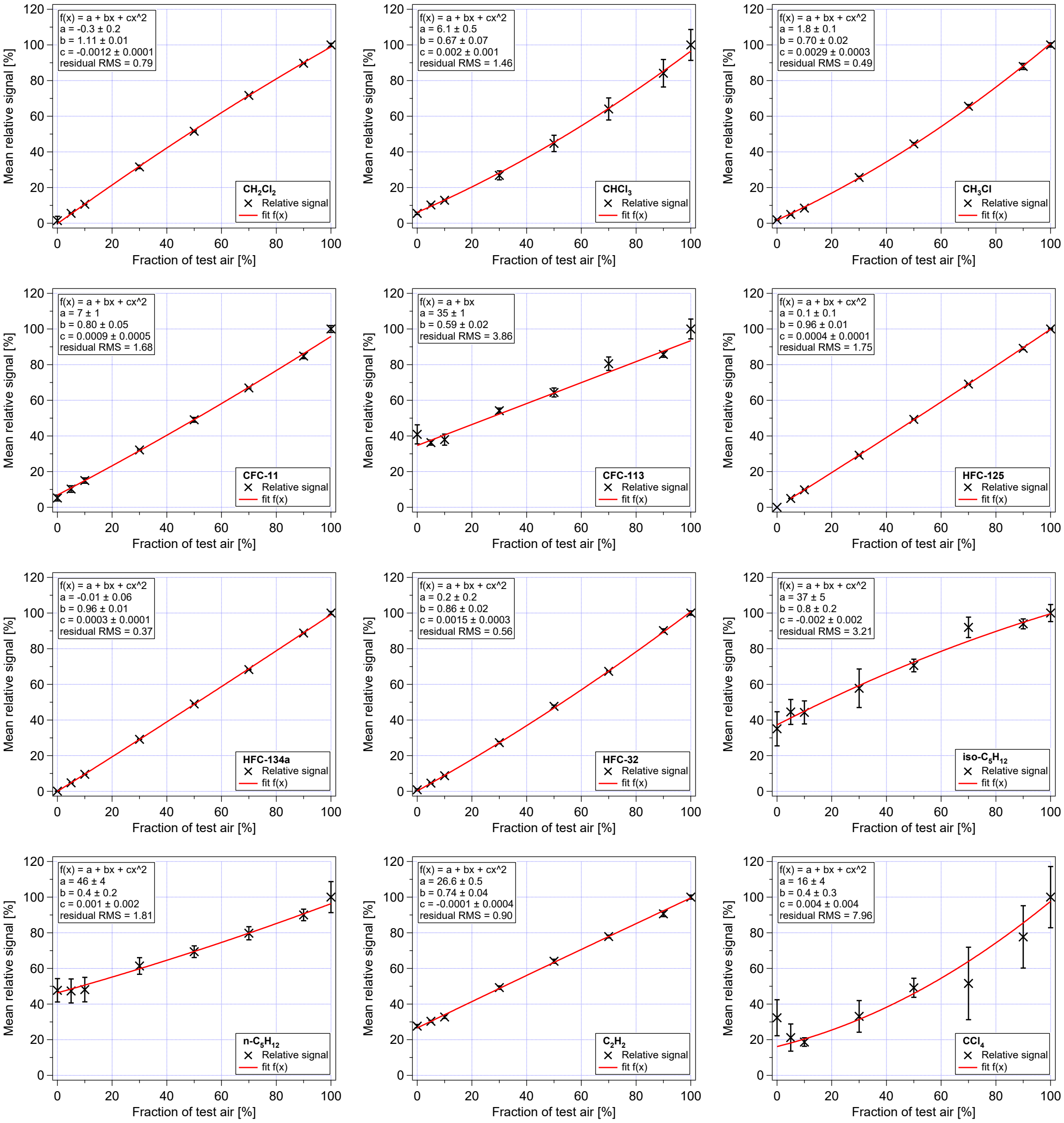

Figure B.7: Individual results from a signal response test. The averaged relative signals from different fractions of test air are fitted with a quadratic function.

because only S varies and N is constant[16]. In case of HAGAR-V, the most representative LODs are determined from operation during flight. Due to the usage of two in-flight calibration gases an eventual non-linear signal response can be compensated (see Section 3.3) and the LOD can be estimated from in-flight measurements during WISE.

---

[16] N is dependent on the choice of dwell time and measurement frequency within the relevant time intervals in which the mass fragment of the analyzed peak is selected (cf. Section 2.5.2)

N is the standard deviation of the non-sloping and peak free background signal next to the peak of interest. Interpreting N as a peak height the (notional) mixing ratio of N was calculated according to Section 3.3. The LOD is three times this value. Table 2.2 shows the LODs determined from WISE flight #12.

Appendix C

HAGAR-V during the aircraft campaign WISE

In this chapter standard procedures to treat HAGAR-V between flights and issues discovered during WISE are discussed. In addition, the instrumental parameters of the MS module used during WISE are listed in Appendix C.3.

C.1 Pre-flight preparations

Water somewhere inside the GC/MS sample line definitely has to be avoided. It can deactivate the separation column leading to a faster elution and therefore to shortened retention times which can shift peaks out of the time interval of measurement. In addition, it can influence the sensitivity of the detector having a negative effect on the measurement precision. Usually, the problem of getting water vapor inside the GC/MS system (other than from within an air sample) is minimized by constantly evacuating the MS and by keeping the carrier gas flow upright. HAGAR-V has to be turned off when there is no electrical supply at the aircraft. That is at least once per day for several hours during a campaign. In that time the vacuum of the detector lessens and air diffuses in backwards through the pumps and eventually through tiny leaks. The carrier gas flow is also turned off without electricity. Therefore, before a flight the instrument needs some time to get its heaters at operational temperatures and further to heat out the water that accumulated during the turn off phase.

Most of the tubing is not directly heated, thus water that sticks to its walls needs to be desorbed by passive heating. This can only be accomplished with the use of high temperatures of nearby heat sources and the dry carrier gas flow. For the GC/MS module the high temperatures mainly come from the preconcentration traps. In addition, the columns and the two valves (2-PosA and 2-PosB, see Figure A.7) can also be used to passively heat the different sample lines and slowly flush the water vapor through the MS vacuum chamber out of the system. The vacuum chamber itself is passively heated by the temperature of the ion source (250 °C) and the quadrupole (230 °C).

It takes about three hours to get the cumulated water out of the system when HAGAR-V has been turned off for one night. Measurement with the MS module is possible before that, although the performance might suffer.

There is the possibility to check for the water vapor content within the system by detecting the main fragment of water (m/z = 18) with the MSD. Unfortunately the counts are strongly dependent on how the detector configuration has been tuned. Therefore, an absolute number for an acceptable amount of water inside the MS system cannot be given here. From experience the counts can change within an order of magnitude depending on the (auto-)tuning of the mass spectrometers operational parameters (using ChemStation, Version E.02.02.1431, Agilent Technologies). During WISE, the measure for a properly baked out system was less than 20000 counts of m/z = 18 during a normal MS cycle without the enrichment of a sample.

To remove water vapor from the sample lines leading to the different modules, dry N_2 was sampled via the “blank-to-pump” option before a flight (see Figure A.4). There is no absolute necessity for this procedure but once it was done regularly before flights, no unexpected high water vapor at the beginning of a flight (as it was observed during WISE flight #10) has appeared anymore. For about 5–10 MS-cycles (15–30 min) N_2 was sampled short before takeoff.

Regarding general flight preparations, the ECD ovens have to be heated to their operational temperature of 340 °C at least two hours before takeoff to guarantee a stable performance of the detectors. In addition, it has to be validated whether or not there is enough gas in the flight bottles. The average gas consumption during WISE flights (from flight #7 to #16) is listed in Table C.1.

C.2 Issues during WISE

In this section several of the instrumental issues discovered during WISE are discussed. As far as a solution was found it is presented and analyzed.

Table C.1: Mean gas usage from each of the five gas bottles built in HAGAR-V during WISE flights. The gas usage is averaged over the flights #7 to #16. The four bottles built in the bottle module are of 2 l volume. The He bottle (used only for the MS module) is of 0.5 l.

Gas	Max. pressure [bar]	Mean usage [bar/h]	Used for...
SPAN	200	4.4	Calibration of all modules “SPAN-to-pump”
CAL	200	2.1	Calibration of all modules
$N_2(1)$	200	9.5	Carrier gas ECD Blank measurement of all modules Activate pneumatic valves
$N_2(2)$	200	6.7	Carrier gas ECD
He	200	1.8	Carrier gas MS Activate pneumatic valves

C.2.1 Overheating

Overheating of instrumental parts is primarily an issue during ground-based operations inside the aircraft. Nevertheless, important calibrations and flight preparations need to be done on ground with the necessity for a proper execution to ensure useful scientific data from the flights. During the first phase of WISE in Oberpfaffenhofen, HAGAR-V was confronted with high ambient temperatures of up to 30 °C. This led to even higher temperatures (up to 45 °C) within HALO when the mission power and other instruments were running. Convectional cooling of the separation columns with a fan to their initial set point of 35 °C is not possible when surrounding temperatures easily exceed this value.

Even more critical is the overheating of the Stirling Cooler which can actually lead to the destruction of instrumental parts. The temperature sensor at the coolers circuit board regularly crossed the advised maximum operational temperature of 35 °C up to a value of 45 °C. In addition, there is a temperature sensor at the fins where the Stirling cooler releases its waste heat. Higher temperatures than 54 °C cause an emergency shutdown of the cooler. In this case, software controlled constraints also turn off the preconcentration traps and further measurements with the MS module are not possible.

As a solution for the overheating during ground operation, an air conditioning system with a long and flexible exhaustion tube (to fit it inside the aircraft) and a bag of cotton at its exit (for a diffusive outflow) was found. The air conditioning system should not be run on AC mode if this causes the temperature to vary (usually by ± 10 °C) which has a strong influence on the GC/MS performance. It is sufficient to simply use the fan mode to bring outside air into the aircraft where the heat otherwise accumulates. Although for outside temperatures higher than 30 °C this might not work.

Running on APU (aircraft power unit), on the apron and in the air the pilots can turn on the air conditioner of HALO producing very stable temperatures if the aircraft is not ascending or descending. A setpoint of 67 °F (~ 19.4 °C) at the rear of the aircraft where HAGAR-V is positioned provides optimal conditions for the operation of the instrument during flights. The movable nozzles emerging from the aircrafts' wall were turned as such as they pointed towards the ECD and the MS module. A direct cold stream on the bottle module in the center of HAGAR-V should be avoided because it cools down the calibration gas bottles which can reduce the release of high boiling or otherwise "sticky" compounds.

C.2.2 Dehydrating of air samples

Crucial for the proper operation of the MS module are dry air samples (cf. Appendix C.1). For that reason all air samples passing the two pumps get dehydrated. This is always the case for outside air samples and possible for one calibration gas as well as N_2 via the "-to-pump" setting (see Figure A.4).

During the first WISE flights the air sample was dehydrated by magnesium perchlorate hydrate (Merck KGaA, Darmstadt) in an aluminum housing of 100 mL constantly heated to 60 °C during the flights. Instead of dehydrating the air sample, the pre-hydrated magnesium perchlorate (~ 83 % $Mg(ClO_4)_2$ and ~ 17 % H_2O) kept the air sample at a water vapor level of ~ 200 ppm. Different dehydrating trap temperatures from ambient to 80 °C as well as tropospheric (H_2O several hundred ppm) and stratospheric air samples ($H_2O < 10$ ppm) did not significantly change the water vapor level inside the sample. At higher water trap temperatures effects like the re-liquefaction of water can appear and were thus not tested. The result of having around 200 ppm water vapor inside each GC/MS sample is catastrophic and no quantitatively scientific results can be expected from such measurements due to changes in the retention time, in peak shape, and peak area. The other two instrumental modules of HAGAR-V did not show any problems with the relatively high water vapor level or could otherwise compensate it.

To overcome this water problem of the MS module, the water trap was bypassed and the air samples were not dehydrated (or in this case also hydrated) since WISE flight #7. Therefore, the sample valve of the MS module (S1G, see Figure A.7) was closed for every sample passing through the Base module's pumps during takeoff and most parts of the troposphere. If water vapor values were below ~ 60 ppm, the flight operator could switch the S1G valve to sampling mode via a digital switch in the control software. The water vapor could be observed online every few seconds from the in situ data provided by the FISH (Fast In-situ Stratospheric Hygrometer, Zöger et al., 1999) instrument of the research center Jülich.

The S1G valve could also be shut again if water vapor levels should rise to a critical level. No tests were conducted to define a threshold of maximum water vapor within a sample, causing the operator to shut or open the S1G valve. From experience the threshold was set to a water vapor level of ~ 60 ppm and a range of about ± 20 ppm lay in the hands of the operator observing the water vapor trends. During WISE there were four flights (#7, #8, #9, and #14) where the air had to be cut off again for a few samples after the MS module has already started measuring at low water vapor mixing ratios.

Most of the time the MS module measured outside air containing water vapor of around 5 ppm. The overall water vapor median for all flights where the MS module sampled air and of which water vapor measurements are available was 7.4 ppm[1] according to FISH. During the time the MS sampling was switched off, the MS module still measured calibration gases (except for "SPAN-to-pump") and blanks.

Bypassing the faulty dehydration unit made it possible to measure during about 90 % of the WISE flights after this change was made (from flight #7 onward). Nevertheless, this was a workaround and a proper solution has been found for the campaigns following WISE. The use of magnesium perchlorate without the pre-hydration showed good results in terms of sample dehydration even in relatively wet the tropical troposphere.

C.2.3 Regulation of mass flow controller

The mass flow controller MFC1A (see Figure A.7) controls the volume of the preconcentrated sample during a MS module measurement cycle. The maximum sample flow in direction of adsorption is primarily limited by the trap's restriction to ~ 275 ml/min (slightly depending on the filling of the used preconcentration trap). However, the sample volume is further restricted by the regulation of the MFC. Within 60 s preconcentration time, different MFC setpoints in ml/min (50, 100, 150, 200, 250, and 275) were analyzed. The flow regulation of the MFC at the setpoint is very precise (< 1 % of setpoint, own tests) thus the resulting sample volume should be equal to the chosen setpoint in this test. Instead, the sample volume was around 25 ml to 40 ml less than the MFC's setpoint (loss increased in number from lower to higher setpoints). This is due to the regulation behavior of the MFC before reaching the desired setpoint. After an initial opening of the MFC1A

---

[1] n = 496; average: (10 ± 16) ppm

valve to increase the flow, it closes again for several seconds before it opens again to achieve proper sample regulation (e.g. visible in Figure 2.10).

To determine the sample volume the measured (10 Hz) mass flow is integrated over the preconcentration time. This showed that these MFC regulation irregularities are well reproducible for each individual setpoint with a reproducibility of 0.05 % to 0.1 % relative to the chosen setpoint (lowest value for 250 ml/min, highest for 50 ml/min and 100 ml/min). The MFC's regulation behavior could not be fixed but it also did not cause significant problems other than measuring smaller sample volumes than potentially possible. Without this regulation issue the majority of flights could have ~ 18 % larger sample volumes or could require equally less preconcentration time.

C.2.4 Very strong adsorbent

The adsorbent Carboxen 572 (Supelco) is a very efficient trap for low boiling molecules even at room temperature. Although, desorbing high boiling molecules or ones especially well trapped by the adsorbent might exhibit inefficiencies. An incomplete desorption, for example due to a cold spot inside the trap, can lead to false measurements and memory effects that affect succeeding measurements (Appendix B.2.2). To avoid that, usually a weaker adsorbent is put in front of the stronger one for trapping the high boiling molecules while the low boilers break through and get adsorbed by the following strong adsorbent. Thereby the desorption of the high boiling molecules can be significantly improved.

The attempt to use the relatively weak adsorbent Carbotrap B (Supelco) together with the strong adsorbent Carboxen 572 showed very good results in terms of ad- and desorbing properties for the target species (Lauther, 2015). Nevertheless, Carbotrap B was not suitable for the use on an aircraft because it did grind itself to a smeary and very fine powder when exposed to aircraft and instrumental vibrations, thereby putting the instrument on high risk of complete contamination. Therefore during WISE no such weaker adsorbent was used and as a consequence C_2Cl_4 (boiling point of 121 °C[2]) could not be used for scientific analysis due to memory effects.

For campaigns following WISE another adsorbent to replace Carbotrap B was tested. Graphsphere 2017 (Supelco) — remotely comparable with Carbotrap B — is available in the mesh size of the used Carboxen 572 (mesh 20/45) and comparably solid in structure. Promising tests were conducted to investigate its ad- and desorbing behavior in a self built preconcentration trap (see appendices B.1.3 and B.2.2).

---

[2] GESTRIS Database: http://gestis.itrust.de (16.01.2020)

C.2.5 Species that were not usable for scientific analysis

The HAGAR-V MS module measured 12 species during WISE. Five of them could not be used for scientific analysis:

- ▷ Iso- and n-Pentane were measured but in outside air they have been below the detection limit (cf. Table 2.2). This is due to their extremely short tropospheric lifetime (few days) and the fact that during WISE the MS module only measured at the tropopause region and above (Appendix C.2.2) where Iso- and n-Pentane mixing ratios are expected to be below the LOD.
- ▷ CCl_4 was measured only on a very small mass fragment ($m/z = 49$) as the neighbor peak of CH_2Cl_2. CCl_4 could not be properly analyzed on this mass fragment .
- ▷ As mentioned in Appendix C.2.4 C_2Cl_4 exhibited strong memory effects due to the used adsorbent and has therefore not been used for scientific analysis.
- ▷ $C_2H_2Cl_2$ was measured on $m/z = 61$ expressing large peaks. As mentioned in Section 2.3.1 this peak is very likely the result of chemical processes caused by the combination of chlorinated species, water vapor, and the Al_2O_3 stationary phase of the used capillary columns. This and other effects are also mentioned by Noij et al. (1988).

C.3 MS module parameters during WISE

HAGAR-V uses complex sequences to supply the individual modules with different gas samples through one stream selection valve (SSV). The most overruling instrument in the choice of sequence is the MS module that has the longest sample integration time in addition to a sample line purging with the same gas for about 60 s before the sample integration. The ECD module measures every 90 s for about 5 s thus often has to obey the programmed sequence of the MS module. The continuous measurement of the CO_2 analyzer in the MS/Licor module measures whatever one of the other two instruments desires and thereby is calibrated as well. In Figure C.1 the schematic sequence of the gas samples used by the MS module during most of the WISE flights is presented.

The measurement parameters of the MS module changed slightly from its first successful measurement flight until a stable performance could be achieved. Table C.2 gives an overview of the MS module parameters used during WISE as well as the changes that were made after flight #7. Table C.3 shows the used SIM parameters of the MSD for the detection of extremely narrow peaks (cf. Section 2.5.2).

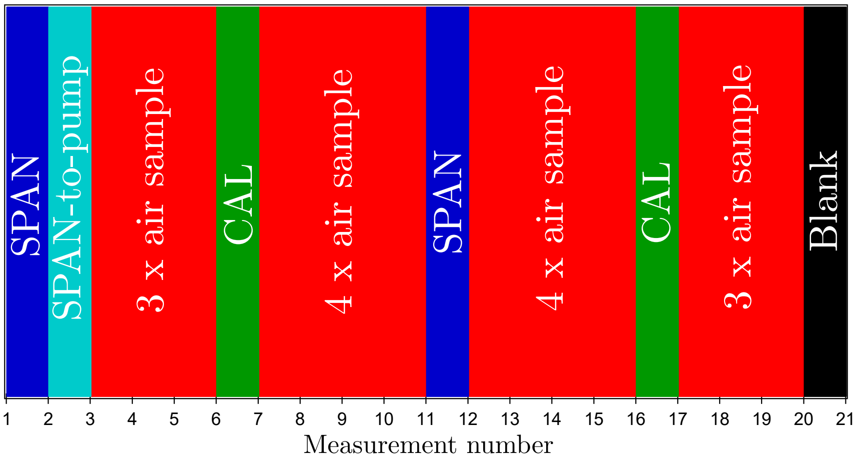

Figure C.1: Sequence of gas samples as received by the MS module during WISE.

Table C.2: Measurement parameters used for the MS module during WISE. Carboxen 572 was always used as adsorbent but the preconcentration trap has changed for flight #16. Al_2O_3/Na_2SO_4 fused silica PLOT columns were used as pre- (4 m) and main-column (5 m) during all WISE flights. The head pressure for sample air was 3 bar(a).

Flights:	#7	#8	#9	#10	#11–#14	#15	#16
Cycle length [s]	240		180				
Adsorption temp. [°C]	5	20					
Adsorption time [s]	58			38			
Sample volume [ml]	79	75	123	100	130		
Trap evacuation [s]	2						
Desorption temp.* [°C]	250						230
Desorption time [s]	120						
Pressure carrier gas [bar(a)]	1.6						1.1
T_{min} pre column [°C]	35						
T_{min} main-column [°C]	40			35			
T_{max} both columns [°C]	160						
Onset pre col. ramp [s]	5						
Rate pre col. [°C/s]	6,3						
Onset main col. ramp [s]	25			50			
Rate main col. [°C/s]	6			3.6			
Onset back flush [s]	60		50				70
Pressure back flush [bar(a)]	0.9					0.91	0.92

*Temperature of heating wire (it differs from the temperature inside the trap, see Section 2.2.3)

Table C.3: MS SIM parameters during WISE for the measurement of extremely narrow peaks. Parameters used since WISE flight #10.

Window [min]		Dwell time of m/z [ms]								Cycles [s^{-1}]
From	To	19	43	49	50	61	83	101	166	
0	0.04	1			13					28.5
0.04	0.1	1			10			2		28.3
0.1	0.25	1	8		5			3		24.9
0.25	0.35	1	7			8	3	3		21.3
0.35	0.45	1		7		8		3		23.7
0.45	0.55	1		7				3		30
0.55	0.65	1		7			35			15.3
0.65	0.75	1		5			40		15	11.8
0.75	End	1					10		45	12.7

Appendix D

MS module: data processing

In this chapter supplemental information about the processing and the correction of WISE MS flight data is given. Experiments analyzing HAGAR-V's several in-flight diagnostic modes are discussed here in great detail. The sections mainly refer to Chapter 3.

D.1 Approximation of the EMG fit

The numerical implementation of the used EMG fit function (equation 3.1) was optimized by using IGOR's erfc(x) function instead of $(1-\mathrm{erf}(x))$ obtaining a higher precision during the computing process. Nevertheless, the used EMG expression can still cause the fit function to crash, if one of the factors of equation 3.1 runs out of the computational range, in particular while iterating the parameter τ close to zero. To avoid such a crash the following constraint is used while fitting:

If $z = \frac{1}{\sqrt{2}}\left(\frac{\sigma}{\tau} - \frac{x-\mu}{\sigma}\right)$ is very large the scaled complementary error function in equation 3.1 ($\mathrm{erfcx}\,(z) = e^{z^2}\mathrm{erfc}\,(z)$) can be approximated by the first of its asymptotic expansion: $\mathrm{erfcx}\,(z) \approx \frac{1}{z\cdot\sqrt{\pi}}$ (Kalambet et al., 2011).

The threshold of $z > 6.71 \cdot 10^7$ when to use this approximation given in Kalambet et al. (2011) did not work with our fitting routine. The used data processing software IGOR (Version 4.0.1.0) does not have an internal erfcx(z) function and calculating the product explicitly instead causes either of the two factors to run out of the computational range more easily (due to an overflow of the used double precision). Thus the threshold when to switch to the use of the approximated EMG function was empirically determined to $z > 25$. The resulting asymptotic expression of the EMG function (equation 3.1) used in such a case is:

$$f(x) = \frac{h \exp\left(-\frac{1}{2}\left(\frac{x-\mu}{\sigma}\right)^2\right)}{1 + \frac{(x-\mu)\tau}{\sigma^2}} \tag{D.1}$$

The empirical threshold ($z > 25$) for the usage of the asymptotic approximation of the EMG function was rarely crossed by any of the peaks detected by the MS module. In fact, only CH_2Cl_2 (0.4 % of all used peaks i.e. 5 out of 1179) and $CHCl_3$ (0.09 % of all used peaks i.e. 1 out of 1154) had a significant number of peaks fitted with the approximated function D.1.

D.2 Analysis of systematic bias of in-flight SPAN measurements

With the use of the calibration gas CAL (and correction of system contamination if needed — see Appendix B.2.1) the single point-calibration was used on the MS flight data according to Section 3.3.1. The thereby also calibrated in-flight measurements of the other calibration gas, SPAN, were split in two data sets for the analysis. From each flight all SPANs as well as only the SPANs that follow an air sample (every second measurement, see Appendix C.3) were analyzed. For each flight and species the flight average as well as the relative precision[1] of these two SPAN data sets were calculated. Significantly biased SPAN measurements were determined if the difference between the flight average of all SPANs and only the SPANs that succeed an air sample is significantly different (by one standard error) from zero (left panels in figures D.1 and D.2). According to the comparison with the ECD module in Section 3.4 this implies that the SPAN measurements following a blank sample are biased.

Before biased SPAN measurements were rejected it was determined if this would have a negative effect on the SPAN precision. Drifting detector signals are corrected linearly between two calibrations in the detrending process (cf. Section 3.3.1). To leave out every second calibration can have a significant effect on the regarded calibration gas precision in case of non-linear drifts. Consequently this would affect the calculation of mixing ratios of air samples. Therefore, a worse precision of the unbiased SPAN measurements (following air samples) than of all SPAN measurements suggests the bias of SPANs that follow a blank measurement is smaller than the effect of non-linear signal drifts during the flight. Thus, in case of biased SPAN measurements it was additionally considered if the gained

---

[1] Standard deviation of respective SPAN measurements divided by the respective nominal CAL mixing ratio (see Table E.2) in percent

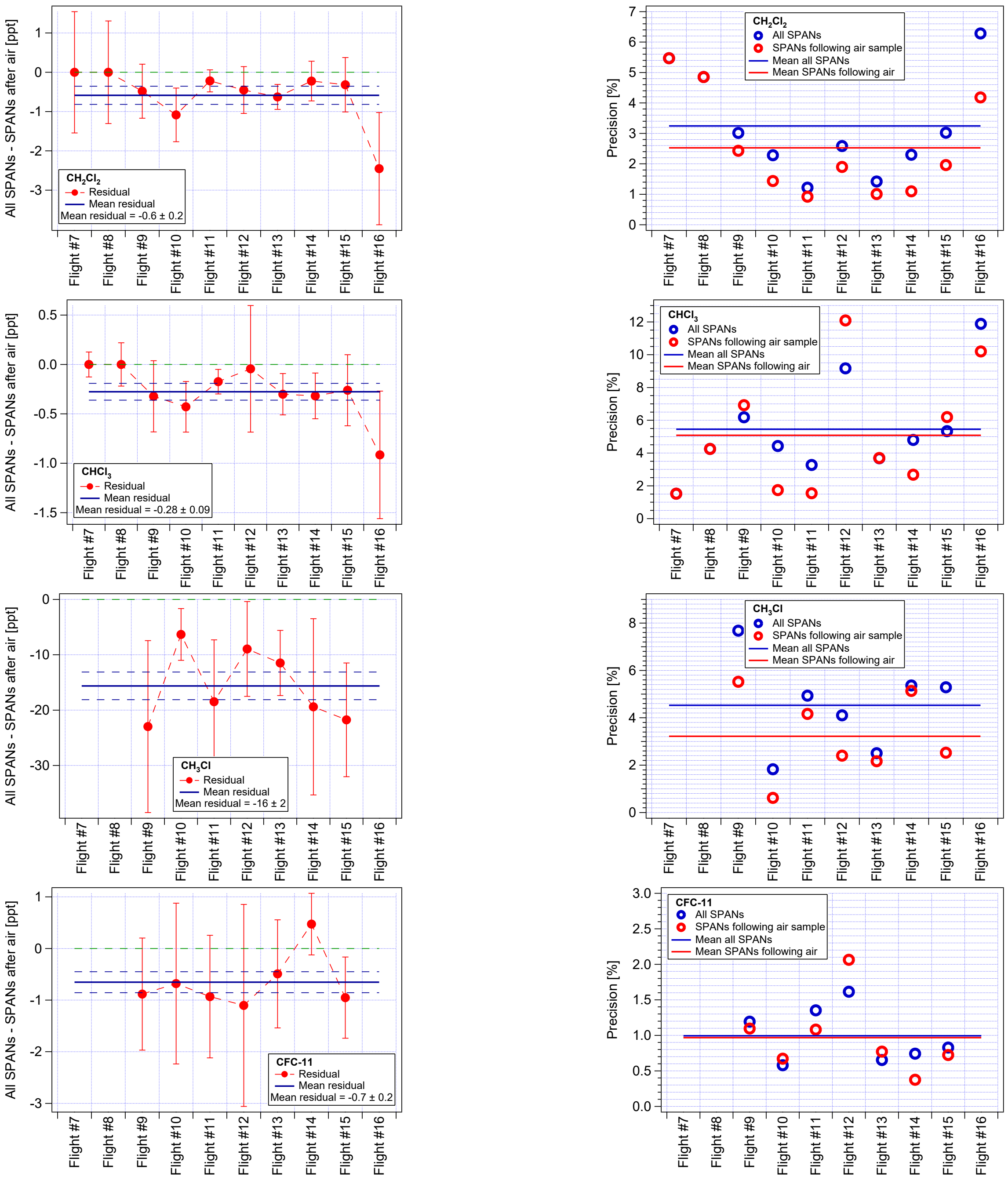

Figure D.1: Comparison of all SPAN measurements and only the ones that follow an air sample. Left panels show for each WISE flight the difference between the average of all SPANs and the average of only the ones that follow an air sample. Right panels show for each flight the relative precision (relative to CAL, Table E.2) of the regarded set of SPAN measurements.

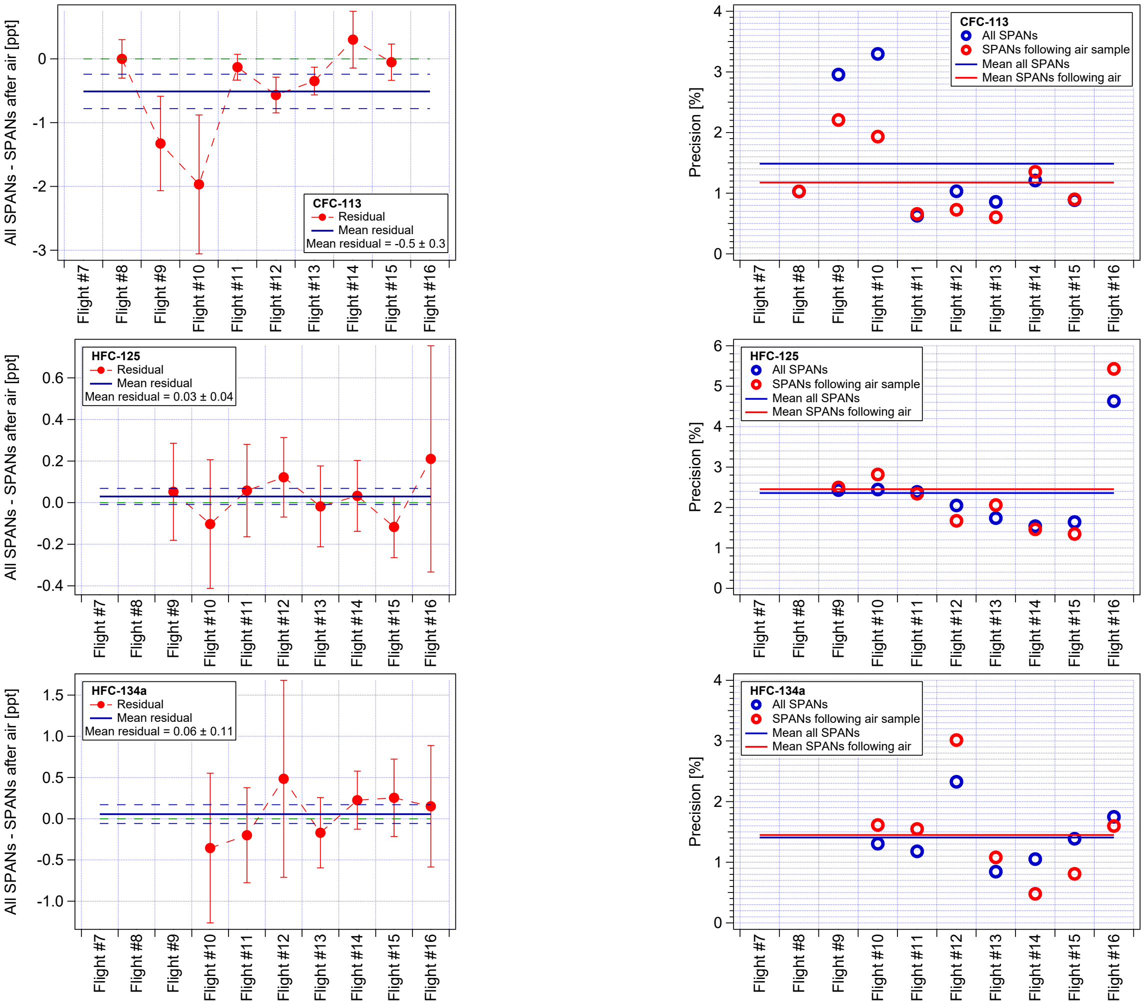

Figure D.2: See description of Figure D.1

accuracy and precision by discarding the biased SPANs is not overruled by less resolved drift corrections. Biased SPAN measurements were discarded when the precision of all SPANs was worse or equal to the precision of the unbiased SPAN measurements of the regarded flight.

The flights #7 and #8 had a different measurement sequence without any SPAN measurement following a blank measurement. Therefore these two flights show no biased SPAN measurements. An overview of the results is given in Table 3.2.

D.3 Peak height vs peak area

In general, the peak area taken from the fitting function is used as response R to evaluate MS signals (Section 3.2). The possibility and the impact of varying peak shapes (including the peak height) are higher than to loose molecule counts in the time of peak elution. Thus interpreting the peak area of MS data generally yields more robust results.

During WISE no significant differences between the calculation of mixing ratios from peak areas or peak heights could be determined for all species but CH_3Cl. The average mixing ratios of CH_3Cl calculated from peak heights are (20.5 ± 0.4) ppt larger than the mixing ratios calculated from peak areas. This is about 3.4 % of the tropospheric background gas CAL (Table E.2). The absolute difference of the same comparison was similarly (20.8 ± 0.4) ppt for all flights implying a very constant offset.

The mixing ratio of CH_3Cl was determined from the mass fragment m/z = 50. Figure D.3 shows a representative example peak of each an air, a CAL, and a SPAN measurement. Regardless of the sampled gas the peak appears to tail. In addition, a very small fragment of HFC-125 (< 1 % of all HFC-125 mass fragments) elutes at the the tail of CH_3Cl's peak, impacting its peak shape insignificantly. However, in air and CAL gas samples no coeluting compound at the front of CH_3Cl's peak is visible whereas the SPAN measurement exhibits a small knee at the peak's front side. This small peak at the front of CH_3Cl's SPAN peaks is too small and too close to the peak center to be corrected by a double peak fit (Section 3.2.2). Therefore the two calibration gases are not exactly comparable and could not be used both for calibrating CH_3Cl. However, the results from Section 2.4 and Appendix E.2 show a non-linear detector response for CH_3Cl mixing ratios, implying the necessity to use both calibration gases (two-point calibration) to determine accurate mixing ratios of air samples.

The larger peak area of the affected SPAN measurements implies an underestimation of the mixing ratios calculated for the unaffected air measurements. The peak height is therefore less affected by the small coeluting peak at the front side of CH_3Cl because only the tail of the disturbing peak could impact CH_3Cl's peak height if it extends that far. In addition, the mass fragment of HFC-125 eluting at CH_3Cl's peak tail does not influence CH_3Cl's peak height either. This leads to the conclusion that the analysis of peak heights instead of peak areas yields the most accurate mixing ratios for CH_3Cl.

The average measurement precision of CH_3Cl is not affected when either calculated from peak areas ((2.9 ± 0.2) % of CAL) or peak heights ((2.8 ± 0.3) % of CAL). The precisions of the individual flights are comparable when determined from peak heights or peak areas. Exceptions are WISE flights #9 and #13 where mixing ratios calculated from peak heights

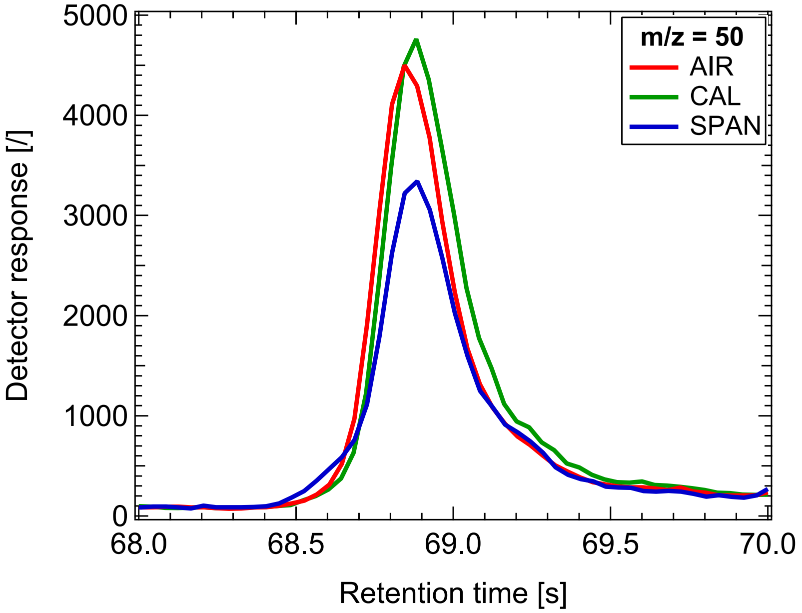

Figure D.3: Example peaks of air (red), CAL (green), and SPAN (blue) samples of the mass fragment m/z = 50 to determine CH_3Cl. The SPAN peak exhibits a coeluting compound at its front.

are significantly more precise and flight #10 where the mixing ratios calculated from peak areas are more precise (the individual precisions from peak heights are shown in Table 2.3). This implies no general loss of measurement precision when calculating the CH_3Cl mixing ratios from peak heights instead of peak areas. Thus, the calculation of CH_3Cl mixing ratios from peak heights instead of peak areas leads to more accurate and equally precise mixing ratios.

D.4 Analysis of system contamination during WISE

In this section supplemental information about Section 3.3.5 is provided. Considerations regarding the consequences implied by the results of the analysis of in-flight blank measurements are discussed.

The determined mean mixing ratio of the blank measurements of one flight ($\overline{\chi}_{blank}$) was considered relevant only when at least half of the blank measurements in that flight were above the detection limit (Appendix B.4) and marked red in Figure D.4. Otherwise the contamination at the regarded flight was considered to be not significant and marked green. In such a case none of the blank peaks were detectable for the regarded species and WISE

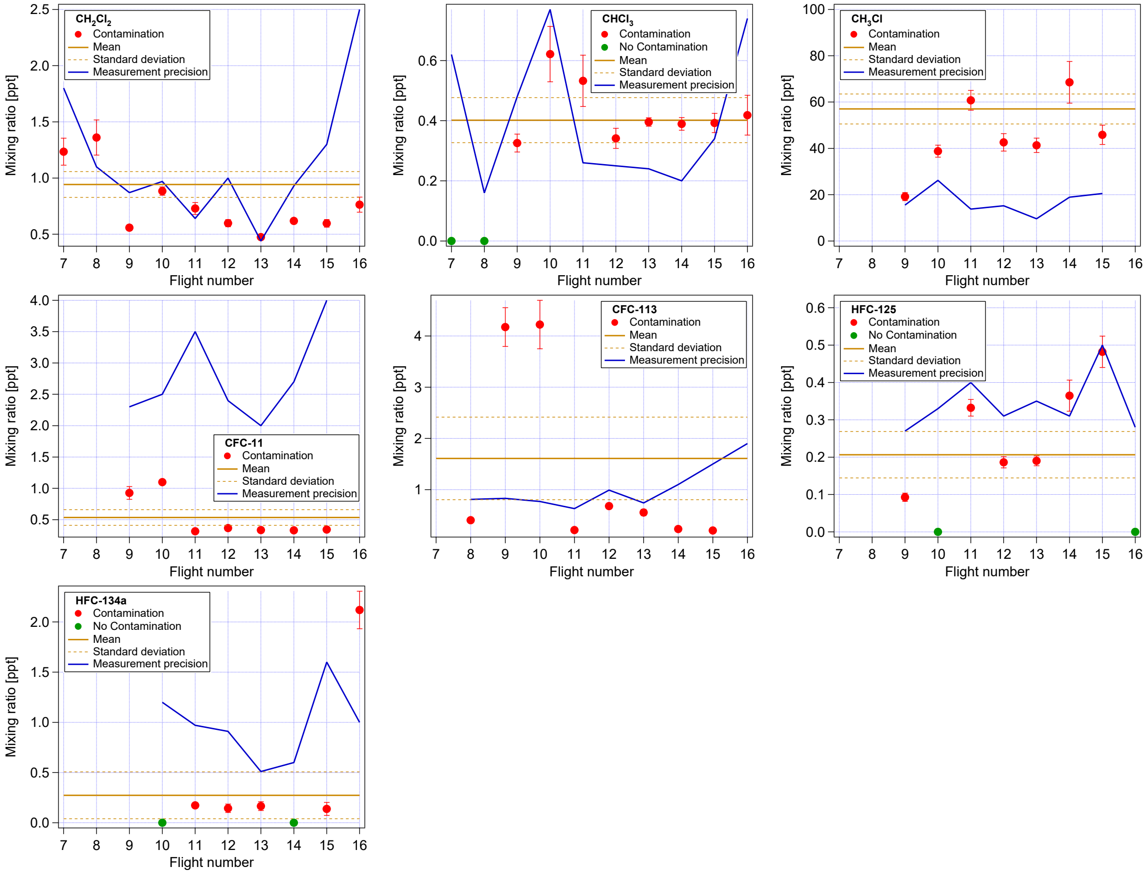

Figure D.4: Plots of identified possible contamination during WISE flights. Red markers implicate the average mixing ratio of all blank measurements per flight where at least half of the blanks showed peaks above the limit of detection. Green markers implicate clean blank measurements for the respective flight. The ocher line is the contamination average for all flights with its respective standard deviation in dashed lines. The blue line is the determined measurement precision for each flight (see Section 2.5.3).

flight. The error bars in Figure D.4 represent the standard error of the respective averaged blank measurements.

The N_2 used for in-flight blank measurements was purified[2] in three different steps as described in Appendix A. However, there is no guarantee that the blank gas was completely free of any target species. In addition, the N_2 gas bottle used for the in-flight blanks were refilled before every flight (due to its main usage as ECD carrier gas) leaving a small risk of gas contamination during the refilling process. The N_2 flight bottles were refilled from two different main bottles. Differing contamination in the main bottles could lead to

---

[2] A gas purity comparable to 6.0, implicating a gas purity of 99.9999 % or a total impurity of max. 1 ppm of other gases

varying in-flight blank contamination depending on flight. Also mixtures of the two main N_2 gas bottles are possible because the residual gas was kept insight the flight bottles before refilling. This implies that different contamination in the main bottles could cause an impurity of the in-flight blank gas that varies after each refilling process. With that in mind the correction of any measurements for the appearance of contamination needs to be considered well.

Without any direct reason to assume contaminated blank gas it is plausible to consider correcting the measurements in such cases where the majority of the averaged blank mixing ratios is significantly larger than the respective measurement precision of the regarded species. In such a case the affected species was considered to be contaminated and consequently all WISE flights were corrected for the respective contamination of this species. In case of obvious outliers only the outlying flights were corrected.

Figure D.4 shows that only CH_3Cl and $CHCl_3$ exhibit a majority of flights with blank mixing ratios larger than their measurement precision. They both were corrected for system contamination in all flights consequently even if the contamination was not significant in all flights.

Outliers are regarded separately and were observed only for CFC-113 (flights #9 and #10) and HFC-134a (flight #16). Obviously in these flights something different from the other flights was causing the system contamination (cf. Figure D.4). The possibility that only in these flights the N_2 gas used for the blank measurements was contaminated with CFC-113 or HFC-134a has to be considered. A contamination of the blank gas itself would lead to a false correction. However, the comparison with CFC-113 measured by the ECD module (Appendix D.6.4) showed no significant difference to the MS data that were corrected for CFC-113 contamination. In addition, the ECD module did not detect CFC-113 contamination within the ECD blank measurements of these flights. This supports the assumption that the used N_2 gas for the blank measurements did not cause the irregularly high CFC-113 contamination during flights #9 and #10. The outlier of HFC-134a at flight #16 is comprehensible under the consideration that for flight #16 a new preconcentration trap was used. Without the proper time for conditioning the adsorbent inside the new trap, outgassing of any substance is plausible. Therefore both CFC-113 and HFC-134a were corrected for system contamination but only for the discussed flights.

D.5 Analysis of SPAN-to-pump measurements

In this section supplemental information about the analysis of SPAN-to-pump measurements from Section 3.3.6 is provided.

The difference between the mean mixing ratio of the SPAN-to-pumps and the nominal SPAN gas value was calculated for each species and flight. An exception is $CHCl_3$ which is calibrated linearly without using the SPAN measurements (cf. Section 3.3.2). For $CHCl_3$ the SPAN mixing ratios were calculated from a single point calibration (using CAL) in the same way as the SPAN-to-pump values to provide a fair comparison that minimizes the influence of eventual signal non-linearity. Instead of the nominal SPAN value the determined mean mixing ratio of the SPAN measurements of the respective flight was used for the $CHCl_3$ comparison.

Figure D.5 shows the differences between the average SPAN-to-pump measurements and the SPAN mixing ratio. The error bars indicate two standard errors of the respective mean SPAN-to-pump mixing ratio. In case of $CHCl_3$ the standard error is the propagated errors of the average SPAN-to-pumps as well as of the averaged SPAN measurements. Systematically biased SPAN-to-pump measurements were identified when the the difference between SPAN and the average SPAN-to-pump measurements were significantly (by the measure of the error bars) different from zero. A positive difference indicates larger signals over the pumps and a negative difference indicates smaller signals over the pumps.

Some species exhibit a clear tendency for the SPAN-to-pumps to be larger (or smaller in the case of CH_3Cl) than the SPAN values but each species has at least one flight with a smaller mean SPAN-to-pump value. This strongly suggests that for most of the species the difference between SPAN-to-pump and SPAN is not only dominated by the different pathway the gas takes, it is very likely that other parameters also influence these flight-to-flight variations. On the one hand, biasing effects could be caused by the pumps in the form of outgassing or ad-/desorbing effects. These effects can further be dependent on ambient temperature, sample pressure or sample flow. On the other hand, due to the sample preconcentration also MS specific parameters can be thought of to possibly cause biasing effects on the resulting measurement. Pressure differences during the adsorption process or disturbances of the water vapor equilibrium in the sample line are just two examples that could potentially have an influence on different measurement signals between SPAN and SPAN-to-pump.

Confidence in the hypothesis that there are also MS specific parameters influencing the SPAN-to-pump measurements gives the comparison of CFCs measured by the ECD module. The ECD SPAN-to-pump measurements of CFC-11 and CFC-113 show no significant

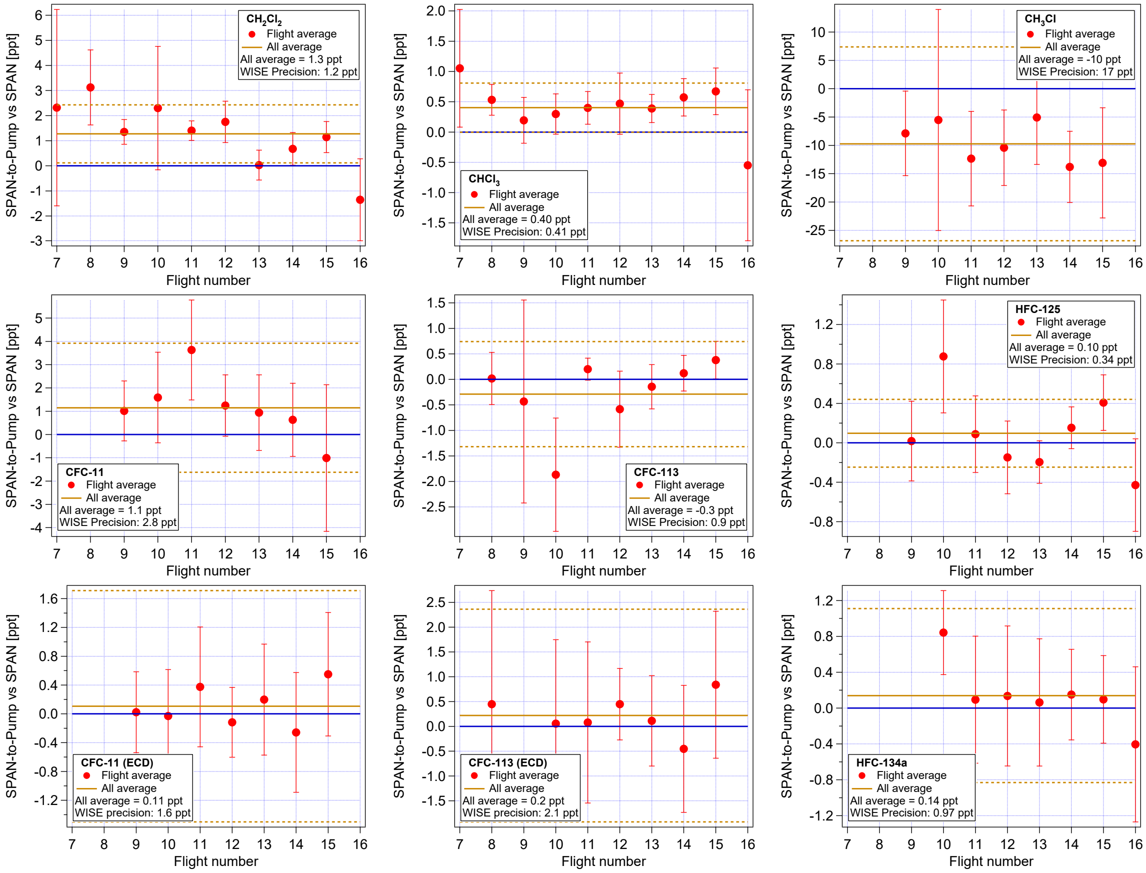

Figure D.5: Differences between average SPAN-to-pump measurements and the SPAN mixing ratio for each WISE flight. The error bars represent two times the standard error of the SPAN-to-pump measurements. The solid ocher line shows the average difference for all flights and the dashed lines are added and subtracted to that the average precision determined in Section 2.5.3. $CHCl_3$ uses measured values of SPAN to compare with the SPAN-to-pumps. The error of the $CHCl_3$ SPAN measurements is propagated to the shown error bars. CFC-11 (ECD) and CFC-113 (ECD) are the results measured by the ECD module.

differences to the respective SPAN mixing ratio (see Figure D.5). Thus at least for these two species it can be said with high confidence that there is no outgassing or de-/adsorbing sources/sinks in the sample line before the sample gets distributed to the measuring modules. It is more likely that the observed differences are caused by other parameters on to which only the MS module is sensitive.

As shown for the CFCs, MS specific effects on the measured SPAN-to-pump values have to be considered for all target species. Thus, it remains unsure if the sample pathway through the pumps does have a direct effect on the measured species. In addition, it cannot be determined if MS specific influences on samples passing through the pumps only affect the SPAN-to-pump measurements or also the outside air samples. Therefore, the provided in-flight analysis of the influence of the suction pumps is not sufficient to specify the cause of differing SPAN-to-pump measurements. The analysis of the differences between SPAN-to-pump and SPAN therefore has to be interpreted more generally as an indication for a potential systematic bias that might also apply to the air samples.

Without any further information on the cause of differing SPAN-to-pump measurements a specific concept for a correction of the data is difficult to formulate. However, a trivial attempt for data correction is adding or subtracting a constant offset for flights with obviously outlying SPAN-to-pumps. In case of larger SPAN-to-pump values than SPAN the average SPAN-to-pump value of the respective flight was subtracted from the air samples, otherwise the average SPAN-to-pump value was added to the air samples. To test the quality of this zero order correction tracer-tracer correlations of the corrected species were analyzed to decide if the correction makes the resulting mixing ratios more realistic in an atmospheric context.

The tested offset correction proved to be unfit for all but one flight and species which will be discussed separately below. In general, tracer-tracer correlations became less compact after such a data correction implying no direct transformation of an observed offset of SPAN-to-pump measurements to the air samples. Thus, the general assumption and correction of a zero order effect is too trivial for the observed phenomenon. This could also indicate that observed offsets were only affecting the SPAN-to-pumps and had no influence on the air measurements. However, this cannot be proven on the given data basis and an uncertainty of a systematic bias on the MS air measurements remains. To include this uncertainty in a global MS data uncertainty it was accordingly formulated and quantified.

Each target MS species exhibits at least one flight with a significant difference between SPAN-to-pump and SPAN. This implies an uncertainty concerning all air measurements of each MS target species. Due to a rather clear tendency in the SPAN-to-pump offsets and only a few significant offsets for most of the flights and species, a fair but mostly conservative general uncertainty estimate was formulated. For each species the absolute average SPAN-to-pump offset for all flights approximates the uncertainty of a systematic bias in each single flight — even if the flight does not exhibit a significant SPAN-to-pump offset. To provide a relative uncertainty the WISE absolute average SPAN-to-pump offsets are calculated in percent relative to SPAN thereby including potential dependencies on the air samples' mixing ratios. The results (σ_{S2P}) are added to the relative accuracy (σ_{Global}) of WISE MS measurements and are given in Table E.4.

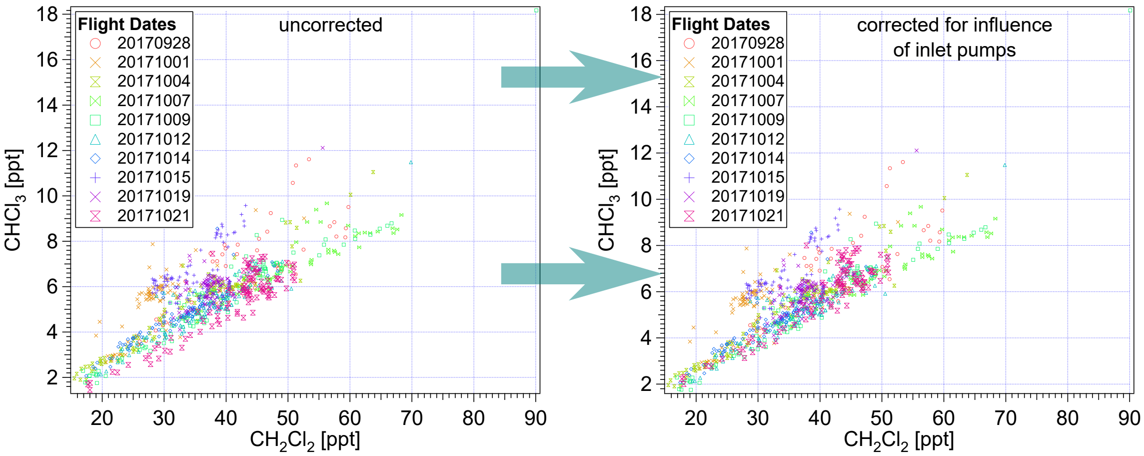

Figure D.6: $CHCl_3$-CH_2Cl_2 correlation of all WISE flights. Flight #16 (20171021; pink color) was corrected for a $CHCl_3$ SPAN-to-pump offset in the right panel.

The only species corrected for differing SPAN-to-pump measurements was $CHCl_3$. Figure D.6 shows two plots depicting the $CHCl_3$-CH_2Cl_2 correlation. Both species have similar sources and sinks but CH_2Cl_2 has a much stronger pronounced seasonality which explains the outlying relatively lower CH_2Cl_2 mixing ratios (see sections 1.3, 4.2.2 and 4.3.1). The uncorrected plot in Figure D.6 (left) shows a clear offset of $CHCl_3$ data from flight #16 (20171021; pink color) to the compact background correlation. On the right plot the $CHCl_3$ SPAN-to-pump offset of WISE flight #16 was added to the $CHCl_3$ measurements. With the offset correction of 0.5 ppt flight #16 fits well to the other flights in the expected compact background correlation and provides high confidence that this correction improves the quality of $CHCl_3$ data. Correlations with other tracers strengthen this statement but are not shown in the present work.

D.6 Detailed comparison with other instruments

In this section the detailed analysis of the comparison of CFC-11 and -113 measured by the MS and ECD module is presented. The summarized results are given in Section 3.4. Figures D.7 and D.8 show for each flight the measurements of the ECD and the MS module of CFC-11 and -113, respectively. The MS data are processed according to Table 3.2. The measurements of both modules agree well with the exception of a few outliers.

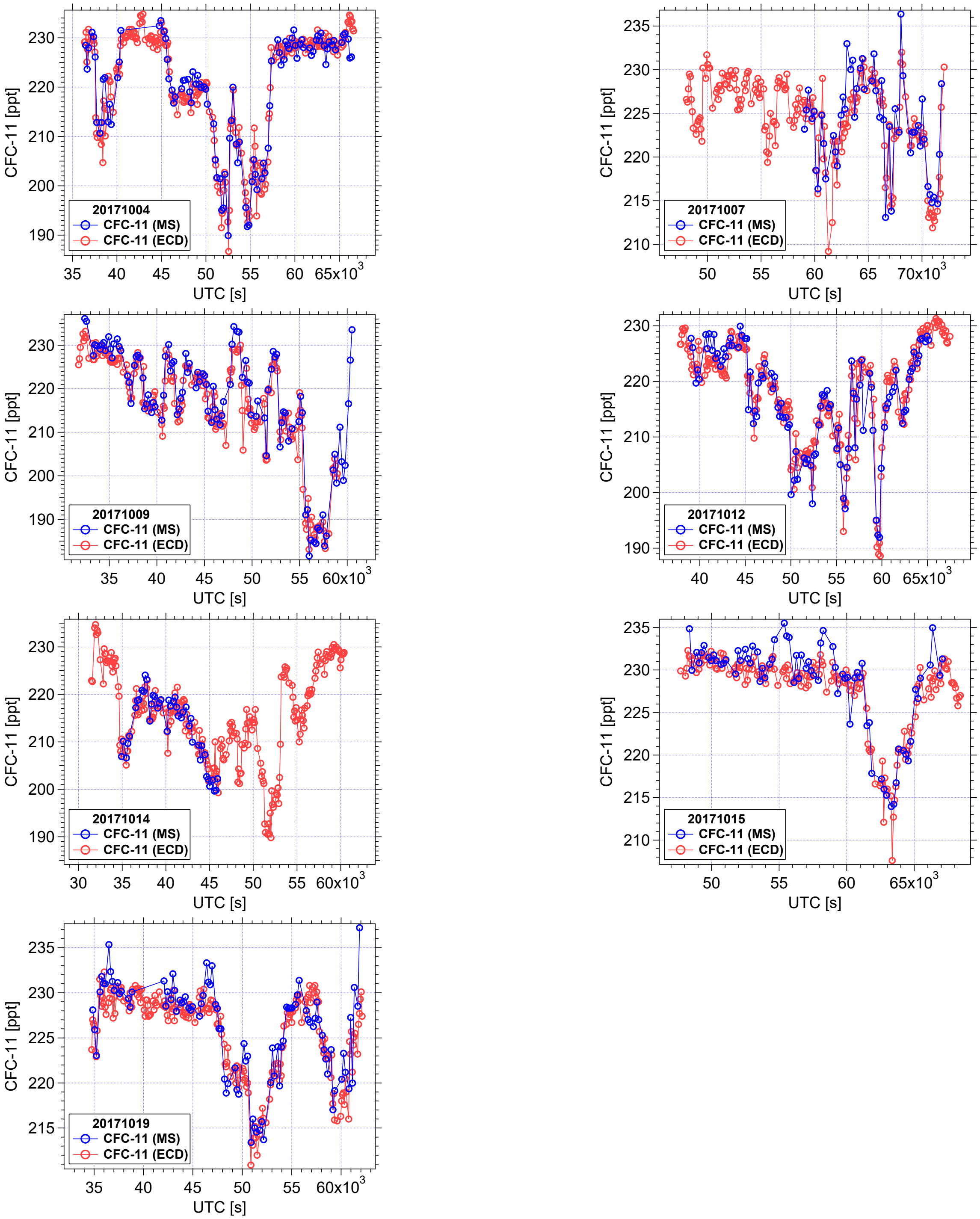

Figure D.7: CFC-11 time series of the ECD (red) and MS (blue) module during WISE flights. The MS data are processed according to Table 3.2.

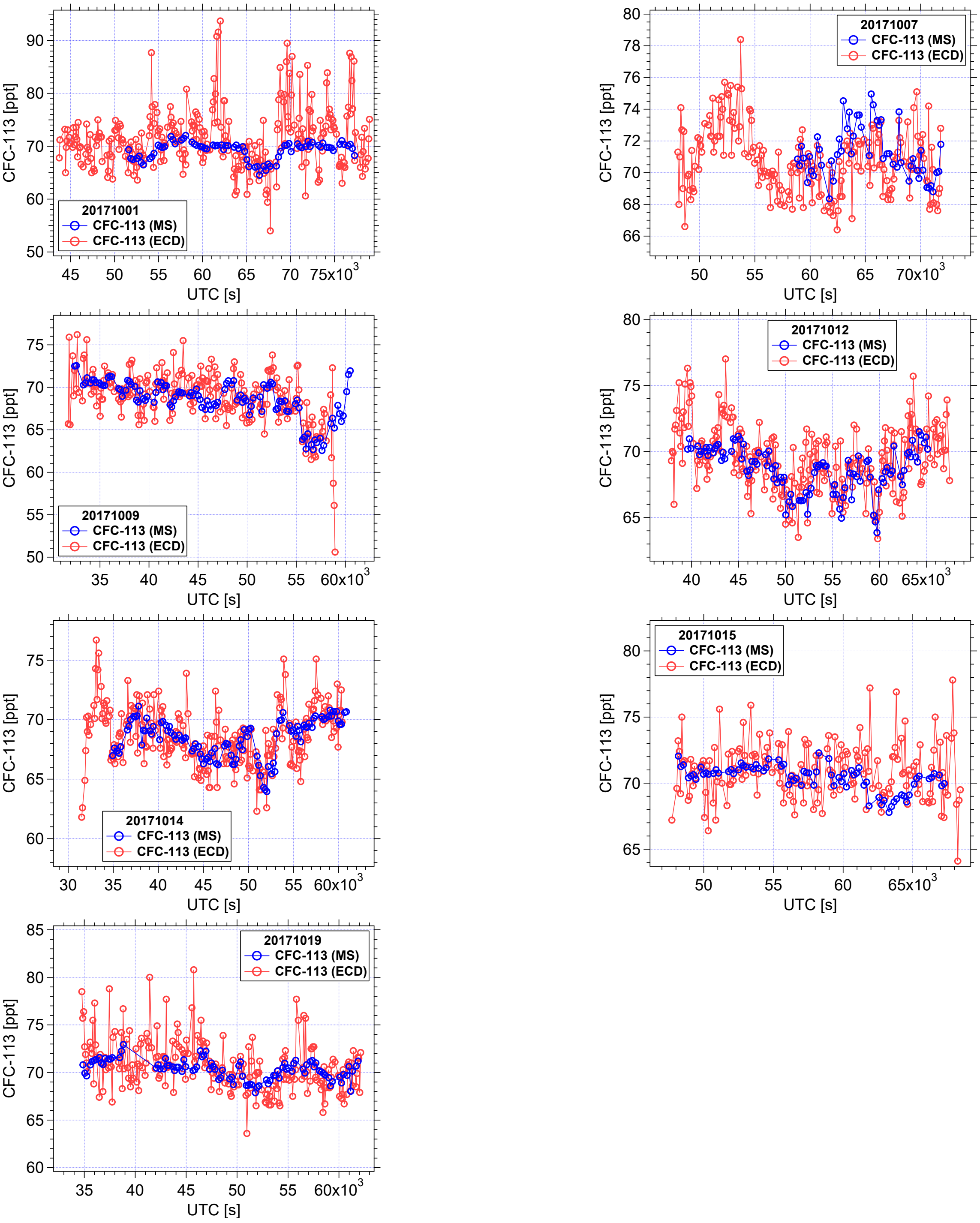

Figure D.8: CFC-113 time series of the ECD (red) and MS (blue) module during WISE flights. The MS data are processed according to Table 3.2.

D.6.1 Different tested methods to calculate mixing ratios

Due to the usage of two in-flight calibration gases several different calibration methods can be used as suggested in Section 3.3.2. Table D.1 gives a total overview on different ways of calculating mixing ratios tested on MS data. Due to the results from Section 3.3.4 the SPAN calibration gas was analyzed in three different ways: all SPAN measurements, only the ones that follow an air sample (half of all SPANs), or only the ones that follow a blank measurement (half of all SPANs). All listed methods use the principle of either a single-point calibration (use of one in-flight calibration gas and the reference point zero), a linear two-point calibration (use of both in-flight calibration gases), or a non-linear two-point calibration (use of both in-flight calibration gases and zero).

All these different methods for the calculation of mixing ratios were applied on CFC-11. In the following sections the resulting mixing ratios of these different methods were individually compared with the mixing ratios of CFC-11 measured by the ECD module (CFC-11 (ECD)). The mixing ratios of CFC-11 (ECD) were calculated by a linear two-point calibration as the default calibration method of the ECD module. More details on the calibration of ECD measurements are given by Riediger (2000), Werner (2007), Ivanova (2007), and Hösen (2013).

D.6.2 Direct comparison of MS and ECD CFC-11 averages

It is not expected that the MS and the ECD data yield the exact same results due to different sample integration times (MS module: ~ 40 s; ECD module: ~ 5 s). In addition, the ECD module has twice as many data points as the MS module due to cycle lengths of 90 s (ECD) and 180 s (MS) and less than half of the ECD sample times overlap with the MS preconcentration times. Nevertheless, to get a better understanding of trends and comparability between those two modules the measurement differences were analyzed (counting only the data points where there is overlap between the integration time of the MS and the ECD measurement).

The CFC-11 mixing ratios of the MS module were calculated in ways listed in Table D.1. For this species there is no significant difference between a quadratic, an exponential, and a logarithmic calibration curve using the non-linear two-point calibration, thus reducing the number of compared methods to 11. This result suggests a linear or at least a non-significant non-linear detector signal response to CFC-11 (MS) mixing ratios and supports the results of the linearity test (Section 2.4).

Table D.1: List of tested methods for the calculation of mixing ratios and their respective short cuts as used in the text and graphs.

1)	CAL & zero in a linear relationship	C0
2)	CAL & SPAN in a linear relationship	CS
3)	CAL & SPANs that follow an air measurement in a linear relationship	$\mathrm{CS_{Air}}$
4)	CAL & SPANs that follow a blank measurement in a linear relationship	$\mathrm{CS_{Blank}}$
5)	CAL, SPAN & zero in a quadratic relationship	CS0
6)	CAL, SPAN & zero in an exponential relationship	
7)	CAL, SPAN & zero in a logarithmic relationship	
8)	CAL, SPANs that follow an air measurement & zero in a quadratic relationship	$\mathrm{CS_{Air}0}$
9)	CAL, SPANs that follow a blank measurement & zero in a quadratic relationship	$\mathrm{CS_{Blank}0}$
10)	CAL, mean SPAN* & zero in a quadratic relationship	$\mathrm{CS_{mean}0}$
11)	CAL, mean SPANs* that follow an air measurement & zero in a quadratic relationship	$\mathrm{CS_{Air,\ mean}0}$
12)	CAL, SPAN-to-pump & zero in a quadratic relationship	$\mathrm{CS_{Pump}0}$
13)	Individual calibrations per flight according to Table 3.2	Criteria

*on the basis of flight-average CAL/SPAN ratios as described in Section 3.3.2

In the following analysis, which will be further referred to as the direct comparison, CFC-11 (ECD) mixing ratios sampled during the preconcentration time of the MS module were subtracted from the respective CFC-11 (MS) mixing ratio calculated in the above mentioned ways. To get a measure of tendencies or trends between the results of the different calibration methods of CFC-11 (MS) and the CFC-11 (ECD) mixing ratios, the mean differences were calculated per flight (Figure D.9, top) and as averages over all comparable flights (Figure D.9, bottom) for each calibration method. In addition, the same was done for the absolute differences between CFC-11 (MS) and CFC-11 (ECD) data (Figure D.10). The plots sorted by flight only show a selected number of tested methods due to several similar results and to avoid overloading the figure.

In some flights a few tested methods express significantly (by one standard error) larger CFC-11 (MS) mixing ratios than the ones of the ECD module (Figure D.9, top). The largest mean offset to the CFC-11 (ECD) values for almost all flights exhibits the calibration method using only one calibration gas (C0). This suggests that the MS detector response is not completely linear to the mixing ratio of CFC-11 and the usage of both calibration gases instead of only one does improve (or at least does not worsen) the calculation of CFC-11 (MS) mixing ratios.

There is no significant difference between all linear two-point calibrations that use a different set of SPAN measurements and their respective non-linear two-point calibration mirror method. This implies that on the one hand, CFC-11 air samples are well bracketed between the mixing ratio of the two calibration gases and on the other hand that a (potential) non-linearity can be well linearly approximated between the two calibration gases. However, for almost all flights there is a clear trend visible in the mean offsets comparing the different two-point calibrations. For all flights (except #14 where all methods match) the offset towards CFC-11 (ECD) mixing ratios of the calibration method CS(0) is between the offsets of $\mathrm{CS_{Blank}}(0)$ (larger mean offset) and $\mathrm{CS_{Air}}(0)$ (smaller mean offset). Thereby the tendency for a difference in the choice of SPAN measurements used for calibrating the data becomes visible. The CFC-11 SPAN measurements did not show a systematic bias for all but one WISE flight (Table 3.2) but showed on average 0.7 ppt lower mixing ratios when following a blank measurement (cf. Figure D.1). This translates into higher mixing ratios of the $\mathrm{CS_{Blank}}(0)$ method compared to CS(0) and $\mathrm{CS_{Air}}(0)$. It is visible that the use of $\mathrm{CS_{Air}}0$ for the calculation of CFC-11 (MS) mixing ratios tends to give not only on average over all flights the closest results to the CFC-11 (ECD) mixing ratios, this also holds for all but two flights (#9 and #12) individually (the special case of $\mathrm{CS_{Pump}}0$ is discussed in Appendix D.6.3). However, even by using the $\mathrm{CS_{Air}}0$ method to calculate CFC-11 (MS) mixing ratios a mean offset for all flights of (0.4 ± 0.2) ppt towards CFC-11 (ECD) mix-

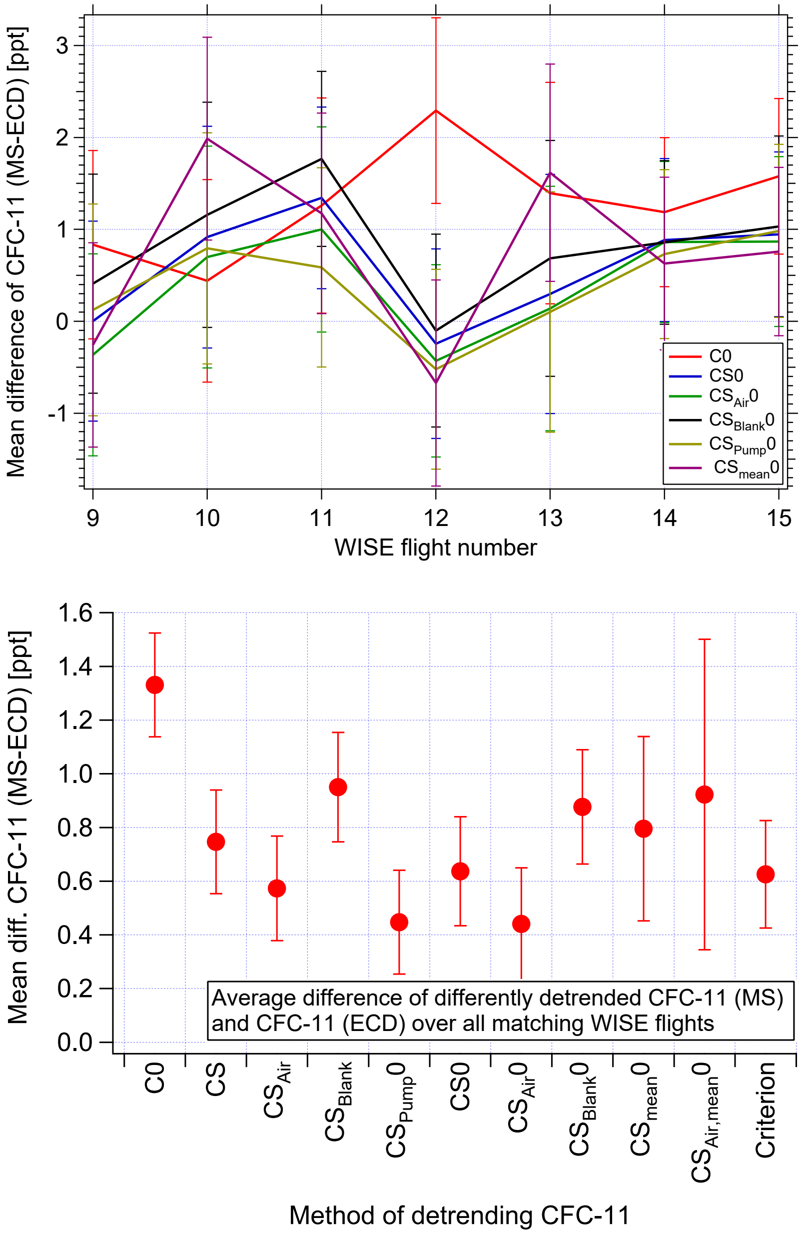

Figure D.9: Mean differences of differently calculated CFC-11 (MS) mixing ratios and the reference CFC-11 (ECD) for each flight (upper panel) and as average over all comparable flights (bottom panel). The error bars indicate one standard error.

ing ratios remains, suggesting an instrumental bias towards higher CFC-11 (MS) mixing ratios.

An analysis of the mean values of the absolute differences between MS and ECD CFC-11 mixing ratios shows no significant difference between the different tested calibration

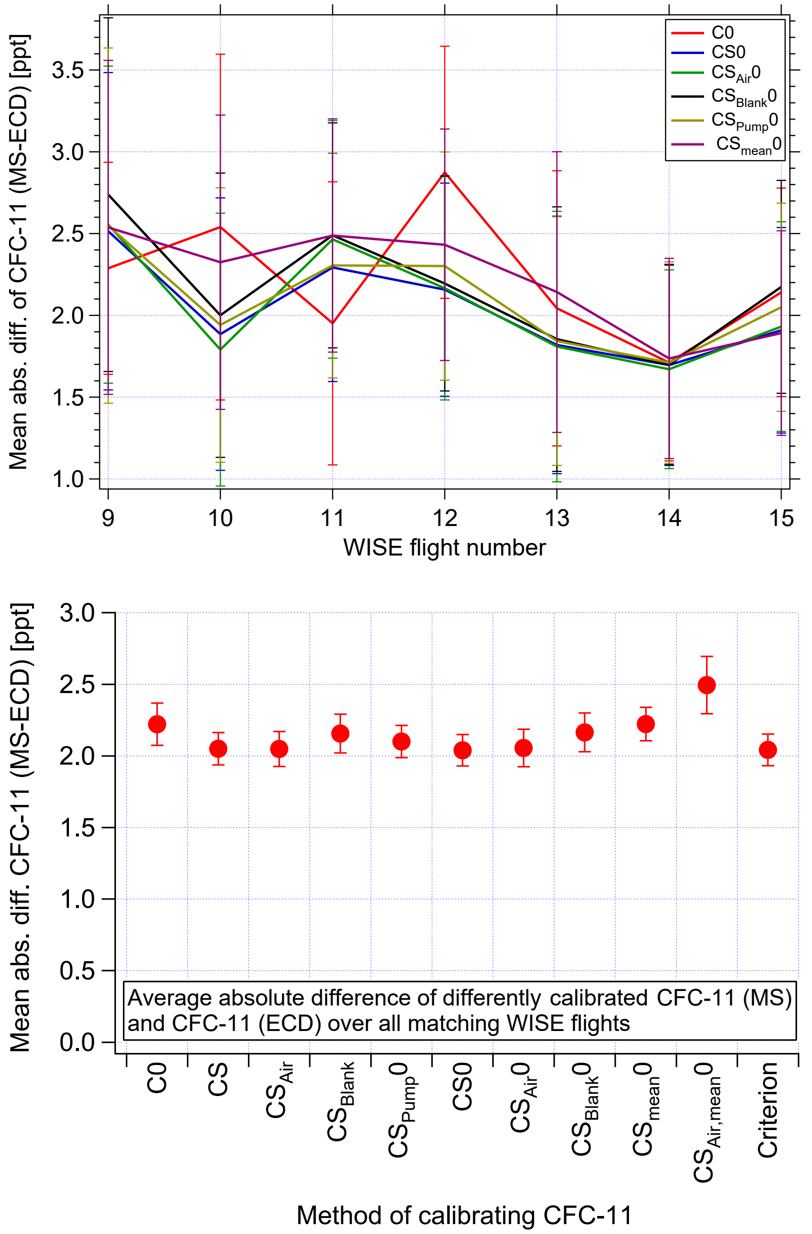

Figure D.10: Absolute mean differences of differently calculated CFC-11 (MS) mixing ratios and the reference CFC-11 (ECD) for each flight (upper panel) and as average over all comparable flights (bottom panel). The error bars indicate one standard error.

methods averaged over all flights (Figure D.10, bottom). In each individual flight there might be (more or less statistically scattered) differences between the tested calibration methods but over all the comparable flights a rather clear difference of ~ 2 ppt between the MS and the ECD CFC-11 mixing ratios is visible. Compared to the tropospheric CAL gas

(232.5 ppt, Table E.2) this is a difference of less than 1 % and on the order of the CFC-11 (MS) measurement precision (see Table 2.3).

The average over all SPANs (CS_{mean} 0) relative to the CAL measurements (cf. Section 3.3.2) generally tends to yield CFC-11 (MS) mixing ratios less similar to the CFC-11 (ECD) mixing ratios than the other tested methods — in particular when leaving out the SPANs that follow a blank sample ($CS_{Air,mean}0$). This suggests that in case of CFC-11, which expressed a slight trend to differences between the different SPAN measurements, the use of all SPANs for calibration tends to compensate better for instrumental drifts. Therefore averaging the SPANs (by the use of the CAL/SPAN signal response) does not improve the calculation of mixing ratios because real system variations get smoothed out and are in the case of CFC-11 (MS) larger than the differences between the individual SPAN measurements.

This direct comparison of CFC-11 measured by the MS and the ECD module shows a significant mean absolute difference between the two modules of around 2 ppt. However, this difference is not significant regarding the measurement precision of the MS module during WISE (Table 2.3). Nevertheless a tendency towards higher CFC-11 (MS) mixing ratios is visible in all tested calibration methods.

D.6.3 Comparison of different CFC-11-N_2O correlations

The direct comparison between the ECD and the MS module might yield biased results due to the different sample integration times of the two modules. Therefore another test, further referred to as the indirect comparison, was performed. The correlation of CFC-11 with another long-lived tracer without a strong seasonality gives a different and more independent perspective on the different calibration methods. In particular if this tracer was sampled at high time resolution. N_2O is an ideal tracer fulfilling these requirements and was measured during WISE with the instrument UMAQS (University of Mainz Airborne QCL Spectrometer; Müller et al., 2015) by the University of Mainz. Most of HAGAR-V MS and ECD measurements have a corresponding N_2O measurement of UMAQS (except for the few times when one of the instruments was calibrated). The N_2O data were averaged over the MS integration time (40 s) for the correlation with MS data and averaged over 5 s for the correlation with the ECD data. Assuming the ECD data provide the most realistic CFC-11 values, the CFC-11 (ECD)-N_2O correlation serves as a reference correlation for the compared MS calibration methods.

For a comparable correlation the CFC-11 (ECD) data were filtered to contain only the measurements that fit timely into the integration windows of the MS measurements. Thereby

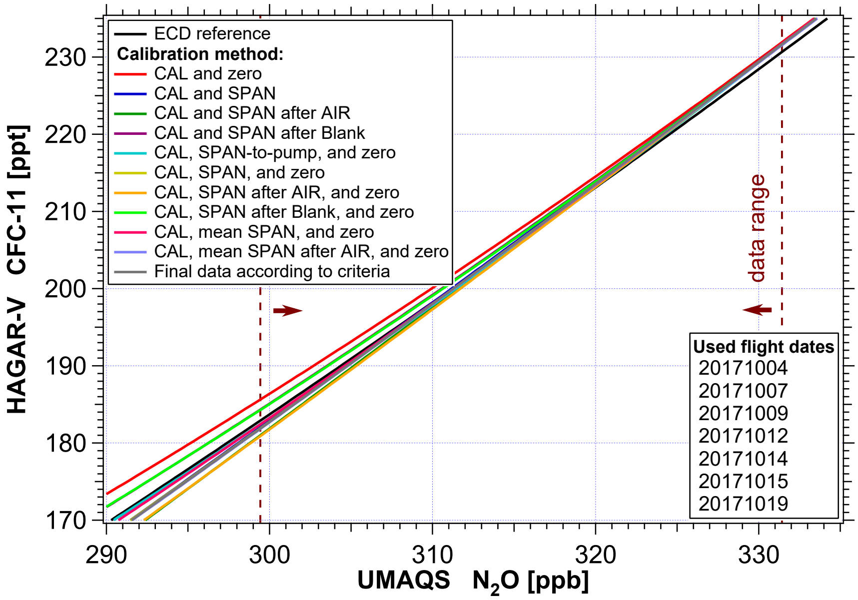

Figure D.11: Results of quadratic fits of CFC-11-N_2O correlations with differently calibrated CFC-11 (MS) data and with CFC-11 (ECD) as reference.

the correlation of all different CFC-11 data sets covered a similar range of N_2O mixing ratios with a total of 554 data points from flight #9 to #15. Each correlation was fitted quadratically. The resulting fits were extrapolated to include the CFC-11 mixing ratios of CAL (232.5 ppt) and SPAN (175.8 ppt) and plotted together in Figure D.11. The used CFC-11 data correspond to N_2O mixing ratios between 299.4 ppb and 331.4 ppb.

Figure D.11 shows that all calibration methods exhibit a mean positive offset of around 1 ppt against the ECD correlation fit at $N_2O \simeq 331$ ppb, which marks the chemical tropopause (Kunkel et al., 2019). This offset is not visible in the direct comparison and could be the result of a small peak of an unknown short lived substance eluting at the same time as CFC-11 in the MS module. However, such a species could not be identified and this hypothesis therefore not be verified.

Between 299.4 ppb and 331.4 ppb of N_2O, 128 points were equally distributed along the correlation fits. The CFC-11 (MS) mixing ratio at each of these points was subtracted from the CFC-11 (ECD) mixing ratio at the respective N_2O value. Figure D.12 shows for each calibration method the mean value of the absolute differences of these 128 compared points along the correlation fits. Thereby a measure for the similarity of the MS correlation fits and the ECD correlation fit for the relevant N_2O mixing ratio range is obtained.

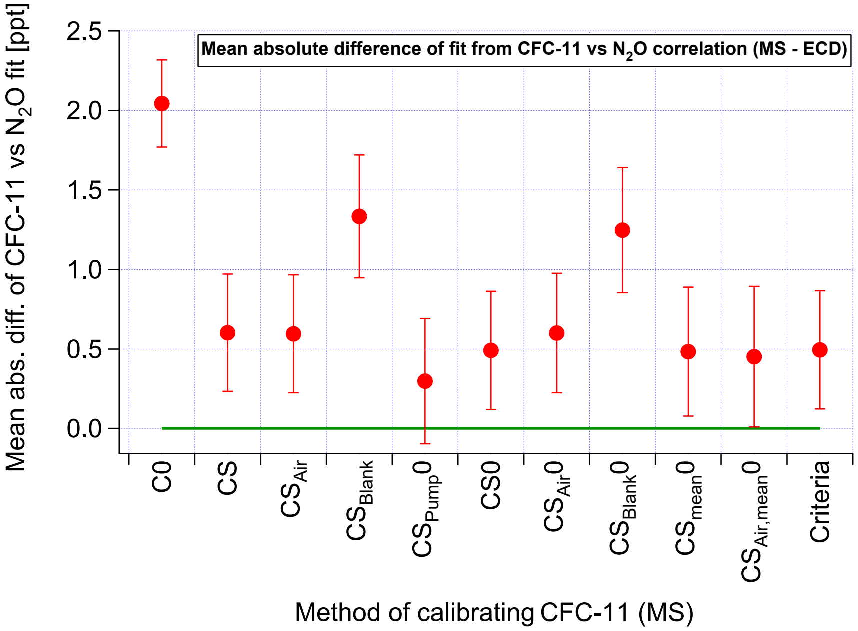

Figure D.12: Mean absolute differences of quadratic fits of CFC-11-N_2O correlations, each with differently calibrated CFC-11 (MS) data, and the fit of the CFC-11 (ECD)-N_2O correlation. The ECD reference correlation fit is subtracted from the respective MS correlation fit. The error bars represent the propagated errors from the respective two correlation fits.

For the calculation of error bars the residual root mean square (as a measure of the scattering data points around the fit) of the data from each individual method was treated as the standard deviation (σ) of the correlation fit, thereby allowing the calculation of the correlation fit uncertainty ($s_{fit} = \sigma/\sqrt{n}$). The error bars in Figure D.12 are the root of the sum of the quadratic uncertainties of the correlation fit of the ECD and the respective MS data: $s_{diff} = \sqrt{s_{fit}(MS)^2 + s_{fit}(ECD)^2}$.

The method C0 exhibits the largest difference between its correlation fit and the one from the ECD module compared to the fits of the other calibration methods (figures D.11 and D.12). Similar to the direct comparison the comparison of the correlation fits shows a slight non-linearity between the CFC-11 (MS) mixing ratios and the detector response. This implies that the use of only one calibration gas for calculating CFC-11 (MS) mixing ratios would overestimate the mixing ratios stronger the lower they are. Thus the indirect comparison shows as well as the direct comparison that both calibration gases have to be used for the calculation of CFC-11 (MS) mixing ratios. This is also in accordance with the tendency shown in the analysis of the detector response in Section 2.4.

All two-point calibration methods show no significant difference between a quadratic two-point calibration (with zero) or the linear two-point calibration. This result agrees with the direct comparison of MS and ECD CFC-11 mixing ratios. In addition, this result strengthens the indication of a sufficiently good detector non-linearity compensation by the assumption of a linear dependency between the two calibration gases (the CFC-11 air measurements are well bracketed between CAL and SPAN).

The visible differences between the use of different SPAN measurements in the calibration methods are also agreeing with the results from the direct comparison. On the one hand, the methods CS_{Blank} and $CS_{Blank}0$ clearly yield the largest mean absolute difference to the CFC-11 (ECD)-N_2O correlation fit. On the other hand the results from the methods CS_{Air} and $CS_{Air}0$ do not differ from the results of the methods CS and CS0 (Figure D.12). This suggests that the SPANs following a blank measurement are biased and shows that the use of these biased SPANs has a negative influence on the calculation of CFC-11 (MS) mixing ratios when the unbiased SPANs are ignored. In addition, Figure D.12 shows that the use of non-linear two-point calibrations tend to yield results slightly closer to the ECD correlation fit than the equvalent linear two-point calibration method. This suggests the preferred usage of a quadratic two-point calibration over a linear two-point calibration for the calculation of CFC-11 (MS) mixing ratios. This observation is in accordance to the results of the direct comparison.

In the relevant N_2O mixing ratio region (299.4 ppb to 331.4 ppb) only the CFC-11 (MS) data calibrated with the $CS_{Pump}0$ method is not significantly different from the ECD correlation fit. However, as shown in Section 3.3.6 the SPAN-to-pump measurements from the two modules did not agree very well. In addition it is not logical to use one calibration gas that took a pathway that very likely biases the measurements when the other calibration gas is not measured in the same way. Thus, the matching results of the $CS_{Pump}0$ calibration method is considered to be a result of pure chance. SPAN-to-pump measurements in general should only be used for the calculation of mixing ratios if the regularly measured calibrations cannot be used and then only as a single-point calibration as the only calibration gas measurements.

The second closest to the CFC-11 (ECD)-N_2O correlation fit are the CFC-11 (MS) results from the $CS_{mean}0$ and $CS_{Air,mean}0$ calibration methods. These methods are not significantly different from CS(0) and $CS_{Air}(0)$. Thus, without any significant reason to average the SPAN measurements, these two methods should not be used for the calculation of CFC-11 (MS) mixing ratios. Nevertheless, this result shows that this rather unusual calibration method does not negatively impact the results when used with only slightly biased SPAN measurements.

The calibration method CS0 tends to yield the best of the logical results compared to the CFC-11 (ECD) correlation fit. The difference between CS0 and $\mathrm{CS_{Air}0}$ is negligibly small but their results are clearly closer to the ECD data than $\mathrm{CS_{Blank}0}$. This result shows that before rejecting every second SPAN measurement due to systematic differences between the SPANs, it needs to be considered if the use of all SPANs for the calculation of mixing ratios can instead compensate the systematic differences between the SPANs by a better drift correction. In Section 3.3.4 a criterion to consider this effect was formulated and, among other corrections, is used in the calibration method Criteria (calibration according to Table 3.2). Criteria yields CFC-11 (MS) mixing ratios equally close to the CFC-11 (ECD) correlation fit as those of CS0. This provides confidence that the corrections used on MS data, according to the different criteria defined in Section 3.3.1, yield valuable results.

Combining the results from the direct and the indirect comparison of CFC-11 measured by the MS and the ECD module gives an overview on the comparability of the two modules for this particular species. The indirect comparison showed similar results to the direct comparison. This includes a mean relative offset towards CFC-11 (ECD) data for all tested calibration methods. However, the indirect comparison suggests that this offset of the calibration method yielding the closest results to the CFC-11 (ECD) data is smaller than that derived from the direct comparison. The minimal mean absolute offset of the indirect comparison is (0.5 ± 0.4) ppt and would only be of significance for a CFC-11 measurement precision below ~ 0.2 % of CAL (232.5 ppt). This is a requirement both modules do not fulfill. In addition, the comparisons suggest a slight non-linear MS detector response to CFC-11 mixing ratios and a small bias of CFC-11 (MS) SPAN measurements when following a blank sample. Nevertheless, the optimal method for the calculation of CFC-11 (MS) mixing ratios according to these considerations is the use of a quadratic two-point calibration without rejecting or averaging any calibration measurements.

D.6.4 Direct and indirect comparison of CFC-113 MS vs ECD

Comparisons, similar to the comparisons between MS and ECD CFC-11 measurements, were conducted for CFC-113 (cf. appendices D.6.2 and D.6.3). Unfortunately, the measurement precision of CFC-113 (ECD) during WISE is significantly worse than that of the MS module. Nevertheless, due to the large number of measurements trends can be derived.

For the comparison measurements of WISE flights #8, and #10 to #15 were used. Similar to CFC-11, the direct comparison and the indirect comparison of CFC-113 were analyzed.

For the the comparison of CFC-113 MS and ECD measurements fewer calibration methods than for the comparison of CFC-11 are presented due to insignificant differences of the results. Similar to CFC-11, the resulting CFC-113 (MS) mixing ratios did not differ between a quadratic, an exponential or a logarithmic two-point calibration.

The analyzed calibration methods used for the direct comparison of MS and ECD CFC-113 mixing ratios show no significant difference between the calibration methods using different SPAN measurements (upper two rows in Figure D.13). In general, there are no significant difference between all of the tested methods. This implies on the one hand, no significant disturbances from blank measurements on the following SPAN measurements and on the other hand, a linear detector response for CFC-113 (MS) mixing ratios within the measurement range. This is in agreement with the results from Section 2.4.

In Flight #8 CFC-113 (MS) exhibits around 2 ppt lower mean mixing ratios than measured by the ECD module (upper left panel in Figure D.13). All the other comparable flights did more or less scatter around the same mean value of MS and ECD CFC-113 mixing ratios. Nevertheless, the mean difference between the MS and the ECD CFC-113 mixing ratios over all flights and for all tested calibration methods shows the tendency to smaller CFC-113 (MS) mixing ratios.

The question if the smaller CFC-113 (MS) mixing ratios of flight #8 were biased could not be clearly answered because the uncertainties were large enough to make the measurements of both modules agree within the margin of error. However, there is the possibility of the CFC-113 (MS) mixing ratios from flight #8 being biased because CFC-11 (determined from the same mass fragment (m/z = 101) as CFC-113) showed inexplicable low mixing ratios during that flight and was therefore wholly rejected. In case the inexplicably low CFC-11 mixing ratios were caused by something affecting the mass fragment itself, CFC-113 might also be affected. The effect for the low CFC-11 measurements in flight #8 is very puzzling and could not be understood, thus a direct connection to the slight offset of CFC-113 (MS) against the ECD data can only be hypothesized.

The absolute differences show for all flights a significant difference towards CFC-113 (ECD) mixing ratios. Without flight #8 this offset is about (1.5 ± 0.1) ppt for all tested calibration methods. Combined with the large absolute difference in flight #8 of (4.5 ± 0.5) ppt the mean absolute difference over all tested flights is (1.9 ± 0.4) ppt, equally for all tested calibration methods.

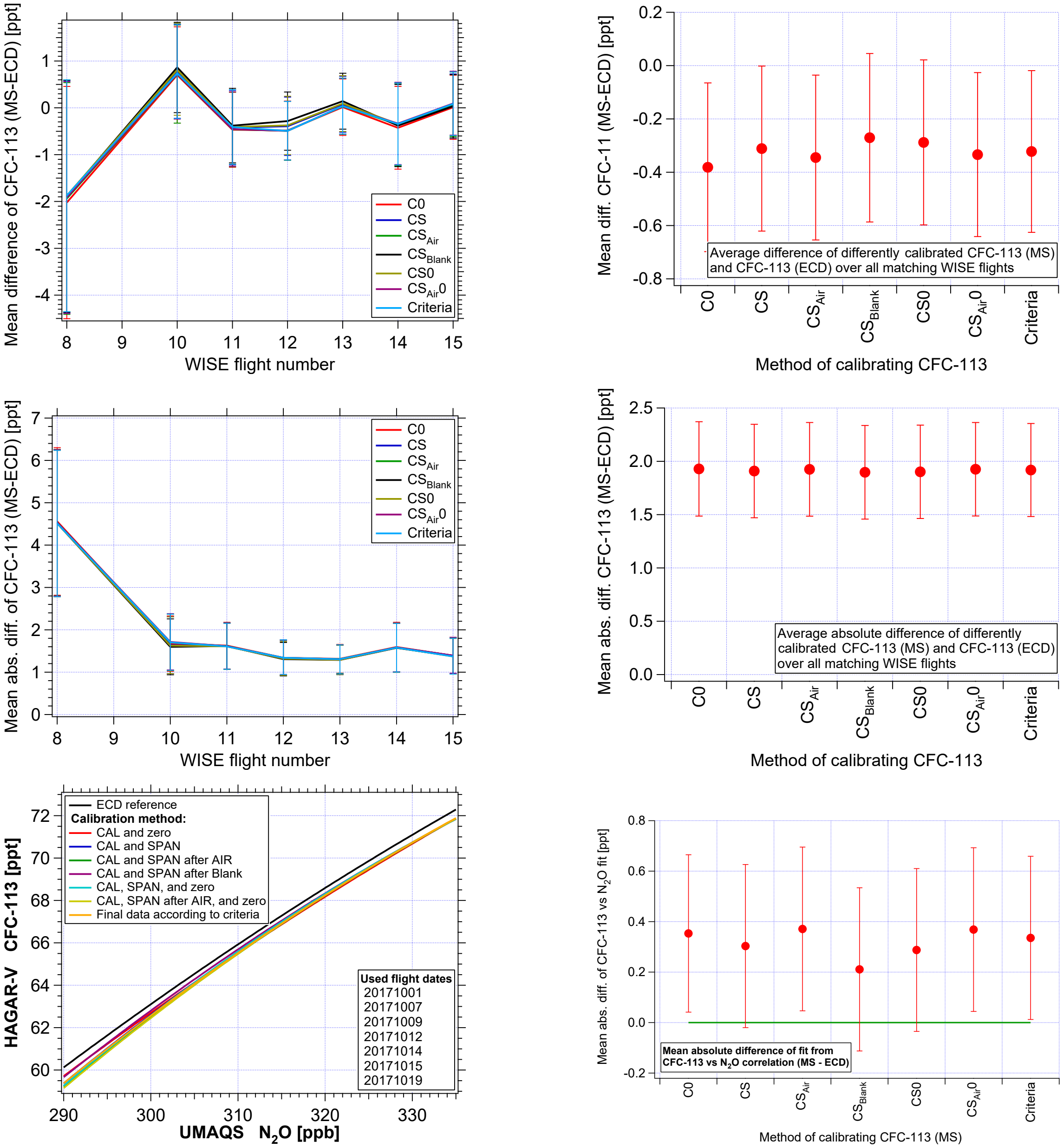

Figure D.13: Direct and indirect comparison between differently calculated mixing ratios of CFC-113 (MS) and CFC-113 (ECD). Upper row: mean difference of measurements overlapping in time by flight (left) and averaged over all flights (right). Middle row: mean absolute difference of measurements overlapping in time by flight (left) and averaged over all flights (right). Bottom row: quadratic fit result of different CFC-113-N$_2$O correlations (left) and the mean absolute difference of these fits relative to the correlation fit of CFC-113 (ECD) (right).

The indirect comparison of MS and ECD CFC-113-N$_2$O correlation was very much in agreement with the results from the direct comparison. All different calibration methods show no significant difference between each other. This supports the findings from the direct comparison of a linear detector response to CFC-113 (MS) mixing ratios and no significantly biased SPAN measurements. Similar to the direct comparison the indirect comparison shows an offset between MS and ECD CFC-113 mixing ratios over all comparable flights. However, the offset resulting from the indirect comparison is about (0.3 ± 0.3) ppt for most tested methods suggesting only an insignificant difference between the two modules.

As a conclusion from these comparisons of MS and ECD CFC-113 measurements no clear favorite calibration method for CFC-113 (MS) can be determined. Without any significant difference between the tested methods and without any reason to flag or average calibration gas measurements, the method CS0 is the most reasonable choice for the calculation of CFC-113 (MS) mixing ratios. In addition, the results from CS0 do not differ significantly from the calibration method Criteria that uses the data corrections shown in Table 3.2. This supports the defined criteria used to decide which data corrections are applied on a target species (Section 3.3).

Appendix E

Calibrations and relative accuracy

This section describes the calibration of mixing ratios in the working standards CAL and SPAN. In the following and throughout the whole thesis, mother bottle defines the primary working standard. The flight bottles, used for in-flight calibration, are filled with gas from the mother bottles. Thus, even if the gas (CAL or SPAN) is the same in a flight and a mother bottle, the flight bottles are attached with an additional uncertainty, due to the filling process. Based on the calibrations presented in this chapter, estimations of the relative accuracy of all WISE MS measurements are given in Section E.3.

E.1 Calibration of primary working standard

The MSD is a relative detector and mixing ratios of MS module measurements are determined using the calibration gases CAL and SPAN (cf. Section 3.3). These two calibration gases (also called working standards) contain compressed atmospheric background air. A water trap filled with magnesium perchlorate was used to dehydrate the outside air before it was compressed into the respective bottle. The bottling of CAL was done in December 2015 at the Hohenpeissenberg observatory of the German Meteorological Service (DWD) — a relatively remote mountain site to obtain relatively "clean" tropospheric background air.

The calibration gas SPAN is a mixture of different gases. Originally, air of the SPAN mother bottle was filled in Winter 2009/10 at the University of Wuppertal (i.e. urban air with significant anthropogenic influence). Residuals of ~ 44 % of that air were mixed with air from the Hohenpeissenberg observatory in December 2015 and was further diluted with about 25 % of synthetic air. The dilution with synthetic air produces lower stratospheric

Table E.1: Information about the laboratory and the measurement technique that determined the mixing ratios of the target species of CAL and SPAN.

	Laboratory	Technique
CH_2Cl_2	University of Wuppertal	GC/MS
$CHCl_3$	Universities of Wuppertal & of Frankfurt	GC/MS
CH_3Cl	University of Frankfurt	GC/MS
CFC-11	University of Wuppertal	GC/ECD
CFC-113	University of Wuppertal	GC/MS
HFC-125	University of Frankfurt	GC/MS
HFC-134a	University of Wuppertal	GC/MS
Iso-Pentane	DWD Hohenpeissenberg	GC/FID
n-Pentane	DWD Hohenpeissenberg	GC/FID
HFC-32	University of Frankfurt	GC/MS
C_2Cl_4	University of Frankfurt	GC/MS
CCl_4	University of Frankfurt	GC/MS

background mixing ratios for most of HAGAR-V's long-lived target species. In addition, to achieve CO_2 mixing ratios close to the lowest mixing ratios expected to measure in the stratosphere, the SPAN mother bottle was spiked with a CO_2 gas mixture.

The mixing ratios of CAL and SPAN were obtained from different calibrations and laboratories. Not all target species could be calibrated at the University of Wuppertal. The mixing ratios obtained from other laboratories were taken with the uncertainties given by the respective laboratory. Table E.1 lists the target species, where, and how they were measured.

The two working standards calibrated in Wuppertal were measured against a reference gas (called NOAA I) that was commercially acquired from NOAA in Boulder, USA. NOAA I was measured by NOAA against their own gravimetrically determined reference gas and has a measurement uncertainty. The uncertainty of their own reference is unknown and referred to a scale to which all gases that were calibrated against NOAA I are further referred to. The uncertainty of this scale is considered small compared to the measurement precisions in this chain of calibrations. The same holds for the respective reference scales of the calibrations performed in other laboratories.

The GC/MS measurements performed in Wuppertal used a single-point calibration to determine the mixing ratios of CAL and SPAN. The linearity of the signal response was cross-checked with diluted reference gas and confirmed within the measurement precision.

To eliminate possible memory effects and for a statistical benefit, six measurements of the gas to be calibrated were bracketed by two blocks of each four measurements of the reference gas NOAA I.

The mixing ratios were determined according to Section 3.3 with the difference that the average over all four reference gas measurements in one block were used to detrend the data and to calculate the mixing ratios. As a first order estimate the following formula was used to determine the mixing ratio χ of a target species in a gas bottle (i.e. CAL, SPAN, or test air):

$$\chi_{Bottle} = \chi_{NOAA\ I} \frac{\bar{A}_{Bottle}}{\frac{\bar{A}_{NOAA\ I,\ 1}}{2} + \frac{\bar{A}_{NOAA\ I,\ 2}}{2}} \tag{E.1}$$

With $\chi_{NOAA\ I}$ being the mixing ratio of the NOAA I reference gas, $\bar{A}_{NOAA\ I,\ 1}$ the averaged peak area of the four NOAA I measurements before and $\bar{A}_{NOAA\ I,\ 2}$ the respective NOAA I mean peak area after the measurements of the gas to be calibrated, and $\bar{A}_{Bottle}$ the averaged and detrended peak area of the six measurements of the gas to be calibrated.

All of these variables have uncertainties propagating on to the uncertainty of χ_{Bottle}. For the estimation of the uncertainty of χ_{Bottle} ($\sigma_{\chi_{Bottle}}$), it is assumed that the NOAA I measurements in a block before and after the measurements of the gas to be calibrated do not differ significantly. With this assumption, the individual quadratic relative uncertainties can be summed up:

$$\sigma_{\chi_{Bottle}} = \chi_{Bottle} \sqrt{\left(\frac{\sigma_{NOAA\ I}}{\chi_{NOAA\ I}}\right)^2 + \left(\frac{\sigma_{A_{Bottle}}}{\bar{A}_{Bottle}}\right)^2 + \left(\frac{\sigma_{\bar{A}_{NOAA\ I,\ 1}}}{2\bar{A}_{NOAA\ I,\ 1}}\right)^2 + \left(\frac{\sigma_{\bar{A}_{NOAA\ I,\ 2}}}{2\bar{A}_{NOAA\ I,\ 2}}\right)^2} \tag{E.2}$$

With σ_{A_X} being the standard deviation and $\sigma_{\bar{A}_X}$ the standard error of all measured peak areas of species X. The uncertainty on $\chi_{NOAA\ I}$ ($\sigma_{NOAA\,I}$) is given by NOAA. The value $\chi_{NOAA\ I}$ of $CHCl_3$ is the only one determined at the University of Frankfurt because of drifting $CHCl_3$ mixing ratios in the NOAA I bottle. Unfortunately, some disturbances during the calibration in Frankfurt caused the measurement precision of this species to be worse than usual. Due to time reasons this test could not be repeated during the present work and therefore $\chi_{\mathrm{CHCl_3}}$ is attached with a considerable uncertainty in all bottles.

To obtain $CHCl_3$ mixing ratios for the working standards with a better precision it was determined in the above mentioned GC/MS calibration in Wuppertal anew. As a reference the SPAN $CHCl_3$ mixing ratio obtained in Frankfurt was used. This yielded more precise

CAL and test air mixing ratios for this species even with the use of a relatively imprecise reference gas value.

The GC/ECD calibration for CFC-11 was performed as described by Hader (2017) and the two Pentanes were measured by the DWD, Hohenpeissenberg. The Pentane measurements were performed shortly after bottling CAL and SPAN, thus mixing ratio changes after the measurement are possible due to a usual time for mixing ratios to equilibrate in the bottles on the order of weeks. A second calibration for these VOCs could not be performed during the present work and the first values obtained do suffice for the presented analysis.

An overview of the used mixing ratios, their uncertainties and the scale they refer to is given in Table E.2.

Table E.2: Overview on mixing ratios and scales of the used calibration or test gases. All mixing ratios (χ) are given in ppt and $\sigma_{A_{Bottle}}$ is the respective standard deviation (precision) of the respective bottle during calibration and σ_{Total} is the total uncertainty on the given mixing ratio. For the GC/MS measurements performed in Wuppertal $\sigma_{Total} = \sigma_{\chi_{Bottle}}$ from equation E.2.

[ppt]	NOAA I		CAL			SPAN			Test air			Scale
	χ	σ_{Total}	χ	$\sigma_{A_{Bottle}}$	σ_{Total}	χ	$\sigma_{A_{Bottle}}$	σ_{Total}	χ	$\sigma_{A_{Bottle}}$	σ_{Total}	
CH_2Cl_2	39.7	0.3	59.4	0.86	1.2	86.1	2.3	2.5	152.7	0.87	2.5	NOAA-03
$CHCl_3$	5.6	0.7	11.1	0.08	1.4	12.4	0.23	1.6	26.8	0.27	3.4	SIO-98
CH_3Cl	601.1	6.2	601.5	-	3.9	464.5	-	3.0	571.6	-	2.6	SIO-05
CFC-11	244.1	0.5	232.5	-	0.7	175.8	-	0.5	236	1.9	2.1	NOAA-93
CFC-113	77.3	0.2	72.7	0.77	1.1	56.3	1.6	1.7	73.9	0.39	0.48	NOAA-02
HFC-125	7.73	0.09	22.91	-	0.25	36.11	-	0.40	42.83	-	0.47	UB-98
HFC-134a	53.13	0.19	95.88	0.54	0.93	90.42	0.74	1.03	159	0.98	1.7	NOAA-95
Iso-Pentane	-	-	126	2	5	206	3	8	-	-	-	NPL-12
n-Pentane	-	-	51.22	0.07	3	153	1	9	-	-	-	NPL-12
HFC-32	3.47	0.08	15.12	-	0.35	10.93	-	0.26	34.79	-	0.81	SIO-07
C_2Cl_4	1.71	0.42	3.4	-	0.8	3.5	-	0.9	21	-	5	NOAA-03
CCl_4	59	4.1	81.9	-	5.7	54.7	-	3.8	78.2	-	5.4	SIO-05

E.2 Calibration of in-flight calibration gases

The 2 l gas bottles of CAL and SPAN used for the in-flight calibration were refilled from the mother bottles every 2–3 flights during WISE. To determine eventual contamination from the refilling process as well as drifting mixing ratios during the gases residence time inside the flight bottles, regular calibration sequences were run on-ground before refilling the flight bottles anew.

The sequences of the flight bottle calibrations for the MS module always contained twice 2–3 measurements of a flight bottle gas bracketed by two measurements of the respective mother bottle. Differences between the nominal mixing ratios and the content of the flight bottle of both CAL and SPAN were analyzed. Significant differences were considered to be corrected.

Some of the calibrations were conducted under unfavorable circumstances without the time for a proper instrumental preparation. In addition, unheated long tubing reached from outside the aircraft to HAGAR-V inside HALO for the measurement of the mother bottles. Thus ad- and desorbing effects might be possible for the calibration's reference gases (mother bottles).

With the general assumption that the gas inside the flight bottles is equal to the gas in the mother bottles, a discrepancy in the calibration has to be without doubt before a correction on flight data is made. To support the analysis of the flight bottle differences the SPAN/CAL ratios of the flight bottles and the SPAN/CAL ratios of the mother bottles during the calibrations were analyzed. Inconsistencies were considered to be caused by a corrupted calibration.

Figures E.1 and E.2 show two different plots. On the left hand side the differences of the flight bottle measurements and their respective nominal mixing ratio are depicted for the calibrations. The error bars represent two times the standard error of the respective flight bottle calibration. The mixing ratios were calculated as for flight data according to Table 3.2 by the use of one or both mother bottle measurements.

Figures E.1 and E.2 (right) show the SPAN/CAL ratios of the flight bottles for each individual flight (blue) and for the calibrations (green). In addition, the SPAN/CAL ratios of the mother bottles (red) of each on-ground calibration are included in the plots. All ratios were determined by a single-point detrending method with the use of CAL (see Section 3.3.1) to capture the drift corrected difference between the two calibration gas detector signals. Thus the CAL mixing ratio was always set to its nominal mixing ratio and the SPAN mixing ratios were calculated in relation to CAL. The CAL gas used

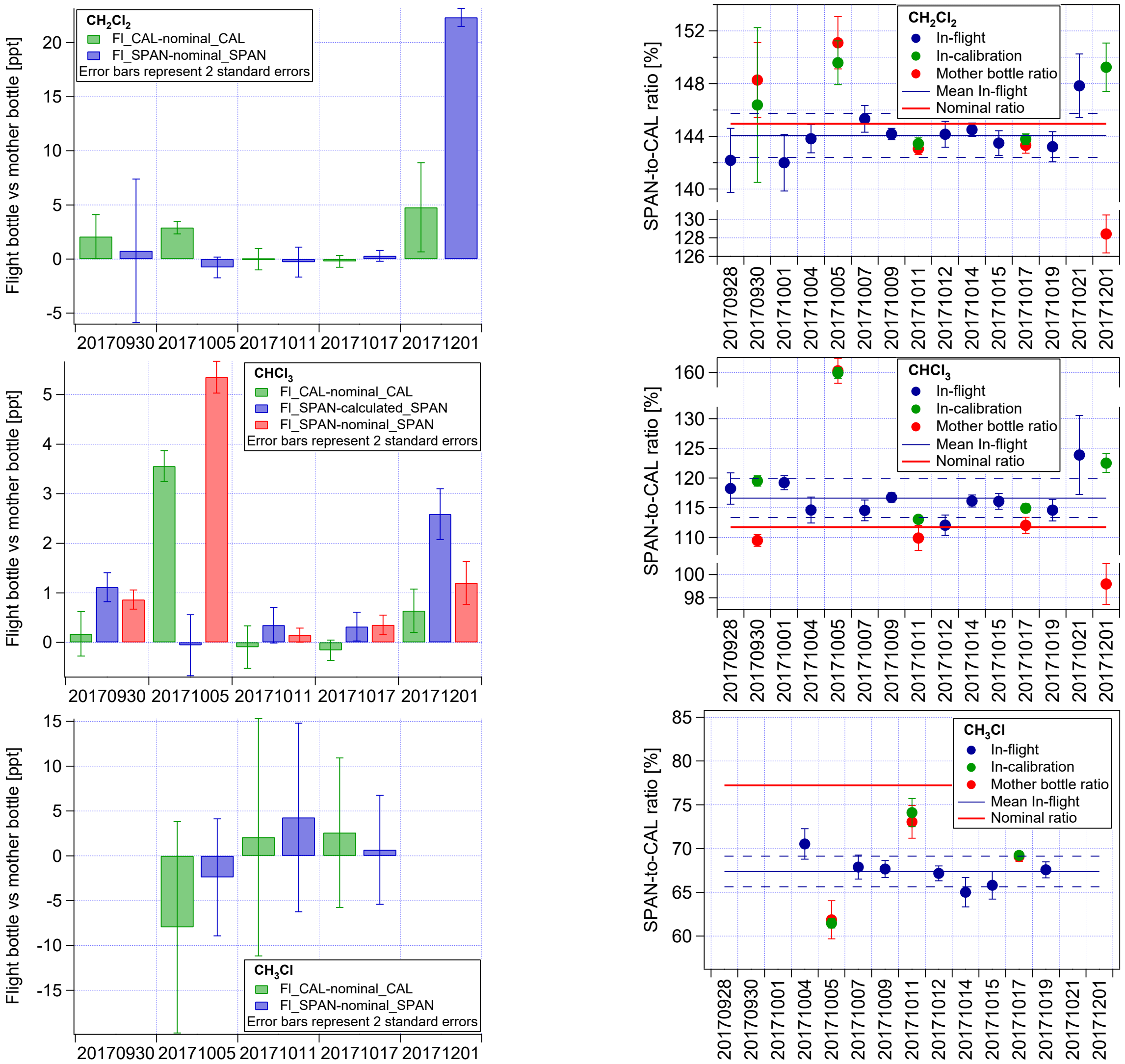

Figure E.1: Left side panels: Difference between flight bottle and nominal value of respective mother bottle during on-ground calibrations. CAL in green, SPAN in blue. $CHCl_3$ differentiates between the difference of flight bottle SPAN and nominal SPAN (red) and the difference of flight bottle SPAN and measured SPAN mother (green). Error bars indicate two standard errors. Right side panels: SPAN/CAL ratio of flight bottles in-flight (blue), and during on-ground calibration (green). SPAN/CAL ratio of mother bottles from on-ground calibrations in red. The red line represents the nominal SPAN/CAL ratio, the blue line the mean flight bottle ratio with one standard deviation (dashed lines). Note eventual broken y-axes.

to calibrate the on-ground calibrations came from the mother bottles while the in-flight measurements were calibrated by the CAL gas from the flight bottle.

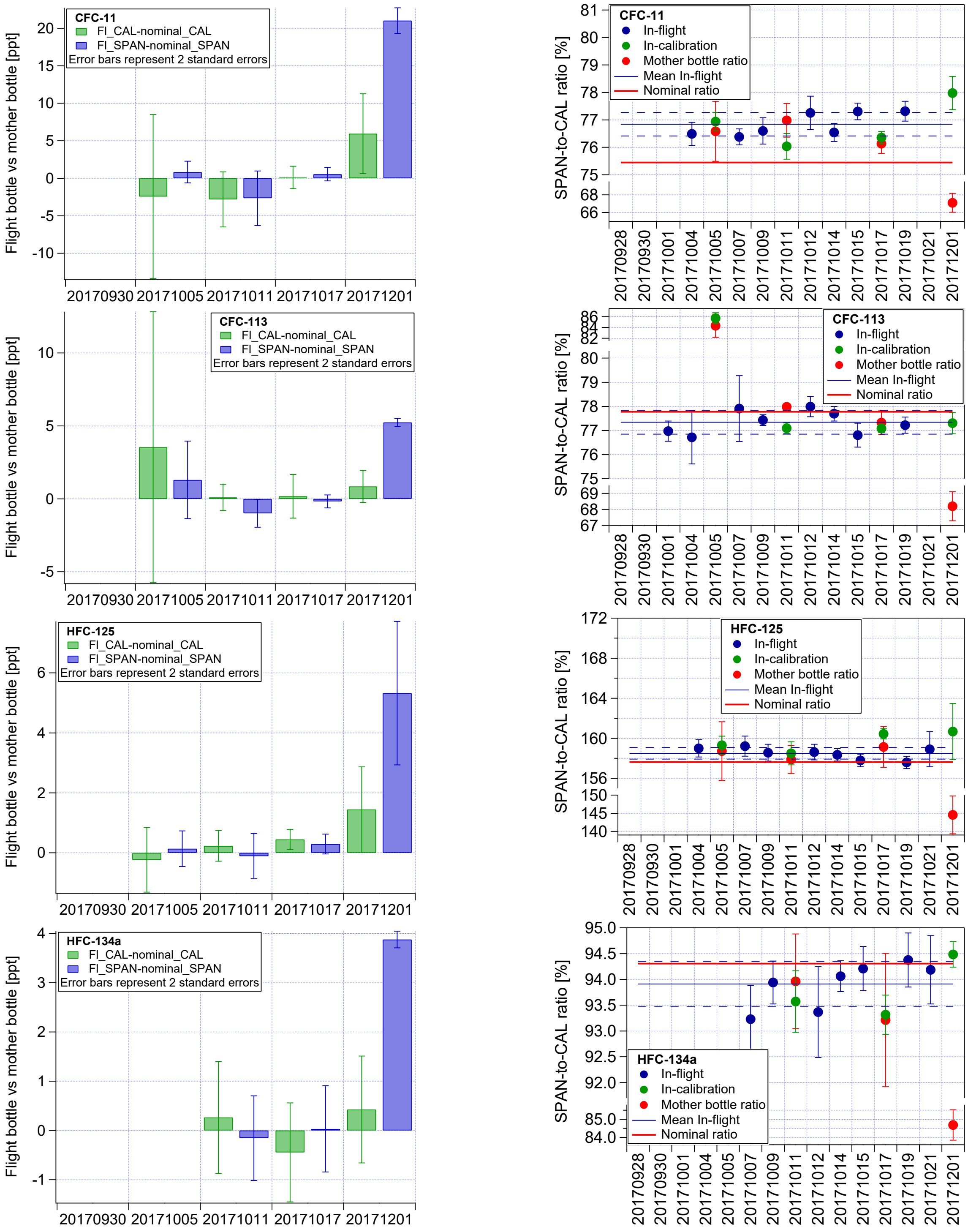

Figure E.2: See description of Figure E.1.

A flight bottle is considered to be biased if its difference to the nominal value from the mother bottle is significantly (range of two standard errors) different from zero. To assure that such a difference is not due to a corrupted calibration, the SPAN/CAL ratio of the calibration (green marker in right side plots) has to agree with the 2–3 flight bottle ratios (blue markers) from the dates before within the uncertainty range of the in-flight measurements. This assures that the difference from the calibration is comparable to what was observed during the flights. Thereby a constant day-to-day (non-)linear detector signal response to mixing ratios is presumed.

In addition, the ratio of the mother bottles (red markers in right side plots) should agree with the majority of the mother bottle ratios during WISE calibrations. Otherwise the measurements of one or both of the mother bottles is biased and the calibration cannot be properly interpreted.

Table E.3 gives a brief overview of the analysis' results. Whenever one of the two flight bottles was considered to be significantly different from the mother bottle value, the respective entry in the Diff row in Table E.3 is marked with X. Otherwise it is marked with ✓. An entry in the Ratio row is marked with X if any of the above mentioned criteria declared the respective calibration to be not trustworthy. In such a case an eventual significant difference between flight bottle and mother bottle was ignored for that calibration. Otherwise the respective entry in the Ratio row was marked with ✓, implying that this calibration can be trusted for the regarded species.

The WISE flight bottles were not corrected for any potential bias visible in the calibrations. Those calibrations were in all cases considered to be not trustworthy enough to correct the flight data. However, this implies an uncertainty on the used value for the in-flight calibration gases and therefore an uncertainty on the calculated mixing ratio of the air measurements. This uncertainty is estimated in Appendix E.2.1.

E.2.1 Uncertainty estimation of flight bottles

To estimate a global uncertainty regarding the flight bottles used for in-flight calibrations during WISE, the on-ground calibrations were used (Section E.2). The differences between the flight bottles and their respective mother bottle are available from the calibrations. The most transparent estimate for a global flight bottle uncertainty is the standard deviation of the differences from each on-ground calibration. However, several of the calibrations were considered not trustworthy for individual species resulting in very poor statistics for that estimate (see Table E.3).

Table E.3: Overview on results of the flight bottle calibration analysis. Listed are the interpretations of the differences towards the mother bottles (Diff) and the test for credibility of the calibration according to the bottles' ratios (Ratio). Any negative finding is marked with X otherwise no significant differences were found or the calibration can be trusted which is both marked with ✓.

Calibration	Test	CH_2Cl_2	$CHCl_3$*	CH_3Cl	CFC-11	CFC-113	HFC-125	HFC-134a
2017-09-30	Diff	✓	✓					
	Ratio	X	✓					
2017-10-05	Diff	X	X	✓	✓	✓	✓	
	Ratio	X	X	X	✓	✓	✓	
2017-10-11	Diff	✓	✓	✓	✓	✓	✓	✓
	Ratio	✓	✓	X	✓	✓	✓	✓
2017-10-17	Diff	✓	✓	✓	✓	✓	X	✓
	Ratio	✓	✓	X	✓	✓	X	X
2017-12-01	Diff	X	X		X	X	X	X
	Ratio	X	X		X	X	X	X

* Only CAL is of interest for this species (cf. Section 3.3.2)

Another approach to estimate the global uncertainty of the flight bottle mixing ratios uses the average over all individual errors of the flight bottle measurement during the on-ground calibrations respectively for CAL and SPAN. This gives a measure on the average quality of the on-ground calibrations. In most of the calibrations the individual uncertainty of the flight bottle measurement is larger than the difference between the flight and the mother bottle.

To make a most conservative uncertainty estimate under consideration of only a few (0–3) trusted calibrations per species, the approach yielding the larger uncertainty of the two described ones was used. In case of no trusted calibration (CH_3Cl) the best guess is to nevertheless use all the calibrations for the uncertainty estimate. The results are given as σ_{FB} relative to the nominal value of the respective mother bottle in Table E.4.

E.3 WISE MS relative accuracy estimates

Precise measurements during scientific flights are important for detailed data analysis. The accuracy of the data is none the less important and mainly dependent on the quality of the calibration of the working standards. The working standards define the mixing ratio scale for the in-flight measurements and the mixing ratios have uncertainties (Appendix E.1). In addition, the in-flight calibrations use different gas bottles containing fillings from the mother bottles of these working standards. This is attached with the uncertainty of a difference between the mixing ratio in the flight bottles and the nominal values from the mother bottles and was analyzed in Appendix E.2.

A third global uncertainty was determined during the analysis of in-flight measurements of calibration gas sampled over the same instrumental pathway used for outside air samples (Section 3.3.6). Effects that could yield biased measurements were found and global uncertainty estimates derived (Appendix D.5).

The three individual uncertainties were combined to the relative accuracy applying to all MS data from the WISE mission. The uncertainties of the mother bottle σ_{MB} were taken from Table E.2, the uncertainties on the flight bottles σ_{FB} were estimated in Appendix E.2.1, and the uncertainties regarding biasing effects from the sample line (σ_{S2P}) were estimated in Appendix D.5.

The uncertainties were calculated relative to the respective mother bottle value (e.g. $\sigma_{\mathrm{FB,\ CAL}}$ relative to CAL and $\sigma_{\mathrm{FB,\ SPAN}}$ relative to SPAN). In case both working standards were used to calculate the mixing ratios, the uncertainty was calculated from the average uncertainty of the two working standards (e.g. $\sigma_{\mathrm{MB}} = 1/2\,(\sigma_{\mathrm{MB,\ CAL}} + \sigma_{\mathrm{MB,\ SPAN}})$). Else, only the uncertainty of the calibration gas used for the calibration of flight data was used (i.e. $\sigma_{\mathrm{MB}} = \sigma_{\mathrm{MB,\ CAL}}$ and $\sigma_{\mathrm{FB}} = \sigma_{\mathrm{FB,\ CAL}}$ for $CHCl_3$; cf. Section 3.3.2). The impact of the working standards' uncertainty on air samples is less the more the air samples differ from the mixing ratio of either of the working standards (Section 3.3.2). Thus, the use of an average uncertainty from the two working standards still is a fair contribution to the relative accuracy estimation of MS air measurements.

The relative accuracy (σ_{Global}) of WISE MS data is calculated as follows (first order estimate):

$$\sigma_{\mathrm{Global}} = \sqrt{(\sigma_{\mathrm{MB}})^2 + (\sigma_{\mathrm{FB}})^2 + (\sigma_{\mathrm{S2P}})^2} \tag{E.3}$$

Table E.4 lists the individual relative global uncertainty estimates and the relative accuracy of each analyzed MS target species. These relative accuracy values should be applied for example if absolute values of MS flight data were compared with other instruments.

Table E.4: Relative accuracy of WISE MS data (σ_{Global}). The values include the uncertainties on the mother bottle values (σ_{MB}), possible differences in the bottles used for in-flight calibration (σ_{FB}), and a potential bias on the pathway of the air samples (σ_{S2P}). The values are given in percent.

[%]	σ_{MB}	σ_{FB}	σ_{S2P}	σ_{Global}
CH_2Cl_2	1.8	0.59	1.8	2.6
$CHCl_3$	12.6	1.6	4	13.3
CH_3Cl	0.65	0.91	2.1	2.4
CFC-11	0.29	1.1	0.82	1.4
CFC-113	2.3	0.93	0.84	2.6
HFC-125	1.1	1.3	0.8	1.9
HFC-134a	1.1	0.53	0.28	1.2

Appendix F

Supplemental information about the CH_2Cl_2-N_2O correlation

F.1 Supplemental information about measurement locations

Figure F.1 shows the CH_2Cl_2-N_2O correlation color coded by avionic data from the Basic HALO Measurement and Sensor System (BAHAMAS; Krautstrunk and Giez, 2012; Giez et al., 2017). The left panel shows the potential temperature at the measurement location and the right panel shows the aircraft's altitude during the measurement.

Figure F.2 shows the CH_2Cl_2-N_2O correlation color coded by the latitudinal position of the aircraft during measurement (left) and the longitudinal position of the aircraft during measurement (right).

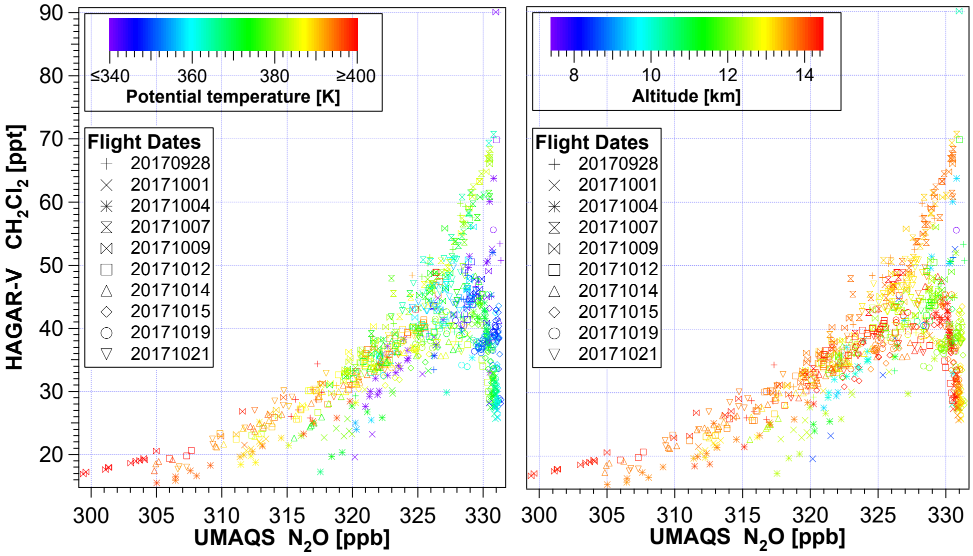

Figure F.1: CH_2Cl_2-N_2O correlation during WISE color coded by the potential temperature (left) and the altitude (right) of the aircraft at the position of measurement.

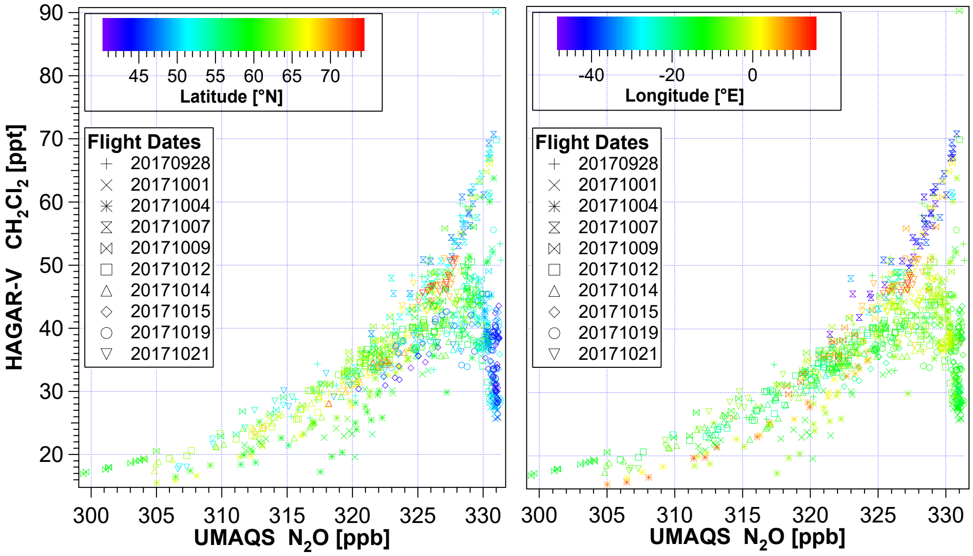

Figure F.2: CH_2Cl_2-N_2O correlation during WISE color coded by the latitude (left) and the longitude (right) of the aircraft at the position of measurement.

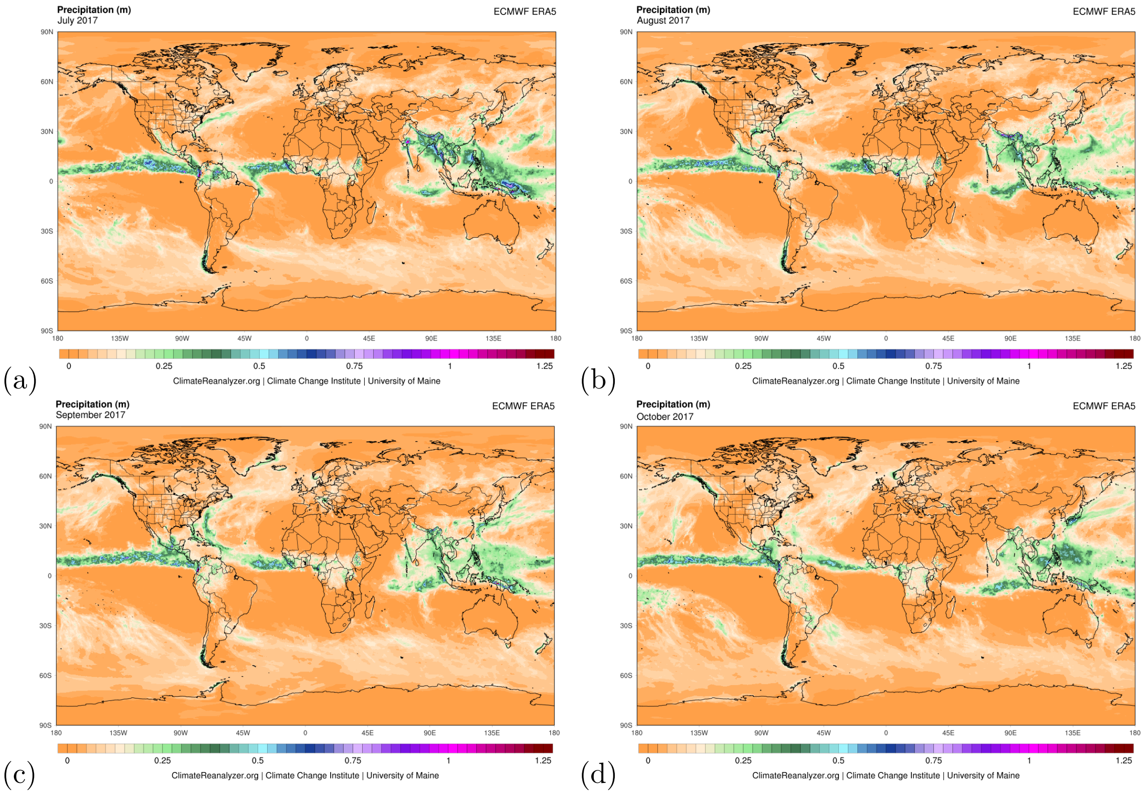

Figure F.3: Monthly mean precipitation calculated from ECMWF ERA5 reanalysis data (Hersbach et al., 2020) to visualize the ITCZ of (a) July, (b) August, (c) September, and (d) October 2017. The greenish belt around the equator is considered to mark the ITCZ. Graphs from Climate Reanalyzer (https://ClimateReanalyzer.org), Climate Change Institute, University of Maine, USA.

F.2 Supplemental graphs of emission tracers

F.2.1 The ITCZ in summer 2017

Figure F.3 shows the location of the inter-tropical convergence zone (ITCZ) for the months July (a), August (b), September (c), and October (d) in 2017. The ITCZ is a convective belt around the globe and visualized here by the monthly mean precipitation values from ECMWF ERA5 reanalysis data (Hersbach et al., 2020). High precipitation (the greenish belt-like structure along the equator) is considered to mark the ITCZ. The precipitation as a representation of the location of the ITCZ is best over sea and might not cover all of the main convection zone over land. However, these figures are a sufficiently good representation of the ITCZ and support well the analysis from sections 4.2.3 and 4.2.5.

F.2.2 All individual emission tracers

This section shows several plots of the CH_2Cl_2-N_2O correlation observed during the WISE mission in 2017 color coded with different emission tracers calculated by CLaMS (Section 4.1). Figures F.4, F.5, and F.6 show the correlation color coded with each individual emission tracer.

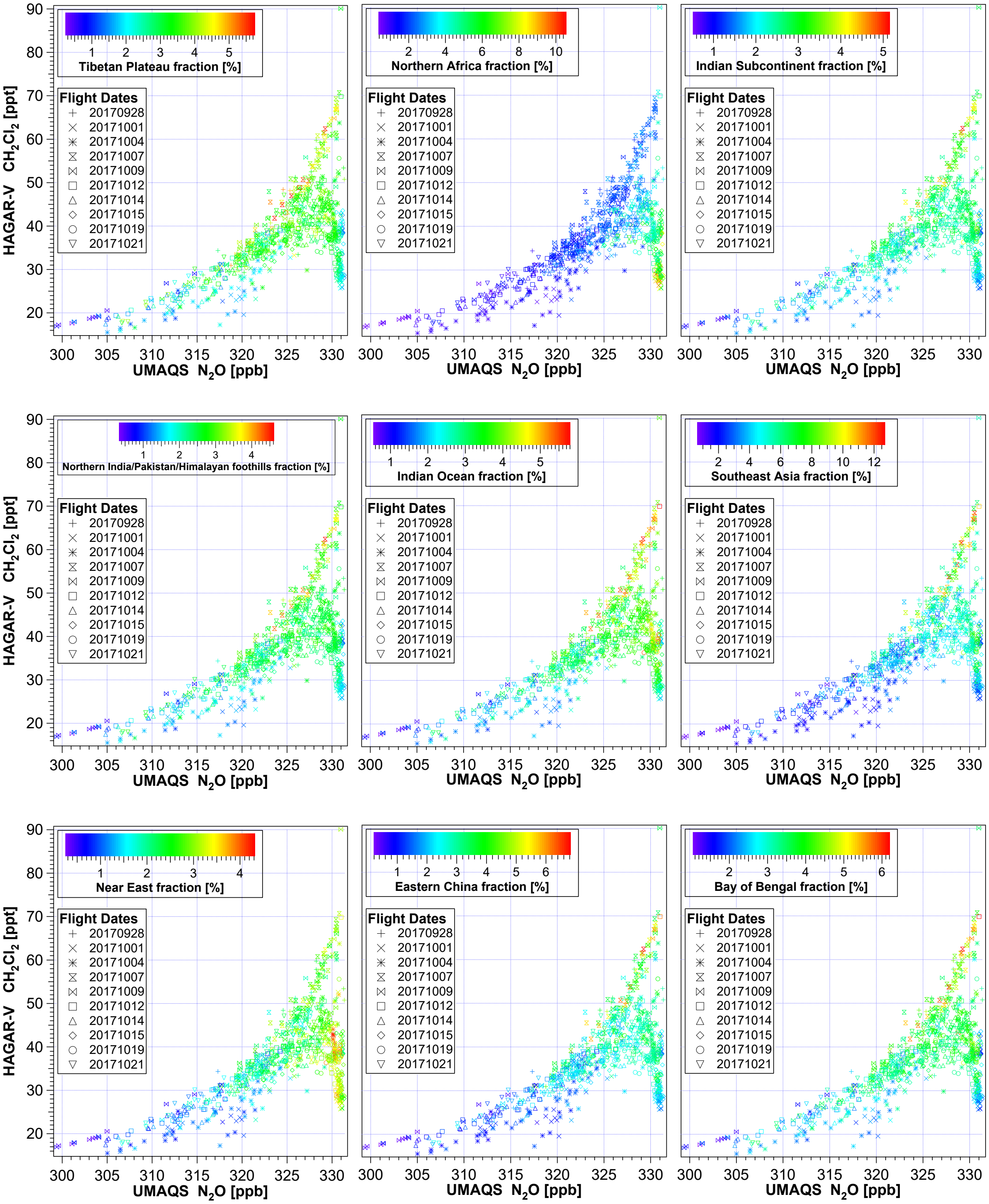

Figure F.4: CH_2Cl_2-N_2O correlation during WISE color coded with each individual emission tracer simulated with CLaMS. The boundaries of the emission tracers are given in Figure 4.1.

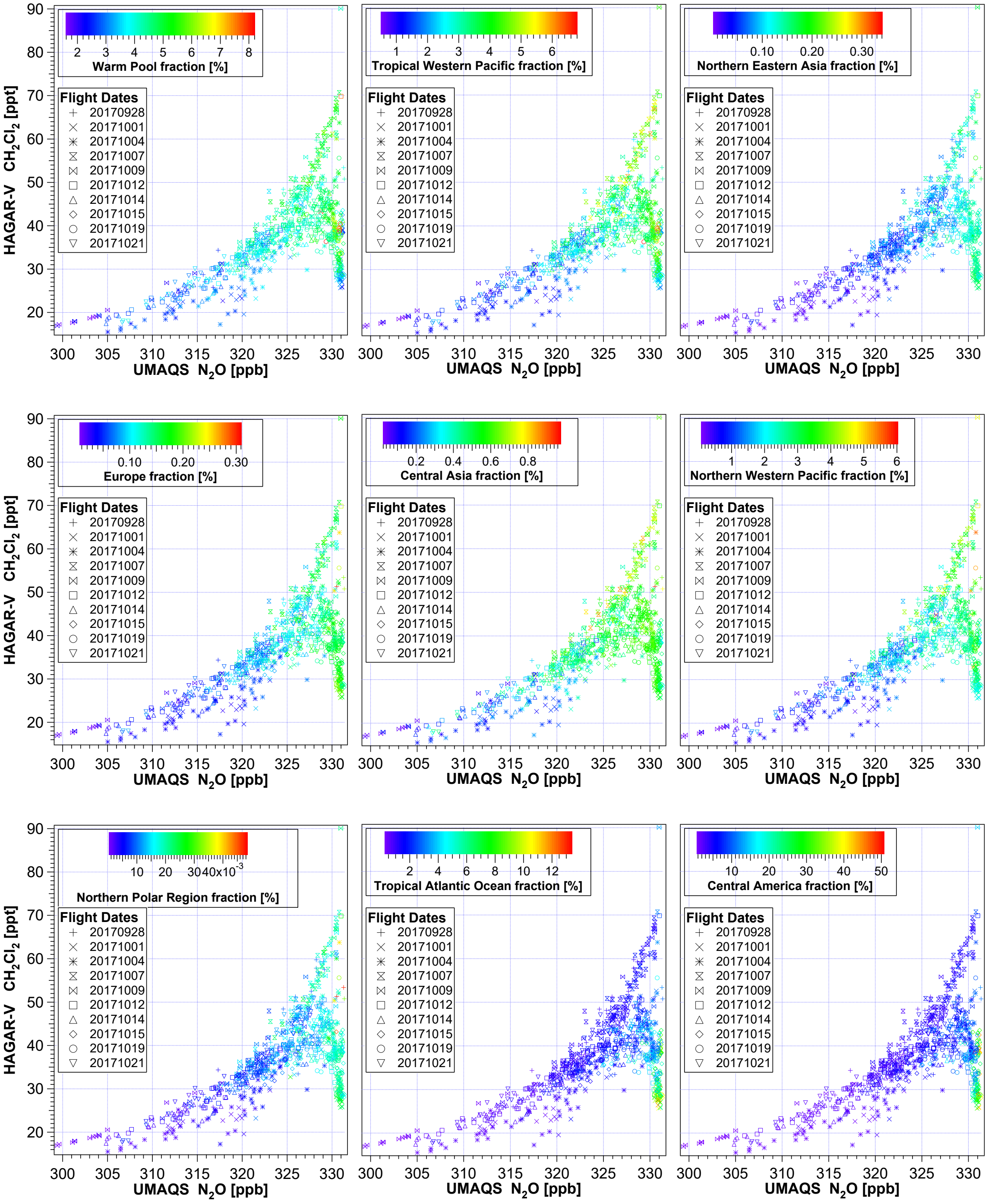

Figure F.5: CH_2Cl_2-N_2O correlation during WISE color coded with each individual emission tracer simulated with CLaMS. The boundaries of the emission tracers are given in Figure 4.1.

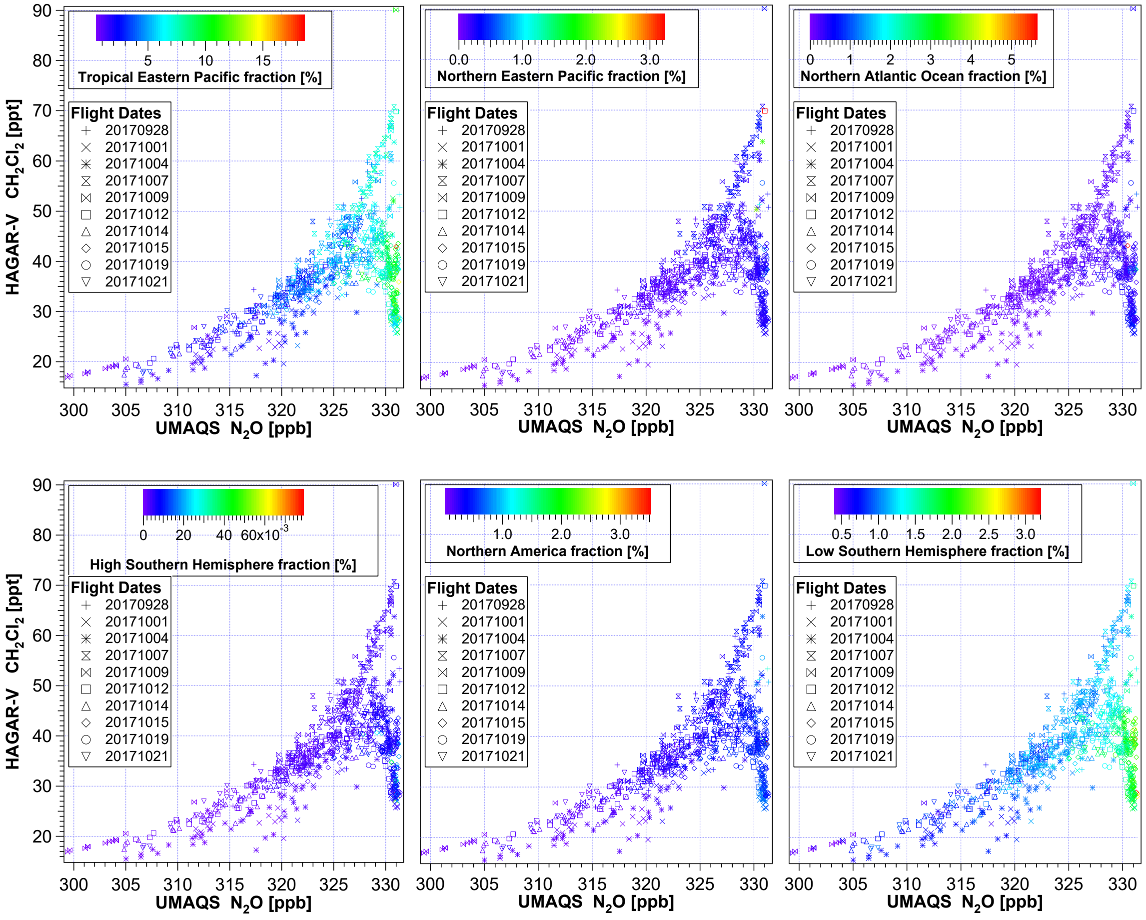

Figure F.6: CH_2Cl_2-N_2O correlation during WISE color coded with each individual emission tracer simulated with CLaMS. The boundaries of the emission tracers are given in Figure 4.1.

F.2.3 Normalized emission tracers

Figure F.7 shows different correlations regarding the combined and normalized emission tracers SaEA and W-ITCZ. It is visible that the CH_2Cl_2 mixing ratios correlate ($R = 0.67$) with the normalized fraction of air from southern and eastern Asia (i.e. fraction of air younger than six months). This indicates that young air masses from southern and eastern Asia impact the UTLS over the Atlantic and Europe with CH_2Cl_2-rich air. An anticorrelation ($R = -0.66$) is visible for CH_2Cl_2 mixing ratios measured during WISE vs the normalized fraction of W-ITCZ. This indicates that the western ITCZ is the main source region for CH_2Cl_2-poor air in the NH UTLS in summer. In general, the normalized fractions of SaEA vs W-ITCZ at the positions of measurement are anticorrelated ($R = -0.99$),

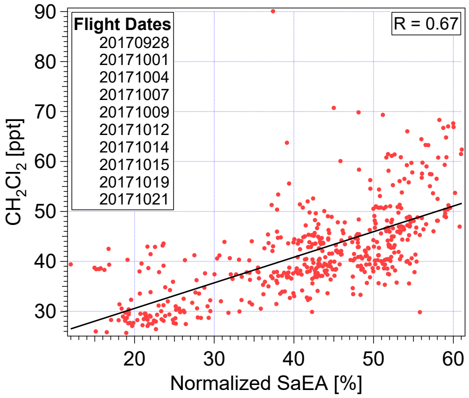

(a)

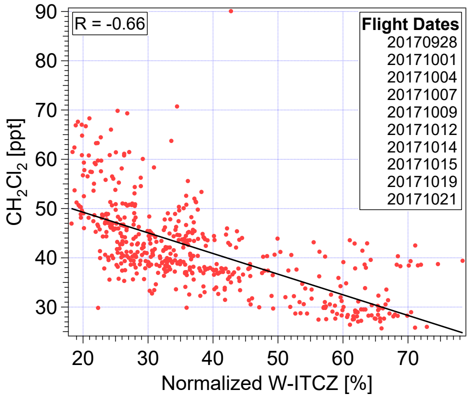

(b)

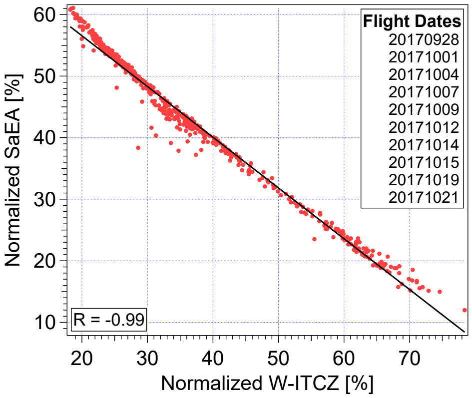

(c)

Figure F.7: Correlations of normalized emission tracers and the measurements of CH_2Cl_2 during WISE. (a) shows CH_2Cl_2 vs normalized fraction of the SaEA tracer, (b) shows CH_2Cl_2 vs normalized fraction of the W-ITCZ tracer, (c) shows the normalized SaEA tracer vs the normalized W-ITCZ tracer at the time and position of all CH_2Cl_2 measurements during WISE.

indicating that each measured air parcel consists of a relatively constant total of ~ 85 % of young air from these two source regions.

F.3 Supplemental statistics about the correlation branch filter

In this section different tables list information on WISE measurements of the upper and the lower branch (cf. Section 4.2.1). The tables show different properties like the number of data points in the filtered data set, median mixing ratios, and median information on sampling position (Table F.1), as well as median fractions of different emission tracers (Table F.2), and the number of backward trajectories in the filtered data set that reached the BL within 120 days, median transport times on calculated trajectories, and median maximum change in potential temperature on calculated trajectories (Table F.3) for each flight individually and for all flights. The use of the median instead of the average yields similar results for most of the quantities but are a better representation of the center information if they differ. In the present work averages are marked as $\overline{\mathrm{X}}$ and medians are marked as $\widetilde{\mathrm{X}}$.

Table F.1: Information on mixing ratios and aircraft data associated with the upper branch and the lower branch (cf. Section 4.2.1). For each relevant WISE flight date, the number of data points (N) within the respective branch and the median values of CH_2Cl_2 mixing ratios ($\widetilde{\mathrm{CH_2Cl_2}}$) in ppt, of $CHCl_3$ mixing ratios ($\widetilde{\mathrm{CHCl_3}}$) in ppt, of the potential temperature ($\widetilde{\Theta}$) at point of measurement in K, of the altitude ($\widetilde{\mathrm{Alt}}$) at the point of measurement in m, of the Latitude ($\widetilde{\mathrm{Lat}}$) at the point of measurement in °N, and of the Longitude ($\widetilde{\mathrm{Lon}}$) at the point of measurement in °E are listed. The bottom row gives the respective column quantity for all matching WISE flights.

Upper branch

Flight date	N	$\widetilde{\mathrm{CH_2Cl_2}}$ [ppt]	$\widetilde{\mathrm{CHCl_3}}$ [ppt]	$\widetilde{\Theta}$ [K]	$\widetilde{\mathrm{Alt}}$ [m]	$\widetilde{\mathrm{Lat}}$ [°N]	$\widetilde{\mathrm{Lon}}$ [°E]
Sept, 28	10	57.1	8.2	378.9	13727	55.7	−6.36
Oct, 01	-	-	-	-	-	-	-
Oct, 04	2	61.9	10.6	330.4	9440	58.2	−3.5
Oct, 07	42	56.5	7.7	378.6	13851	50.3	−40.6
Oct, 09	15	59	8.1	381.1	13727	63.9	2.1
Oct, 12	2	59.4	8.9	369.1	12905	59.1	−13.6
Oct, 14	-	-	-	-	-	-	-
Oct, 15	-	-	-	-	-	-	-
Oct, 19	-	-	-	-	-	-	-
Oct, 21	6	50.9	7.1	362.8	13125	73.2	6.7
All flights	77	56.5	7.9	377.5	13727	52.7	−23.9

Lower branch

Flight date	N	$\widetilde{\mathrm{CH_2Cl_2}}$ [ppt]	$\widetilde{\mathrm{CHCl_3}}$ [ppt]	$\widetilde{\Theta}$ [K]	$\widetilde{\mathrm{Alt}}$ [m]	$\widetilde{\mathrm{Lat}}$ [°N]	$\widetilde{\mathrm{Lon}}$ [°E]
Sept, 28	1	39.8	7.8	338.9	11585	55.9	−6.2
Oct, 01	48	29	5.7	363.3	13130	50.54	−13.4
Oct, 04	22	38	5.9	368.2	14336	48.8	−2.1
Oct, 07	-	-	-	-	-	-	-
Oct, 09	-	-	-	-	-	-	-
Oct, 12	6	32.7	5.7	383	14337	55	−7.1
Oct, 14	9	32.6	6	372.2	14342	50.8	−4
Oct, 15	52	33.7	6.4	357.8	13125	44.2	−15.3
Oct, 19	46	37.1	6.2	353	12207	47.8	−6.1
Oct, 21	2	37.1	6.5	363.2	13041	48.2	5.3
All flights	186	34.2	6.1	361.6	13125	48.8	−12

Table F.2: Information on tracers of air mass origin associated with the upper branch and the lower branch (cf. Section 4.2.1). For each relevant WISE flight date, the number of data points (N) within the respective branch and the median values of the sum of all emission tracers ($\widetilde{\text{ALL}}$) in %, of the fraction of the SaEA tracer ($\widetilde{\text{SaEA}}$) in %, of the fraction of the CAM tracer ($\widetilde{\text{CAM}}$) in %, of the fraction of the western ITCZ tracer ($\widetilde{\text{W-ITCZ}}$) in %, of the SaEA tracer normalized in the sum of all emission tracers ($\widetilde{\text{rel SaEA}}$) in %, and of the western ITCZ tracer normalized on the sum of all emission tracers (rel $\widetilde{\text{W-ITCZ}}$) in % are listed. The bottom row gives the respective column quantity for all matching WISE flights. For information on the emission tracers see Section 4.2.3.

Upper branch

Flight date	N	$\widetilde{\text{ALL}}$ [%]	$\widetilde{\text{SaEA}}$ [%]	$\widetilde{\text{CAM}}$ [%]	$\widetilde{\text{W-ITCZ}}$ [%]	rel $\widetilde{\text{SaEA}}$ [%]	rel $\widetilde{\text{W-ITCZ}}$ [%]
Sept, 28	10	47.1	27.4	3.2	9.7	57.26	20.1
Oct, 01	-	-	-	-	-	-	-
Oct, 04	2	64.1	27	7.9	20.3	42.5	31.4
Oct, 07	42	69.7	36.7	4.6	15.4	54.5	23.8
Oct, 09	15	61.8	34	4	13.6	56.1	22.3
Oct, 12	2	73.3	38.6	5.6	16.9	53.6	22.5
Oct, 14	-	-	-	-	-	-	-
Oct, 15	-	-	-	-	-	-	-
Oct, 19	-	-	-	-	-	-	-
Oct, 21	6	56.3	28.8	5.1	15.1	50.9	26.9
All flights	77	63.8	34	4.4	14.9	54.6	23.5

Lower branch

Flight date	N	$\widetilde{\text{ALL}}$ [%]	$\widetilde{\text{SaEA}}$ [%]	$\widetilde{\text{CAM}}$ [%]	$\widetilde{\text{W-ITCZ}}$ [%]	rel $\widetilde{\text{SaEA}}$ [%]	rel $\widetilde{\text{W-ITCZ}}$ [%]
Sept, 28	1	61	27.2	8.4	20.4	44.5	33.4
Oct, 01	48	83.8	17.8	27.5	52.5	21.4	62.5
Oct, 04	22	70.8	30.8	7.1	22.7	44	32.8
Oct, 07	-	-	-	-	-	-	-
Oct, 09	-	-	-	-	-	-	-
Oct, 12	6	68.1	25.2	11.8	28.8	37.3	42.3
Oct, 14	9	80	26.6	19.2	39.1	32.7	48.5
Oct, 15	52	88.5	20.6	29.4	52.5	23.6	60.1
Oct, 19	46	71.1	28.5	11.9	28.6	40.9	38.6
Oct, 21	2	81.2	29.3	15	35.5	35.9	43.8
All flights	186	81.5	23.7	20.8	43	29.2	52.8

Table F.3: Information on backward trajectories associated with the upper branch and the lower branch (cf. Section 4.2.1). For each relevant WISE flight date and for each of the two correlation branches, the number of data points whose backward trajectory reached the boundary layer within 120 days (N (BL in $\leq$ 120 d)), as well as the median values of trajectory transport time ($\widetilde{\text{transp.}}$ t) in days, of the maximum ascent rate along a trajectory ($\widetilde{\text{max.}\ \dot{\Theta}}$) in K/18 h, of the Latitude ($\widetilde{\text{Lat}}$) of the trajectory end points at the BL in °N, and of the longitude ($\widetilde{\text{Lon}}$) of the trajectory end points at the BL in °E are listed. The bottom row gives the respective column quantity for all matching WISE flights.

		Upper branch			
Flight date	N (BL in $\leq$ 120 d)	$\widetilde{\text{transp.}}$ t [d]	$\widetilde{\text{max.}\ \dot{\Theta}}$ [K/18 h]	$\widetilde{\text{Lat}}$ [°N]	$\widetilde{\text{Lon}}$ [°E]
Sept, 28	6	50.9	21	28.5	32.2
Oct, 01	-	-	-	-	-
Oct, 04	1	50.5	35.8	20.5	94
Oct, 07	35	64.6	14.2	25	97.1
Oct, 09	12	66.1	16	22.8	88.9
Oct, 12	2	72.1	18.4	24.3	124.3
Oct, 14	-	-	-	-	-
Oct, 15	-	-	-	-	-
Oct, 19	-	-	-	-	-
Oct, 21	2	89.3	21.3	20.6	−87.5
All flights	58	64.5	16.1	23.9	91.4

		Lower branch			
Flight date	N (BL in $\leq$ 120 d)	$\widetilde{\text{transp.}}$ t [d]	$\widetilde{\text{max.}\ \dot{\Theta}}$ [K/18 h]	$\widetilde{\text{Lat}}$ [°N]	$\widetilde{\text{Lon}}$ [°E]
Sept, 28	1	87.5	41.3	26.5	97.2
Oct, 01	47	21.9	24.4	13.6	−55.4
Oct, 04	19	49	17.4	19	97.4
Oct, 07	-	-	-	-	-
Oct, 09	-	-	-	-	-
Oct, 12	5	71.2	25	23.8	91.2
Oct, 14	8	35.3	15.2	10.7	−59.8
Oct, 15	52	44.7	17	12.1	−60.6
Oct, 19	35	55.8	15.5	18.2	−10.8
Oct, 21	1	41.1	24.6	15.1	113.9
All flights	168	42.3	17.7	14.7	−28.4

Appendix G

Supplemental information about the $CHCl_3$-N_2O correlation

G.1 The positions of measurement

This section shows several scatter plots of the $CHCl_3$-N_2O correlation of the WISE mission in 2017 color coded with different information about the sample positions. Figure G.1 shows the potential temperature (left) and the altitude (right) of the aircraft's position during the preconcentration process of the MS module. Figure G.2 shows the latitude (left) and the longitude (right) of the aircraft's position during the preconcentration process of the MS module.

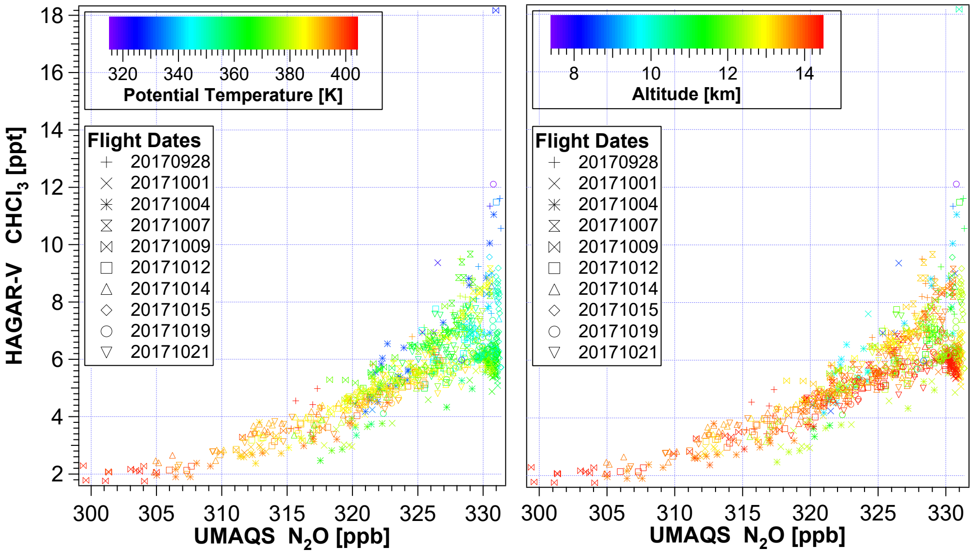

Figure G.1: CHCl$_3$-N$_2$O correlation during WISE color coded with the potential temperature (left) and the altitude (right) of the aircraft at the position of measurement.

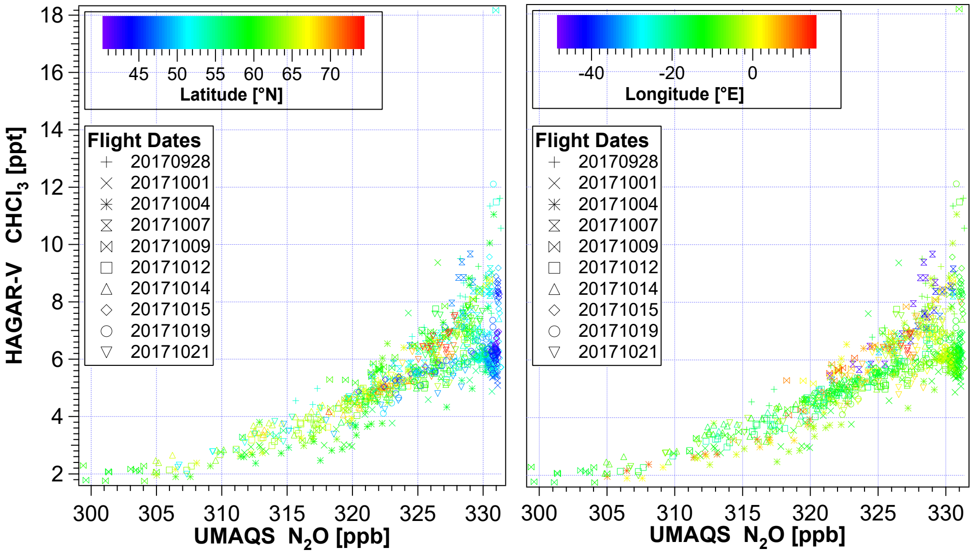

Figure G.2: CHCl$_3$-N$_2$O correlation during WISE color coded with the latitude (left) and the longitude (right) of the aircraft at the position of measurement.

G.2 Supplemental information about emission tracers

This section shows several plots of the CHCl$_3$-N$_2$O correlation observed during the WISE mission in 2017 color coded with different emission tracers calculated by CLaMS (Section 4.1). Figure G.3 shows the sum of all emission tracers (left) and the fraction of the emission

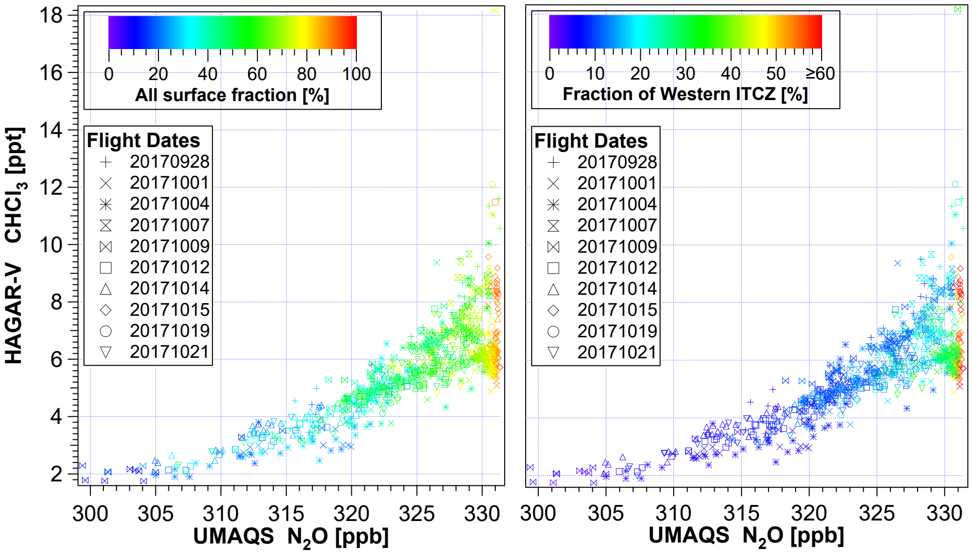

Figure G.3: CHCl$_3$-N$_2$O correlation during WISE color coded with the sum of all emission tracers (left) and the W-ITCZ (right) tracer simulated by CLaMS. The boundaries of the emission tracers are given in Figure 4.1.

tracers along the western ITCZ (right). Figures G.4, G.5, and G.6 show each individual emission tracer.

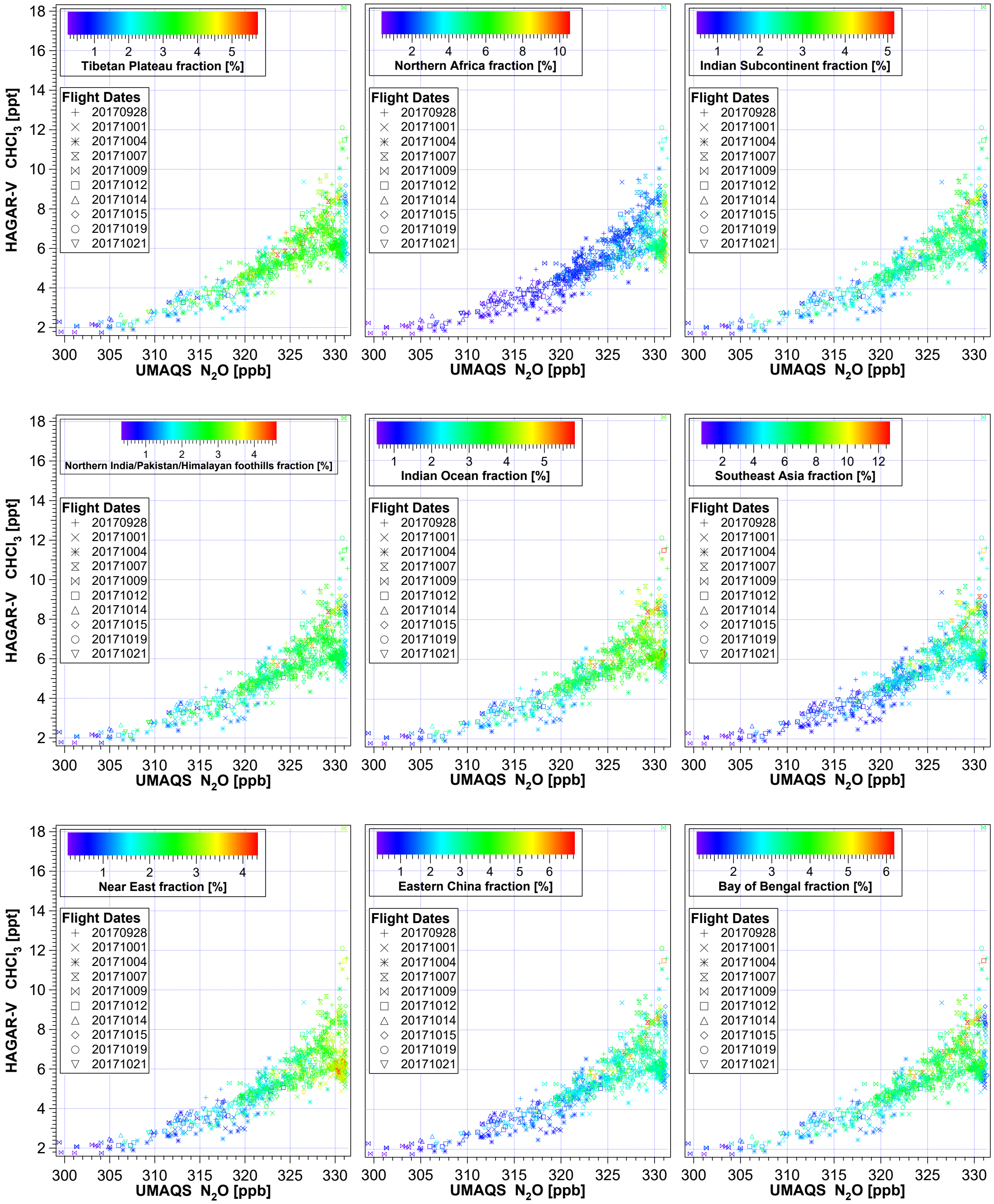

Figure G.4: CHCl$_3$-N$_2$O correlation during WISE color coded with each individual emission tracer simulated with CLaMS. The boundaries of the emission tracers are given in Figure 4.1.

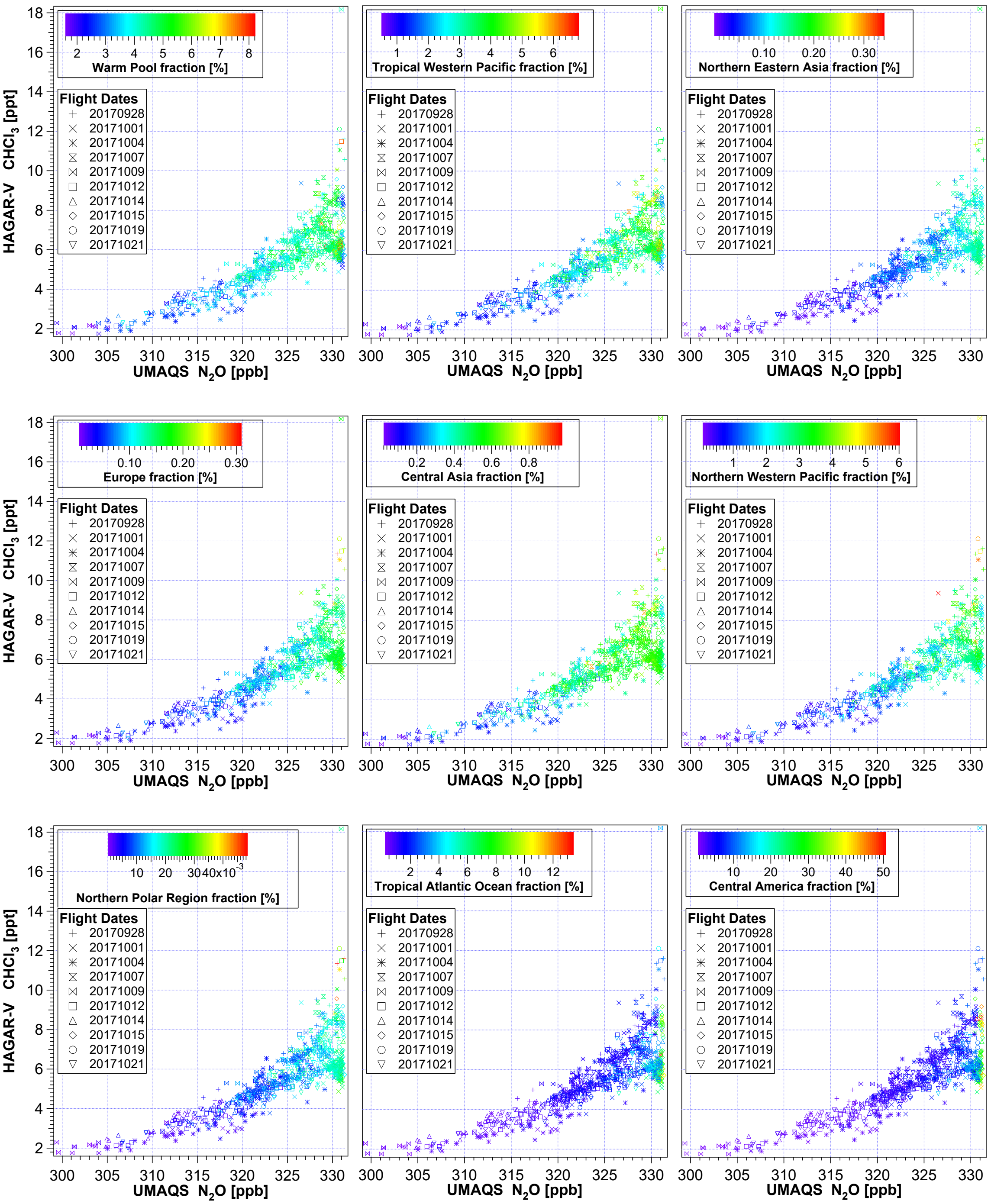

Figure G.5: $CHCl_3$-N_2O correlation during WISE color coded with each individual emission tracer simulated with CLaMS. The boundaries of the emission tracers are given in Figure 4.1.

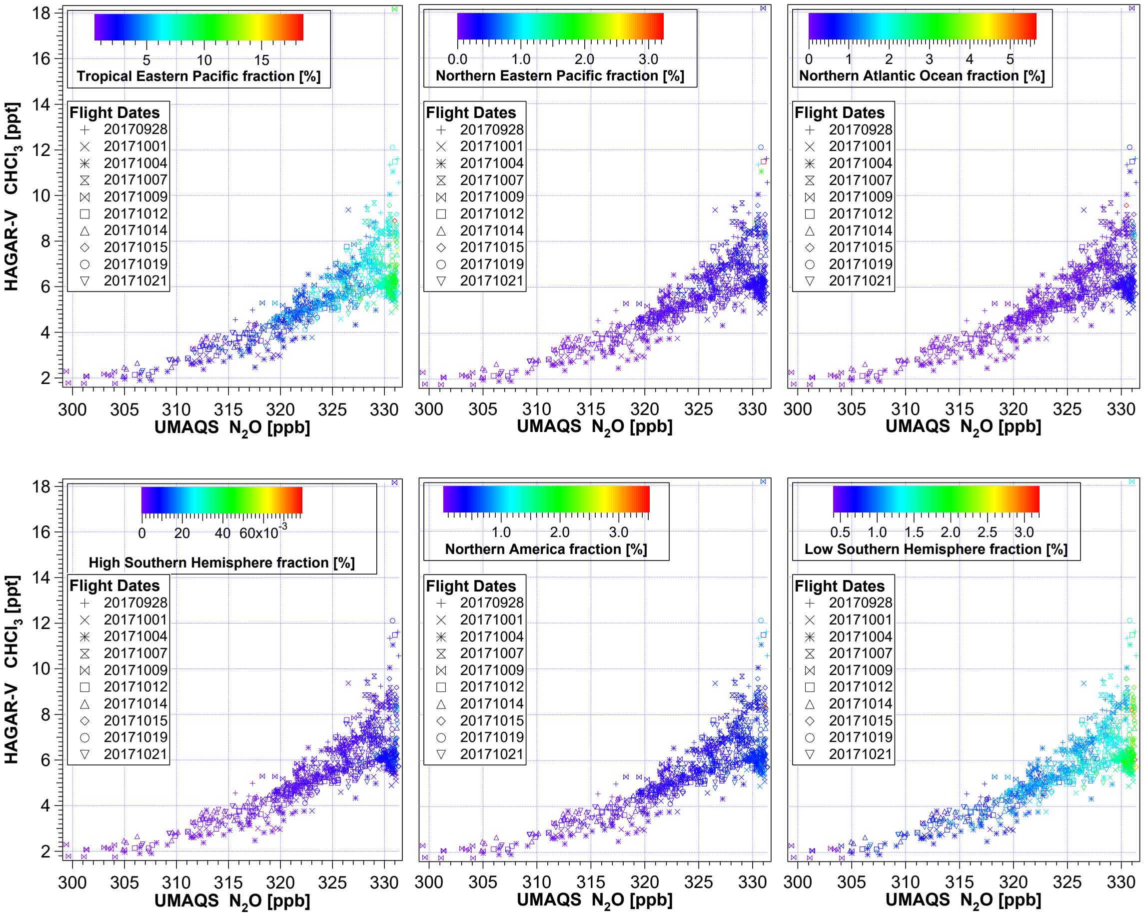

Figure G.6: CHCl$_3$-N$_2$O correlation during WISE color coded with each individual emission tracer simulated with CLaMS. The boundaries of the emission tracers are given in Figure 4.1.

G.3 Seasonal dominance of source regions for CHCl$_3$

Similar to the analysis of normalized emission tracers with the CH$_2$Cl$_2$-N$_2$O correlation in Section 4.2.4, the normalized tracers of SaEA and W-ITCZ (cf. Figure 4.1) were analyzed with the CHCl$_3$-N$_2$O correlation. The predominant influence of the young ($<$ 6 months) air masses from southern and eastern Asia mark almost the whole correlation in the LMS with a fraction $>$ 50 % (Figure G.7, left). Close to the chemical tropopause the dominance of the normalized SaEA tracer only marks CHCl$_3$-rich air with fractions $>$ 55 %. However, other than for CH$_2$Cl$_2$, also CHCl$_3$-rich air in the LMS is marked with fractions $<$ 50 %. This indicates that young air masses from other source regions than southern and eastern Asia contribute with CHCl$_3$-rich air to the composition of the LMS. Tropical background air is associated with CHCl$_3$-poor measurements in the LMS close to the chemical tropopause

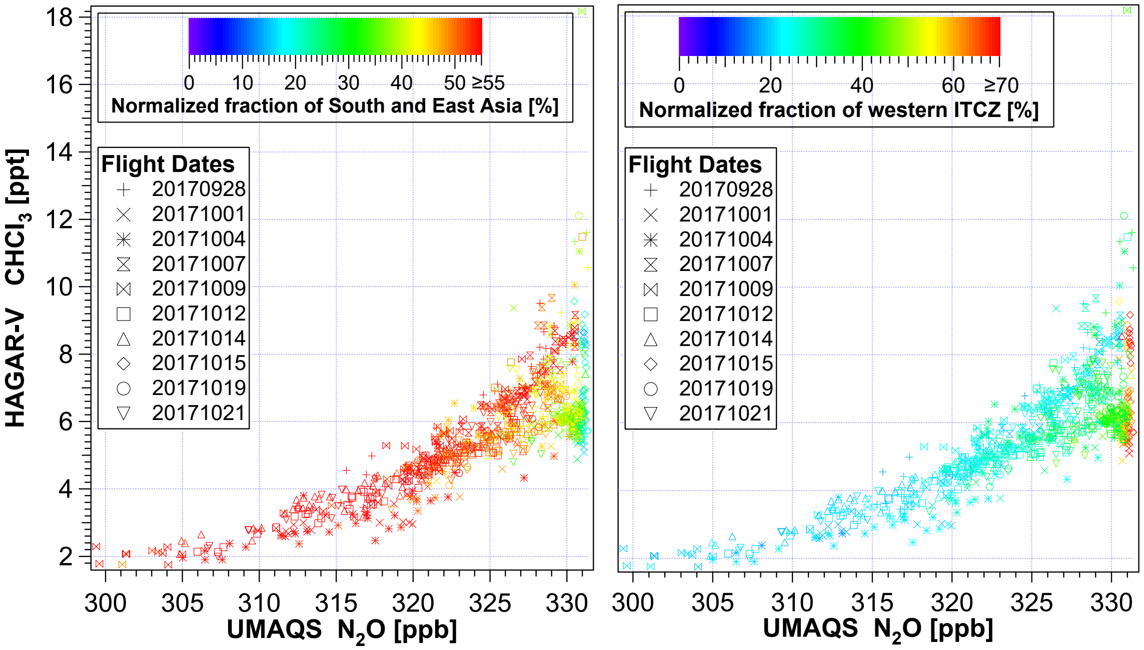

Figure G.7: $CHCl_3$-N_2O correlation during WISE color coded with the normalized SaEA (left) and the normalized W-ITCZ (right) emission tracer. The boundaries of the emission tracers are given in Figure 4.1, the sum of all emission tracers are given in Figure G.3, left.

and the measurements in the UT (Section 4.3.1). These measurements express the lowest fraction of the normalized SaEA tracer and are thus much less influenced by young air originating in southern and eastern Asia.

The normalized fraction of the W-ITCZ emission tracer shows a large fraction at measurements marked with a low fraction of the normalized SaEA tracer (Figure G.7, right). In particular the UT predominantly is influenced by young air from the region of the western ITCZ. Measurements in the UT show a wide range of $CHCl_3$ mixing ratios. In difference to the observations on CH_2Cl_2 (Section 4.2.4), a significant number of measurements of $CHCl_3$-rich air are marked with a normalized W-ITCZ fraction of ≥ 40 %. The mixed air of almost equally high fractions of young air from southern and eastern Aisa and the western ITCZ identified between the two branches in the CH_2Cl_2-N_2O correlation tends to be of measurements of $CHCl_3$-rich air. This indicates that southern and eastern Asia is not the single predominant source region for $CHCl_3$-rich air in the LMS during NH summer.

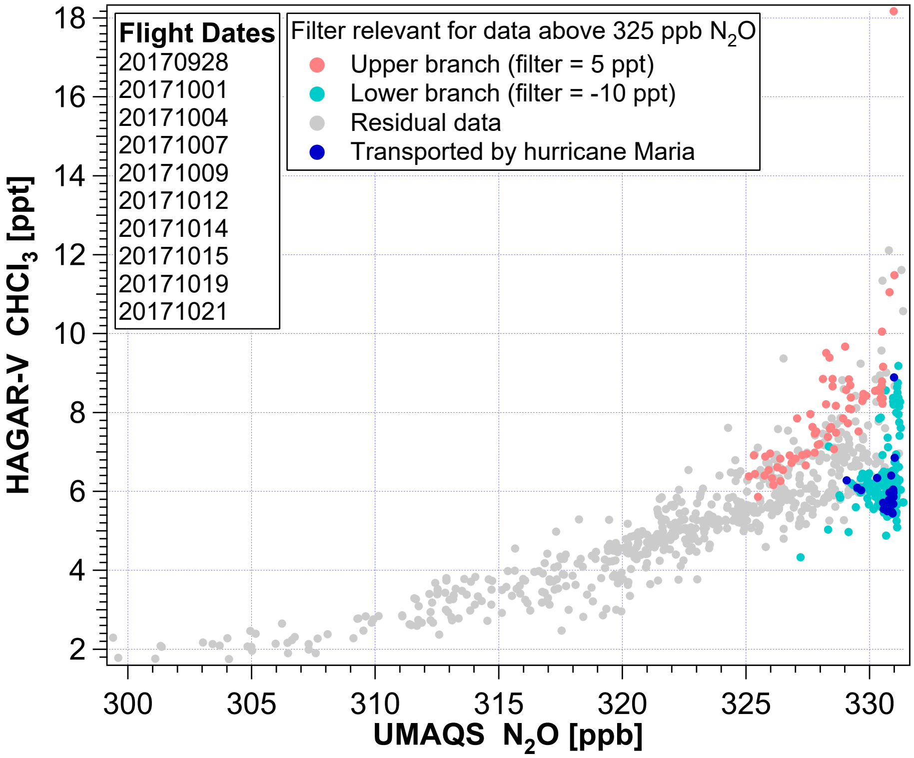

Figure G.8: CHCl$_3$-N$_2$O correlation with colors marking data uplifted by hurricane Maria (blue) and according to the branch filter (upper branch: light red, lower branch: light blue, data between the branches: gray).

G.4 Supplemental information about measurements associated with hurricane Maria

Figure G.8 shows the WISE CHCl$_3$-N$_2$O correlation. The two branches are marked by different colors (upper branch: light red; lower branch: light blue; data between the branches: gray) and measurements associated with uplift by hurricane Maria are marked blue. Similar to the impact on CH$_2$Cl$_2$, the majority of measurements uplifted by hurricane Maria are of CHCl$_3$-poor air. Hence, hurricane Maria could be identified to have acted as a convective transport pathway from the source region into the UTLS of primarily CH$_2$Cl$_2$-poor and CHCl$_3$-poor air.

Appendix H

Supplemental information about backward trajectories

In this section supplemental information about the backward trajectories are shown. The positions where the backward trajectories first touch the BL are shown in Appendix H.1. The full backward trajectories sorted by flight and branch are shown in Appendix H.2. In addition, Appendix H.2 shows the full trajectories of data uplifted by hurricane Maria.

H.1 Source regions at boundary layer

Figure H.1 shows the end points at the boundary layer of 120 day backward trajectories color coded with the respective measured value of (a) CH_2Cl_2 and (b) $CHCl_3$. It is visible that almost all the backward trajectories from the WISE measurements end along the ITCZ. The plots also show that the mixing ratios of CH_2Cl_2 tend to be higher when originating in the region of southern and eastern Asia than from some other region along the ITCZ. This tendency is much less pronounced for $CHCl_3$, indicating a more equally distributed $CHCl_3$ mixing ratio along the ITCZ.

Figure H.2 shows the 120 day backward trajectory end points of the upper and of the lower branch color coded with CH_2Cl_2 mixing ratios (top), $CHCl_3$ mixing ratios (middle), and the potential temperature (bottom) at the position of measurement. The same color scale was used for data of the upper and the lower branch to make differences between the two branches visible.

Figure H.3 shows the backward trajectory end points of WISE measurements uplifted by hurricane Maria. The trajectory end points are marked either with (a) the measured

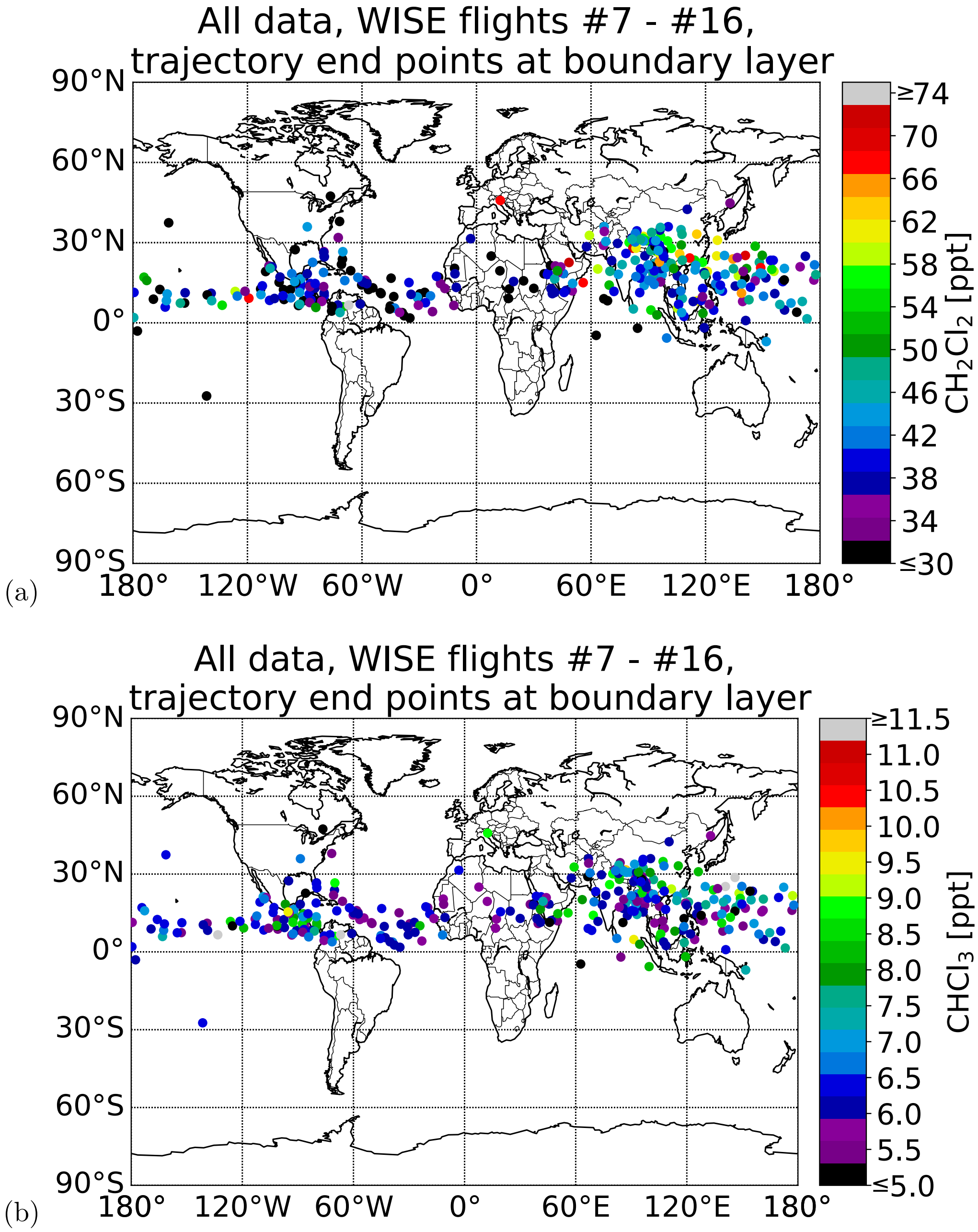

Figure H.1: 120 day backward trajectory end points at the boundary layer calculated with CLaMS for all HAGAR-V MS WISE measurements and color coded with (a) the CH_2Cl_2 mixing ratio and (b) the $CHCl_3$ mixing ratio. The color scale for CH_2Cl_2 was limited from 30 ppt to 75 ppt and for $CHCl_3$ from 5 ppt to 11.5 ppt.

CH_2Cl_2 mixing ratios, (b) the measured $CHCl_3$ mixing ratios, or (c) the potential temperature at the position of measurement. The plots show that the source region of most

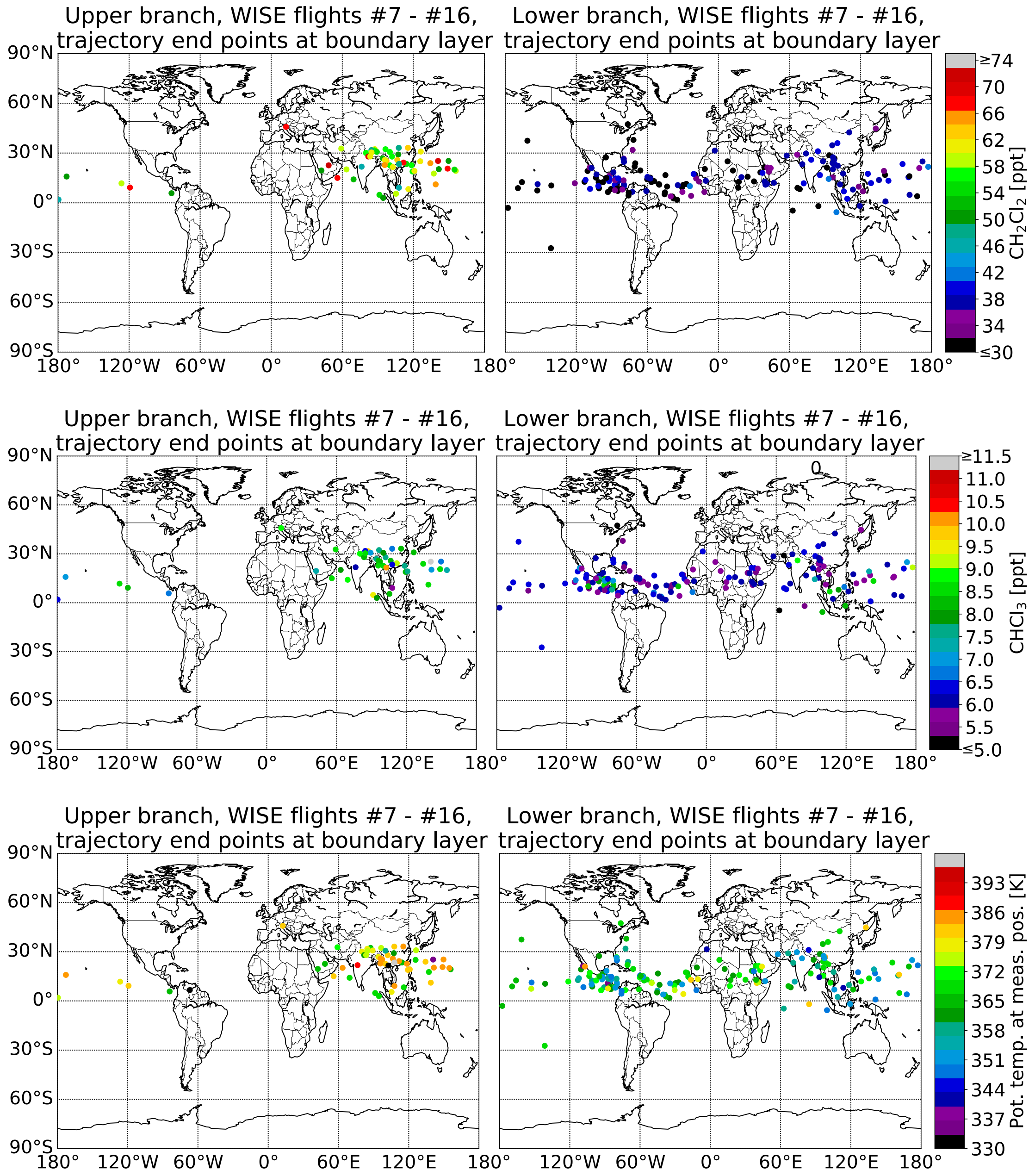

Figure H.2: 120 day backward trajectory end points at the boundary layer (BL) calculated with CLaMS for HAGAR-V MS WISE measurements color coded with CH_2Cl_2 (upper row), $CHCl_3$ (middle row), and potential temperature (bottom row) at the position of measurement. Left plots show only the trajectory end points of measurements of the upper branch and right plots show measurements of the lower branch. The color scale of CH_2Cl_2 is limited from 30 ppt to 75 ppt and that of $CHCl_3$ from 5 ppt to 11.5 ppt.

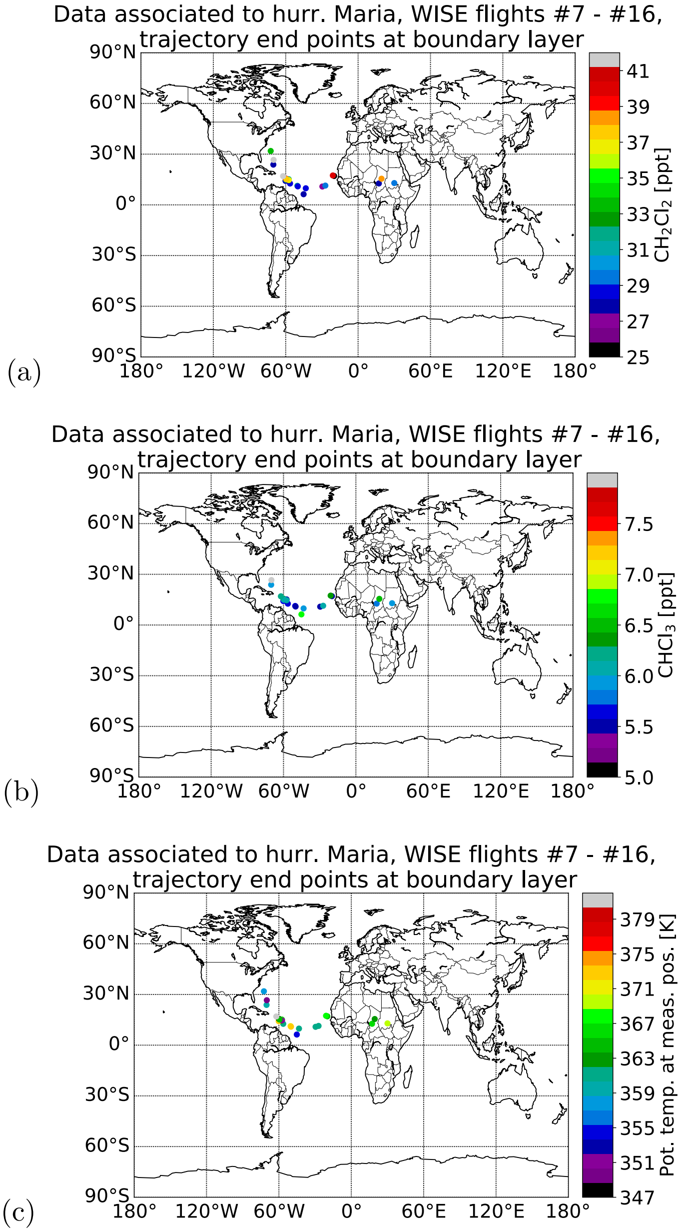

Figure H.3: Backward trajectory end points at the boundary layer of WISE measurements associated with uplift by hurricane Maria and different color coding. (a) is color coded with the measured CH_2Cl_2 mixing ratio, (b) is color coded with the measured $CHCl_3$ mixing ratio, and (c) is color coded with the potential temperature at the respective position of measurement.

air parcels uplifted by hurricane Maria is above water and distributed eastwards from the storm track along the ITCZ.

H.2 Full backward trajectories

In this section the full 120 day backward trajectories of different WISE flights and the different branches are shown. The backward trajectories are projected in plots of latitude vs longitude as well as latitude or longitude vs potential temperature to better comprehend their respective trace.

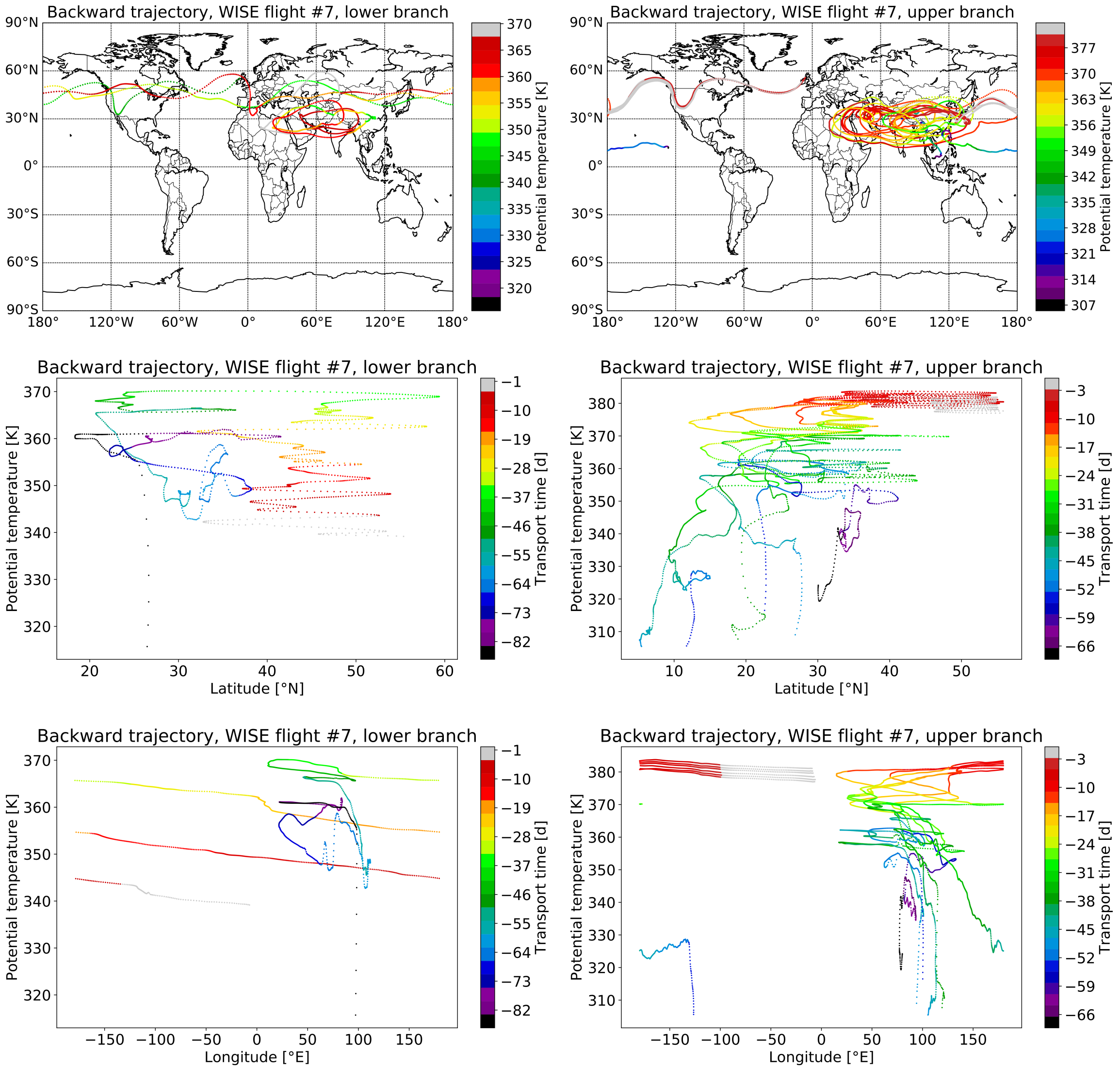
Backward trajectory, WISE flight #7, lower branch

Backward trajectory, WISE flight #7, upper branch

Backward trajectory, WISE flight #7, lower branch

Backward trajectory, WISE flight #7, upper branch

Backward trajectory, WISE flight #7, lower branch

Backward trajectory, WISE flight #7, upper branch

Figure H.4: Backward trajectories of measurements of the lower branch (left) and the upper branch (right) of WISE flight #7 down to the BL. The upper row shows latitude vs longitude color coded with the potential temperature. The middle row shows the potential temperature vs latitude color coded with the transport time from the position of measurement to the respective position of the trajectory. The bottom row shows the same content as the middle row only plotted against the longitude instead of the latitude.

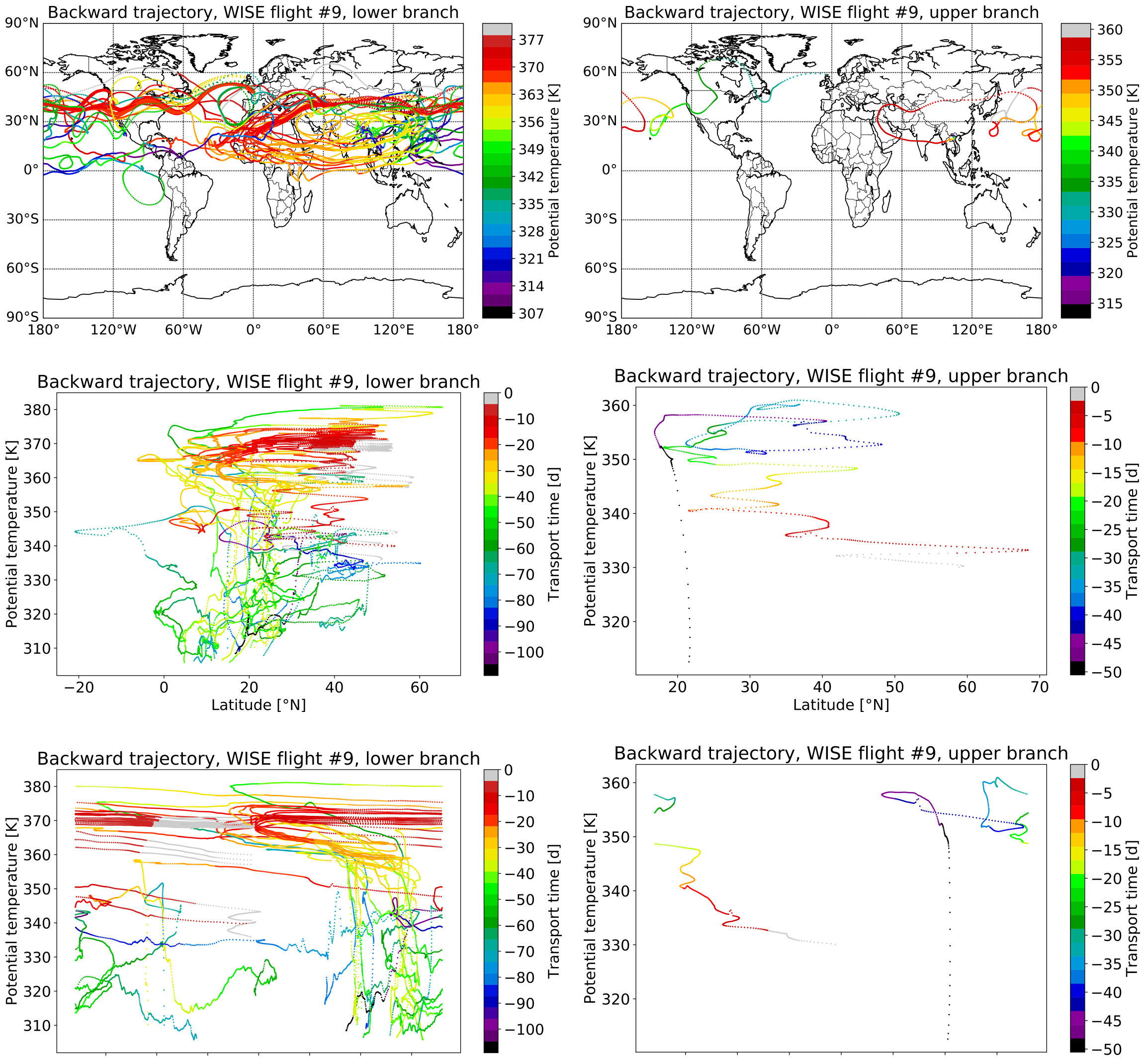

Figure H.5: Backward trajectories of measurements of the lower branch (left) and the upper branch (right) of WISE flight #9 down to the BL. The upper row shows latitude vs longitude color coded with the potential temperature. The middle row shows the potential temperature vs latitude color coded with the transport time from the position of measurement to the respective position of the trajectory. The bottom row shows the same content as the middle row only plotted against the longitude instead of the latitude.

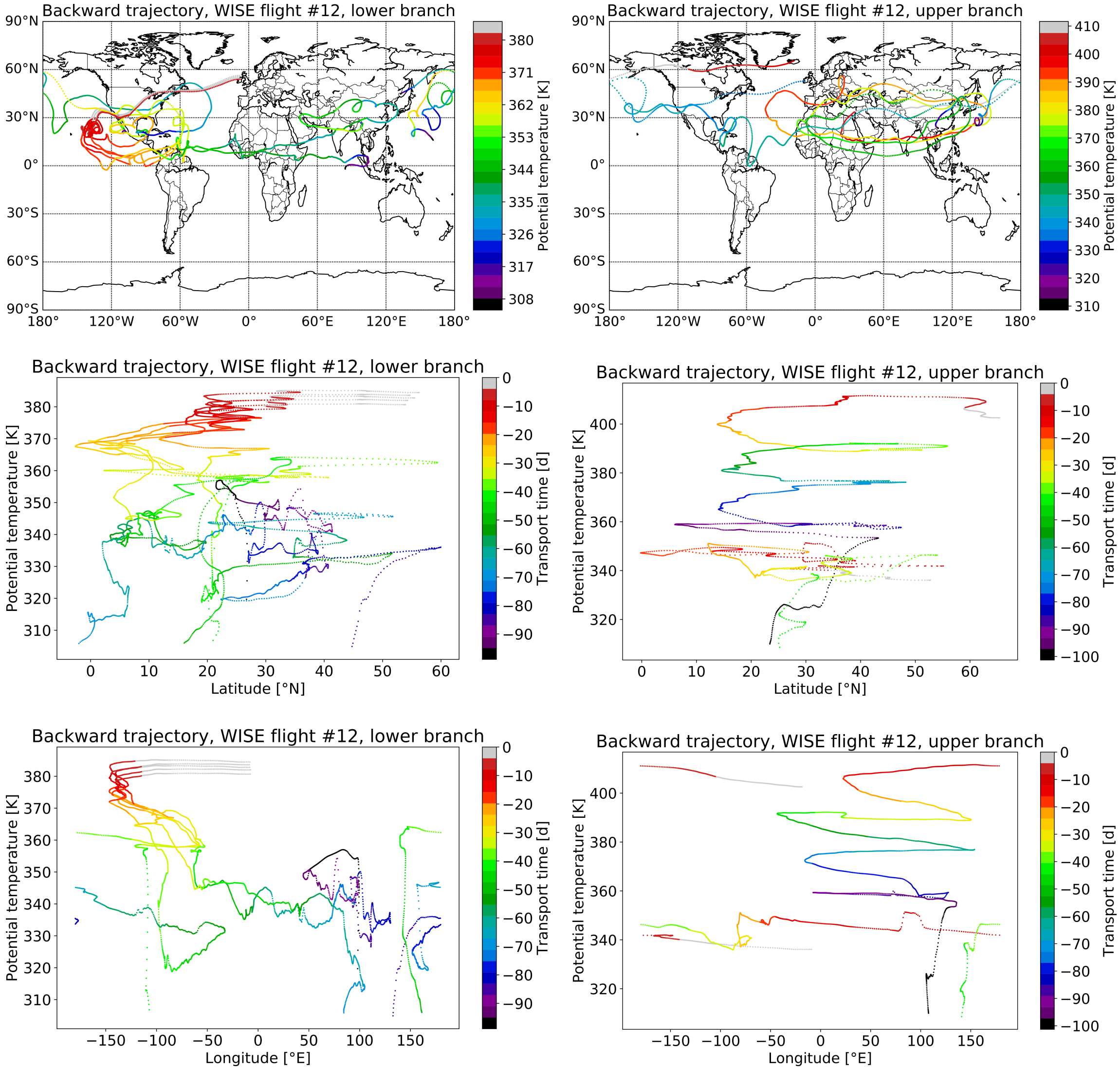

Figure H.6: Backward trajectories of measurements of the lower branch (left) and the upper branch (right) of WISE flight #12 down to the BL. The upper row shows latitude vs longitude color coded with the potential temperature. The middle row shows the potential temperature vs latitude color coded with the transport time from the position of measurement to the respective position of the trajectory. The bottom row shows the same content as the middle row only plotted against the longitude instead of the latitude.

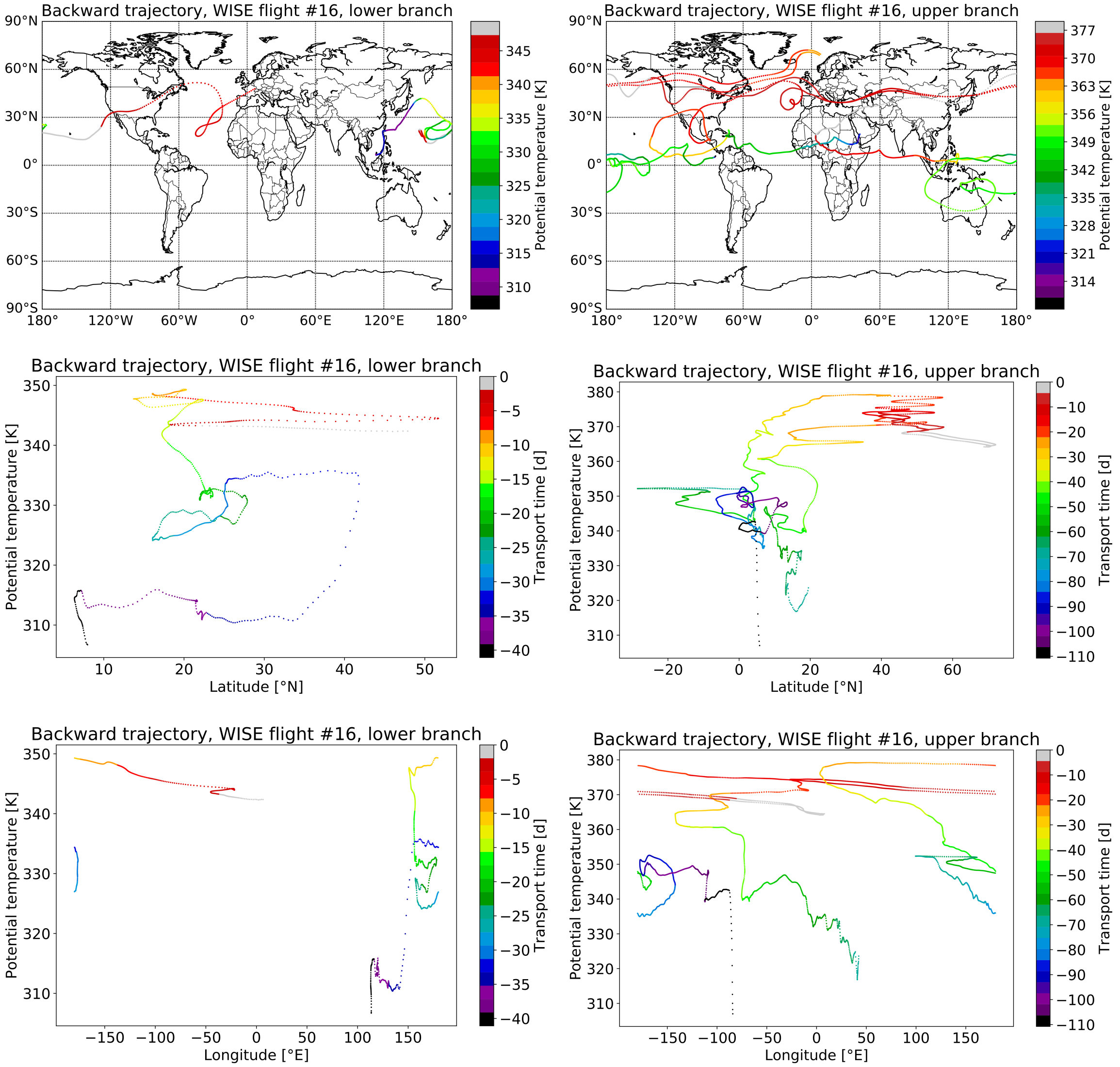

Figure H.7: Backward trajectories of measurements of the lower branch (left) and the upper branch (right) of WISE flight #16 down to the BL. The upper row shows latitude vs longitude color coded with the potential temperature. The middle row shows the potential temperature vs latitude color coded with the transport time from the position of measurement to the respective position of the trajectory. The bottom row shows the same content as the middle row only plotted against the longitude instead of the latitude.

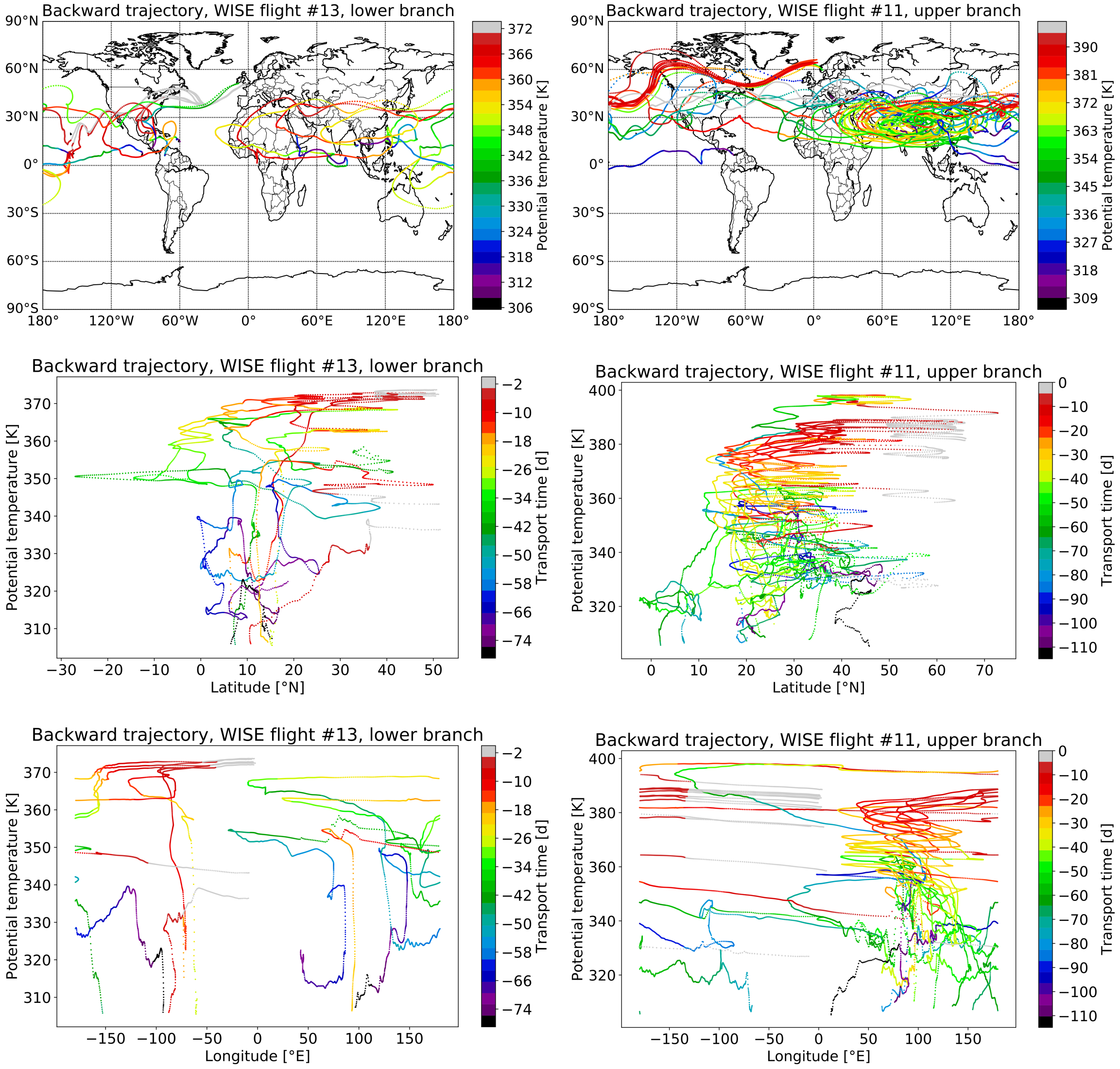

Backward trajectory, WISE flight #13, lower branch

Backward trajectory, WISE flight #11, upper branch

Figure H.8: Backward trajectories of measurements of the lower branch of WISE flight #13 (left) and of the upper branch of WISE flight #11 (right) down to the BL. The upper row shows latitude vs longitude color coded with the potential temperature. The middle row shows the potential temperature vs latitude color coded with the transport time from the position of measurement to the respective position of the trajectory. The bottom row shows the same content as the middle row only plotted against the longitude instead of the latitude.

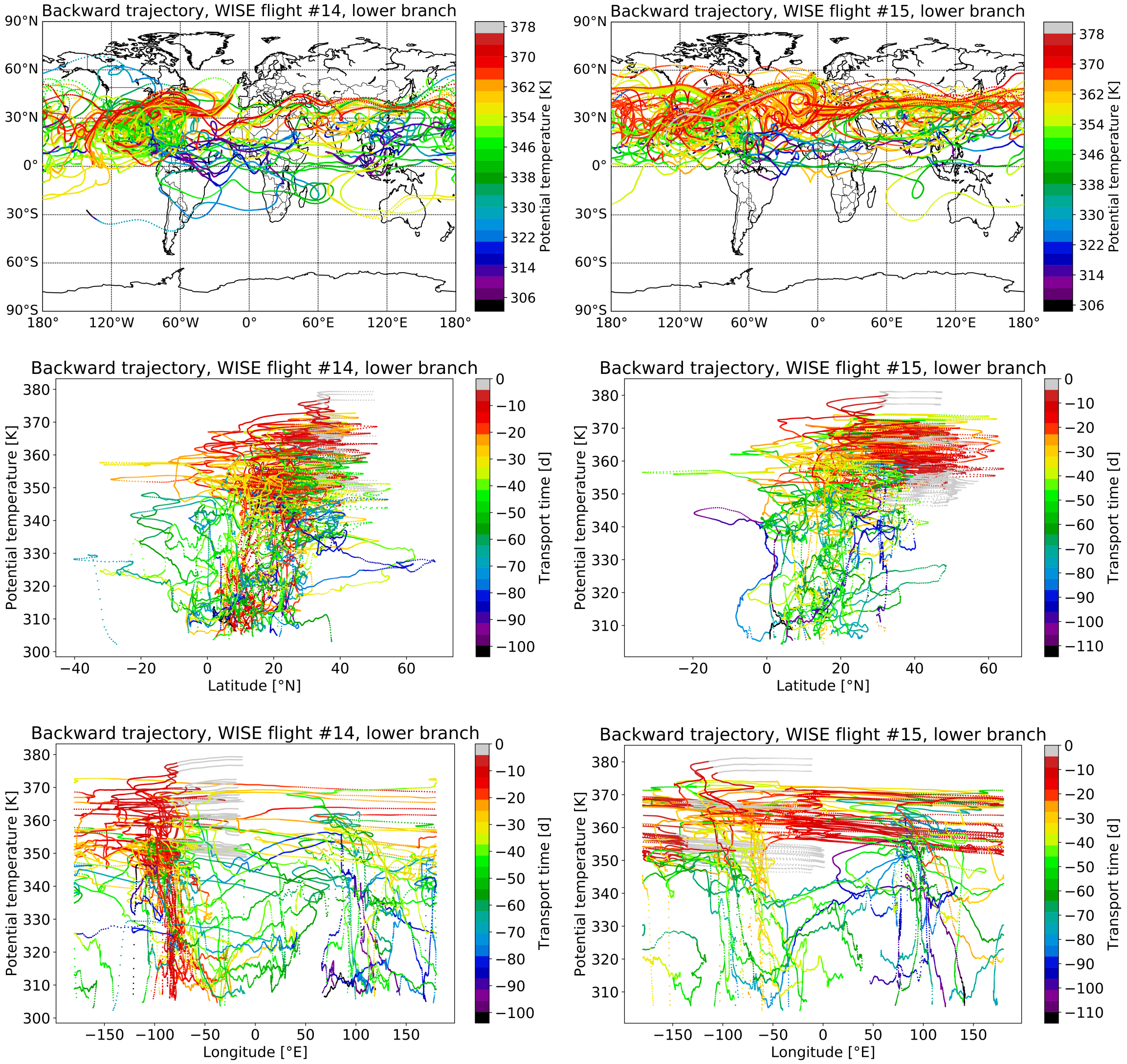

Figure H.9: Backward trajectories of measurements of the lower branch of WISE flight #14 (left) and of WISE flight #15 (right) down to the BL. The upper row shows latitude vs longitude color coded with the potential temperature. The middle row shows the potential temperature vs latitude color coded with the transport time from the position of measurement to the respective position of the trajectory. The bottom row shows the same content as the middle row only plotted against the longitude instead of the latitude.

Figure H.10 shows the full 120 day backward trajectories down to the BL of measurements uplifted by hurricane Maria. The transport pathway of measurements associated with hurricane Maria during flight #8 (October 1) directly enter the extratropics after being lifted up by the convection over the region of Central America. In contrast, measurements during flight #15 (October 19) uplifted by hurricane Maria followed the subtropical jet around the globe before entering the extratropics.

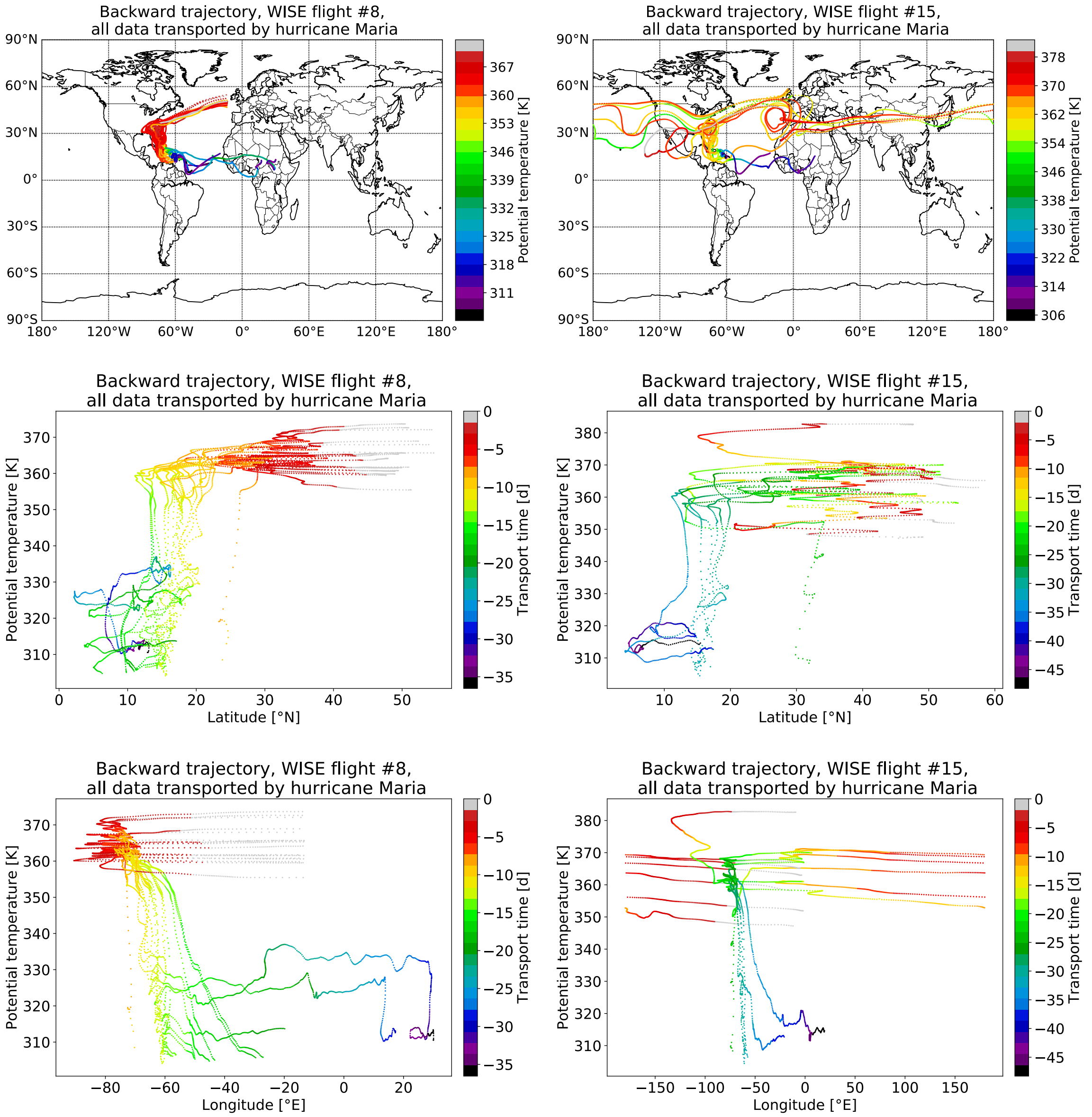

Figure H.10: 120 day backward trajectories down to the BL of measurements uplifted by hurricane Maria during WISE flight #8 (left) and WISE flight #15 (right). The upper row shows latitude vs longitude color coded with the potential temperature. The middle row shows the potential temperature vs latitude color coded with the transport time from the position of measurement to the respective position of the trajectory. The bottom row shows the same content as the middle row only plotted against the longitude instead of the latitude.

Appendix I

Supplemental information about MIRAH and EMeRGE–Asia samples

I.1 Whole air sampler MIRAH and EMeRGE–Asia

MIRAH is mounted in two Do-228 racks. One contains the compressing pump system and the electronics, the other contains 24 Sulfinert™ coated stainless steel canisters. A partially temperature controlled inlet tube with a built in ozone removal unit (reaction on surfaces) connects the instrument with the outside of HALO via the TGI (Trace Gas Inlet). During each flight up to 24 canisters can be filled with air from outside the aircraft usually in sample sizes of 30 l (~ 15 bar). The duration of the filling process and therefore the spatial resolution of the sample is dependent on the pressure outside the aircraft, usually ~ 500 hPa. With an average aircraft speed of 120 m/s (BL) and 180 m/s (UT) the spatial resolution is in the range of 10 km (BL) and 25 km (UT).

To avoid eventual drifts of reactive species inside the canisters the whole air samples are transported as soon as possible to the laboratory at the University of Wuppertal. There they are analyzed for stable carbon isotope ratios in volatile organic compounds (VOC) by the use of a gas chromatograph combustion isotope ratio mass spectrometer (GC-C-IRMS). The residence time in the canisters for the samples discussed in the present work is between 2 and 4 months. Long-term tests up to 143 days showed only very small drifts in carbon isotope ratios for a few VOC after a storage period of several month (vom Scheidt, 2013a). Eventual mixing ratio drifts of CH_2Cl_2 and $CHCl_3$ stored in MIRAH canisters have not been analyzed but other studies on uncoated canisters suggest that only insignificant impacts on the mixing ratios of these species could be expected in the absence of O_3 (e.g. Laube et al., 2008; Schuck et al., 2020).

Mainly for control reasons and compound identification a fraction of the sample is split off before the combustion to be detected by a quadrupole MS monitoring the proper separation of target species. Regular measurements of a monitoring and calibration gas provide the necessary information for data interpretation.

Among others, MIRAH has been deployed on HALO for the EMeRGE–Asia[1] mission. This mission was aimed at the experimental investigation of plumes from major population centers to understand transport and transformation patterns of pollution from Asian conurbations[2]. During March and April 2018 MIRAH collected a total of 133 air samples on 12 scientific flights in Asia, starting from Tainan, Taiwan. In addition, on seven days at the end of March a total of 18 canisters were filled on ground in Manila, Philippines, and Taipeh, Taiwan. The average duration of the sample collection on ground was ~ 9 min due to the use of small pumps. Figure 4.19 shows the averaged locations of sampling for each canister color coded by the averaged flight altitude during the sampling process (circles) as well as the ground-based sampling positions (crosses). In-flight samples mostly were obtained in the BL and lower troposphere. Note that several measurements were obtained at the same location but in different altitudes and might thus be not clearly visible in the plot.

The collected samples from EMeRGE–Asia were measured in the laboratory in Wuppertal. The calibration gas used for the analysis of VOC does not contain information about halogenated VOC. For the analysis of CH_2Cl_2 and $CHCl_3$ the Test air (Table E.2) was occasionally measured between the measurements of the EMeRGE–Asia whole air samples as additional calibration gas. To extract the mixing ratios of those two species within the canisters of sampled air, the fraction of air split to the quadrupole MS was analyzed. With this fraction of the whole sample being variable in volume and mainly serving as monitoring tool relatively imprecise results are expected. More precise would be the results from the IRMS due to much more stable sample sizes but those measurements could not be processed during the time period of the present work. The EMeRGE–Asia measurements cover parts of Asia and are a snapshot over a certain time period, therefore they cannot be used as an emission inventory for CH_2Cl_2 and $CHCl_3$ sources in Asia. Nevertheless, they

---

[1] Effect of Megacities on the transport and transformation of pollutants on the Regional and Global scales – in Asia

[2] http://www.iup.uni-bremen.de/emerge/home/home.html

are representative for the order of magnitude of CH_2Cl_2 and $CHCl_3$ emissions in East Asia and in particular for their correlation.

The MS detector signals of CH_2Cl_2 (m/z = 49) and $CHCl_3$ (m/z = 83) from the analyzed EMeRGE–Asia canisters were integrated with the Data Analysis software as part of the MS control software package ChemStation (Version E.02.02.1431; Agilent Technologies). The resulting peak areas were normalized on the respective sample volume of the whole air sample (assuming a constant split ratio to the MS), linearly detrended and processed according to Section 3.3. Measurement precisions (cf. Section 2.5.3) of CH_2Cl_2 and $CHCl_3$ were calculated from the standard deviation of the calibration measurements to be 12.8 ppt and 2.4 ppt, respectively (~ 22 % of tropospheric background air CAL, Table E.2). In addition the uncertainty on absolute values of the calibration gas have to be taken into account (1.6 % of CH_2Cl_2, 12.7 % of $CHCl_3$, cf. Appendix E.1). Despite the relatively imprecise measurements the data extracted from the EMeRGE–Asia canisters still provide a very useful impression of emission sources from East Asia from where a significant impact on CH_2Cl_2 mixing ratios in the LMS is assumed.

I.2 Supplemental figures about data of EMeRGE–Asia

This section shows some supplemental figures of air samples from the EMeRGE–Asia mission (Section 4.4). Figure I.1 shows the sampling locations of MIRAH during EMeRGE–Asia color coded with (a) the average potential temperature of the aircraft during the sampling procedure, (b) the CH_2Cl_2 mixing ratio, and (c) the $CHCl_3$ mixing ratio. The color scale of (b) is limited from 50 ppt to 500 ppt and the color scale of (c) is limited from 6 ppt to 60 ppt. The plots (b) and (c) show the highest mixing ratios sampled between Taiwan and South Korea close to the coast of eastern China.

Figure I.2 shows the $CHCl_3$-CH_2Cl_2 correlation sampled by MIRAH (left) and on-ground (right) in Taipeh (Taiwan, blue) and Manila (Philippines, red). The correlation of each of the different measurements during EMeRGE–Asia were investigated. With a Pearson's correlation coefficient R = 0.91 the ground samples from Manila show the clearest $CHCl_3$-CH_2Cl_2 correlation. However, the correlation of the in-flight data is almost equally well (R = 0.88). The weakest $CHCl_3$-CH_2Cl_2 correlation was found in the samples collected in Taipeh (R = 0.72) which nevertheless shows a correlation of the two target species. However, the precision of the presented measurements of EMeRGE–Asia samples still need improvement and to this day there is not enough information available on the individual samples to draw any solid conclusions from these $CHCl_3$-CH_2Cl_2 correlations.

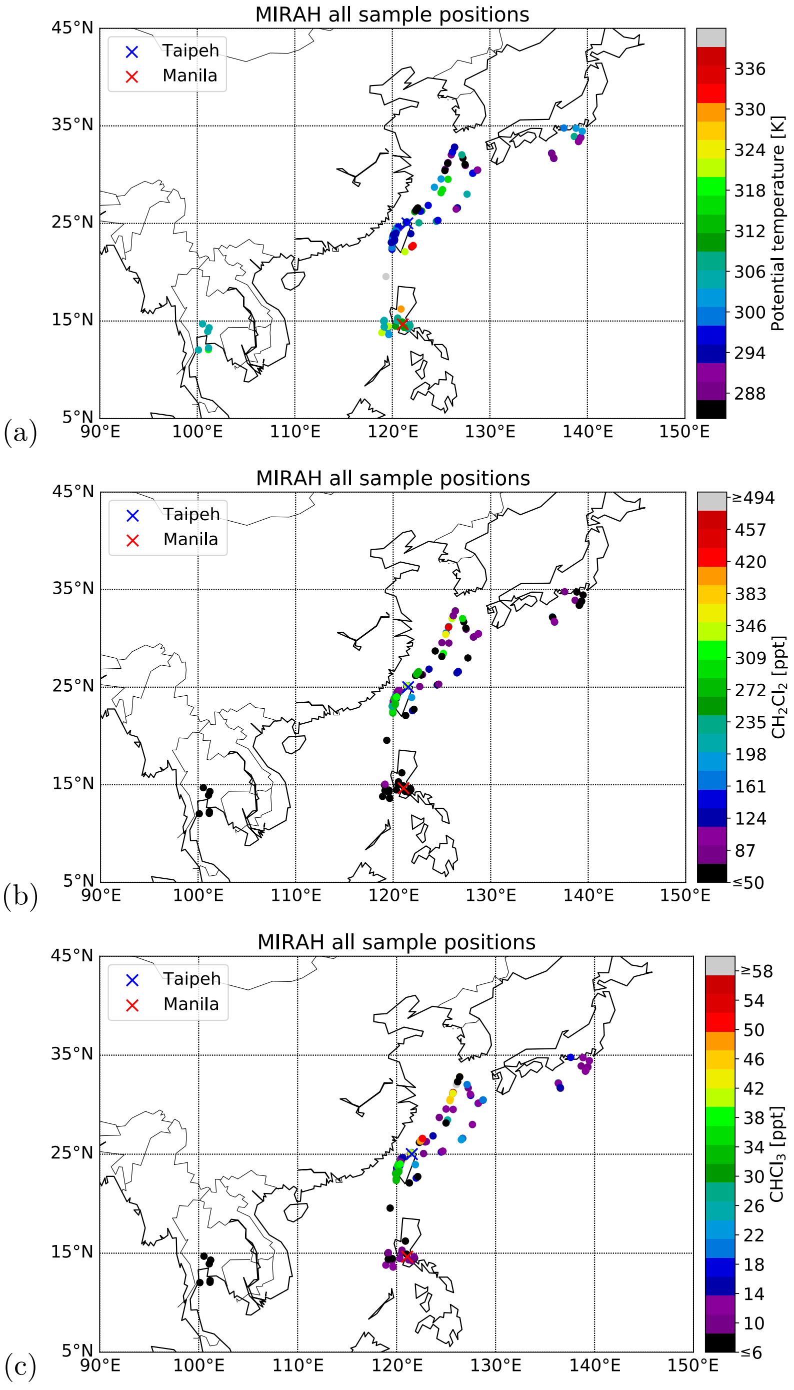

Figure I.1: Location of collected whole air samples with MIRAH during EMeRGE–Asia color coded with (a) the average potential temperature of the aircraft during the sampling process, (b) the CH_2Cl_2 mixing ratio, and (c) the $CHCl_3$mixing ratio of the respective sample. The color scale is limited in map (a) from 50 ppt to 500 ppt and in map (b) from 6 ppt to 60 ppt. Note that several measurements were obtained at the same location but in different altitudes.

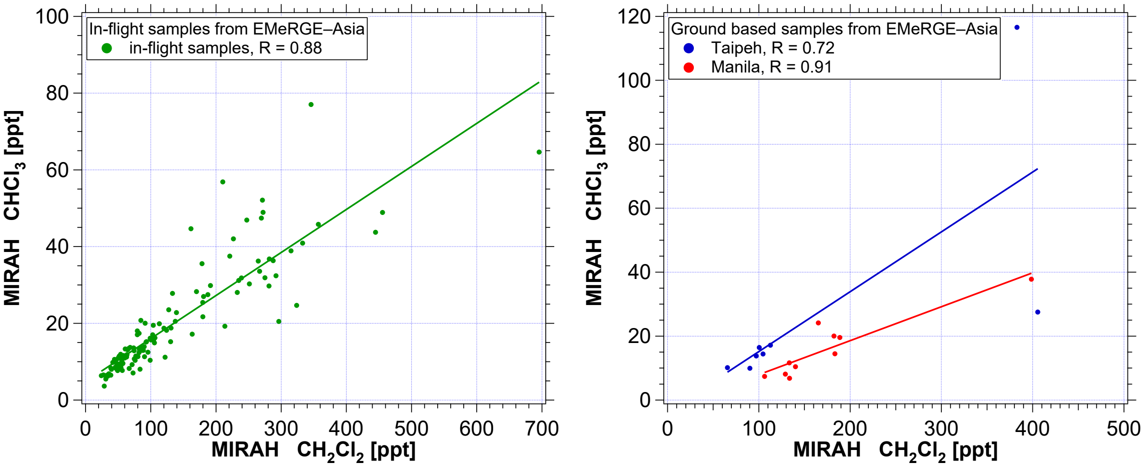

Figure I.2: $CHCl_3$-CH_2Cl_2 correlation sampled during EMeRGE–Asia with MIRAH (left) and on ground (right) in Taipeh (Taiwan, blue) and Manila (Philippines, red). Line fits show the respective Pearson's correlation coefficient R = 0.88 (in-flight data), R = 0.72 (Taipeh), and R = 0.91 (Manila).

Nomenclature

General Abbreviations

AGAGE	Advanced Global Atmospheric Gases Experiment
ASM	Asian Summer Monsoon
ASMA	Asian Summer Monsoon Anticyclone
BAHAMAS	Basis HALO Measurement and Sensor System
BTV	Breakthrough Volume
CARIBIC	Civil Aircraft for the Regular Investigation of the atmosphere Based on an Instrument Container
CLaMS	Chemical Lagrangian Model of the Stratosphere
DWD	Deutscher Wetter Dienst / German Meteorological Service
ECD	Electron Capture Detector
EMeRGE	Effect of Megacities on the transport and transformation of pollutants on the Regional and Global scales
FID	Flame Ionization Detector
FISH	Fast In-situ Stratospheric Hygrometer
GC	Gas Chromatography
GC-C-IRMS	Gas Chromatograph Combustion Isotope Ratio Mass Spectrometer
HAGAR	High Altitude Gas Analyzer
HALO	High Altitude and Long range (research aircraft)

IAGOS	In-Service Aircraft for a Global Observing System
ITCZ	Inter-Tropical Convergence Zone
LMS	Lower most stratosphere
LOD	Limit Of Detection
MBL	Marine Boundary Layer
MIRAH	Measurements of Stable Carbon Isotope Ratios aboard HALO
MS	Mass Spectrometer
MSD	Mass Spectrometer Detector
NH	Northern Hemisphere
NOAA	National Oceanic and Atmospheric Administration
ODP	Ozone Depleting Potential
PHILEAS	Probing High Latitude Export of air from the Asian Summer Monsoon
SH	Southern Hemisphere
SIM	Selective Ion Monitoring
SouthTRAC	Transport and Composition of the Southern Hemisphere UTLS
TACTS	Transport and Composition in the Upper Troposphere and Lower Stratosphere
TGI	Trace Gas Inlet
TTL	Tropical Tropopause Layer
UMAQS	University of Mainz Airborne QCL Spectrometer
UTLS	Upper Troposphere - Lower Stratosphere
VOC	Volatile Organic Compound
WISE	Wave-driven Isentropic Exchange

Chemical Formula

C_2Cl_4	Tetrachloroethylene / TCE
C_2H_2	Acetylene / Ethyne
CCl_4	Tetrachloromethane
CFC-11	Freon 11 / F11 / Trichlorfluormethane / CCl_3F
CFC-113	Freon 113 / F113 / 1,1,2-Trichloro-1,2,2-trifluoroethane / $C_2Cl_3F_3$
CH_2Cl_2	Dichloromethane / DCM
CH_2ClCH_2Cl	1,2-dichloroethane
CH_3Cl	Chloromethane / Methylchloride
$CHCl_3$	Chloroform / Trichloromethane
CHClO	Formyl chloride
CO	Carbon monoxide
$COCl_2$	Phosgene
H_2O	Water
HCl	Hydrogen chloride
HFC-125	Pentafluoroethane / C_2HF_5
HFC-134a	Norflurane / $C_2H_2F_4$
HFC-32	Difluoromethane / CH_2F_2
iso-C_5H_{12}	iso-Pentane
$Mg(ClO_4)_2$	Magnesium perchlorate
N_2	Molecular Nitrogen
N_2O	Nitrous oxide / laughing gas
n-C_5H_{12}	n-Pentane
O_3	Ozone
OH	Hydroxyl radical

Mathematical Abbreviations and Symbols

χ	Mixing ratio
$\overline{X}$	Average of quantity X
σ	Statistical error (can be standard deviation if no statistical independence is given)
τ	Relaxation term in exponential function
$\widetilde{X}$	Median of quantity X
A	(Peak) area
EMG	Exponentially Modified Gauss
h	(Peak) height
m/z	"Mass over charge" / Ionized mass fragment
N	Total number
n	Individual number
RMS	Root Mean Square

Units

ppb	parts per billion (by volume) / 10^{-9}
ppm	parts per million (by volume) / 10^{-6}
ppq	parts per quadrillion (by volume) / 10^{-15}
ppt	parts per trillion (by volume) / pmol/mol / 10^{-12}
UTC	Coordinated Universal Time

List of Figures

List of Tables

Bibliography

Adams, D. K. and Comrie, A. C. The north american monsoon. *Bulletin of the American Meteorological Society*, 78(10):2197–2213, doi:10.1175/1520-0477(1997)078<2197:tnam>2.0.co;2, (1997).

Adcock, K. E., Fraser, P. J., Hall, B. D., Langenfelds, R. L., Lee, G., Montzka, S. A., Oram, D. E., Röckmann, T., Stroh, F., Sturges, W. T., Vogel, B., and Laube, J. C. Aircraft-based observations of ozone-depleting substances in the upper troposphere and lower stratosphere in and above the Asian summer monsoon. *Journal of Geophysical Research*, (in review).

Andrews, S. J., Carpenter, L. J., Apel, E. C., Atlas, E., Donets, V., Hopkins, J. R., Hornbrook, R. S., Lewis, A. C., Lidster, R. T., Lueb, R., Minaeian, J., Navarro, M., Punjabi, S., Riemer, D., and Schauffler, S. A comparison of very short lived halocarbon (VSLS) and DMS aircraft measurements in the tropical west Pacific from CAST, ATTREX and CONTRAST. *Atmospheric Measurement Techniques*, 9(10):5213–5225, doi:10.5194/amt-9-5213-2016, (2016).

Andrews, S. J., Jones, C. E., and Carpenter, L. J. Aircraft measurements of very short-lived halocarbons over the tropical Atlantic Ocean. *Geophysical Research Letters*, 40(5):1005–1010, doi:10.1002/grl.50141, (2013).

Apel, E. C. A fast-GC/MS system to measure C2 to C4 carbonyls and methanol aboard aircraft. *Journal of Geophysical Research*, 108(D20), doi:10.1029/2002jd003199, (2003).

Arneth, A., Denton, F., Agus, F., Elbehri, A., Erb, K., Elasha, B. O., Rahimi, M., Rounsevell, M., Spence, A., and Valentini, R. *Climate Change and Land: an IPCC special report on climate change, desertification, land degradation, sustainable land management, food security, and greenhouse gas fluxes in terrestrial ecosystems*, chapter Framing and Context, pages 49–91. In press, (2019).

Atlas, E. NSF/NCAR GV HIAPER Airborne Instrument Solicitation (HAIS) Advanced Whole Air Sampler. Version 1.0. doi:10.5065/D6DF6PK9, (2014).

Aucott, M. L., McCulloch, A., Graedel, T. E., Kleiman, G., Midgley, P., and Li, Y.-F. Anthropogenic emissions of trichloromethane (chloroform, $CHCl_3$) and chlorodifluoromethane (HCFC-22): Reactive Chlorine Emissions Inventory. *Journal of Geophysical Research: Atmospheres*, 104(D7):8405–8415, doi:10.1029/1999jd900053, (1999).

Barletta, B., Meinardi, S., Simpson, I. J., Atlas, E. L., Beyersdorf, A. J., Baker, A. K., Blake, N. J., Yang, M., Midyett, J. R., Novak, B. J., McKeachie, R. J., Fuelberg, H. E., Sachse, G. W., Avery, M. A., Campos, T., Weinheimer, A. J., Rowland, F. S., and Blake, D. R. Characterization of volatile organic compounds (VOCs) in asian and north american pollution plumes during INTEX-B: identification of specific chinese air mass tracers. *Atmospheric Chemistry and Physics*, 9(14):5371–5388, doi:10.5194/acp-9-5371-2009, (2009).

Beckert, T. Charakterisierung des GC/ECD-Moduls des Messgerätes HAGAR-V im Rahmen der Flugzeugmesskampagne WISE. Master's thesis, Bergische Universität Wuppertal, (2019).

Bethan, S., Vaughan, G., and Reid, S. J. A comparison of ozone and thermal tropopause heights and the impact of tropopause definition on quantifying the ozone content of the troposphere. *Quarterly Journal of the Royal Meteorological Society*, 122(532):929–944, doi:10.1002/qj.49712253207, (1996).

Birner, T., Dörnbrack, A., and Schumann, U. How sharp is the tropopause at midlatitudes? *Geophysical Research Letters*, 29(14):45–1–45–4, doi:10.1029/2002gl015142, (2002).

Bönisch, H., Engel, A., Curtius, J., Birner, T., and Hoor, P. Quantifying transport into the lowermost stratosphere using simultaneous in-situ measurements of SF6 and CO2. *Atmospheric Chemistry and Physics*, 9(16):5905–5919, doi:10.5194/acp-9-5905-2009, (2009).

Boering, K. A., Daube, B. C., Wofsy, S. C., Loewenstein, M., Podolske, J. R., and Keim, E. R. Tracer-tracer relationships and lower stratospheric dynamics: CO_2 and N_2O correlations during SPADE. *Geophysical Research Letters*, 21(23):2567–2570, doi:10.1029/94gl01985, (1994).

Bourtsoukidis, E., Helleis, F., Tomsche, L., Fischer, H., Hofmann, R., Lelieveld, J., and Williams, J. An aircraft gas chromatograph–mass spectrometer System for Organic Fast Identification Analysis (SOFIA): design, performance and a case study of Asian monsoon pollution outflow. *Atmospheric Measurement Techniques*, 10(12):5089–5105, doi:10.5194/amt-10-5089-2017, (2017).

Brewer, A. W. Evidence for a world circulation provided by the measurements of helium and water vapour distribution in the stratosphere. *Quarterly Journal of the Royal Meteorological Society*, 75(326):351–363, doi:10.1002/qj.49707532603, (1949).

Chipperfield, M. P., Dhomse, S., Hossaini, R., Feng, W., Santee, M. L., Weber, M., Burrows, J. P., Wild, J. D., Loyola, D., and Coldewey-Egbers, M. On the Cause of Recent Variations in Lower Stratospheric Ozone. *Geophysical Research Letters*, 45(11):5718–5726, doi:10.1029/2018gl078071, (2018).

Chipperfield, M. P., Hossaini, R., Montzka, S. A., Reimann, S., Sherry, D., and Tegtmeier, S. Renewed and emerging concerns over the production and emission of ozone-depleting substances. *Nature Reviews Earth & Environment*, 1(5):251–263, doi:10.1038/s43017-020-0048-8, (2020).

Claxton, T., Hossaini, R., Wild, O., Chipperfield, M. P., and Wilson, C. On the Regional and Seasonal Ozone Depletion Potential of Chlorinated Very Short-Lived Substances. *Geophysical Research Letters*, 46(10):5489–5498, doi:10.1029/2018gl081455, (2019).

Cox, M. L., Sturrock, G. A., Fraser, P. J., Siems, S. T., Krummel, P. B., and O'Doherty, S. Regional sources of methyl chloride, chloroform and dichloromethane identified from AGAGE observations at Cape Grim, Tasmania, 1998–2000. *Journal of Atmospheric Chemistry*, 45(1):79–99, doi:10.1023/a:1024022320985, (2003).

Daniel, J. S., Velders, G. J. M., Solomon, S., McFarland, M., and Montzka, S. A. Present and future sources and emissions of halocarbons: Toward new constraints. *Journal of Geophysical Research*, 112(D2), doi:10.1029/2006jd007275, (2007).

Danielsen, E. F., Hipskind, R. S., Gaines, S. E., Sachse, G. W., Gregory, G. L., and Hill, G. F. Three-dimensional analysis of potential vorticity associated with tropopause folds and observed variations of ozone and carbon monoxide. *Journal of Geophysical Research*, 92(D2):2103, doi:10.1029/jd092id02p02103, (1987).

Dee, D. P., Uppala, S. M., Simmons, A. J., Berrisford, P., Poli, P., Kobayashi, S., Andrae, U., Balmaseda, M. A., Balsamo, G., Bauer, P., Bechtold, P., Beljaars, A. C. M., van de Berg, L., Bidlot, J., Bormann, N., Delsol, C., Dragani, R., Fuentes, M., Geer, A. J., Haimberger, L., Healy, S. B., Hersbach, H., Hólm, E. V., Isaksen, L., Kållberg, P., Köhler, M., Matricardi, M., McNally, A. P., Monge-Sanz, B. M., Morcrette, J.-J., Park, B.-K., Peubey, C., de Rosnay, P., Tavolato, C., Thépaut, J.-N., and Vitart, F. The ERA-Interim reanalysis: configuration and performance of the data assimilation system. *Quarterly Journal of the Royal Meteorological Society*, 137(656):553–597, doi:10.1002/qj.828, (2011).

Delley, R. Series for the exponentially modified Gaussian peak shape. *Analytical Chemistry*, 57(1):388–388, doi:10.1021/ac00279a094, (1985).

Dethof, A., O'Neill, A., Slingo, J. M., and Smit, H. G. J. A mechanism for moistening the lower stratosphere involving the Asian summer monsoon. *Quarterly Journal of the Royal Meteorological Society*, 125(556):1079–1106, doi:10.1002/qj.1999.49712555602, (1999).

Dettmer-Wilde, K. and Engewald, W., Ed. *Practical Gas Chromatography.* Springer Berlin Heidelberg, doi:10.1007/978-3-642-54640-2, (2014).

Dickerson, R. R., Huffman, G. J., Luke, W. T., Nunnermacker, L. J., Pickering, K. E., Leslie, A. C. D., Lindsey, C. G., Slinn, W. G. N., Kelly, T. J., Daum, P. H., Delany, A. C., Greenberg, J. P., Zimmerman, P. R., Boatman, J. F., Ray, J. D., and Stedman, D. H. Thunderstorms: An Important Mechanism in the Transport of Air Pollutants. *Science*, 235(4787):460–465, doi:10.1126/science.235.4787.460, (1987).

Dobson, G. M. B. Origin and distribution of the polyatomic molecules in the atmosphere. *Proceedings of the Royal Society of London. Series A. Mathematical and Physical Sciences*, 236(1205):187–193, doi:10.1098/rspa.1956.0127, (1956).

Fang, X., Park, S., Saito, T., Tunnicliffe, R., Ganesan, A. L., Rigby, M., Li, S., Yokouchi, Y., Fraser, P. J., Harth, C. M., Krummel, P. B., Mühle, J., O'Doherty, S., Salameh, P. K., Simmonds, P. G., Weiss, R. F., Young, D., Lunt, M. F., Manning, A. J., Gressent, A., and Prinn, R. G. Rapid increase in ozone-depleting chloroform emissions from China. *Nature Geoscience*, 12(2):89–93, doi:10.1038/s41561-018-0278-2, (2018).

Feng, Y., Bie, P., Wang, Z., Wang, L., and Zhang, J. Bottom-up anthropogenic dichloromethane emission estimates from China for the period 2005 - 2016 and predictions of future emissions. *Atmospheric Environment*, 186:241–247, doi:10.1016/j.atmosenv.2018.05.039, (2018).

Fischer, H., Wienhold, F. G., Hoor, P., Bujok, O., Schiller, C., Siegmund, P., Ambaum, M., Scheeren, H. A., and Lelieveld, J. Tracer correlations in the northern high latitude lowermost stratosphere: Influence of cross-tropopause mass exchange. *Geophysical Research Letters*, 27(1):97–100, doi:10.1029/1999gl010879, (2000).

Gentner, D. R., Miller, A. M., and Goldstein, A. H. Seasonal Variability in Anthropogenic Halocarbon Emissions. *Environmental Science & Technology*, 44(14):5377–5382, doi:10.1021/es1005362, (2010).

GERSTEL. *Betriebsanweisung: Online Thermodesorptionssystem TDS G.* GERSTEL GmbH & Co.KG, (2008).

Gettelman, A., Hoor, P., Pan, L. L., Randel, W. J., Hegglin, M. I., and Birner, T. The extratropical upper troposphere and lower stratosphere. *Reviews of Geophysics*, 49(3), doi:10.1029/2011RG000355, (2011).

Gettelman, A. and Wang, T. Structural diagnostics of the tropopause inversion layer and its evolution. *Journal of Geophysical Research: Atmospheres*, 120(1):46–62, doi:10.1002/2014jd021846, (2015).

Giez, A., Mallaun, C., Zöger, M., Dörnbrack, A., and Schumann, U. Static Pressure from Aircraft Trailing-Cone Measurements and Numerical Weather-Prediction Analysis. *Journal of Aircraft*, 54(5):1728–1737, doi:10.2514/1.c034084, (2017).

Götmar, G., Fornstedt, T., and Guiochon, G. Peak Tailing and Mass Transfer Kinetics in Linear Chromatography - Dependence on the Column Length and the Linear Velocity of the Mobile Phase. *J. Chromatogr. A*, 831(1):17–35, (1999).

Gribble, G. W. *Naturally Occurring Organohalogen Compounds - A Comprehensive Update*. Springer Vienna, doi:10.1007/978-3-211-99323-1, (2010).

Gross, J. H. *Mass Spectrometry*. Springer Berlin Heidelberg, doi:10.1007/978-3-642-10711-5, (2011).

Hader, F. Auswertung der Messungen langlebiger Tracer während der Flugzeugmesskampagne POLSTRACC im Winter 2016. Bachelor's thesis, Bergische Universität Wuppertal, (2017).

Hanisco, T. F., Lanzendorf, E. J., Wennberg, P. O., Perkins, K. K., Stimpfle, R. M., Voss, P. B., Anderson, J. G., Cohen, R. C., Fahey, D. W., Gao, R. S., Hintsa, E. J., Salawitch, R. J., Margitan, J. J., McElroy, C. T., and Midwinter, C. Sources, Sinks, and the Distribution of OH in the Lower Stratosphere. *The Journal of Physical Chemistry A*, 105(9):1543–1553, doi:10.1021/jp002334g, (2001).

Hanumanthu, S., Vogel, B., Müller, R., Brunamonti, S., Fadnavis, S., Li, D., Ölsner, P., Naja, M., Singh, B. B., Kumar, K. R., Sonbawne, S., Jauhiainen, H., Vömel, H., Luo, B., Jorge, T., Wienhold, F. G., Dirkson, R., and Peter, T. Strong variability of the Asian Tropopause Aerosol Layer (ATAL) in August 2016 at the Himalayan foothills. *Atmospheric Chemistry and Physics*, doi:10.5194/acp-2020-552, (2020).

Harrison, J. J., Chipperfield, M. P., Hossaini, R., Boone, C. D., Dhomse, S., Feng, W., and Bernath, P. F. Phosgene in the Upper Troposphere and Lower Stratosphere: A Marker for Product Gas Injection Due to Chlorine-Containing Very Short Lived Substances. *Geophysical Research Letters*, 46(2):1032–1039, doi:10.1029/2018gl079784, (2019).

Hegglin, M. I., Boone, C. D., Manney, G. L., and Walker, K. A. A global view of the extratropical tropopause transition layer from Atmospheric Chemistry Experiment Fourier Transform Spectrometer O_3, H_2O, and CO. *Journal of Geophysical Research*, 114, doi:10.1029/2008jd009984, (2009).

Hegglin, M. I. and Shepherd, T. G. Large climate-induced changes in ultraviolet index and stratosphere-to-troposphere ozone flux. *Nature Geoscience*, 2(10):687–691, doi:10.1038/ngeo604, (2009).

Hersbach, H., Bell, B., Berrisford, P., Hirahara, S., Horányi, A., Muñoz-Sabater, J., Nicolas, J., Peubey, C., Radu, R., Schepers, D., Simmons, A., Soci, C., Abdalla, S., Abellan, X., Balsamo, G., Bechtold, P., Biavati, G., Bidlot, J., Bonavita, M., Chiara, G., Dahlgren, P., Dee, D., Diamantakis, M., Dragani, R., Flemming, J., Forbes, R., Fuentes, M., Geer, A., Haimberger, L., Healy, S., Hogan, R. J., Hólm, E., Janisková, M., Keeley, S., Laloyaux, P., Lopez, P., Lupu, C., Radnoti, G., Rosnay, P., Rozum, I., Vamborg, F., Villaume, S., and Thépaut, J.-N. The ERA5 global reanalysis. *Quarterly Journal of the Royal Meteorological Society*, doi:10.1002/qj.3803, (2020).

Hinshaw, J. V. Pinning Down Tailing Peaks. *LCGC*, 12(3), (2009).

Hipskind, R. S., Gregory, G. L., Sachse, G. W., Hill, G. F., and Danielsen, E. F. Correlations between ozone and carbon monoxide in the lower stratosphere, folded tropopause, and maritime troposphere. *Journal of Geophysical Research*, 92(D2):2121, doi:10.1029/jd092id02p02121, (1987).

Holton, J. R., Haynes, P. H., McIntyre, M. E., Douglass, A. R., Rood, R. B., and Pfister, L. Stratosphere-troposphere exchange. *Reviews of Geophysics*, 33(4):403–439, doi:10.1029/95RG02097, (1995).

Hoor, P., Fischer, H., Lange, L., Lelieveld, J., and Brunner, D. Seasonal variations of a mixing layer in the lowermost stratosphere as identified by the CO-O_3 correlation from in situ measurements. *Journal of Geophysical Research: Atmospheres*, 107(D5):ACL 1–1–ACL 1–11, doi:10.1029/2000jd000289, (2002).

Hoor, P., Fischer, H., and Lelieveld, J. Tropical and extratropical tropospheric air in the lowermost stratosphere over Europe: A CO-based budget. *Geophysical Research Letters*, 32(7), doi:10.1029/2004gl022018, (2005).

Hoor, P., Gurk, C., Brunner, D., Hegglin, M. I., Wernli, H., and Fischer, H. Seasonality and extent of extratropical TST derived from in-situ CO measurements during SPURT. *Atmospheric Chemistry and Physics*, 4(5):1427–1442, doi:10.5194/acp-4-1427-2004, (2004).

Hoskins, B. J., McIntyre, M. E., and Robertson, A. W. On the use and significance of isentropic potential vorticity maps. *Quarterly Journal of the Royal Meteorological Society*, 111(470):877–946, doi:10.1002/qj.49711147002, (1985).

Hoskins, B. J. and Rodwell, M. J. A Model of the Asian Summer Monsoon. Part I: The Global Scale. *Journal of the Atmospheric Sciences*, 52(9):1329–1340, doi:10.1175/1520-0469(1995)052<1329:amotas>2.0.co;2, (1995).

Hossaini, R., Atlas, E., Dhomse, S. S., Chipperfield, M. P., Bernath, P. F., Fernando, A. M., Mühle, J., Leeson, A. A., Montzka, S. A., Feng, W., Harrison, J. J., Krummel, P., Vollmer, M. K., Reimann, S., O'Doherty, S., Young, D., Maione, M., Arduini, J., and Lunder, C. R. Recent Trends in Stratospheric Chlorine From Very Short-Lived Substances. *Journal of Geophysical Research: Atmospheres*, 124(4):2318–2335, doi:10.1029/2018jd029400, (2019).

Hossaini, R., Chipperfield, M. P., Montzka, S. A., Leeson, A. A., Dhomse, S. S., and Pyle, J. A. The increasing threat to stratospheric ozone from dichloromethane. *Nature Communications*, 8:15962, doi:10.1038/ncomms15962, (2017).

Hossaini, R., Chipperfield, M. P., Montzka, S. A., Rap, A., Dhomse, S., and Feng, W. Efficiency of short-lived halogens at influencing climate through depletion of stratospheric ozone. *Nature Geoscience*, 8(3):186–190, doi:10.1038/ngeo2363, (2015a).

Hossaini, R., Chipperfield, M. P., Saiz-Lopez, A., Harrison, J. J., von Glasow, R., Sommariva, R., Atlas, E., Navarro, M., Montzka, S. A., Feng, W., Dhomse, S., Harth, C., Mühle, J., Lunder, C., O'Doherty, S., Young, D., Reimann, S., Vollmer, M. K., Krummel, P. B., and Bernath, P. F. Growth in stratospheric chlorine from short-lived chemicals not controlled by the Montreal Protocol. *Geophysical Research Letters*, 42(11):4573–4580, doi:10.1002/2015gl063783, (2015b).

Hösen, M. E. *Untersuchung von Transport, Mischung und Ozonverlust in der arktischen Polarregion im Winter 2009/2010 basierend auf flugzeuggestützten in-situ Messungen.* PhD thesis, Bergische Universität Wuppertal, (2013).

Hsu, C. J. and Plumb, R. A. Nonaxisymmetric Thermally Driven Circulations and Upper-Tropospheric Monsoon Dynamics. *Journal of the Atmospheric Sciences*, 57(9):1255–1276, doi:10.1175/1520-0469(2000)057<1255:ntdcau>2.0.co;2, (2000).

Hsu, K.-J. and DeMore, W. B. Rate constants for the reactions of OH with CH_3Cl, CH_2Cl_2, $CHCl_3$, and CH_3Br. *Geophysical Research Letters*, 21(9):805–808, doi:10.1029/94gl00601, (1994).

Ivanova, E. *Evaluation of transport and ozone loss in the Antarctic polar vortex by using tracer-based coordinates.* PhD thesis, Johann Wolfgang Goethe Universität Frankfurt am Main, (2007).

Jost, H.-J. Mixing events revealed by anomalous tracer relationships in the Arctic vortex during winter 1999/2000. *Journal of Geophysical Research*, 107(D24), doi:10.1029/2002jd002380, (2002).

Kalambet, Y., Kozmin, Y., Mikhailova, K., Nagaev, I., and Tikhonov, P. Reconstruction of chromatographic peaks using the exponentially modified Gaussian function. *Journal of Chemometrics*, 25(7):352–356, doi:10.1002/cem.1343, (2011).

Klemp, M. and Sacks, R. Sample decomposition in an electrically heated cold-trap inlet system for high speed gas chromatography. *Journal of High Resolution Chromatography*, 14(4):235–240, doi:10.1002/jhrc.1240140406, (1991).

Ko, M. K. W., Newman, P. A., Reimann, S., and Strahan, S. E. SPARC Report on Lifetimes of Stratospheric Ozone-Depleting Substances, Their Replacements, and Related Species. Technical report, SPARC, (2013).

Kolusu, S. R., Schlünzen, K. H., Grawe, D., and Seifert, R. Chloromethane and dichloromethane in the tropical Atlantic Ocean. *Atmospheric Environment*, 150:417–424, doi:10.1016/j.atmosenv.2016.11.037, (2017).

Kolusu, S. R., Schlünzen, K. H., Grawe, D., and Seifert, R. Determination of chloromethane and dichloromethane in a tropical terrestrial mangrove forest in

Brazil by measurements and modelling. *Atmospheric Environment*, 173:185–197, doi:10.1016/j.atmosenv.2017.10.057, (2018).

Konopka, P., Günther, G., Müller, R., dos Santos, F. H. S., Schiller, C., Ravegnani, F., Ulanovsky, A., Schlager, H., Volk, C. M., Viciani, S., Pan, L. L., McKenna, D.-S., and Riese, M. Contribution of mixing to upward transport across the tropical tropopause layer (TTL). *Atmospheric Chemistry and Physics*, 7(12):3285–3308, doi:10.5194/acp-7-3285-2007, (2007).

Konopka, P., Grooß, J.-U., Günther, G., Ploeger, F., Pommrich, R., Müller, R., and Livesey, N. Annual cycle of ozone at and above the tropical tropopause: observations versus simulations with the Chemical Lagrangian Model of the Stratosphere (CLaMS). *Atmospheric Chemistry and Physics*, 10(1):121–132, doi:10.5194/acp-10-121-2010, (2010).

Konopka, P. and Pan, L. L. On the mixing-driven formation of the Extratropical Transition Layer (ExTL). *Journal of Geophysical Research: Atmospheres*, 117(D18), doi:10.1029/2012jd017876, (2012).

Koppmann, R., Johnen, F. J., Plass-Dülmer, C., and Rudolph, J. Distribution of methylchloride, dichloromethane, trichloroethene and tetrachloroethene over the north and south Atlantic. *Journal of Geophysical Research*, 98(D11):20517, doi:10.1029/93jd01864, (1993).

Krause, J., Hoor, P., Engel, A., Plöger, F., Grooß, J.-U., Bönisch, H., Keber, T., Sinnhuber, B.-M., Woiwode, W., and Oelhaf, H. Mixing and ageing in the polar lower stratosphere in winter 2015–2016. *Atmospheric Chemistry and Physics*, 18(8):6057–6073, doi:10.5194/acp-18-6057-2018, (2018).

Krautstrunk, M. and Giez, A. The Transition From FALCON to HALO Era Airborne Atmospheric Research. In *Atmospheric Physics*, pages 609–624. Springer Berlin Heidelberg, doi:10.1007/978-3-642-30183-4_37, (2012).

Kunkel, D., Hoor, P., Kaluza, T., Ungermann, J., Kluschat, B., Giez, A., Lachnitt, H.-C., Kaufmann, M., and Riese, M. Evidence of small-scale quasi-isentropic mixing in ridges of extratropical baroclinic waves. *Atmospheric Chemistry and Physics*, 19(19):12607–12630, doi:10.5194/acp-19-12607-2019, (2019).

Kunz, A., Konopka, P., Müller, R., Pan, L. L., Schiller, C., and Rohrer, F. High static stability in the mixing layer above the extratropical tropopause. *Journal of Geophysical Research*, 114(D16), doi:10.1029/2009jd011840, (2009).

Lanning, L. A., Sacks, R. D., Mouradian, R. F., Levine, S. P., and Foulke, J. A. Electrically heated cold trap inlet system for computer-controlled high-speed gas chromatography. *Analytical Chemistry*, 60(18):1994–1996, doi:10.1021/ac00169a036, (1988).

Laturnus, F., Haselmann, K. F., Borch, T., and Grøn, C. Terrestrial natural sources of trichloromethane (chloroform, $CHCl_3$) – An overview. *Biogeochemistry*, 60(2):121–139, doi:10.1023/a:1019887505651, (2002).

Laube, J. C., Engel, A., Bönisch, H., Möbius, T., Worton, D. R., Sturges, W. T., Grunow, K., and Schmidt, U. Contribution of very short-lived organic substances to stratospheric chlorine and bromine in the tropics – a case study. *Atmospheric Chemistry and Physics*, 8(23):7325–7334, doi:10.5194/acp-8-7325-2008, (2008).

Lauther, V. *Entwicklung und Charakterisierung einer Messmethode zur Detektion ausgewählter VOC mittels GC/MS*. Master's thesis, Bergische Universität Wuppertal, (2015).

Leedham-Elvidge, E. C., Oram, D. E., Laube, J. C., Baker, A. K., Montzka, S. A., Humphrey, S., O'Sullivan, D. A., and Brenninkmeijer, C. A. M. Increasing concentrations of CH_2Cl_2 inferred from CARIBIC air samples collected 1998–2012. *Atmospheric Chemistry and Physics*, 15(4):1939–1958, doi:10.5194/acp-15-1939-2015, (2015).

Lelieveld, J., Berresheim, H., Borrmann, S., Crutzen, P. J., Dentener, F. J., Fischer, H., Feichter, J., Flatau, P. J., Heland, J., Holzinger, R., Korrmann, R., Lawrence, M. G., Levin, Z., Markowicz, K. M., Mihalopoulos, N., Minikin, A., Ramanathan, V., de Reus, M., Roelofs, G. J., Scheeren, H. A., Sciare, J., Schlager, H., Schultz, M., Siegmund, P., Steil, B., Stephanou, E. G., Stier, P., Traub, M., Warneke, C., Williams, J., and Ziereis, H. Global Air Pollution Crossroads over the Mediterranean. *Science*, 298(5594):794–799, doi:10.1126/science.1075457, (2002).

Lelieveld, J., Bourtsoukidis, E., Brühl, C., Fischer, H., Fuchs, H., Harder, H., Hofzumahaus, A., Holland, F., Marno, D., Neumaier, M., Pozzer, A., Schlager, H., Williams, J., Zahn, A., and Ziereis, H. The South Asian monsoon–pollution pump and purifier. *Science*, 361(6399):270–273, doi:10.1126/science.aar2501, (2018).

Lelieveld, J., Gromov, S., Pozzer, A., and Taraborrelli, D. Global tropospheric hydroxyl distribution, budget and reactivity. *Atmospheric Chemistry and Physics*, 16(19):12477–12493, doi:10.5194/acp-16-12477-2016, (2016).

Lerner, B. M., Gilman, J. B., Aikin, K. C., Atlas, E. L., Goldan, P. D., Graus, M., Hendershot, R., Isaacman-VanWertz, G. A., Koss, A., Kuster, W. C., Lueb, R. A., McLaughlin, R. J., Peischl, J., Sueper, D., Ryerson, T. B., Tokarek, T. W., Warneke, C., Yuan, B., and de Gouw, J. A. An improved, automated whole air sampler and gas chromatography mass spectrometry analysis system for volatile organic compounds in the atmosphere. *Atmospheric Measurement Techniques*, 10(1):291–313, doi:10.5194/amt-10-291-2017, (2017).

Levine, J. G., Braesicke, P., Harris, N. R. P., Savage, N. H., and Pyle, J. A. Pathways and timescales for troposphere-to-stratosphere transport via the tropical tropopause layer and their relevance for very short lived substances. *Journal of Geophysical Research*, 112(D4), doi:10.1029/2005jd006940, (2007).

Li, D., Vogel, B., Bian, J., Müller, R., Pan, L. L., Günther, G., Bai, Z., Li, Q., Zhang, J., Fan, Q., and Vömel, H. Impact of typhoons on the composition of the upper troposphere within the Asian summer monsoon anticyclone: the SWOP campaign in Lhasa 2013. *Atmospheric Chemistry and Physics*, 17(7):4657–4672, doi:10.5194/acp-17-4657-2017, (2017).

Li, D., Vogel, B., Müller, R., Bian, J., Günther, G., Ploeger, F., Li, Q., Zhang, J., Bai, Z., Vömel, H., and Riese, M. Dehydration and low ozone in the tropopause layer over the Asian monsoon caused by tropical cyclones: Lagrangian transport calculations using ERA-Interim and ERA5 reanalysis data. *Atmospheric Chemistry and Physics*, 20(7):4133–4152, doi:10.5194/acp-20-4133-2020, (2020).

Luong, J., Gras, R., Mustacich, R., and Cortes, H. Low thermal mass gas chromatography: Principles and applications. *Journal of chromatographic science*, 44:253–61, doi:10.1093/chromsci/44.5.253, (2006).

McCulloch, A. Chloroform in the environment: occurrence, sources, sinks and effects. *Chemosphere*, 50(10):1291–1308, doi:10.1016/s0045-6535(02)00697-5, (2003).

McCulloch, A. and Midgley, P. M. The production and global distribution of emissions of trichloroethene, tetrachloroethene and dichloromethane over the period 1988–1992. *Atmospheric Environment*, 30(4):601 – 608, doi:https://doi.org/10.1016/1352-2310(09)50032-5, (1996).

McKenna, D. S. A new Chemical Lagrangian Model of the Stratosphere (CLaMS) 1. Formulation of advection and mixing. *Journal of Geophysical Research*, 107(D16), doi:10.1029/2000jd000114, (2002a).

McKenna, D. S. A new Chemical Lagrangian Model of the Stratosphere (CLaMS) 2. Formulation of chemistry scheme and initialization. *Journal of Geophysical Research*, 107(D15), doi:10.1029/2000jd000113, (2002b).

Millet, D. B., Atlas, E. L., Blake, D. R., Blake, N. J., Diskin, G. S., Holloway, J. S., Hudman, R. C., Meinardi, S., Ryerson, T. B., and Sachse, G. W. Halocarbon Emissions from the United States and Mexico and Their Global Warming Potential. *Environmental Science & Technology*, 43(4):1055–1060, doi:10.1021/es802146j, (2009).

Müller, R., Tilmes, S., Konopka, P., Grooß, J.-U., and Jost, H.-J. Impact of mixing and chemical change on ozone-tracer relations in the polar vortex. *Atmospheric Chemistry and Physics*, 5(11):3139–3151, doi:10.5194/acp-5-3139-2005, (2005).

Müller, S., Hoor, P., Berkes, F., Bozem, H., Klingebiel, M., Reutter, P., Smit, H. G. J., Wendisch, M., Spichtinger, P., and Borrmann, S. In situ detection of stratosphere-troposphere exchange of cirrus particles in the midlatitudes. *Geophysical Research Letters*, 42(3):949–955, doi:10.1002/2014gl062556, (2015).

Müller, S., Hoor, P., Bozem, H., Gute, E., Vogel, B., Zahn, A., Bönisch, H., Keber, T., Krämer, M., Rolf, C., Riese, M., Schlager, H., and Engel, A. Impact of the Asian monsoon on the extratropical lower stratosphere: trace gas observations during TACTS over Europe 2012. *Atmospheric Chemistry and Physics*, 16(16):10573–10589, doi:10.5194/acp-16-10573-2016, (2016).

Montzka, S. A., Krol, M., Dlugokencky, E., Hall, B., Jöckel, P., and Lelieveld, J. Small Interannual Variability of Global Atmospheric Hydroxyl. *Science*, 331(6013):67–69, doi:10.1126/science.1197640, (2011).

Moore, F., Dutton, G., Elkins, J. W., Hall, B., Hurst, D., Nance, J. D., and Thompson, T. PANTHER Data from SOLVE-II Through CR-AVE: A Contrast Between Long and Short Lived Compounds. American Geophysical Union, Fall Meeting 2006, abstract Nr. A41A-0025, (2006).

Moore, R. M. Dichloromethane in North Atlantic waters. *Journal of Geophysical Research*, 109(C9), doi:10.1029/2004jc002397, (2004).

Noij, T., Rijks, J. A., and Cramers, C. A. Problems caused by the activity of Al_2O_3-PLOT columns in the capillary gas chromatographic analysis of volatile organic compounds. *Chromatographia*, 26(1):139–141, doi:10.1007/bf02268138, (1988).

Nützel, M., Podglajen, A., Garny, H., and Ploeger, F. Quantification of water vapour transport from the Asian monsoon to the stratosphere. *Atmospheric Chemistry and Physics*, 19(13):8947–8966, doi:10.5194/acp-19-8947-2019, (2019).

Obersteiner, F., Bönisch, H., Keber, T., O'Doherty, S., and Engel, A. A versatile, refrigerant- and cryogen-free cryofocusing–thermodesorption unit for preconcentration of traces gases in air. *Atmospheric Measurement Techniques*, 9(11):5265–5279, doi:10.5194/amt-9-5265-2016, (2016).

Oram, D. E., Ashfold, M. J., Laube, J. C., Gooch, L. J., Humphrey, S., Sturges, W. T., Leedham-Elvidge, E., Forster, G. L., Harris, N. R. P., Mead, M. I., Samah, A. A., Phang, S. M., Ou-Yang, C.-F., Lin, N.-H., Wang, J.-L., Baker, A. K., Brenninkmeijer, C. A. M., and Sherry, D. A growing threat to the ozone layer from short-lived anthropogenic chlorocarbons. *Atmospheric Chemistry and Physics*, 17(19):11929–11941, doi:10.5194/acp-17-11929-2017, (2017).

Ou-Yang, C.-F., Liao, W.-C., Wang, P.-C., Fan, G.-J., Hsiao, C.-C., Chuang, M.-T., Chang, C.-C., Lin, N.-H., and Wang, J.-L. Construction of a cryogen-free thermal desorption gas chromatographic system with off-the-shelf components for monitoring ambient volatile organic compounds. *Journal of Separation Science*, 39(8):1489–1499, doi:10.1002/jssc.201501336, (2016).

Pan, L. L., Honomichl, S. B., Kinnison, D. E., Abalos, M., Randel, W. J., Bergman, J. W., and Bian, J. Transport of chemical tracers from the boundary layer to stratosphere associated with the dynamics of the Asian summer monsoon. *Journal of Geophysical Research: Atmospheres*, 121(23):14,159–14,174, doi:10.1002/2016jd025616, (2016).

Pan, L. L., Randel, W. J., Gary, B. L., Mahoney, M. J., and Hintsa, E. J. Definitions and sharpness of the extratropical tropopause: A trace gas perspective. *Journal of Geophysical Research: Atmospheres*, 109(D23), doi:10.1029/2004jd004982, (2004).

Pan, L. L., Randel, W. J., Gille, J. C., Hall, W. D., Nardi, B., Massie, S., Yudin, V., Khosravi, R., Konopka, P., and Tarasick, D. Tropospheric intrusions associated with the secondary tropopause. *Journal of Geophysical Research*, 114(D10), doi:10.1029/2008jd011374, (2009).

Park, S., Atlas, E. L., Jiménez, R., Daube, B. C., Gottlieb, E. W., Nan, J., Jones, D. B. A., Pfister, L., Conway, T. J., Bui, T. P., Gao, R.-S., and Wofsy, S. C. Vertical transport rates and concentrations of OH and Cl radicals in the Tropical Tropopause

Layer from observations of CO_2 and halocarbons: implications for distributions of long- and short-lived chemical species. *Atmospheric Chemistry and Physics*, 10(14):6669–6684, doi:10.5194/acp-10-6669-2010, (2010).

Pasch, R. J., Penny, A. B., and Berg, R. Tropical Cyclone Report: Hurricane Maria (AL152017). Technical report, National Hurricane Center, (2019).

Ploeger, F., Günther, G., Konopka, P., Fueglistaler, S., Müller, R., Hoppe, C., Kunz, A., Spang, R., Grooß, J.-U., and Riese, M. Horizontal water vapor transport in the lower stratosphere from subtropics to high latitudes during boreal summer. *Journal of Geophysical Research: Atmospheres*, 118(14):8111–8127, doi:10.1002/jgrd.50636, (2013).

Ploeger, F., Gottschling, C., Griessbach, S., Grooß, J.-U., Guenther, G., Konopka, P., Müller, R., Riese, M., Stroh, F., Tao, M., Ungermann, J., Vogel, B., and von Hobe, M. A potential vorticity-based determination of the transport barrier in the Asian summer monsoon anticyclone. *Atmospheric Chemistry and Physics*, 15(22):13145–13159, doi:10.5194/acp-15-13145-2015, (2015).

Ploeger, F., Konopka, P., Günther, G., Grooß, J.-U., and Müller, R. Impact of the vertical velocity scheme on modeling transport in the tropical tropopause layer. *Journal of Geophysical Research*, 115(D3), doi:10.1029/2009jd012023, (2010).

Plumb, R. A. Stratospheric Transport. *Journal of the Meteorological Society of Japan. Ser. II*, 80(4B):793–809, doi:10.2151/jmsj.80.793, (2002).

Plumb, R. A. Tracer interrelationships in the stratosphere. *Reviews of Geophysics*, 45(4), doi:10.1029/2005rg000179, (2007).

Plumb, R. A. and Ko, M. K. W. Interrelationships between mixing ratios of long-lived stratospheric constituents. *Journal of Geophysical Research: Atmospheres*, 97(D9):10145–10156, doi:10.1029/92jd00450, (1992).

Plumb, R. A., Waugh, D. W., and Chipperfield, M. P. The effects of mixing on tracer relationships in the polar vortices. *Journal of Geophysical Research: Atmospheres*, 105(D8):10047–10062, doi:10.1029/1999jd901023, (2000).

Pommrich, R., Müller, R., Grooß, J.-U., Konopka, P., Ploeger, F., Vogel, B., Tao, M., Hoppe, C. M., Günther, G., Spelten, N., Hoffmann, L., Pumphrey, H.-C., Viciani, S., D'Amato, F., Volk, C. M., Hoor, P., Schlager, H., and Riese, M. Tropical troposphere to stratosphere transport of carbon monoxide and long-lived trace species in the Chemical Lagrangian Model of the Stratosphere (CLaMS). *Geoscientific Model Development*, 7(6):2895–2916, doi:10.5194/gmd-7-2895-2014, (2014).

Popovic, J. M. and Plumb, R. A. Eddy Shedding from the Upper-Tropospheric Asian Monsoon Anticyclone. *Journal of the Atmospheric Sciences*, 58(1):93–104, doi:10.1175/1520-0469(2001)058<0093:esftut>2.0.co;2, (2001).

Poulida, O., Dickerson, R. R., and Heymsfield, A. Stratosphere-troposphere exchange in a midlatitude mesoscale convective complex: 1. observations. *Journal of Geophysical Research: Atmospheres*, 101(D3):6823–6836, doi:10.1029/95jd03523, (1996).

Prinn, R. G., Weiss, R. F., Arduini, J., Arnold, T., DeWitt, H. L., Fraser, P. J., Ganesan, A. L., Gasore, J., Harth, C. M., Hermansen, O., Kim, J., Krummel, P. B., Li, S., Loh, Z. M., Lunder, C. R., Maione, M., Manning, A. J., Miller, B. R., Mitrevski, B., Mühle, J., O'Doherty, S., Park, S., Reimann, S., Rigby, M., Saito, T., Salameh, P. K., Schmidt, R., Simmonds, P. G., Steele, L. P., Vollmer, M. K., Wang, R. H., Yao, B., Yokouchi, Y., Young, D., and Zhou, L. History of chemically and radiatively important atmospheric gases from the Advanced Global Atmospheric Gases Experiment (AGAGE). *Earth System Science Data*, 10(2):985–1018, doi:10.5194/essd-10-985-2018, (2018).

Prinn, R. G., Weiss, R. F., Fraser, P. J., Simmonds, P. G., Cunnold, D. M., Alyea, F. N., O'Doherty, S., Salameh, P., Miller, B. R., Huang, J., Wang, R. H. J., Hartley, D. E., Harth, C., Steele, L. P., Sturrock, G., Midgley, P. M., and McCulloch, A. A history of chemically and radiatively important gases in air deduced from ALE/GAGE/AGAGE. *Journal of Geophysical Research: Atmospheres*, 105(D14):17751–17792, doi:10.1029/2000jd900141, (2000).

Randel, W. J. and Park, M. Deep convective influence on the Asian summer monsoon anticyclone and associated tracer variability observed with Atmospheric Infrared Sounder (AIRS). *Journal of Geophysical Research*, 111(D12), doi:10.1029/2005jd006490, (2006).

Randel, W. J., Park, M., Emmons, L., Kinnison, D., Bernath, P., Walker, K. A., Boone, C., and Pumphrey, H. Asian Monsoon Transport of Pollution to the Stratosphere. *Science*, 328(5978):611–613, doi:10.1126/science.1182274, (2010).

Ratnam, M. V., Babu, S. R., Das, S. S., Basha, G., Krishnamurthy, B. V., and Venkateswararao, B. Effect of tropical cyclones on the stratosphere–troposphere exchange observed using satellite observations over the north Indian Ocean. *Atmospheric Chemistry and Physics*, 16(13):8581–8591, doi:10.5194/acp-16-8581-2016, (2016).

Ray, E. A. Descent and mixing in the 1999–2000 northern polar vortex inferred from in situ tracer measurements. *Journal of Geophysical Research*, 107(D20), doi:10.1029/2001jd000961, (2002).

Riediger, O. *Entwiklung und Einsatz eines flugzeuggetragenen Instrumentes zur in-situ-Messung langlebiger Spurengase in der Stratosphäre*. PhD thesis, Johann Wolfgang Goethe Universität Frankfurt, (2000).

Riese, M., Ploeger, F., Rap, A., Vogel, B., Konopka, P., Dameris, M., and Forster, P. Impact of uncertainties in atmospheric mixing on simulated UTLS composition and related radiative effects. *Journal of Geophysical Research: Atmospheres*, 117(D16), doi:10.1029/2012JD017751. D16305, (2012).

Robertson, A. W., Mechoso, C. R., Ropelewski, C. F., and Grimm, A. M. The American Monsoon Systems. doi:10.7916/D8ST803T, (2005).

Rolf, C., Vogel, B., Hoor, P., Afchine, A., Günther, G., Krämer, M., Müller, R., Müller, S., Spelten, N., and Riese, M. Water vapor increase in the lower stratosphere of the Northern Hemisphere due to the Asian monsoon anticyclone observed during the TACTS/ESMVal campaigns. *Atmospheric Chemistry and Physics*, 18(4):2973–2983, doi:10.5194/acp-18-2973-2018, (2018).

Rudolph, J., Khedim, A., Koppmann, R., and Bonsang, B. Field study of the emissions of methyl chloride and other halocarbons from biomass burning in Western Africa. *Journal of Atmospheric Chemistry*, 22(1-2):67–80, doi:10.1007/bf00708182, (1995).

Sala, S., Bönisch, H., Keber, T., Oram, D. E., Mills, G., and Engel, A. Deriving an atmospheric budget of total organic bromine using airborne in situ measurements from the western pacific area during SHIVA. *Atmospheric Chemistry and Physics*, 14(13):6903–6923, doi:10.5194/acp-14-6903-2014, (2014).

Salawitch, R. J., Fahey, D. W., Hegglin, M. I., McBride, L. A., Tribett, W. R., and Doherty, S. J. Twenty Questions and Answers About the Ozone Layer: 2018 Update, Scientific Assessment of Ozone Depletion: 2018. Technical report, World Meteorological Organization, Geneva, Switzerland, (2019).

Say, D., Ganesan, A. L., Lunt, M. F., Rigby, M., O'Doherty, S., Harth, C., Manning, A. J., Krummel, P. B., and Bauguitte, S. Emissions of halocarbons from India inferred through atmospheric measurements. *Atmospheric Chemistry and Physics*, 19(15):9865–9885, doi:10.5194/acp-19-9865-2019, (2019).

Scheeren, H. A., Lelieveld, J., de Gouw, J. A., van der Veen, C., and Fischer, H. Methyl chloride and other chlorocarbons in polluted air during INDOEX. *Journal of Geophysical Research*, 107(D19), doi:10.1029/2001jd001121, (2002).

Scheeren, H. A., Lelieveld, J., Roelofs, G. J., Williams, J., Fischer, H., de Reus, M., de Gouw, J. A., Warneke, C., Holzinger, R., Schlager, H., Klüpfel, T., Bolder, M., van der Veen, C., and Lawrence, M. The impact of monsoon outflow from India and Southeast Asia in the upper troposphere over the eastern Mediterranean. *Atmospheric Chemistry and Physics*, 3(5):1589–1608, doi:10.5194/acp-3-1589-2003, (2003).

Schmidt, T., Cammas, J.-P., Smit, H. G. J., Heise, S., Wickert, J., and Haser, A. Observational characteristics of the tropopause inversion layer derived from CHAMP/GRACE radio occultations and MOZAIC aircraft data. *Journal of Geophysical Research: Atmospheres*, 115(D24), doi:10.1029/2010jd014284, (2010).

Schuck, T. J., Blank, A.-K., Rittmeier, E., Williams, J., Brenninkmeijer, C. A. M., Engel, A., and Zahn, A. Stability of halocarbons in air samples stored in stainless- steel canisters. *Atmospheric Measurement Techniques*, 13(1):73–84, doi:10.5194/amt-13-73-2020, (2020).

Schuck, T. J., Brenninkmeijer, C. A. M., Slemr, F., Xueref-Remy, I., and Zahn, A. Greenhouse gas analysis of air samples collected onboard the CARIBIC passenger aircraft. *Atmospheric Measurement Techniques*, 2(2):449–464, doi:10.5194/amt-2-449-2009, (2009).

Simmonds, P. G., Manning, A. J., Cunnold, D. M., McCulloch, A., O'Doherty, S., Derwent, R. G., Krummel, P. B., Fraser, P. J., Dunse, B., Porter, L. W., Wang, R. H. J., Greally, B. R., Miller, B. R., Salameh, P., Weiss, R. F., and Prinn, R. G. Global trends, seasonal cycles, and European emissions of dichloromethane, trichloroethene, and tetrachloroethene from the AGAGE observations at Mace Head, Ireland, and Cape Grim, Tasmania. *Journal of Geophysical Research*, 111(D18), doi:10.1029/2006jd007082, (2006).

Simmonds, P. G., O'Doherty, S., Nickless, G., Sturrock, G. A., Swaby, R., Knight, P., Ricketts, J., Woffendin, G., and Smith, R. Automated Gas Chromatograph/Mass Spectrometer for Routine Atmospheric Field Measurements of the CFC Replacement Compounds, the Hydrofluorocarbons and Hydrochlorofluorocarbons. *Analytical Chemistry*, 67(4):717–723, doi:10.1021/ac00100a005, (1995).

Simmonds, P. G., Rigby, M., McCulloch, A., Vollmer, M. K., Henne, S., Mühle, J., O'Doherty, S., Manning, A. J., Krummel, P. B., Fraser, P. J., Young, D., Weiss, R. F., Salameh, P. K., Harth, C. M., Reimann, S., Trudinger, C. M., Steele, L. P., Wang, R. H. J., Ivy, D. J., Prinn, R. G., Mitrevski, B., and Etheridge, D. M. Recent increases in the atmospheric growth rate and emissions of HFC-23 (CHF−3) and the link to HCFC-22 ($CHClF_2$) production. *Atmospheric Chemistry and Physics*, 18(6):4153–4169, doi:10.5194/acp-18-4153-2018, (2018).

Simpson, I. J., Akagi, S. K., Barletta, B., Blake, N. J., Choi, Y., Diskin, G. S., Fried, A., Fuelberg, H. E., Meinardi, S., Rowland, F. S., Vay, S. A., Weinheimer, A. J., Wennberg, P. O., Wiebring, P., Wisthaler, A., Yang, M., Yokelson, R. J., and Blake, D. R. Boreal forest fire emissions in fresh Canadian smoke plumes: C_1-C_{10} volatile organic compounds (VOCs), CO_2, CO, NO_2, NO, HCN and CH_3CN. *Atmospheric Chemistry and Physics*, 11(13):6445–6463, doi:10.5194/acp-11-6445-2011, (2011).

Skoog, D. A. and Leary, J. J. *Instrumentelle Analytik*. Springer Berlin Heidelberg, doi:10.1007/978-3-662-07916-4, (1996).

Solomon, S., Rosenlof, K. H., Portmann, R. W., Daniel, J. S., Davis, S. M., Sanford, T. J., and Plattner, G.-K. Contributions of Stratospheric Water Vapor to Decadal Changes in the Rate of Global Warming. *Science*, 327(5970):1219–1223, doi:10.1126/science.1182488, (2010).

Song, C.-F., Kitamura, Y., Li, S.-H., and Ogasawara, K. Design of a cryogenic CO_2 capture system based on Stirling coolers. *International Journal of Greenhouse Gas Control*, 7:107–114, doi:10.1016/j.ijggc.2012.01.004, (2012).

Spivakovsky, C. M., Logan, J. A., Montzka, S. A., Balkanski, Y. J., Foreman-Fowler, M., Jones, D. B. A., Horowitz, L. W., Fusco, A. C., Brenninkmeijer, C. A. M., Prather, M. J., Wofsy, S. C., and McElroy, M. B. Three-dimensional climatological distribution of tropospheric OH: Update and evaluation. *Journal of Geophysical Research: Atmospheres*, 105(D7):8931–8980, doi:10.1029/1999jd901006, (2000).

Trudinger, C. M., Etheridge, D. M., Sturrock, G. A., Fraser, P. J., Krummel, P. B., and McCulloch, A. Atmospheric histories of halocarbons from analysis of Antarctic firn air: Methyl bromide, methyl chloride, chloroform, and dichloromethane. *Journal of Geophysical Research: Atmospheres*, 109(D22), doi:10.1029/2004jd004932, (2004).

Vogel, B., Günther, G., Müller, R., Grooß, J.-U., Afchine, A., Bozem, H., Hoor, P., Krämer, M., Müller, S., Riese, M., Rolf, C., Spelten, N., Stiller, G. P., Ungermann, J., and Zahn, A. Long-range transport pathways of tropospheric source gases originating in Asia into the northern lower stratosphere during the Asian monsoon season 2012. *Atmospheric Chemistry and Physics*, 16(23):15301–15325, doi:10.5194/acp-16-15301-2016, (2016).

Vogel, B., Günther, G., Müller, R., Grooß, J.-U., Hoor, P., Krämer, M., Müller, S., Zahn, A., and Riese, M. Fast transport from Southeast Asia boundary layer sources to northern Europe: rapid uplift in typhoons and eastward eddy shedding of the Asian monsoon anticyclone. *Atmospheric Chemistry and Physics*, 14(23):12745–12762, doi:10.5194/acp-14-12745-2014, (2014).

Vogel, B., Günther, G., Müller, R., Grooß, J.-U., and Riese, M. Impact of different Asian source regions on the composition of the Asian monsoon anticyclone and of the extratropical lowermost stratosphere. *Atmospheric Chemistry and Physics*, 15(23):13699–13716, doi:10.5194/acp-15-13699-2015, (2015).

Vogel, B., Müller, R., Günther, G., Spang, R., Hanumanthu, S., Li, D., Riese, M., and Stiller, G. P. Lagrangian simulations of the transport of young air masses to the top of the Asian monsoon anticyclone and into the tropical pipe. *Atmospheric Chemistry and Physics*, 19(9):6007–6034, doi:10.5194/acp-19-6007-2019, (2019).

Vogel, B., Pan, L. L., Konopka, P., Günther, G., Müller, R., Hall, W., Campos, T., Pollack, I., Weinheimer, A., Wei, J., Atlas, E. L., and Bowman, K. P. Transport pathways and signatures of mixing in the extratropical tropopause region derived from Lagrangian model simulations. *Journal of Geophysical Research*, 116(D5), doi:10.1029/2010jd014876, (2011).

Volk, C. M. *Stratospheric transport and lifetimes from airborne in-situ observations*. PhD thesis, University of Colorado, Boulder, (1996).

Volk, C. M., Elkins, J. W., Fahey, D. W., Dutton, G. S., Gilligan, J. M., Loewenstein, M., Podolske, J. R., Chan, K. R., and Gunson, M. R. Evaluation of source gas lifetimes from stratospheric observations. *Journal of Geophysical Research: Atmospheres*, 102(D21):25543–25564, doi:10.1029/97jd02215, (1997).

Volk, C. M., Elkins, J. W., Fahey, D. W., Salawitch, R. J., Dutton, G. S., Gilligan, J. M., Proffitt, M. H., Loewenstein, M., Podolske, J. R., Minschwaner, K., Margitan, J. J., and Chan, K. R. Quantifying Transport Between the Tropical and Mid-Latitude Lower Stratosphere. *Science*, 272(5269):1763–1768, doi:10.1126/science.272.5269.1763, (1996).

vom Scheidt, M. *Charakterisierung und Einsatz des Luftprobensammlers MIRAH zur Untersuchung von Verhältnissen stabiler Kohlenstoffisotope in atmosphärischen flüchtigen organischen Verbindungen.* PhD thesis, Bergische Universität Wuppertal, (2013a).

vom Scheidt, M. *Entwicklung und Charakterisierung eines GC/MS-Systems für zeitlich hochaufgelöste Flugzeugmessungen.* PhD thesis, Bergische Universität Wuppertal, (2013b).

Wallace, J. M. and Hobbs, P. V. *Atmospheric Science.* Elsevier LTD, Oxford, (2006).

Waugh, D. W., Plumb, R. A., Elkins, J. W., Fahey, D. W., Boering, K. A., Dutton, G. S., Volk, C. M., Keim, E., Gao, R.-S., Daube, B. C., Wofsy, S. C., Loewenstein, M., Podolske, J. R., Chan, K. R., Proffitt, M. H., Kelly, K. K., Newman, P. A., and Lait, L. R. Mixing of polar vortex air into middle latitudes as revealed by tracer-tracer scatterplots. *Journal of Geophysical Research: Atmospheres*, 102(D11):13119–13134, doi:10.1029/96jd03715, (1997).

Werner, A. *Quantifying Transport Into the Lowermost Stratosphere.* PhD thesis, Johann Wolfgang Goethe Universität Frankfurt, (2007).

Werner, A., Volk, C. M., Ivanova, E. V., Wetter, T., Schiller, C., Schlager, H., and Konopka, P. Quantifying transport into the Arctic lowermost stratosphere. *Atmospheric Chemistry and Physics*, 10(23):11623–11639, doi:10.5194/acp-10-11623-2010, (2010).

WMO. Scientific Assessment of Ozone Depletion: 2014, Global Ozone Research and Monitoring Project-Report No. 55. Technical report, WMO (World Meteorological Organization), Geneva, Switzerland, (2014).

WMO. Scientific Assessment of Ozone Depletion: 2018, Global Ozone Research and Monitoring Project-Report No. 56. Technical report, WMO (World Meteorological Organization), Geneva, Switzerland, (2018).

Wofsy, S. C. HIAPER Pole-to-Pole Observations (HIPPO): fine-grained, global-scale measurements of climatically important atmospheric gases and aerosols. *Philosophical Transactions of the Royal Society A: Mathematical, Physical and Engineering Sciences*, 369(1943):2073–2086, doi:10.1098/rsta.2010.0313, (2011).

Worton, D. R., Sturges, W. T., Schwander, J., Mulvaney, R., Barnola, J.-M., and Chappellaz, J. 20th century trends and budget implications of chloroform and related tri-and dihalomethanes inferred from firn air. *Atmospheric Chemistry and Physics*, 6(10):2847–2863, doi:10.5194/acp-6-2847-2006, (2006).

Yan, X., Konopka, P., Ploeger, F., Podglajen, A., Wright, J. S., Müller, R., and Riese, M. The efficiency of transport into the stratosphere via the Asian and North American summer monsoon circulations. *Atmospheric Chemistry and Physics*, 19(24):15629–15649, doi:10.5194/acp-19-15629-2019, (2019).

Yihui, D. and Chan, J. C. L. The East Asian summer monsoon: an overview. *Meteorology and Atmospheric Physics*, 89(1-4):117–142, doi:10.1007/s00703-005-0125-z, (2005).

Yu, P., Rosenlof, K. H., Liu, S., Telg, H., Thornberry, T. D., Rollins, A. W., Portmann, R. W., Bai, Z., Ray, E. A., Duan, Y., Pan, L. L., Toon, O. B., Bian, J., and Gao, R.-S. Efficient transport of tropospheric aerosol into the stratosphere via the Asian summer monsoon anticyclone. *Proceedings of the National Academy of Sciences*, 114(27):6972–6977, doi:10.1073/pnas.1701170114, (2017).

Zahn, A., Brenninkmeijer, C. A. M., Maiss, M., Scharffe, D. H., Crutzen, P. J., Hermann, M., Heintzenberg, J., Wiedensohler, A., Güsten, H., Heinrich, G., Fischer, H., Cuijpers, J. W. M., and van Velthoven, P. F. J. Identification of extratropical two-way troposphere-stratosphere mixing based on CARIBIC measurements of O_3, CO, and ultrafine particles. *Journal of Geophysical Research: Atmospheres*, 105(D1):1527–1535, doi:10.1029/1999jd900759, (2000).

Zöger, M., Afchine, A., Eicke, N., Gerhards, M.-T., Klein, E., McKenna, D. S., Mörschel, U., Schmidt, U., Tan, V., Tuitjer, F., Woyke, T., and Schiller, C. Fast in situ stratospheric hygrometers: A new family of balloon-borne and airborne Lyman α photofragment fluorescence hygrometers. *Journal of Geophysical Research: Atmospheres*, 104(D1):1807–1816, doi:10.1029/1998jd100025, (1999).

Zhan, R. and Wang, Y. Contribution of tropical cyclones to stratosphere-troposphere exchange over the northwest Pacific: Estimation based on AIRS satellite retrievals and ERA-Interim data. *Journal of Geophysical Research: Atmospheres*, 117(D12), doi:10.1029/2012jd017494, (2012).

Acknowledgments

First of all I want to thank my doctoral supervisor Prof. Dr. C. Michael Volk for giving me the opportunity to work on such a versatile project as HAGAR-V turned out to be, for the many detailed discussions that strongly influenced my way of approaching scientific topics, and for trusting me with responsible tasks to gain priceless experience over the last years.

I also want to thank Dr. Rolf Müller for reviewing this work and for the very helpful comments about my results.

A warm thanks goes to the whole team HAGAR-V. In particular to Dr. Markus vom Scheidt for being my mentor in the early days of HAGAR-V, to Johannes Wintel for all the support on the software side and for so many good conversations which mostly lead to a breakthrough when I got stuck in my working progress, to Emil Gerhardt for the help with IGOR and my first programming steps, and to Andrea Rau for processing the ECD data I used.

In general I want to thank the whole atmospheric physics department of the University of Wuppertal. In particular I want to thank Peter Knieling for the huge support on the electronic side — without him HAGAR-V would only be a piece of metal. Many thanks to Dr. Marc Krebsbach for letting me use the MIRAH data and for many interesting discussions about GC/MS. I also want to thank Dr. Christoph Kalicinsky for always being there when I needed to discuss something and for prove reading parts of my thesis. I also want to thank Prof. Dr. Ralf Koppmann for many encouraging conversations.

Many important parts of HAGAR-V would not be as efficient as they are if it were not for Axel Frohschauer and the team from the physics workshop. Thanks for all the support! I also want to thank Bernd Rose (GERSTEL) for a very cooperative support during the development of the HAGAR-V MS module.

Special thanks go to my colleagues from the University of Frankfurt. To Dr. Tanja Schuck for the calibration of our reference gases and to Timo Keber for many MS advises in my early days and of course for all the good times we shared. I also want to thank everyone from Frankfurt who has supervised HAGAR-V during WISE flights on our shared HALO operator seat: Prof. Dr. Andreas Engel, Timo Keber, Dr. Tanja Schuck, and Fides Lefrancois.

I also want to thank Prof. Dr. Peter Hoor and Björn Kluschat from the University of Mainz for providing the N_2O data and for making the long flight hours appear much shorter by operating on the seat next to me.

A very important part of the presented analysis was the use of CLaMS data and I want to thank everyone who ever supported to make this model such a successful tool. In particular I want to thank Dr. Bärbel Vogel for providing me the emission tracers and the backward trajectories as well as for the fruitful conversations and comments regarding the interpretation of the results and the writing of my thesis.

The working standards of HAGAR-V during WISE were filled with the help of Dr. Anja Claude who also measured the VOC in these standards. Many thanks!

Without HALO I could never have measured in the UTLS. Therefore I want to thank the whole HALO team at DLR for taking care of this great aircraft. In particular I want to thank Dr. Andreas Minikin for the management and for making little miracles happen when needed. A special thanks goes to Tommy Leder for always being uncompromisingly supportive, for keeping HALO extra shiny, and for always keeping up the good spirit that is sorely needed after long working days and nights. I also want to thank the HALO pilots Michael Grossrubatscher, Dr. Marc Puskeiler, Stefan Grillenbeck, and Roland Welser for being very supportive in realizing most of the unconventional flight wishes of the scientists and for flying me safely through hurricane Ophelia. Also many thanks go to the BAHAMAS team for providing the avionic data I used to interpret the presented results.

I want to thank the PIs of the WISE mission Prof. Dr. Martin Riese, Prof. Dr. Peter Hoor, Dr. Daniel Kunkel, and Dr. Martin Kaufmann for realizing this very successful campaign in Ireland. Of course also everyone participating in the WISE campaign took part in the successful execution of this project and I want to thank everyone in the community for that.

Many thanks go to the FISH team from FZ Jülich (in particular Dr. Christian Rolf and Nicole Spelten) for providing live in situ water vapor mixing ratios to let the HAGAR-V operator know when to measure with the MS module during WISE.

Without Enviscope GmbH HAGAR-V would have never been stated to fly on HALO. Thanks a lot for the patience and the quick support when needed.

For the years 2015 to 2018 my work on this theses was mainly financed by the HITEC (Helmholtz Interdisciplinary Doctoral Training in Energy and Climate Research) scholarship funded by the Helmholtz Association.

I also want to thank my family and friends for accompanying me all the way through ups and downs to the present day.

Finally, I want to thank my partner Kathi Hager for everything, including the warm support during my work on this PhD project and for enduring my long absence during campaigns.